Non-equilibrium dynamics of one-dimensional strongly correlated bosons

Dissertation
by

Milena Horvath

submitted to
the Faculty of Mathematics, Computer Science and Physics
of the University of Innsbruck

Advisor: Univ. Prof. Dr. Hanns-Christoph Nägerl
Innsbruck, August 2025

Abstract

Strongly interacting many-body quantum systems give rise to a range of fascinating phenomena, but are notoriously difficult to solve theoretically. With decreasing dimensionality this becomes particularly evident as the quantum fluctuation and interaction effects begin to dominate. Ultracold atoms offer a unique platform to study these phenomena with isolation from the environment and unprecedented control over the system parameters. This thesis investigates fundamental quantum phenomena in one-dimensional many-body systems using ultracold atomic gases as quantum simulators. Here we present four experimental studies that access previously unobserved quantum states and dynamics. First, we demonstrate the creation of Bethe strings, by dynamically tuning interactions in ultracold Bose gases. We measure the binding energies of the strings that reveal bound states of over seven particles, with results matching predictions from generalized hydrodynamics. Second, we observe emergent anyonic correlations through spin-charge separation, where a mobile impurity enables continuous tuning of the statistical phase from bosonic to fermionic, confirmed through asymmetric momentum distributions. Third, we track a mobile impurity in a one-dimensional gas with high temporal and momentum resolution, revealing a quantum bifurcation phenomenon when the impurity exceeds the speed of sound. Finally, we achieve Bose-Einstein condensation in a non-ground-state configuration using cesium atoms in the Zeeman-excited state, identifying regions of magnetic field with sufficiently low inelastic loss processes.

CONTENTS

1 Introduction **1**

1.0.1 Thesis outline . . . 3

1.1 The degenerate Bose gas . . . 4

1.1.1 Condensate transition of a non-interacting Bose gas . . . 4

1.1.2 The interacting Bose gas . . . 6

1.2 Atomic scattering and Feshbach resonances . . . 9

1.2.1 Elastic scattering of ultracold atoms . . . 9

1.2.2 Feshbach resonances . . . 10

1.2.3 Inelastic collisions . . . 13

1.3 The cesium atom . . . 15

1.3.1 Interaction properties of cesium . . . 16

1.4 A brief glimpse at atoms in an optical lattice . . . 17

1.5 Interacting systems in lower dimensions . . . 19

1.5.1 Luttinger liquid . . . 19

1.5.2 The Lieb-Liniger gas . . . 21

1.5.3 Two-particle problem . . . 23

1.5.4 N-particle Bethe ansatz . . . 26

1.5.5 Bethe string states . . . 29

1.6 Emergent hydrodynamics in closed quantum systems . . . 31

1.6.1 Generalized hydrodynamics . . . 33

1.7 Adding a lonely impurity in a Lieb-Liniger gas . . . 34

1.7.1 The Yang-Gaudin model (and emergent anyons) . . . 34

1.7.2 Quantum flutter: the dance between a particle and a hole . . . 38

1.8 Conclusion and outlook . . . 40

1.9 List of publications . . . 44

2 Publication I **47**

2.1 Introduction . . . 48

2.2 Experimental protocol . . . 50

2.3 Release energy measurements . . . 53

2.4 Temperature dependence . . . 53

2.5 Conclusion . . . 55

2.6 Supplementary notes . . . 56

2.6.1 Estimating the populations of atoms in the tubes and fitting the initial conditions . . . 56
2.6.2 Summary of generalized hydrodynamics . . . 59
2.6.3 Determining the release energies of the system via the second moment . . . 60
2.6.4 Atom loss and lifetime measurements . . . 61
2.6.5 Simulating the Tonks-Girardeau regime . . . 62
2.6.6 Characterizing the rapidity distribution in the Tonks-Girardeau regime . . . 63
2.6.7 Generalized hydrodynamics and simulations at finite interactions . . . 64
2.6.8 The virial theorem and generalized hydrodynamics . . . 70

3 Publication II 73
3.1 Introduction . . . 74
3.2 Our system . . . 76
3.3 Asymmetric momentum distributions . . . 76
3.4 Dynamical fermionization . . . 79
3.5 Conclusion . . . 81
3.6 Methods . . . 82
3.6.1 Experiment . . . 82
3.6.2 Role of finite force and finite interaction . . . 83
3.6.3 Exchange symmetry engineering . . . 84
3.6.4 Emergence of anyons via spin-charge separation . . . 86
3.6.5 Anyon-Hubbard model . . . 87
3.6.6 Dynamical evolution with sBHM . . . 88
3.6.7 Swap model . . . 89
3.6.8 Rapidity of anyons in 1D . . . 90
3.7 Supplementary materials . . . 90
3.7.1 Exact solution via Bethe ansatz . . . 90
3.7.2 Lee-Low-Pines transformation . . . 91
3.7.3 Bethe ansatz solution for arbitrary coupling . . . 92
3.7.4 Anyon-Hubbard model in a nutshell . . . 95
3.7.5 Ground-state properties of the swap model $\hat{H}_{\mathrm{Swap}}$ . . . 96
3.7.6 Dynamical evolution governed by $\hat{H}_{\mathrm{sBHM}}$ . . . 97

4 Publication III 101
4.1 Introduction . . . 102
4.2 Experimental procedure . . . 104
4.3 Supersonic vs. subsonic impurity . . . 106
4.4 Relaxation timescales . . . 108
4.5 Steady-state momentum . . . 109
4.6 Conclusion . . . 110
4.7 Supplemenatary materials . . . 110
4.7.1 Superfluidity theory: how Landau criterion interplays with dimensionality of the system and finite impurity mass . . . 110
4.7.2 Momentum distribution of host . . . 114
4.7.3 Interaction dependence . . . 114

4.7.4 Preparation of 1D tubes . . . 114
4.8 Experimental system parameters . . . 115
4.8.1 Impurity creation via RF transfer . . . 115

5 Publication IV **117**
5.1 Introduction . . . 117
5.2 BEC of Cs in the state (3,2). . . . 120
5.3 Exploring the zero crossing around 148 G. . . . 122
5.4 Measurement of loss-coefficients. . . . 124
5.5 Discussion . . . 127
5.6 Materials and methods . . . 129
5.6.1 Fitting of loss measurements . . . 129
5.7 Supplementary notes . . . 130
5.7.1 Calculated resonance parameters . . . 130
5.7.2 Resonances in the range of $B = 138$ to 145 G . . . 130
5.7.3 Three-body recombination processes assisted by spin exchange 131

6 Additional publications **133**

7 Acknowledgements **189**

CHAPTER 1

INTRODUCTION

At the beginning of the twentieth century, experimental observations, such as the photoelectric effect [1], atomic spectra [2], and blackbody radiation [3], revealed phenomena that defied classical explanations and led to the development of quantum theory. Planck's quantization of energy [4], Einstein's photon hypothesis [5], and Bohr's atomic model [6] were pivotal milestones in this scientific revolution. Schrödinger's wave equation provided a powerful framework to describe the microscopic behavior of particles, uncovering the probabilistic and wave-like nature of matter. Despite the initial success of quantum mechanics, it soon became clear that describing systems of many interacting particles is an inherently challenging task. This difficulty arises from the exponential growth of the Hilbert space with the number of constituents, making it infeasible to directly compute the properties of many-body quantum systems on classical computers. As Philip Anderson so eloquently remarked [7], more is different: the collective behavior of interacting quantum particles gives rise to phenomena that cannot be trivially reduced to the sum of their parts.

Understanding emergent quantum phenomena, such as high-temperature superconductivity, low-temperature transport, or quantum magnetism, remains a challenge in modern physics. These effects often originate from strong correlations, and their study and understanding requires simplified minimal low-energy models, such as Heisenberg spin chains, Hubbard-type models, or Luttinger liquids [8–10]. However, even these paradigmatic models can quickly become computationally intractable due to the complexity of their dynamics and the sheer size of the accessible Hilbert space. A key motivation for studying these systems is the realization that there are unexplored corners of the Hilbert space where novel many-body phenomena may emerge. A prime example of this is the observation of many-body quantum scars in Rydberg atom arrays [11]. Understanding the dynamics of interacting many-body systems, especially those far-from-equilibrium, is another frontier of contemporary research. Conventional numerical methods often struggle to capture these dynamics, highlighting the need for alternative approaches to probe the intricate interplay of quantum correlations and interactions. In this context, rapid experimental advances in atomic, molecular, and optical physics have opened new pathways to address these challenges. Ultracold atomic systems, in particular, provide an unprecedented level of control over parameters such as interaction strength, dimensionality, and exter-

nal potentials. These systems have now reached a point where model Hamiltonians from field theory and condensed matter physics can be directly realized in laboratory settings [12–18]. This capability has ushered in the era of "quantum simulation," an idea first proposed by Richard Feynman in 1982 [19]. Feynman suggested that, rather than relying on classical computers, one could design a highly controllable quantum system governed by the same underlying model. Such a system, often referred to as an analog quantum simulator, can experimentally mimic the behavior of the target system, providing a powerful tool for exploring quantum many-body physics. Ultracold atoms allow precise tunability of interactions, lattice geometries, and external fields [20, 21]. Recent developments have turned atomic physics into a highly interdisciplinary research area, bridging condensed matter, statistical physics, and quantum information science. The ability to simulate the dynamics of strongly interacting systems and explore previously inaccessible regimes holds promise for uncovering new quantum phenomena and deepening our understanding of complex many-body systems both in- and out-of-equilibrium.

The first realization of a Bose-Einstein condensates (BEC) in 1994 [22–24] enabled experimental studies of matter-wave interference [25], superfluidity and vortex formation [26, 27], and solitons [28–30]. Building on these concepts, optical lattices offered a platform to access regimes where particle correlations become significant, rendering mean-field approaches insufficient to describe system properties. A trailblazing experiment in this field was the first implementation of the Hubbard model with bosonic atoms, which demonstrated the quantum phase transition from a superfluid to a Mott insulator [31]. Optical lattices have since become a valuable platform for simulating isolated condensed matter phenomena. Their versatility also allows the tuning of the dimensionality of the system. Restricting the motion of atoms along a single line enhances the effect of quantum fluctuations as well as inter-particle correlations, giving rise to novel quantum phases and unique transport properties. The experimental realization of low-dimensional quantum gases [32–34] has facilitated in-depth studies of classic examples in statistical physics. These include Ising chains [35], Tonks-Girardeau [36, 37], super-Tonks [17] and Yang-Yang gases [38], Luttinger liquids [39, 40], as well as the quantum sine-Gordon [14, 41], one-dimensional (1D) Hubbard model [42], and Yang-Gaudin models [43–45]. Compared to higher dimensions, 1D systems are of particular interest due to the accessibility of advanced numerical techniques for their study. Methods such as time-dependent density-matrix renormalization group (t-DMRG) [46–51], Monte Carlo simulations [52, 53], and the recently developed framework of generalized hydrodynamics (GHD) [54, 55] are powerful tools for benchmarking quantum simulations based on ultracold atoms.

The theoretical understanding of 1D quantum systems has developed through several interconnected frameworks that collectively explain the rich physics observed in these experimental platforms. The Luttinger liquid theory [8–10] serves as the universal low-energy effective field theory for gapless 1D quantum systems, where spatial constraints prevent the formation of conventional quasi-particles found in higher-dimensional Fermi liquids [56, 57] and instead give rise to collective excitations characterized by phenomena such as spin-charge separation and power-law decay of correlation functions [58]. This universal theory connects directly to more specific models such as the Lieb-Liniger model [59, 60], which describes bosons with

contact interactions and is exactly solvable via the Bethe ansatz [61], characterizing interactions through a single parameter γ that spans from weakly interacting condensates to the strongly correlated Tonks-Girardeau regime [36, 62, 63] where bosons exhibit fermion-like impenetrability. For fermionic systems, the Yang-Gaudin model [43–45] extends this integrability framework to multi-component fermions with contact interactions. The Yang-Gaudin model also applies to two-component bosons with SU(2) symmetric interaction [64], providing analytical solutions across interaction regimes and displaying Luttinger liquid behavior in the low-energy sector. When a periodic potential is introduced to a Luttinger liquid, the quantum sine-Gordon model [14, 65–67] emerges, describing the competition between kinetic energy and the pinning potential and featuring topological excitations such as solitons and breathers, with the system capable of undergoing a Berezinskii-Kosterlitz-Thouless quantum phase transition [34]. Central to these theories is the concept of integrability, a mathematical property indicating the existence of an infinite set of conserved quantities that drastically alters system dynamics, enabling exact solutions through techniques such as the Bethe ansatz and leading to distinctive physical consequences including ballistic rather than diffusive transport [68]. Unlike in higher dimensions, quasi-particles in 1D systems manifest as collective excitations such as holons and spinons in fermionic systems, phonons in bosonic systems, and solitons in the sine-Gordon model, all of which can be detected through spectroscopic measurements in ultracold atom experiments, providing direct evidence for theoretical predictions that bridge the gap between abstract mathematical frameworks and observable quantum phenomena.

1.0.1 Thesis outline

This thesis is comprised of a collection of articles that were prepared and published as part of the research conducted during the course of this PhD. The primary focus of this research is the study of quantum many-body dynamics of strongly interacting bosons in a 1D setting. This thesis highlights four main publications. This chapter is intended as a broad introduction to these four key publications. We begin with a general overview of BECs with a particular emphasis on the role of interactions. In the same spirit we discuss Feshbach resonances and inelastic collisions as well as the properties of cesium. In the second half of the introductory chapter, we shift our focus to 1D systems, including those with an additional impurity. While the first part of this chapter provides theoretical background for the publication discussed in chapter 5, the latter part serves as a foundation for the publications presented in chapters 2, 3 and 4, respectively. The chapter concludes with a brief outlook on possible future experiments.

In chapter 2, we report the realization of Bethe strings in a 1D Bose gas by sweeping the interactions from the repulsive regime to the attractive regime, passing through the non-interacting point. We measure the rapidity distribution of the system. Additionally, we directly measure the mean binding energy of the strings in the attractive regime, and Tan's contact for both the repulsive as well as the attractive gas. We find excellent agreement when comparing our results with the recently developed theory of GHD.

Chapter 3 discusses the emergence of hard-core anyons in the finite momentum

ground state of a system of 1D bosons with an embedded impurity. The addition of an impurity that strongly interacts with the host results in spin-charge separation. We engineer the spin sector to create a spin wave with variable momenta. This spin texture dresses the charge sector with an emergent flux, leading to a system that can be mapped onto a system of anyons with tunable statistical angle. The anyonic characteristics of this system is measured via the momentum distribution of the impurity. Furthermore, going beyond equilibrium, we demonstrate dynamical fermionization of anyons via the impurity.

In chapter 4 we inject a mobile impurity into a strongly-interacting Bose gas from subsonic to supersonic regimes and track the subsequent relaxation dynamics of the impurity. At odds to conventional wisdom of relaxation, we find that the impurity never comes to a full stop, but instead forms a correlated quantum state with the surrounding gas that travels without friction through the strongly interacting gas. Furthermore, both experimental results and simulations reveal significantly different decay mechanisms for an impurity introduced into the host gas with subsonic versus supersonic velocities, giving new insights into quantum transport in low-dimensional systems.

Finally, in chapter 5 we report the realization of a Bose-Einstein condensate in an excited state of cesium. While this publication does not focus on many-body dynamics, the successful creation of a cesium condensate in a non-ground state opens up access to further interaction regimes for future impurity experiments. In this chapter, we characterize the relevant interaction regimes through both expansion and lifetime measurements. Additionally, we observe unexpectedly high three-body loss in the 40 G region suggesting the presence of a three-body spin-exchange resonance.

1.1 The degenerate Bose gas

The idea of a Bose-Einstein condensate (BEC) traces back to 1924 when, with the inspiration from a paper by Satyendra Nath Bose [69], Albert Einstein first predicted that a gas of non-interacting bosons undergoes a phase transition as its temperature crosses a critical temperature [70]. Specifically the formation of a BEC occurs when the atomic de-Broglie wavelength exceeds the typical interparticle distance, leading to a macroscopic occupation of the absolute ground state. As a result all particles can be described by the same wavefunction. It took another 70 years before this peculiar phase of matter was first experimentally realized using rubidium, sodium and lithium [22–24]. This achievement, building on decades of previous work in laser cooling and trapping [71–73], opened up an extremely rich field of research and gave access to quantum phenomena on a macroscopic scale. In this section we take a brief look at the phase transition to a condensate state and then we will focus on the behavior of a condensate in different interaction regimes. We will follow a similar approach to references [74–76].

1.1.1 Condensate transition of a non-interacting Bose gas

Bose-Einstein condensates are a consequence of the physics underlying the indistinguishability of identical bosons. In particular, for bosons the wavefunction of the total system must remain symmetric under the exchange of particles. In a simplified picture, the formation of a BEC can also be understood by considering the relevant

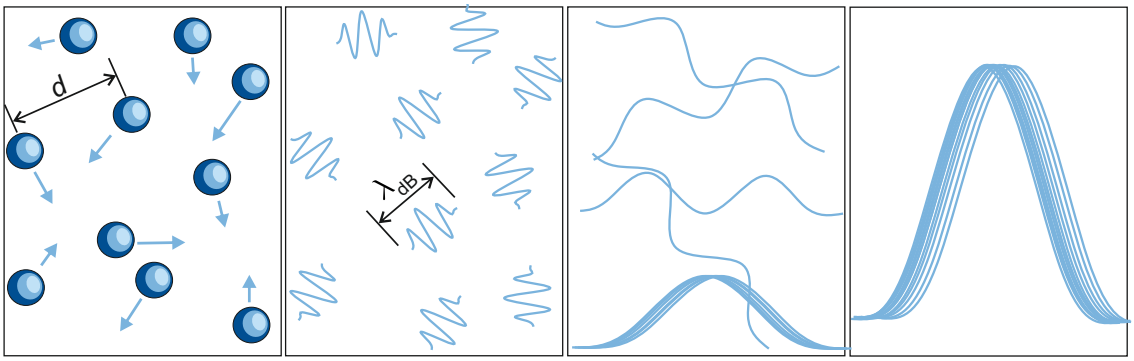

Figure 1.1: Illustration of a Bose-Einstein condensate phase transition. As the temperature of the system is decreases (left to right) the deBroglie wavelength λ_{dB} of each atom increases, until it becomes comparable to the inter-particle distance d and the system undergoes a phase transition to its absolute ground state. This is know as a Bose-Einstein condensate and the entire gas can be described in terms of a single wavefunction. This depiction was adapted from reference [77].

length scales describing the system. The mean interparticle distance d is set by the average spatial density of the gas $n^{-1} = d^3$. Each particle in a gas, with momentum p and mass m, also has an associated wavelength $2\pi\hbar/p$, where $\hbar$ is the reduced Plank's constant. This is known as the deBroglie wavelength λ_{dB}, and for a thermal gas is given by

$$\lambda_{\mathrm{dB}} = (2\pi\hbar^2/mk_{\mathrm{B}}T)^{(1/2)}, \tag{1.1}$$

where T is the temperature of the system, and k_{B} is the Boltzmann constant. At high temperatures, the particles are well localized and $\lambda_{\mathrm{dB}} \ll d$. As the temperature decreases, λ_{dB} increases and the wave nature of the particles as well as the effects of the quantum statistic due to indistinguishability begin to show. When λ_{dB} becomes comparable to the interparticle distance d the individual atomic wavefunctions begin to overlap and eventually collapse to a single wavefunction (see Figure 1.1). This is known as the BEC phase transition.

More quantitatively we can look at the formation of a BEC from the framework of quantum statistical mechanics. Here we assume that the system is non-interacting. We can write the average occupation n_i of the energy state ϵ_i for the ideal Bose gas as

$$n_i = \frac{1}{e^{\beta(\epsilon_i - \mu)} - 1}. \tag{1.2}$$

Here, $\beta = 1/k_{\mathrm{B}}T$ and μ is the chemical potential of the system, which is fixed by the normalization $\sum_i n_i = N$. Equation 1.2 further restrains the chemical potential to be less than the energy of the ground state ϵ_0 in order to prevent negative occupation. As the temperature decreases, μ increases approaching ϵ_0 from below. Simultaneously the occupation number of the ground state n_0 becomes progressively larger. Once a macroscopic occupation of the ground is reached, the system undergoes a phase transition, the BEC transition. The temperature at which this phase transition is induced is known as the critical temperature T_{c}. In this thesis we consider atoms in a 3D harmonic-oscillator potential

$$V_{\mathrm{ext}}(\mathbf{r}) = \frac{1}{2}m\omega_x^2 x^2 + \frac{1}{2}m\omega_y^2 y^2 + \frac{1}{2}m\omega_z^2 z^2, \tag{1.3}$$

where x, y, z are the spatial axes and $\omega_x, \omega_y, \omega_z$ the corresponding trapping frequencies. In this case the transition critical temperature is given by [78, 79]

$$k_{\mathrm{B}} T_c = \hbar\bar{\omega} \left(\frac{N}{\zeta(3)} \right)^{1/3} \approx 0.94 \hbar\bar{\omega} N^{1/3}, \tag{1.4}$$

where $\zeta(3) = 1.202$, with ζ the Riemann zeta function, and $\bar{\omega} = (\omega_x \omega_y \omega_z)^{1/3}$ is the geometrically averaged trapping frequency. The number of condensed atoms N_0 follows [75]

$$\frac{N_0}{N} = 1 - \left(\frac{T}{T_c} \right)^3. \tag{1.5}$$

The cubic scaling of the temperature is a consequence of the harmonic trapping potential and hence will differ for different potentials. The characteristic length scale of the (non-interacting) condensate is given by the harmonic oscillator length

$$a_{\mathrm{ho}} = \left(\frac{\hbar}{m\bar{\omega}} \right)^{1/2}. \tag{1.6}$$

Both in coordinate space as well as momentum space, a condensate cloud is more peaked than a noncondensed sample, making it a commonly used signature to experimentally detect the presence of a condensate [77].

1.1.2 The interacting Bose gas

Up to this point we have only considered a non-interacting Bose gas. We will now turn to an interacting Bose gas, specifically a non-uniform weakly interacting Bose gas trapped in an external potential. Our focus in this section will be on the lowest energy state of the condensate in different interaction regimes.

At low enough energies, the scattering properties of a Bose gas can be described by a single parameter a, the s-wave scattering length, which we will introduce in more detail in section 1.2. In the limit where the average inter-particle spacing is much larger than the scattering length $n|a|^3 \ll 1$, the system is said to be dilute [75]. Here, interacting bosons confined by an external potential can be described by a mean-field approach. For temperatures below the critical temperature where the condensate fraction is substantial, thermal excitations become negligible, allowing the state of the condensate to be described in terms of a non-linear Schrödinger equation, the time-dependent Gross-Pitaevskii (GP) equation [80, 81]

$$i\hbar \frac{\partial}{\partial t} \psi(\mathbf{r}, t) = \left(-\frac{\hbar^2 \nabla^2}{2m} + V_{\mathrm{ext}}(\mathbf{r}) + g|\psi(\mathbf{r}, t)|^2 \right) \psi(\mathbf{r}, t). \tag{1.7}$$

Here ψ is the condensate wavefunction, V_{ext} is the external trapping potential, g the interaction parameter, which is given by

$$g = \frac{4\pi\hbar^2 a}{m}. \tag{1.8}$$

The GP equation describes the macroscopic behavior of the condensate in the weakly interacting regime ($n|a|^3 \ll 1$). In the case of a stationary states $\psi(\mathbf{r}, t) =$

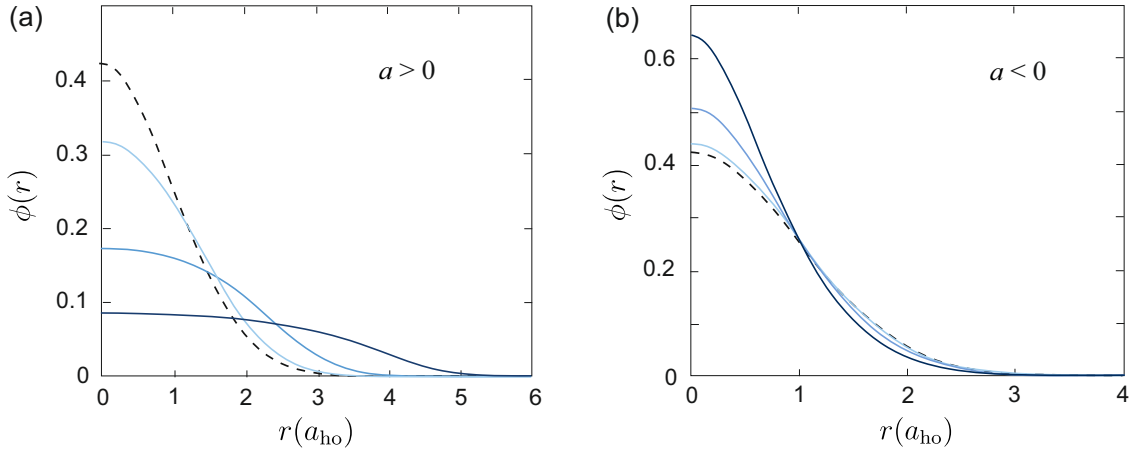

Figure 1.2: Solutions of time-independent Gross-Pitaevskii equation (Eq. (1.9)) for an isotropic harmonic trap and different values of $N|a|/a_{\rm ho}$. Repulsive (attractive) case is shown in (a) ((b)). From light to dark the three solid curves correspond to $N|a|/a_{\rm ho} = 0.5, 0.3$, and 0.1 ($N|a|/a_{\rm ho} = 1, 10$, and 100), respectively. The dashed curve is the result for a non-interacting condensate. Figure is adapted from reference [82].

$\phi(\mathbf{r})\exp(-i\mu t/\hbar)$, where $\phi(\mathbf{r})$ is normalized to the total number of particles $\int \mathrm{d}^3 r|\phi|^2 = N$, Eq. (1.7) simplifies down to the time-independent Gross-Pitaevskii equation

$$\left(-\frac{\hbar^2\nabla^2}{2m} + V_{\rm ext}(\mathbf{r}) + g|\phi(\mathbf{r})|^2 - \mu\right)\phi(\mathbf{r}) = 0. \tag{1.9}$$

For a non-interacting condensate ($g = 0$) Eq. (1.9) is equivalent to the Schrödinger equation for the single-particle Hamiltonian. In the stationary case, and for real $\phi(\mathbf{r})$, the condensate energy is a functional of the density distribution $n(\mathbf{r}) = |\phi(\mathbf{r})|^2$ [82]

$$E[n] = \int \mathrm{d}\mathbf{r}\left[\frac{\hbar^2}{2m}|\nabla n^{1/2}|^2 + nV_{\rm ext}(\mathbf{r}) + \frac{gn^2}{2}\right] = E_{\rm kin} + E_{\rm ho} + E_{\rm int}. \tag{1.10}$$

This equation is comprised of three terms. The first term is the kinetic energy of the condensate $E_{\rm kin}$. Also known as quantum pressure, $E_{\rm kin}$ arises from the uncertainty principle. For a uniform system, with periodic boundary conditions, the quantum pressure is equal to zero because $\nabla n = 0$ [82]. The second term, $E_{\rm ho}$, corresponds to the harmonic oscillator energy and the final term, $E_{\rm int}$, represents the mean-field interaction energy.

For this entire discussion we have assumed that the system is dilute and weakly interacting, i.e., $n|a|^3 \ll 1$. However, it is important to note that because $n|a|^3$ is small, it does not necessarily mean that the effects of interactions are negligible. In order to estimate the importance of the interactions, we must compare the interaction energy with the kinetic energy of the atoms in the trap. It is therefore useful to define the dimensionless quantity $N|a|/a_{\rm ho}$, which is proportional to the ratio of $E_{\rm int}/E_{\rm kin}$ for the ground state of the harmonic oscillator [82].

In the case of repulsive interactions there are two distinct limits: the ideal-gas limit ($N|a|/a_{\rm ho} \ll 1$) and the Thomas-Fermi limit ($N|a|/a_{\rm ho} \gg 1$). In the ideal-gas limit the interactions become negligible and the kinetic energy term in Eq. (1.9)

dominates, thus the density distribution of the condensate is directly determined by the external trapping potential V_{ext}. In the Thomas-Fermi limit, in contrast, the interaction term is large while the kinetic energy can be neglected. In this case the density distribution takes the form

$$n(\mathbf{r}) = |\phi(\mathbf{r})|^2 = \frac{\mu - V_{\text{ext}}(\mathbf{r})}{g}. \tag{1.11}$$

Equation 1.11 is only valid for positions such that $\mu - V_{\text{ext}}(\mathbf{r}) \geq 0$. For $\mu - V_{\text{ext}}(\mathbf{r}) < 0$ the condensate density distribution is equal to zero. In the case of a harmonic potential this leads to a density distribution with an inverted parabolic profile. The size of the condensate along each spatial dimension is no longer determined by the harmonic oscillator length, but instead given by the much larger Thomas-Fermi radius

$$R_i = a_{\text{ho}} \frac{\bar{\omega}}{\omega_i} \left(\frac{15Na}{a_{\text{ho}}} \right)^{1/5}, \qquad i = x, y, z. \tag{1.12}$$

Now, let us consider a condensate with attractive interactions. The behavior in this regime differs significantly from the repulsive case, as illustrated in Figure 1.2, which shows the numerical solution of Eq. (1.9) for various values of $N|a|/a_{\text{ho}}$ for both attractive ($a < 0$) and repulsive ($a > 0$) interactions. For repulsive interactions the condensate broadens as $N|a|/a_{\text{ho}}$ increases. For attractive interactions, the condensate density increases at the center of the trap, leading to a narrower spatial distribution. If the interactions are weak enough, this increase is countered by the quantum pressure and the system is stabilized. However, beyond a certain threshold, this stabilization is no longer possible and the system collapses [82]. This behavior results from a competition between three energies: E_{int}, E_{kin} and E_{ho}. The interaction energy is negative and drives the collapse, while E_{kin} resists compression and E_{ho}, provides external confinement. If the interaction energy becomes too strong, the kinetic energy cannot prevent the condensate from collapsing. To estimate the critical number of atoms leading to a collapse, we consider a simple scaling argument. If the condensate has a characteristic size R, the kinetic energy scales as $E_{\text{kin}} \sim \hbar^2/(mR^2)$, the interaction energy for N atoms as $E_{\text{int}} \sim gN^2/R^3$, and the potential energy for an isotropic harmonic trap $V_{\text{ext}} = 1/2m\omega^2 r^2$ as $E_{\text{ho}} = m\omega^2 R^2$. In order for the condensate to be stable the kinetic, potential and interaction energies must balance. However, for large N, the attractive interaction energy term grows faster than the stabilizing kinetic energy. This leads to a maximum critical number of atoms N_{cr} beyond which no equilibrium solution exists. In a harmonic trap, the point of collapse occurs at [74]

$$N_{\text{cr}} = 0.575 \frac{a_{\text{ho}}}{|a|}. \tag{1.13}$$

It is worth emphasizing that this behavior is dependent on the existence of a trapping potential. In a uniform system without an external potential, where there is no quantum pressure, a Bose gas with attractive interactions is always unstable [82]. Furthermore, at high densities, additional effects such as three-body losses and two-body spin-exchange collisions become significant, and thus close to collapse, the GP equation is no longer an accurate description of the system.

1.2 Atomic scattering and Feshbach resonances

Successfully cooling atoms below the critical temperature largely relies on the types of collisional processes present in the sample. A watershed moment in the realization of the first condensate in 1995 was the use of evaporative cooling [22, 23, 83]. To this day, this technique remains the primary method for achieving a BEC. It involves gradually lowering the depth of a magnetic or optical trap holding pre-cooled atoms. This enables hot atoms to escape while the remaining sample thermalizes to a lower temperature. The efficiency of this process is determined by the ratio of elastic to inelastic collision rates. While elastic collisions determine the rate of equilibration of the system, inelastic collisions lead to heating and atomic loss from the trap. However, not only the condensate formation rate, but also the decay rates and coherence times are governed by inelastic collisions. Understanding both elastic as well as inelastic collisions not only allows for the optimization of the cooling process but also provides an insight into the stability and the dynamics of the BEC. In this section we will begin by briefly considering scattering theory. We will then move onto discussing Feshbach resonances, before finishing with inelastic collisions.

1.2.1 Elastic scattering of ultracold atoms

A cloud of ultracold atoms is orders of magnitude more dilute than the air around us. Due to the low density, the dominant contribution to the interaction properties can be described using a two-body scattering approximation. Here, we briefly discuss the scattering process between two distinguishable particles with equal mass m and relative wavevector k, which interact via a two-body potential $V(\mathbf{r})$, where $\mathbf{r}$ is the relative coordinate. In the case of neutral atoms, the interaction potential consists of two main contributions. At short range, interactions are dominated by exchange forces, which arise due to the Pauli exclusion principle and electron wavefunction overlap. At long range, the interaction is governed by van der Waals forces, which are a result of induced electric dipoles. The scattering potential has a characteristic length scale known as the van der Waals length l_{vdW}, where C_6 is a species-dependent coefficient known as the van der Waals coefficient. For sufficiently large separations $r \gg l_{\mathrm{vdW}} = (mC_6/\hbar^2)^{1/4}$, the potential follows the form $-C_6/r^6$.

To solve this two-body scattering problem analytically, we apply standard techniques from quantum mechanics. Detailed discussions on the scattering theory described below can be found in many other texts, such as in references [76, 84–86]. In a nutshell the two-body problem reduced to a single particle problem by writing the Hamiltonian in terms of the center-of-mass and relative coordinates of the two interacting atoms. Furthermore, assuming spherically symmetric potential $V(\mathbf{r}) = V(r)$, the solution of the resulting relative Hamiltonian can then be formulated in terms of the superposition of partial waves with quantized angular momentum $L = 0, 1, 2, \ldots$. The effect of the interaction potential itself reduces down to a relative phase shift δ_L between the incident and the outgoing wave. At ultralow temperatures collisions higher order partial wave contributions are suppressed, leading to the entire scattering process for bosons being characterized by a single quantity, the s-wave scattering length

$$a = -\lim_{k\to 0} \frac{\tan \delta_0(k)}{k}. \tag{1.14}$$

For $a > 0$ the interactions between the atoms are repulsive, while for $a < 0$ they are attractive. In this thesis a will be given in units of the Bohr radius $a_0 = 5.29 \times 10^{-11}$ m. In order to get an insight into the different interaction limits, one can write the cross-section of the scattering, for two identical bosons, in terms of the scattering length

$$\sigma = \frac{8\pi a^2}{1 + k^2 a^2}. \tag{1.15}$$

Two distinct limits clearly emerge from this equation [87]. The first is the unitarity limit, where $k^2 a^2 \gg 1$. In this regime, the scattering cross-section becomes independent of the scattering length and is instead characterized by the collision energy as $\sigma = 8\pi/k^2$. The second limit, $k^2 a^2 \ll 1$, is the zero-energy limit, in which the cross-section is entirely described by the scattering length and simplifies to $\sigma = 8\pi a^2$.

A deeper understanding of the different interaction regimes can be gained by considering the relevant length scales of the scattering problem. Two length scales are particularly important here. The first is the de Broglie wavelength λ_{dB}. When $a \gg \lambda_{\mathrm{dB}}$ the scattering process is dominated by the relative collision energy. . The second is the previously introduced van der Waals length l_{vdW}, which characterizes the range of the interaction potential. When $a \gg l_{\mathrm{vdW}}$ the scattering process is independent of the details of the scattering potential and is entirely characterized by the scattering length. This is known as the universal regime. The concept of "universality" is frequently used to describe behavior that is independent of the specifics of a particular system. Such behavior is often a consequence of separation of scales. In the case of two interacting atoms, this separation arises between long- and short-range physics.

Thus far, we have considered atomic collisions involving a single interaction potential, ignoring contributions from other atomic states. The scattering length can, however, be dramatically modified when a bound state exists near the scattering threshold. In the universal regime ($a \gg l_{\mathrm{vdW}}$), the energy of such a bound state E_{b} is inversely proportional to the square of the scattering length via [88]

$$E_{\mathrm{b}} = \frac{\hbar^2}{2 m_{\mathrm{r}} a^2} \tag{1.16}$$

where m_{r} is the reduced mass of the participants. For two atoms with equal mass, as is the case throughout this thesis, $m_{\mathrm{r}} = m/2$. These weakly bound states are known as halo states due to the extremely large spatial extent of their wavefunctions [89]. In ultracold systems, halo states can be coherently created near scattering resonances, known as Feshbach resonances [90, 91].

1.2.2 Feshbach resonances

An extraordinary feature of ultracold gases is the controllability of elastic two-body interactions via so-called Feshbach resonances. These resonances were predicted by Ugo Fano in 1935 in the context of atomic physics [92–94]. Independently Herman Feshbach described them in terms of nuclear phyiscs in the late 1950s and early 1960s [95, 96]. The first experimental observation of these resonances in ultracold systems dates back to 1998 [97]. Feshbach resonances arise when two interacting atoms couple into a bound state, causing a divergence of the scattering length. This

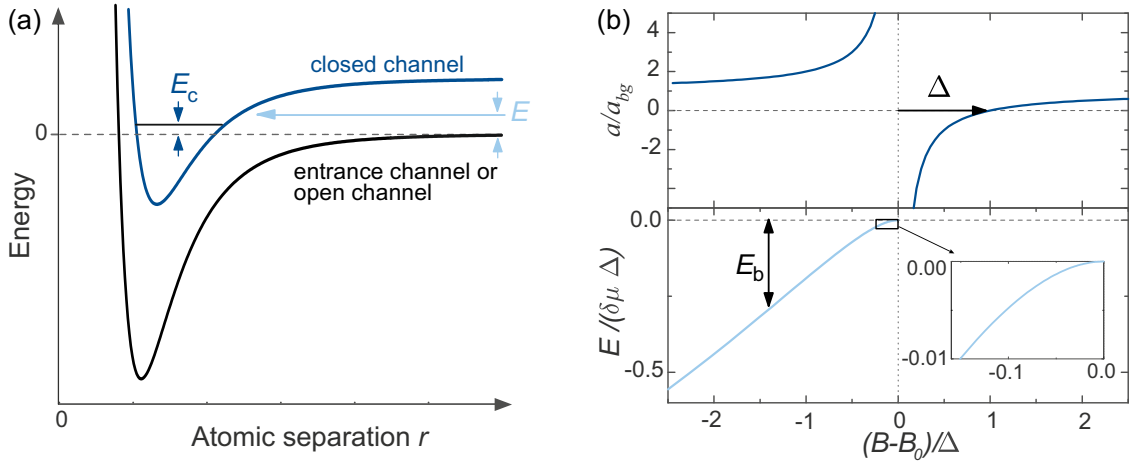

Figure 1.3: A simplified overview of Feshbach resonances. (a) Scattering channel representation of a Feshbach resonance. A Feshbach resonance occurs when energy of two interacting atoms in the entrance channel E becomes degenerate with the energy E_c of a bound state, which is hosted by a closed channel. (b) Upper panel: at the pole of a Feshbach resonance the s-wave scattering length diverges as a function of magnetic field. The width of the resonance is defined as the difference in magnetic field between the pole of the resonance and the field at which $a = 0\ a_0$. Note that the binding energy is $E = -E_b$. Lower panel: A Feshbach dimer with energy E can form for positive scattering lengths. Inset: behavior of the E in the universal regime. This image is adopted from reference [88].

drastic modification provides a powerful tool to precisely tune the collisional properties of the gas via an externally applied magnetic field. For broad enough resonances, the atomic interactions can be set from highly attractive to highly repulsive or even non-interacting. The absolute ground state of cesium features a board resonance at very low magnetic field allowing for exceptional control of the interactions. In this section we take a look at the control of the scattering length via Feshbach resonances. For a thorough review of Feshbach resonances see references [87, 88].

It is useful to introduce the concept of scattering channels to understand the emergence of a Feshbach resonance. Previously, we discussed the collision of two atoms via an interaction potential. The exact form of the interaction potential depends on the quantum numbers of the states involved in the scattering process. These states, which are well-defined at large interatomic distances, define different scattering channels. The channel in which the particles enter the collision is called the *entrance* channel. A collision channel is called *open* if the total energy of the system is above its threshold, allowing atoms to separate to infinity. A *closed* channel is one where the total energy is below the threshold, preventing the atoms from freely escaping. Closed channels can often support metastable bound states. A Feshbach resonance occurs when one of these bound states couples to the entrance channel. The collision partners virtually enter the bound state during the interaction, leading to the divergence of the scattering length. A schematic illustration of a Feshbach resonance is shown in Figure 1.3(a). The bound state and the entrance channel occupy a differing Zeeman substate. The resulting difference in magnetic moments $\delta\mu$ of the channels leads to a magnetic-field dependence of their relative

potential energy. For a broad resonance, the scattering length can thus be tuned to any desired value via the simple application of a bias magnetic field, providing experimental access to highly interacting as well as non-interacting regimes in a controlled manner. This makes Feshbach resonances an extremely powerful tool in ultracold experiments.

In the vicinity of a Feshbach resonance, the scattering length has the following expression as a function of magnetic field B [88]

$$a(B) = a_{\mathrm{bg}}\left(1 - \frac{\Delta}{B - B_0}\right), \tag{1.17}$$

where a_{bg} is the background scattering length defined as the scattering length away from any resonance, B_0 is the position of the pole and Δ is the width of the resonance. A plot of the scattering length as a function of B is shown in Figure 1.3(b). The divergence of the scattering length around the resonance dictates that a universal regime can be associated with each resonance. In the universal regime the energy of the bound state is given by Eq. (1.16). Beyond the universal regime, where the scattering length is small, E_{b} varies linearly with B, with a proportionality constant of $\delta\mu$. The lower panel of Figure 1.3(b) shows E_{b} as a function of magnetic field. The magnetic field region over which universality is applicable is dependent on the coupling strength between the bound state and the entrance channel. In this context it is useful define the strength of the resonance [88]

$$s_{\mathrm{res}} = \frac{a_{\mathrm{bg}}}{\bar{a}}\frac{\delta\mu\Delta}{\bar{E}}, \tag{1.18}$$

where $\bar{E} = \hbar/(2m\bar{a}^2)$, and $\bar{a} = 0.955978\ldots l_{\mathrm{vdW}}$ is the mean scattering length. For $s_{\mathrm{res}} \gg 1$ a resonance is described as a "wide" or "open channel dominated" resonance. This means that across most of the width Δ, the resonance character is determined by the entrance channel. Moreover, for broad resonances, the universal regime spans over a large magnetic field region. For a "narrow" or "closed channel" dominated resonance, on the other hand, the entrance channel only contributes across a small range of Δ and the universal regime is only applicable across a limited magnetic field region.

An important experimental feature of Feshbach resonances that deserves mention here is that the scattering length becomes zero at a magnetic field value of $B_0 + \Delta$. This feature plays a crucial role in our experiments. In the case of cesium, the hyperfine ground state has a shallow zero-crossing at 17.1 G [88]. This not only enables precise control over the scattering length without the need for extreme precision in magnetic field control, but also allows for the interactions to be turned off completely. By taking advantage of this zero-crossing, we can accurately determine the true momentum distribution of the sample by setting the interactions to zero during time-of-flight measurements.

Thus far our discussion has been focused on the modification of elastic scattering in the vicinity of a Feshbach resonance, however, a Feshbach resonance can also lead to drastic enhancement of inelastic scattering. During an inelastic scattering event, the internal state of the collision partners changes as a result of the collision. The excess energy of this process is gained by the participants as kinetic energy. Consequently heating or atom loss from the trap can be observed around Feshbach resonances. In fact, this is a commonly used experimental method for the detection

of these resonances. Inelastic processes themselves not only play an important role during the cooling stages of a condensate, but also impact the lifetime as well as the coherence of the resulting sample. Moreover, experimental control of inelastic losses would open up the possibility of engineering and investigating dissipative systems. In the next section we will discuss the different types of inelastic scattering processes in our system.

1.2.3 Inelastic collisions

In ultracold atomic systems, collisional processes play a crucial role in determining the stability and properties of the trapped gas. Collisions that lead to a change in the internal quantum state of at least one of the participants are known as inelastic collisions [88]. Inelastic collisions are classified by the number of atoms involved in the interaction. The resulting change in energy from an inelastic process is distributed amongst the participants as kinetic energy, often leading to a reduction of lifetime and coherence as well as heating of the trapped gas. Typically these processes are therefore modelled via the rate of change of the particle number and temperature of a sample in a trap over time. The change of density $\dot{n}(\mathbf{r}, t)$ takes the following form:

$$\dot{n}(\mathbf{r}, t) = -k_1 n(\mathbf{r}, t) - k_2 n(\mathbf{r}, t)^2 - k_3 n(\mathbf{r}, t)^3 - \dots \tag{1.19}$$

where k_i is the collision rate coefficient, which characterizes the i-body loss. For ultracold systems $i = 1, 2$, and 3 are relevant. This section gives an overview of each of these inelastic collisions. We also look at the effect that these processes have on a trapped sample and the model we use to fit the evolution of thermodynamic quantities.

We begin with one-body losses[1]. They stem from either interactions with the background gas particles, or the absorption of a photon from the optical trapping light. The loss rate due to these collisions is determined by the quality of the vacuum of the experiment, and by the intensity of the trapping light, respectively. These processes are density independent and follow an exponential decay with a loss rate of $1/k_1$.

Next we turn to two-body collisions. They come in the form of spin exchange and dipolar relaxation collisions. Spin exchange collisions occur as a consequence of the exchange of electronic spin states between colliding atoms conserving the total spin projection, while dipole relaxation involves spin flips induced by the coupling of spin angular momentum and orbital angular momentum. In contrast to elastic collisions where the scattering length is purely real, inelastic processes can be modelled in terms of a complex scattering length $a = \mathrm{Re}(a) + \mathrm{Im}(a)$. The imaginary component arises from atoms being lost from the elastic channel [88]. The two-body loss rate coefficient is given by the imaginary part of the scattering length

$$k_2 = \frac{8\hbar}{m_\mathrm{r}} \mathrm{Im}(a). \tag{1.20}$$

It is worth noting that two-body inelastic collisions only become relevant to systems that are not in their hyperfine ground states.

[1] One-body collisions do not necessarily lead to a change of internal state, and are hence not necessarily inelastic in nature. However, since they result in loss of atoms from the trap they are usually included in the standard inelastic loss models.

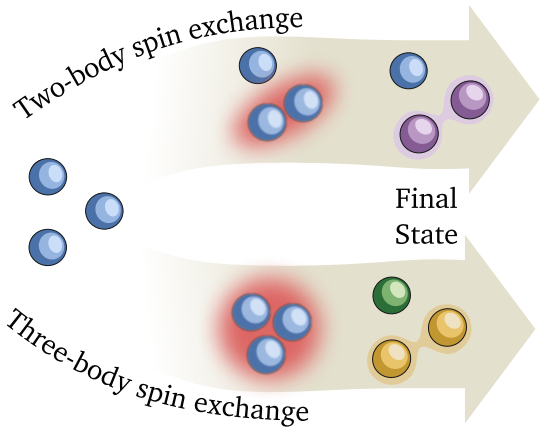

Figure 1.4: Depiction of two separate spin-exchange mechanisms for three-body recombination in the presence of inelastic two-body loss. The spin state of the particles is represented by different colors and a molecule is shown by two connected particles. In the upper pathway one particles conserves its spin throughout the entire collision process. In the lower pathway all three scatterers undergo a spin exchange. This illustration is adapted from reference [98].

Finally, we examine three-body recombination, a molecular formation process requiring three atoms. This three-body requirement stems directly from conservation principles. To understand why, we consider formation of a molecules via two colliding atoms. During the collision their net momentum in the center-of-mass frame is equal to zero. After the atoms form a molecule, they must leave the collision center together. However, since the binding process releases energy, conservation of both energy and momentum cannot be satisfied by just these two atoms alone. A third atom is required in order to absorb some of the released energy and momentum, allowing all conservation laws to be satisfied simultaneously.

In the universal regime, i.e., $a \gg l_{\mathrm{vdW}}$, dimensional analysis implies that the three-body loss rate coefficient k_3 scales as a^4 [99–103]

$$k_3 = C(a)\frac{\hbar a^4}{m}, \tag{1.21}$$

where the dimensionless factor $C(a)$ is an oscillatory function of $\ln(a)$ arising from Efimov physics [100, 104]. The situation can become significantly more complicated in the presence of two-body dissipation, i.e., if the collision participants also undergo a spin flip during a three-body recombination process. Three-body spin exchange collisions can occur via two different spin-exchange pathways illustrated in Figure 1.4 [98]. In the first pathway only one of the participants conserves its spin during the recombination process, while in the second pathway all three atoms experience a spin exchange. In chapter 5 we find indirect evidence the latter of these processes through a dramatic increase of k_3.

We now turn to the expected heating and loss rate of the sample. For any participants that undergo a change of the internal spin state, the energy gained from this process is of the order of the hyperfine splitting, which far exceeds the depth of the optical trap, leading to an immediate ejection of the collision partners from the trap and no further heating. However, for both two- and three-body processes the collision rate has a density dependence, hence a greater atomic loss rate is expected

at the center of the trap, where the density is the highest. Cold atoms preferentially occupy the center of the trap leading to what is known as "anti-evaporative" heating. From Eq. (1.19) we can see that the density dependence for two- and three-body collisions is n^2 and n^3, respectively, meaning that the anti-evaporation is much more significant for three-body scattering.

For three-body recombination, without a spin exchange, there is a further heating process. The kinetic energy gained by the collision participants is equal to the molecular binding energy E_b. In the lab frame the energy on average is divided as 1/3 and 2/3 among the molecule and the atom, respectively. In the universal regime, the molecular binding energy given by $E_\mathrm{b} = \hbar^2/m_\mathrm{r}a^2$ (Eq. (1.16)). This is often far greater than the trap depth and as with the spin-exchange collision would result in an ejection of the participants from the trap. However, close to resonance, where a diverges, the binding energy will be small and the atom as well as the molecule can remain trapped for a longer period of time. This gives rise to further heating, known as recombination heating [105].

All of the processes discussed here result in a loss of atoms and or heating of the trapped sample. The inelastic scattering rates can be determined via the rate of trap loss and heating. Before concluding this section, we will briefly discuss the model used for the time evolution of the number and temperature of atoms that remain trapped. For a thermal sample in a harmonic trap the density has the following form

$$n(\mathbf{r},t) = \frac{N(t)\omega_x\omega_y\omega_z m^{3/2}}{(2\pi k_\mathrm{B}T(t))^{3/2}} \exp\left(-\frac{m(\omega_x^2x^2+\omega_y^2y^2+\omega_z^2z^2)}{2k_\mathrm{B}T(t)}\right), \tag{1.22}$$

where $N(t)$ and $T(t)$ correspond to the remaining number of trapped atoms, and temperature of the remaining distribution, respectively. To obtain the rate of change of $N(t)$ we simply sum Eq. (1.19) over all of space

$$\dot{N}(t) = \int \dot{n}(\mathbf{r},t)\mathrm{d}^3\mathbf{r} = -k_i C^{(i-1)}\left(\frac{N(t)^i}{i^{3/2}T(t)^{(3/2)}}\right), \tag{1.23}$$

where $C = (m\bar{\omega}^2/2\pi k_\mathrm{B})^{3/2}$.

1.3 The cesium atom

The cesium (Cs) atom has 55 electrons, with a single electron occupying the outermost electron shell, the valence shell. Consequently, it is categorized as an alkali metal. Its low ionization energy of 375.7 kJ/mol makes it one of the most reactive elements on the periodic table. Cs has only one naturally occurring stable isotope: ^{133}Cs. For simplicity, we refer to ^{133}Cs simply as "Cs" throughout this work. With a mass of 132.91 g/mol, Cs is the heaviest of the stable alkali atoms.

The valence electron of Cs resides in the $6s$ orbital. Coupling between the orbital angular momentum (L) of the valence electron and its spin angular momentum (S) gives rise to a fine-structure doublet. Since the valence electron occupies an s-orbital ($L = 0$) in the ground state, the fine structure only affects excited states [106]. The two important ground state transitions are known as the D_1 ($6^2S_{1/2} \rightarrow 6^2P_{1/2}$)[2] and

[2]Here the first number refers to the principal quantum number of the valence electron, the superscript is equal to $2S+1$, the letter corresponds to the orbital angular momentum of the outer electron, where $L = 0, 1, \ldots$ gives $S, P, \ldots$ and finally the subscript is equal to J.

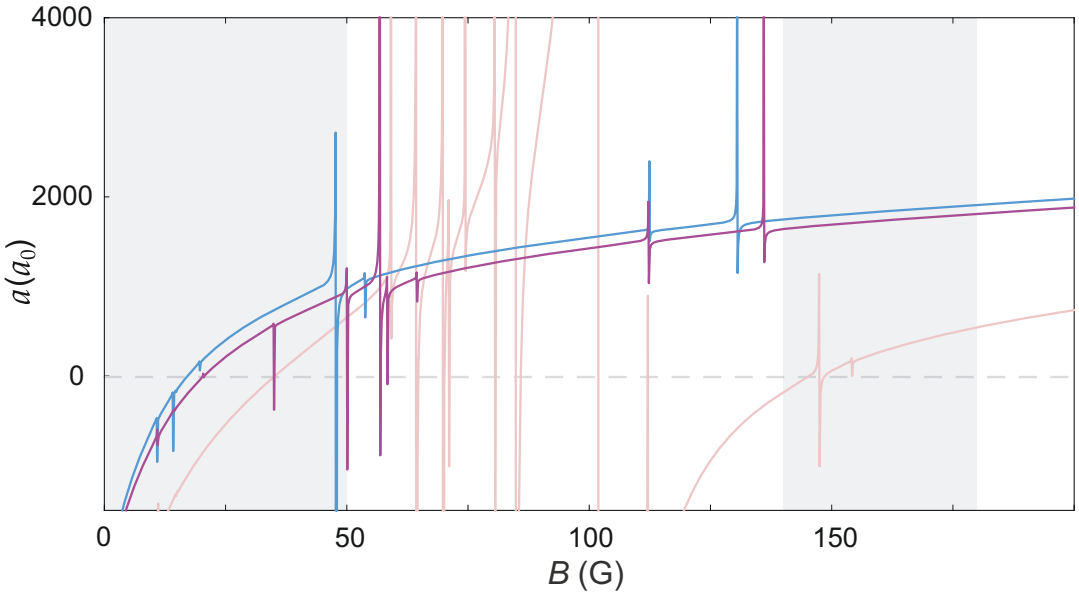

Figure 1.5: Scattering length as a function of magnetic field for spin states $(3,3)$ and $(3,2)$ from $B = 0$ to 200 G. The blue, purple and pink curves are the scattering lengths for $(3,3)+(3,3)$, $(3,3)+(3,2)$, and $(3,2)+(3,2)$ spin channels, respectively. The dashed gray line indicates $a = 0\ a_0$. We usually work in the highlighted region between 0 to 50 G. In chapter 5 a Cs BEC in the $(3,2)$ state was created both in the shaded 150 G region as well as below 50 G. This data is from reference [108].

D_2 ($6^2S_{1/2} \rightarrow 6^2P_{3/2}$) lines, which have a frequency difference of approximately 16.6 THz. On the path to a Cs BEC, the D_2 line, which is a cycling transition, serves as cooling transition for both the magneto-optic trap and the Raman sideband cooling phase in our experiment. For a comprehensive description of the entire cooling process see reference [107]. Further coupling between the total electron angular momentum (J) and the total nuclear spin (I) gives rise to hyperfine structure, characterized by the total angular momentum $F = I \pm J$. In the ground state ($6^2S_{1/2}$), where $J = 1/2$ and $I = 7/2$, the hyperfine structure splits into two levels with $F = 4$ and $F = 3$. This splitting, with the exact value of 9.192631770 GHz, has served as the official definition of the second since 1967. In the presence of an external magnetic field, the hyperfine levels are further split into $2F + 1$ magnetic sublevels, m_F, due to the Zeeman effect. In this thesis, the Cs condensate is prepared in the absolute ground state $(F, m_F) = (3,3)$. In Chapter 5, we also demonstrate the first creation of a BEC in the $(3,2)$ state.

1.3.1 Interaction properties of cesium

Cesium is both cursed and blessed with an extremely rich landscape of Feshbach resonances. It is cursed because in many spin states these resonances make it non-trivial to condense. Many early attempts to condense Cs were unsuccessful [109–113] due to unfavorable scattering lengths and inelastic losses in various spin states. Cesium condensates have thus far been achieved only in the absolute ground state, $(3,3)$. The $(3,3)$ state, being a high-field-seeking state, cannot be magnetically trapped, however, it blessed with both wide and narrow resonances at low magnetic fields as shown in Figure 1.5. Specifically, there is a broad resonance with a pole at

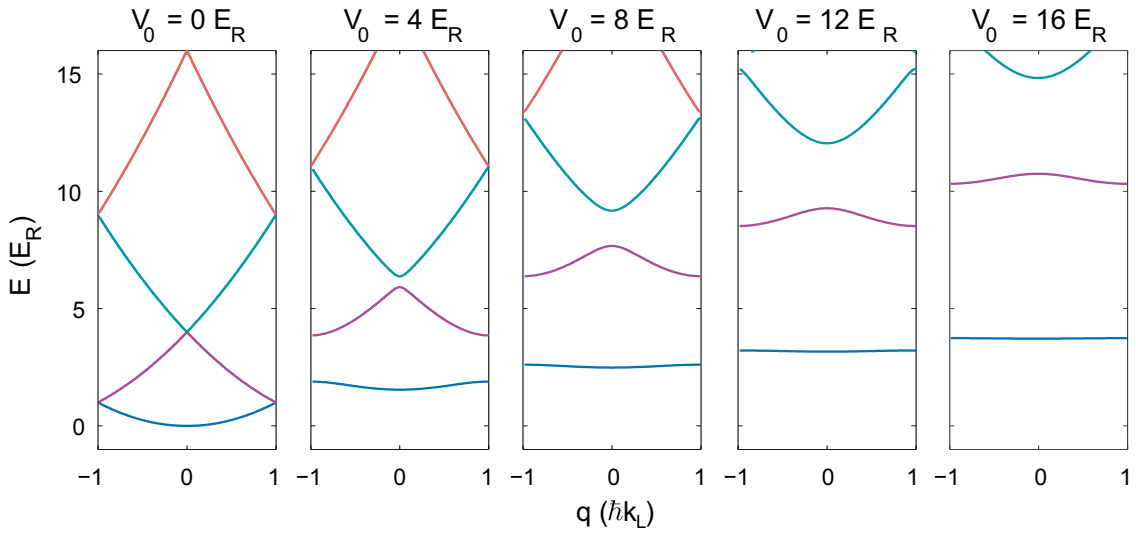

Figure 1.6: Bloch bands for different lattice depths. Eigenstate energies corresponding to the Bloch states as a function of quasi-momentum for lattice depths. This figure is taken from reference [107].

$B = -11.7$ G, which results in a shallow zero crossing at $B = 17.1$ G, and narrow resonances at $B = 19.84$ G and $B = 47.97$ G [88] that are routinely used in our experiment. This combination of broad and narrow resonances enables precise tuning as well as rapid quenching of interactions. Following its initial condensation in 2003 [114], Cs has served as a highly productive testbed for studying a wide range of phenomena, from the observation of Efimov physics [104, 115] to the creation of ultracold molecules [116–118] and strongly correlated 1D physics [14, 17, 45, 119], long-range tunnelling [120], matter-wave jets [121]. While these achievements showcase the versatility of cesium in the $(3, 3)$ state. In chapter 5 we discuss the first realization of of a Cs BEC in the $(3, 2)$ state, expanding the possible interaction ranges for mixtures and impurity physics.

1.4 A brief glimpse at atoms in an optical lattice

In chapters 2, 3, and 4 we present experiments investigating the physics of 1D systems. In our experiment, a 1D system is realized by superimposing two optical lattices. Before delving into the theoretical framework of 1D systems, we will briefly describe the motion of an atom in an optical lattice and the experimental conditions required for a system to be considered 1D. Optical lattices are created by the interference of counter-propagating laser beams. For a laser far-detuned from atomic resonance and with a beam propagation direction along z, the resulting potential for an atom at the beam focus can be described by

$$V_{\text{ext}}(r, z) = -V_0 e^{-2r^2/\omega_0^2} \cos^2(k_{\text{L}} z). \tag{1.24}$$

Here, V_0 is the lattice depth expressed in units of the recoil energy $E_{\text{R}} = \hbar^2 k_{\text{L}}^2/2m$, ω_0 the $1/e^2$-radius of the beam, r is the radial distance from the beam center, and λ is the wavelength of the laser beam. Experimentally, this periodic potential can be created by simply retro-reflecting a single beam. The constructive interference of

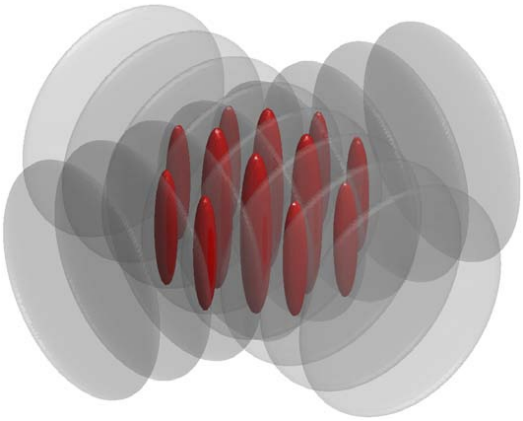

Figure 1.7: Illustration the experimental realization of a 1D system in our experiment. We use two orthogonal retro-reflected laser beams. The beams are superimposed with the BEC resulting in a bunch of vertically oriented tubes. This figure is taken from reference [122].

the incident and reflected beams produces a potential four times deeper than that of a single, non-retroreflected dipole trap of the same intensity. In our experiment we use an optical lattice with a wavelength of $\lambda = 1064$ nm. For Cs this corresponds to the recoil energy 1 $E_{\mathrm{R}} = 64$ nK $\times k_{\mathrm{B}} = 1325$ Hz $\times h$.

The dynamics of a particle in a potential $V_{\mathrm{ext}}(r, z)$ is governed by the Hamiltonian

$$\hat{H} = \frac{\hat{p}^2}{2m} + V_{\mathrm{ext}}(r, z), \tag{1.25}$$

where $\hat{p}$ is the momentum operator. In the absence of a potential ($V_{\mathrm{ext}}(r, z) = 0$) the complete basis of solutions to the Schrödinger equation is given by a set of plane waves with momentum p. For a periodic potential, delocalized Bloch states serve a similar purpose. First described in the context of electrons in a crystal, Bloch waves are products of a plane wave $e^{iqz/\hbar}$ with quasi-momentum q and a spatially periodic function $u_q^n(z)$ such that $u_q^n(z) = u_q^n(z + d)$. The periodicity is given by the lattice period: $d = \lambda/2 = \pi/k_{\mathrm{L}}$. Thus, the Bloch state can be written as $\phi_{n,q}(z) = e^{iqz/\hbar} u_{n,q}(z)$. Due to the periodicity of the potential, q can be restricted to the first Brillouin zone $[-\hbar k_{\mathrm{L}}, \hbar k_{\mathrm{L}}]$ without loss of generality. It should be noted that quasi-momentum q is not equivalent to physical momentum. Within the Brillouin zone the quasi-momentum is conserved. Each q corresponds to a set of energy eigenstates $E_n(q)$ forming discrete levels, indexed by the band number n. Figure 1.6 illustrates the energies of the three lowest bands as functions of quasi-momentum for different lattice depths. In the limit of vanishing lattice depth these bands are parabolic corresponding to free particle dispersion. For larger lattice depths the band gaps opens at the edge of the Brillouin zone. As the lattice depth increases, the gap also increases and the bands flatten over the entire Brillouin zone.

The band structure has direct consequences for creating lower-dimensional quantum systems. In experiments, 1D systems can be realized using a two-dimensional lattice potential created by two orthogonal pairs of retro-reflected laser beams. When a BEC is loaded into this lattice and the lattice depth is adiabatically increased, the band gaps in the transverse directions increase. This increased energy separation between the lowest and first excited bands, which is approximately equal

to the transverse excitation energy $\hbar\omega_\perp$, effectively restricts atomic motion in these directions. As a rule of thumb, a system is considered to be 1D if the transverse level spacing dominates other relevant energy scales. Specifically, when $\hbar\omega_\perp \gg \mu$, $k_\mathrm{B}T$, where $\omega_\perp$ is the transverse frequency of the tube, μ is the chemical potential, and $k_\mathrm{B}T$ is the thermal energy of the system. Under these conditions, atoms lack sufficient energy to occupy higher transverse bands and remain confined to the lowest energy band, with their wave functions "frozen" in the transverse ground state. This results in the confinement of atoms within arrays of parallel 1D tubes, as illustrated in Figure 1.7, where quantum dynamics occur exclusively along the tube axis.

1.5 Interacting systems in lower dimensions

The dimensionality of a system can fundamentally change its behavior and characteristics. In quantum systems, reduced dimensionality amplifies the influence of both interactions and quantum fluctuations giving rise to a range of quantum phenomena that are absent in the higher dimensional counterparts. One-dimensional systems in particular exhibit remarkable properties such as spin-charge separation [58], where spin and charge excitations propagate independently at different velocities, and the conventional binary description of quantum statistics becomes less well defined. The latter is exemplified by the Tonks-Girardeau gas [36, 62, 63] where strongly interacting bosons effectively behave like fermions. In chapter 3 we observe the emergence of entirely different particles known as anyons [123, 124], where the wavefunction acquires an arbitrary phase factor upon exchange. An important feature of 1D systems is also the existence of integrable models. The most notable characteristics shared by these models is that multi-particle scattering decomposes completely into two-particle scattering, and they possess an infinite number of conservation laws that prevent the system from thermalizing [125]. The exact solutions of these integrable models can be found via the Bethe ansatz, which was first developed by Hans Bethe in 1931 [61].

A large portion of the work summarized in this thesis focuses on 1D systems. The following section provides a brief overview of these systems, beginning with Luttinger liquid theory [8–10], which serves as a universal description of interacting particles in 1D. We then examine the Lieb-Liniger model [59, 60], discussing its various interaction regimes and deriving solutions via the Bethe ansatz.

1.5.1 Luttinger liquid

In 1956, Landau first formulated a description of strongly interacting electrons in metallic solids. For a zero-temperature metal without interactions, electrons populate all available momentum states up to the Fermi energy E_F. Removing or adding electrons to the system leads to low energy excitations, which can be described as electron and hole pairs near the Fermi surface. For interacting electrons, instead of describing the motion of the electrons themselves, Landau reformulated the problem in terms of non-interacting quasi-particles. These quasi-particles are essentially dressed electrons, but with a renormalized mass and magnetic moment. Remarkably, this renormalization works even for the case of strong interactions. Today this model, known as the Fermi liquid theory [56, 57], is the standard description

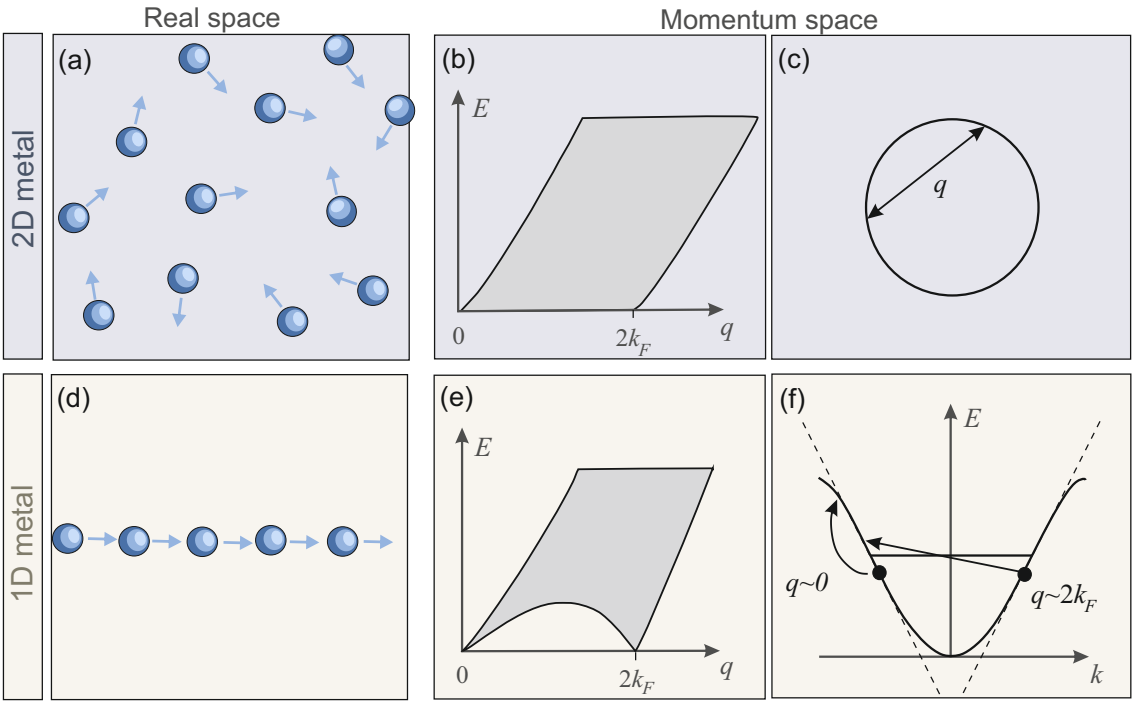

Figure 1.8: Comparison of 1D and higher-dimensional (2D) systems. Top row: Higher dimensional interacting systems can be described in terms of quasi-particles. (a) Due to the large phase-space availability in higher dimensional systems, particles can move without encountering each other, resulting in small collective correlations. (b), (c), In momentum space, all excitations below twice the Fermi momentum k_F are available (gray shaded region in (b)). Bottom row: In an 1D system, (d), the particles are unable to move without encountering a neighboring particle. (e), (f), In momentum space, the Fermi surface reduces to two points thus not all excitations are available. The shaded area in (e) shows the region where excitations are possible. In (f), the energy spectrum close to Fermi momentum can be approximated as linear spectra (dashed line). Two possible low energy excitations on top of the Fermi sea are shown with arrows. This depiction is adapted from reference [58].

of many metals in 2D and 3D and is key to understanding microscopic quantum phenomena such as Landau quantization and BCS superconductivity. It is a powerful theory that can be applied to many different situations, from a Helium-3 liquid to electrons in metals, and further to neutrons in neutron stars. However, in one dimension Landau's quasi-particle picture breaks down. Here a different description is required.

Unlike in higher dimensions, in a 1D configuration excitations are collective [58]. Figure 1.8 shows a schematic illustration of the difference between the 1D and 2D case, but the same arguments also apply for 3D. In 2D and 3D the large available phase space allows the particles to move without encountering each other rendering interactions much less important (Figure 1.8(a)). In contrast, for a 1D geometry any local motion of a single particle results in the collective motion of the entire system (Figure 1.8(d)). Even small interactions hence have a significant effect. The behavior of this system is captured by a low-energy effective field theory known as Luttinger liquid theory [58, 126]. Instead of local quasi-particles, as in the Fermi

liquid theory, here the system is described in terms of wave-like excitations of the density, or the charge. Due to the bosonic nature of these excitations this formulation is known as 'bosonization' [58, 127, 128]. The Fermi surface in the 1D case reduces down to two points resulting in low-energy excitations being well defined by a linear dispersion curve (Figure 1.8(f)). Moreover, this leads to a forbidden region between zero and twice the Fermi momenta k_{F}, where no excitations are allowed (Figure 1.8(e)). This clearly differs from a higher dimensional geometry (Figure 1.8(b) and (c)), where there is no such a forbidden region and zero-energy excitations at arbitrary momentum are always possible.

Another curious consequence of strong correlations in a 1D fermionic system is that the spin and the charge degrees-of-freedom of the particles decouple and behave as independent quantities [129]. Both the spin and the charge propagate independently and carry different types of excitations: holons, or chargeons, for the charge and spinons for the spin. This phenomena, known as spin-charge separation, is fundamentally different from the Fermi-liquid quasi-particle, where the spin and the charge are always coupled. One further intriguing property of Luttinger liquids that deserves a mention here, is that correlation functions exhibit power-law behavior in 1D. Even though Luttinger liquid theory was first developed for weakly interacting fermions, it equally applies to weakly interacting bosons [128].
The Hamiltonian describing the Luttinger liquid is given by the following expression [128]

$$\hat{H}_{\mathrm{LL}} = \frac{\hbar v}{2\pi} \int dz \left[K \left(\frac{\partial}{\partial z} \hat{\phi}(z) \right)^2 + \frac{1}{K} \left(\frac{\partial}{\partial z} \hat{\theta}(z) \right)^2 \right]. \tag{1.26}$$

Here, $\hat{\phi}(z)$ and $\hat{\theta}(z)$ represent the density and phase field operators, respectively. The velocity v is the velocity of collective excitations, or sound-like modes, and the parameter K entirely characterizes the macroscopic properties of the system. The Luttinger parameter K is related to the interaction strength as well as the compressibility of the system. For non-interacting fermions K is equal to one, and for repulsive (attractive) interactions $K<1$ ($K>1$).

The Luttinger liquid theory has proven to be a remarkably successful model for 1D systems providing a universal low-energy description for bosons and fermions [130]. Moreover, it is applicable to arbitrary interaction strengths. However, the Luttinger-liquid model relies on the aforementioned linearization of the energy dispersion around the Fermi points. At high energies, the dispersion becomes nonlinear, causing the Luttinger liquid theory to break down [131]. The Luttinger liquid theory also assumes the system to be gapless and in, or near, equilibrium. It is therefore not applicable in the presence of a lattice, nor does it describe out-of-equilibrium dynamics. Fortunately, in 1D there also exist exactly solvable, or integrable, models. One of these systems is the Lieb-Liniger model describing 1D interacting bosons. This is what we will look at in the next section.

1.5.2 The Lieb-Liniger gas

The Lieb-Liniger model describes 1D bosons with contact interactions. It was first formulated in the early 1960s by Elliot Lieb and Werner Liniger [59, 60] and is

defined by the following Hamiltonian

$$\hat{H}_{\mathrm{LL}} = -\frac{\hbar^2}{2m}\sum_i \frac{\partial^2}{\partial z_i^2} + g_{1\mathrm{D}}\sum_{i<j}\delta(z_i - z_j), \tag{1.27}$$

where the first term describes the kinetic energy of the particles and the second term models the inter-particle contact interactions with strength $g_{1\mathrm{D}}$. What makes this many-body Hamiltonian so remarkable is not just its simplicity, but the fact that it is integrable, and hence one can find an exact solution via the Bethe ansatz.

For many years the Lieb-Liniger model remained a mere theoretical playground for studying non-perturbative effects. However, with the advent of ultracold atoms this model found renewed interest. For ultracold gases, the system is dilute and cold enough, such that we can assume that all of the interactions are well described via two-body contact interactions given by a delta potential. Confining the system in a 2D lattice geometry, as described in section 1.4, freezes out the transverse degrees of freedom. The interaction strength then can be characterized by the parameter [17, 132]

$$g_{1\mathrm{D}} = \frac{2\hbar^2 a_s}{m a_\perp}\left(\frac{1}{1 - 1.0326 a_s/a_\perp}\right), \tag{1.28}$$

where $a_\perp = \sqrt{\hbar/(m\omega_\perp)}$ is the transverse harmonic oscillator length. Equation (1.28) shows that $g_{1\mathrm{D}}$ is influenced by the confinement via $a_\perp$. For $a_s \ll a_\perp$ the coupling strength can be approximated by $2\hbar^2 a_s/(m a_\perp)$. However, if $a_s \sim a_\perp$, as can be realized close to a Feshbach resonance, $g_{1\mathrm{D}}$ diverges and we encounter what is know as a confinement-induced resonance (CIR) [17]. Experimentally these resonances can be utilized to tune the interaction strength in a 1D system.

We now turn to the various interaction regimes of the Lieb-Liniger Hamiltonian (Eq. (1.27)). It is useful to define the dimensionless Lieb-Liniger parameter [59]

$$\gamma = \frac{m g_{1\mathrm{D}}}{\hbar^2 n_{1\mathrm{D}}}, \tag{1.29}$$

where $n_{1\mathrm{D}} = N/L$ is the 1D density, N is equal to the number of particles and L the length of the system. For weak interactions ($\gamma \sim 0$) a large portion of the bosons occupy the zero momentum state forming a quasi-condensate. Note that, even at zero temperature, a true condensate cannot form in 1D, since long-range order is always destroyed by quantum fluctuations [82, 133]. For very strong repulsive interactions ($\gamma \to \infty$) the system becomes more correlated and the bosons become impenetrable. Their strong repulsion resembles the Pauli exclusion principle and they begin to act as free fermions. This is known as the Tonks-Giradeau regime [36, 62, 63].

Within the mean-field regime, one can intuitively interpret γ as the ratio between the interaction energy $E_{\mathrm{int}} \sim n_{1\mathrm{D}} g_{1D}$ and the kinetic energy $E_{\mathrm{kin}} \sim \hbar^2 n_{1\mathrm{D}}^2/m$. Unlike the higher dimensional counterparts, in 1D, the ratio $E_{\mathrm{int}}/E_{\mathrm{kin}}$ is inversely proportional to the density. This peculiarity leads to the system becoming more strongly-correlated as it becomes more dilute. This mean-field interpretation of $\gamma \propto E_{\mathrm{int}}/E_{\mathrm{kin}}$ begins to break down as the atoms build up strong correlations and enter the Tonks regime. Unlike γ, which diverges, the ratio of the interaction and kinetic energy saturates to a finite value [134]. A more accurate way of looking at γ-parameter is in terms of the 1D interaction length $r_g = \hbar^2/(m g_{1\mathrm{D}})$, which quantifies the overlap of the wavefunctions of two repulsively interacting particles [135].

The γ-parameter can thus be viewed as the ratio between the mean inter-particle distance $1/n_{1D}$ and r_g or equivalently the inverse of the average number of particles per interaction length.

Next, we look at the attractive regime of the Lieb-Liniger Hamiltonian. Here the situation becomes more nuanced, since there are two possible states. Firstly the system can form bound states, known as Bethe strings [61]. The ground state is described by the McGuire cluster state [136], where all of the atoms bind to form a giant string. In the thermodynamic limit ($N, L \to \infty$ with N/L fixed), the McGuire cluster is unstable and experimentally unattainable, due to uncontrollable atom loss arising from short-range molecular processes. Higher-lying, small Bethe string states have been recently observed in condensed matter systems [137, 138]. In ultracold systems Bethe strings can be prepared by adiabatically ramping the interactions from the repulsive to the attractive regime [139]. The rate of the sweep crossing the zero interaction point, as well as the initial temperature and density of the gas, determines the bound states population. Once created, these states do not decay to lower lying states due to the integrability of the system. The second state, which is a metastable phase, is achieved when the interactions are quenched across a CIR from the the repulsive Tonks phase to $\gamma = -\infty$. Here the gas retains the strong correlations from the Tonks phase and forms an excited many-body state, which is composed of unbound particles. This state is known as the super-Tonks state [17, 140–143].

It is important to note that one of the main limitations of the Lieb-Liniger Hamiltonian is that it describes a homogeneous system. Many ultracold experiments use an external trapping potential, resulting in a density of particles that varies in space. The typical sizes resulting from the trapping potential are mesoscopic, which makes their effect relevant. The Bethe ansatz solution assumes translational invariance, therefore the trapping potential breaks the integrability of this model. Nonetheless, signatures of integrability are still preserved even in the presence of an external trap [144]. For the remainder of this section we look at the Bethe ansatz solutions of the Lieb-Liniger Hamiltonian. This discussion will mostly follow references [125] and [145]. To begin with, we will focus on the solutions in the repulsive case, and further on in the chapter we will move onto the attractive case. For convenience we will hereon in use $c = mg_{1D}/\hbar^2$ to parameterize the interactions. In this notation, the Lieb-Liniger parameter can also be written as $\gamma = c/n_{1D}$. Since the Tonks regime can be mapped onto free fermions, it is further useful to define a Fermi momentum $k_F = \pi n_{1D}$, a Fermi velocity $v_F = \hbar k_F/m$, and a Fermi energy $E_F = (\hbar k_F)^2/(2m)$ for the system.

1.5.3 Two-particle problem

An important property that is shared by all integrable models is that each N-particle scattering event can be decomposed into a series of two-particle collisions processes. We, therefore, start off by considering a two-particle scattering event. In particular, we determine the resulting scattering phase shift using the Bethe ansatz. In section 1.5.4 we extended this solution the N-particle case. For simplicity we set $\hbar = 2m = 1$ for the remainder of this chapter. For $N = 2$ the Lieb-Liniger

Hamiltonian (Eq. (1.27)) becomes

$$\hat{H} = -\frac{\partial^2}{\partial z_1^2} - \frac{\partial^2}{\partial z_2^2} + 2c\delta(z_1 - z_2). \tag{1.30}$$

For two identical bosons we require the many-body wavefunction to be symmetric under exchange $\psi(z_1, z_2) = \psi(z_2, z_1)$. We, therefore, write a generic eigenstate for this system by dividing the space into the $z_1 < z_2$ and $z_1 > z_2$ regions

$$\psi(z_1, z_2) = f(z_1, z_2)\vartheta(z_2 - z_1) + f(z_2, z_1)\vartheta(z_1 - z_2), \tag{1.31}$$

where

$$\vartheta(z) = \begin{cases} 1 & z > 0 \\ 0 & z < 0 \end{cases} \tag{1.32}$$

is the Heaviside step function. The key insight of the Bethe ansatz is that in regions where $z_1 \neq z_2$, i.e., where the δ-function vanishes, the particles behave like free particles, and the solution can be written as a superposition of plane waves. The solution to the eigenvalue equation, hence, takes the following form

$$\begin{aligned} f(z_1, z_2) &\equiv A(k_1, k_2)e^{i(k_1 z_1 + k_2 z_2)} + A(k_2, k_1)e^{i(k_2 z_1 + k_1 z_2)} \\ &= A_{12}e^{i(k_1 z_1 + k_2 z_2)} + A_{21}e^{i(k_2 z_1 + k_1 z_2)}, \end{aligned} \tag{1.33}$$

where k_1 and k_2 are quasi-momenta known as rapidities [146–149], and A_{12} and A_{21} are coefficients dependent on k_1 and k_2. Equation (1.33) is known as the Bethe ansatz [61, 150–152]. Taking into account the relations $\partial_z \vartheta(z) = \delta(z)$ and $f(z)\partial_z \delta(z) = -\partial_z f(z)\delta(z)$, which holds for any $f(z)$, we get

$$\begin{aligned} \partial_{z_1}^2 \psi(z_1, z_2) =& \partial_{z_1}^2 f(z_1, z_2)\vartheta(z_2 - z_1) + \partial_{z_1}^2 f(z_2, z_1)\vartheta(z_1 - z_2) \\ &- \partial_{z_1} f(z_1, z_2)\delta(z_2 - z_1) + \partial_{z_1} f(z_2, z_1)\delta(z_1 - z_2). \end{aligned} \tag{1.34}$$

The Schrödinger equation, therefore, becomes

$$\begin{aligned} \hat{H}\psi =& (k_1^2 + k_2^2)\psi \\ &+ 2\delta(z_1 - z_2)[c(A_{12} + A_{21}) - i(A_{12} - A_{21})(k_1 - k_2)]e^{i(k_1 + k_2)z_1}. \end{aligned} \tag{1.35}$$

This eigenvalue equation is satisfied, provided that the amplitudes A_{12} and A_{21} satisfy

$$\frac{A_{12}}{A_{21}} = \frac{i(k_1 - k_2) + c}{i(k_1 - k_2) - c}. \tag{1.36}$$

Since Eq. (1.36) has a unit modulus, it can be rewritten as

$$\frac{A_{12}}{A_{21}} = e^{i\tilde{\theta}(k_1 - k_2)}, \tag{1.37}$$

where

$$\tilde{\theta}(k) \equiv 2\arctan\left(\frac{k}{c}\right) + \pi. \tag{1.38}$$

Note that this phase shift is derived from the continuity conditions imposed by the δ-function potential (Eq. (1.36)) and thus specifically corresponds to contact

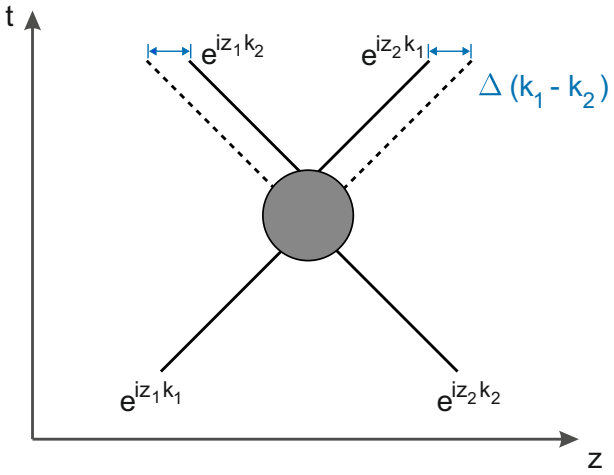

Figure 1.9: Schematic illustration of the Wigner time delay. The scattering phase shift can be interpreted semiclassically as a time delay. For an elastic two-body interaction event in 1D the resulting positions of the particles are shifted by $\Delta(k_1 - k_2)$ with respect to the collision center. This images is adopted from references [145, 153].

interactions. Each integrable potential will have its own characteristic phase-shift function. The phase shift $\tilde{\theta}(k)$ in Eq. (1.38) has two important limiting behaviors. First, as $c \to \infty$, it matches free-fermion scattering. Secondly, for any non-zero c, if $k_1 = k_2$, we have $A_{12} = -A_{21}$ causing the wavefunction to vanish. Hence k_1 and k_2 must necessarily be different. This shows that the Lieb-Liniger model, despite describing bosonic particles, has solutions with distinctly fermionic characteristics. We redefine the scattering phase as an odd function that vanishes at $k = 0$

$$\theta(k) \equiv 2 \arctan\left(\frac{k}{c}\right). \tag{1.39}$$

A remarkable aspect of the Bethe solution is the quasi-particle interpretation of the strongly interacting system. The plane waves in the ansatz can be viewed as quasi-particles characterized by momenta, or rapidities, k_1 and k_2. In this picture, the elementary excitations are not the original bare particles but emergent entities with modified dispersion relations and scattering properties. The rapidities play an important role as they are accessible both theoretically and experimentally. Taking a closer look at the Bethe ansatz (Eq. (1.33)) we can see that it represents a two-body scattering process. In 1D systems, scattering events result in the exchange of momenta between interacting particles. The Bethe ansatz contains both the initial state with rapidities k_1 and k_2 and the scattered state with these rapidities exchanged. The ratio A_{12}/A_{21} quantifies the scattering amplitude between these quasi-particles.

An additional property of this system is that the momentum derivative of the scattering phase can be interpreted as the effective duration of the interaction between the particles [154]. This is know as the Wigner time delay. In Figure 1.9 we give an illustration of this concept. Following the interaction, while the Bethe ansatz describes extended plane wave states, one can consider the dynamics of localized wave packets with central momenta k_1 and k_2. In this wave packet picture,

the position of each packet is equal to [145]

$$z_1 \simeq k_1 t - \Delta(k_2 - k_1), \tag{1.40}$$

and

$$z_2 \simeq k_2 t + \Delta(k_2 - k_1) \tag{1.41}$$

respectively. Here $\Delta(k_2 - k_1)$ is the derivative of the scattering phase

$$\Delta(k) \equiv \frac{\mathrm{d}\theta(k)}{\mathrm{d}k} = -\frac{2c}{c^2 + k^2}. \tag{1.42}$$

For the repulsive Lieb-Liniger model this shift results in a time delay, which plays an important role in the theory of generalized hydrodynamics discussed in section 1.6.

1.5.4 N-particle Bethe ansatz

Having solved the two-particle problem we now move onto the N-particle problem. We now start with the complete Lieb-Liniger Hamiltonian (Eq. (1.27))

$$\hat{H} = -\sum_i \frac{\partial^2}{\partial z_i^2} + 2c \sum_{\langle i,j \rangle} \delta(z_i - z_j). \tag{1.43}$$

We again assume that, away from the discontinuities given by the delta functions, our wavefunction is a superposition of plane waves

$$\Psi(z_1 ... z_N) = \sum_{\mathcal{P}} A_{\mathcal{P}} \exp\left(i \sum_{j=1}^{N} k_{\mathcal{P}_j} z_j \right), \qquad z_1 \leq z_2 \leq \dots z_N \tag{1.44}$$

where k_j are the quasi-momenta, or the rapidities. The permutations of the quasi-momenta order are denoted by $\mathcal{P}$, and the amplitude corresponding to each permutation is given by $A_{\mathcal{P}}$. As previously mentioned, for the Lieb-Liniger model a multi-particle scattering can be factorized in two-particle events. Thus, the same procedure as in the two-particle problem can be applied here leading to a phase shift of

$$\frac{A_{\mathcal{P}}}{A_{\mathcal{P}'}} = e^{i\theta(k-k')}, \tag{1.45}$$

where k and k' are the momenta exchanged between the permutations $\mathcal{P}$ and $\mathcal{P}'$. The permutations $\mathcal{P}$ and $\mathcal{P}'$ are related by the exchange of $\mathcal{P}(j)$ and $\mathcal{P}(j+1)$

$$\mathcal{P}' = (\mathcal{P}(1), \mathcal{P}(2), \dots, \mathcal{P}(j-1), \mathcal{P}(j+1), \mathcal{P}(j), \mathcal{P}(j+2), \dots, \mathcal{P}(N)). \tag{1.46}$$

Next we impose a periodic boundary condition

$$\Psi(z_1, z_2, \dots, z_j + L, \dots, z_N) = \Psi(z_1, z_2, \dots, z_j, \dots, z_N) \qquad j = q, \dots, N. \tag{1.47}$$

This leads to the following conditions

$$e^{ik_j L} = \prod_{l \neq j} \frac{k_j - k_l + ic}{k_j - k_l - ic}, \qquad j = 1, \dots, N. \tag{1.48}$$

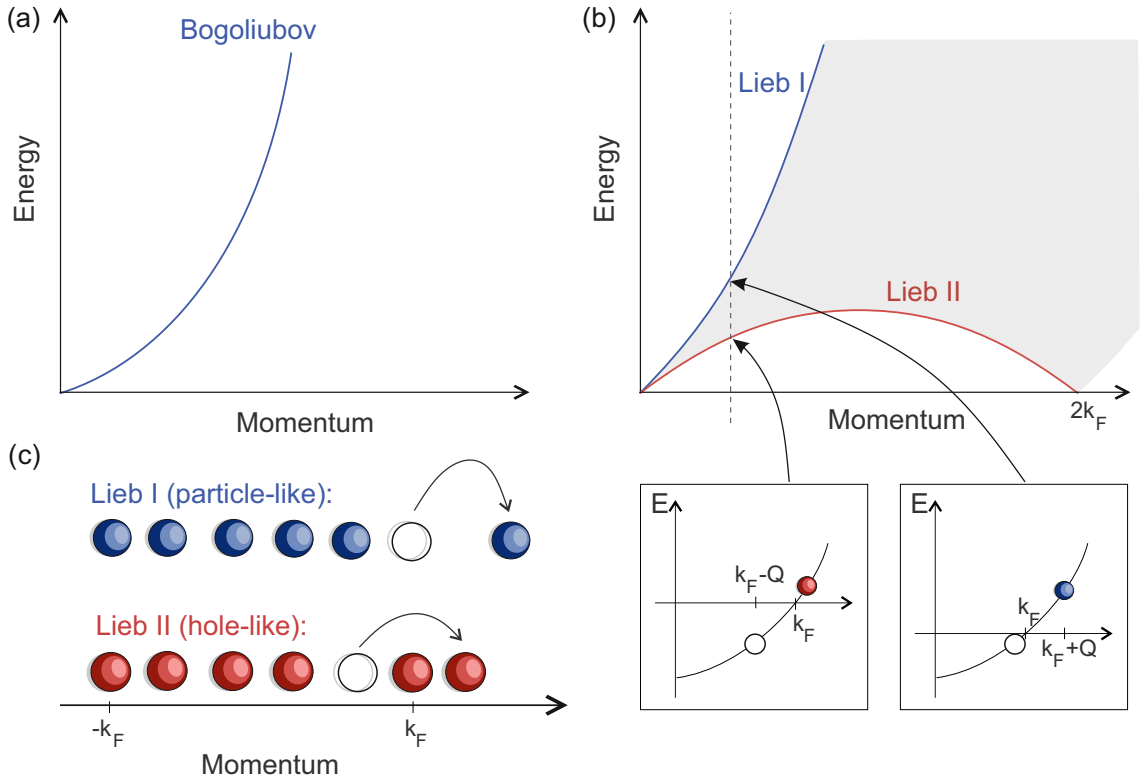

Figure 1.10: Illustration comparing the excitation spectrum of a weakly and a strongly interacting 1D system of bosons. (a) For weak interactions ($\gamma \ll 1$) the excitation spectrum is given by the Bogoliubov theory. (b) For strong interactions ($\gamma \gg 1$) two distinct excitation modes emerge: Lieb I and Lieb II. While Lieb I describes a particle-like excitation, Lieb II is a hole-like excitation. The shaded region represent the allowed excitations. Inset: Illustration of particle- and hole-like excitation on a Fermi surface, where the hollow circle depicts a hole. (c) Pictorial illustration of the two elementary excitations. The different colors highlight the two different types of excitations. This depiction is adapted from references [131, 155].

Taking the logarithm on both sides and using Eq. (1.39) we get

$$k_j L = 2\pi I_j - \sum_{l=1}^{N} \theta(k_j - k_l) \tag{1.49}$$

where I_j are a set of quantum numbers that define the state. They are integers (half-integers) if the number of particles N is odd (even). Equations (1.49) are known as the Bethe equations and can be solved numerically. The total energy and the total momentum of the system are given by

$$E = \sum_{j=1}^{N} k_j^2 \qquad \text{and} \qquad Q = \sum_{j=1}^{N} k_j, \tag{1.50}$$

respectively. For the ground state, I_j form a symmetric set centered around zero, hence the total momentum in the ground state $Q_{\mathrm{GS}} = 0$. Excitations on top of the ground state are constructed by modifying I_j. Particle-like (or Lieb I) excitations involve a particle at k_{F} being excited above the Fermi surface resulting in a hole

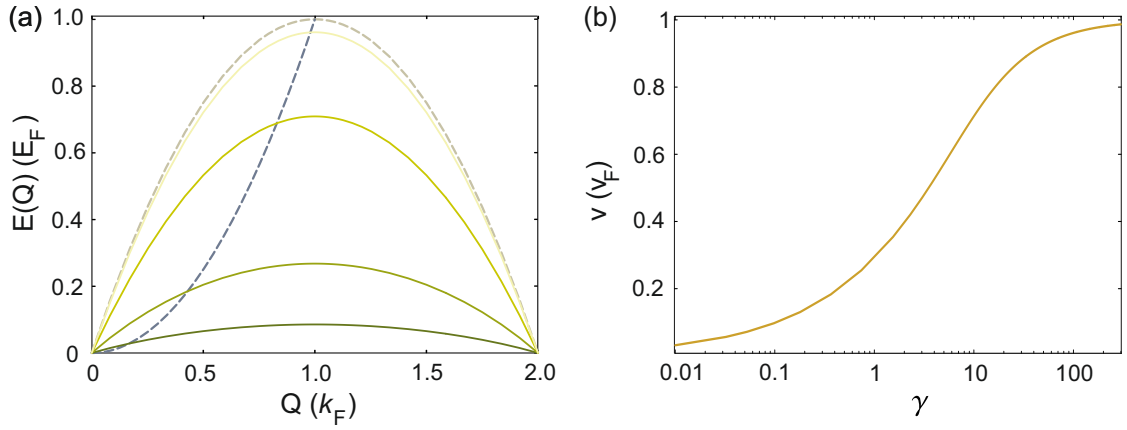

Figure 1.11: Excitation spectrum and speed of sound of a Bose gas for different interaction strengths. (a) Excitation spectrum of a Bose gas. The solid lines correspond to $\gamma = 0.1, 1, 10, 100$ (from bottom to top). The yellow dashed line is $\gamma = \infty$ and the dashed gray line is the free particle dispersion. (b) Speed of sound in a Lieb-Liniger gas as a function of γ. The solid curve is the analytical solution of the velocity of sound.

at k_{F} and single particle alone above k_{F}. For hole-like (or Lieb II) excitations, on the other hand, a particle within the Fermi sea is excited to the edge leaving a hole inside the Fermi sea. Figure 1.10 shows an illustration of the excitation spectrum of a Lieb-Liniger gas in the case of weak and strong interactions. For weak interactions, $\gamma \ll 1$, the excitation spectrum is well described by Bogoliubov theory [156]. As γ increases the excitation spectrum expands into a continuum between Bogoliubov (Lieb I) and Lieb II branch [60]. Compared to Lieb II excitations, Lieb I excitations require higher energy. In the Tonks limit, the low energy excitations are particle-hole excitations, where a particle from the Fermi sea is excited above the Fermi energy leaving behind a hole. Here the dispersion relation is identical to that of a free Fermi gas. A particle-hole excitation involves removing a particle at k_h (leaving behind a hole) and adding a particle at k_p. The resulting momentum transfer to the system is given by $Q = k_p - k_h$, which leads to a change in energy of

$$E = k_p^2 - k_h^2 = k_p^2 - (k_p - Q)^2. \tag{1.51}$$

Here $k_p > k_{\mathrm{F}}$, and $k_h \in [-k_{\mathrm{F}}, k_{\mathrm{F}}]$. The minimum value of k_p for a given Q is, thus, $k_{\mathrm{p}} = k_{\mathrm{F}}$, leading to the following expression for the lower bound of the excitation spectrum of a free Fermi or Tonks gas

$$E(Q) = Q(2k_{\mathrm{F}} - Q), \qquad 0 \leq Q \leq 2k_{\mathrm{F}}. \tag{1.52}$$

In Figure 1.11(a) we show the edge of the excitation spectrum for different values of γ. From here, we can also extract the speed of sound as $v = \partial E/\partial Q$ as $Q \to 0$. In Figure 1.11(b) we plot v as a function of interaction strength γ. As γ increases so does v, eventually saturating for large γ. The velocity of sound is a good approximation for the critical velocity of the system, which will play an important role in section 1.7, where a mobile impurity is added to the system.

It is worth emphasizing the difference between the rapidities of the system and the momentum of the actual particles. In Figure 1.12(a) we show the rapidity

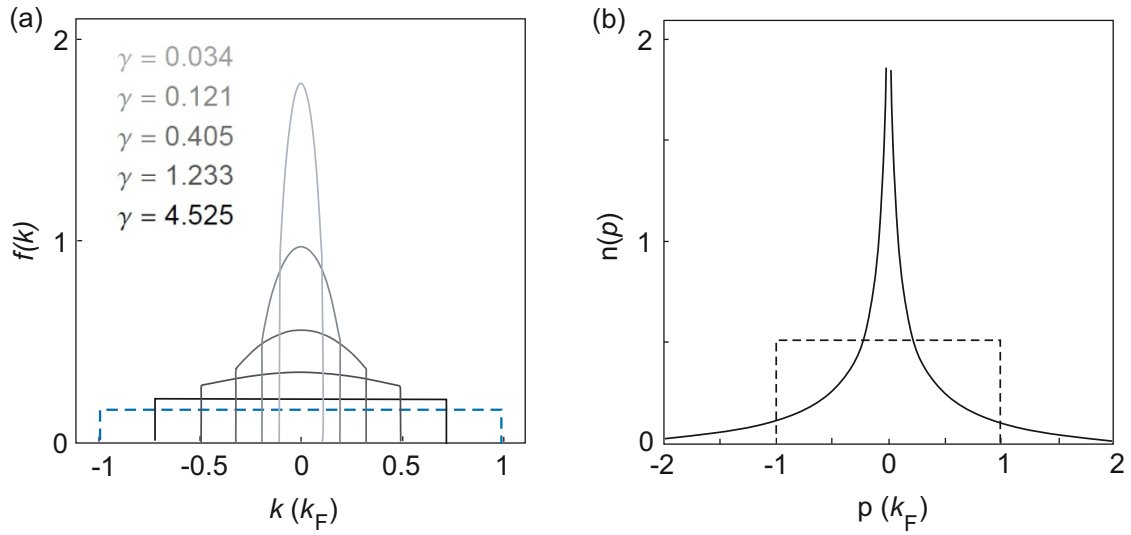

Figure 1.12: Comparison of rapidity and momentum distributions. (a) Rapidity distribution $f(k)$ for increasing interaction parameter γ (low γ gray to high γ black). The dashed blue line is the distribution of a Tonks gas. (b) Momentum distribution $n(p)$ of a Tonks gas (solid line), and for non-interacting fermions (dashed line). Figure (a) and (b) are adapted from reference [59] and [132], respectively.

distribution $f(k)$ of a Bose gas for different interaction strengths γ as obtained via Bethe ansatz. As interactions are increased, the distribution broadens. In the Tonks limit, for $\gamma \to \infty$, all of the quasi-momenta up to k_F are equally occupied, resulting in a distribution that matches the momentum distribution of free fermions. However, the momentum distribution of the interacting Bose gas $n(p)$ is given by

$$n(p) = \frac{1}{2\pi} \int \mathrm{d}r\mathrm{d}r' e^{ip\dot{(}r-r')} g^{(1)}(r, r') \tag{1.53}$$

where, $g^{(1)}(r, r')$ is the first-order correlation function

$$g^{(1)}(r, r') = N \int \mathrm{d}r_2 \ldots \mathrm{d}r_N \Psi^*(r, r_2, \ldots, r_N)\Psi(r', r_2, \ldots, r_N). \tag{1.54}$$

In contrast to the rapidity distribution, $n(p)$ of a (zero-temperature) Tonks gas, shown in Figure 1.12(b), is sharply peaked at $p = 0$ reflecting the bosonic nature of the particles. For low momenta p the momentum distribution follows a power-law behavior $n(p) \propto |p|^{-1/2}$, while for large momenta it follows a universal p^{-4} [157] decay governed by Tan's contact parameter C [158–161]. This asymptotic behavior reflects short-range correlations of the gas. The contact provides a quantitative connection between microscopic interactions and thermodynamic properties [159]. In chapter 2 we present our measurement of Tan's contact in a 1D Bose gas from the strongly repulsive to the strongly attractive regime.

1.5.5 Bethe string states

For the discussion so far we have assumed that the interactions between the particles are repulsive, i.e., $c > 0$. Let us now venture into the attractive regime $c < 0$. For

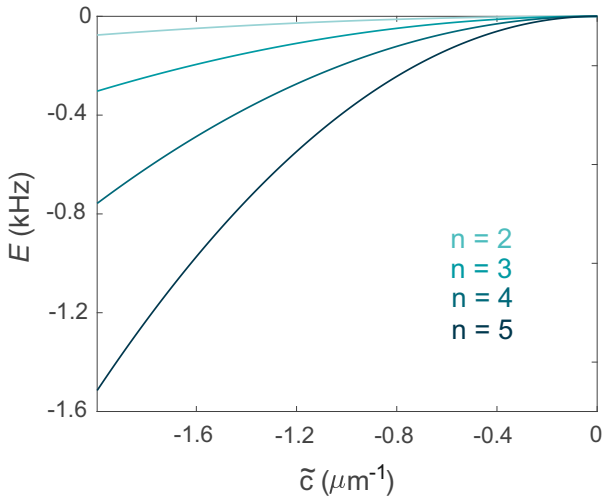

Figure 1.13: Energy of n bound state as a function of the interaction parameter. The solid black to gray curves correspond to the interaction energy (Eq. (1.63)) of the Bethe strings of size $n = 2$ to 5. Here the interaction strength is given in terms of $\tilde{c} = 2mc/\hbar^2$.

this we will go back to the two-particle problem from section 1.5.3 and take a look at the center-of-mass frame. We introduce the relative position and momentum as

$$Z \equiv \frac{z_1 + z_2}{2}, \qquad z \equiv \frac{z_1 - z_2}{2}, \tag{1.55}$$

$$K \equiv k_1 + k_2, \qquad k \equiv k_1 - k_2. \tag{1.56}$$

Now rewriting Eq. (1.31) in the relative coordinates we get the following wavefunction

$$\Psi(Z, z) = e^{iKZ} \begin{cases} A_{12}e^{ikz} + A_{21}e^{-ikz}, & z > 0 \\ A_{21}e^{ikz} + A_{12}e^{-ikz}, & z < 0 \end{cases} \tag{1.57}$$

Similarly Eq. (1.36) can be rewritten as

$$(A_{12} - A_{21})k + ic(A_{12} + A_{21}) = 0. \tag{1.58}$$

Let us now consider bound states, i.e., states with energies less than zero. In the free Schrödinger equation, this corresponds to imaginary k. In this case we require $\mathrm{Im}(K) = 0$ to ensure that the wavefunction is well behaved at $Z \pm \infty$. Similarily, we need $A_{21} = 0$, for $\mathrm{Im}(k) > 0$, and $A_{12} = 0$ for $\mathrm{Im}(k) < 0$. These conditions now dictate that the real part of k must vanish, and from Eq. (1.58) the following must be satisfied:

$$A_{21} = 0 \quad \Rightarrow \quad k = -ic, \tag{1.59}$$

$$A_{12} = 0 \quad \Rightarrow \quad k = ic, \tag{1.60}$$

These conditions lead to the wavefunctions

$$f(z_1, z_2) = e^{iK(z_1+z_2)/2} e^{c|z_1-z_2|/2}. \tag{1.61}$$

The first, and second exponential function in this equation represent the center of mass and relative motion of the two particles, respectively. While the former is

simply a plane wave, the later exponentially localizes the wavefunction for $c < 0$. This indicates that the particles form a bound state, where the characteristic bond length is give by $1/|c|$. Thus the stronger the interactions the tighter the bound state.

This same methodology can be extended to a system of N particles resulting in bound states or strings of length n with momenta

$$k_j = \frac{K}{n} - i\frac{n+1-2j}{2}c, \quad j = 1 \dots n. \tag{1.62}$$

The total momentum of the string is $\sum_j k_j = K$ and the total energy

$$E = \frac{K^2}{n} - \frac{n(n^2-1)}{12}c^2. \tag{1.63}$$

The real component of the rapidities corresponds to the center-of-mass momentum of the string, while the imaginary parts of the rapidities, which are equally spaced, determine the internal structure and binding energy of the string. In Figure 1.13 we plot the energy of the bound states up to $n = 5$ as a function of c for parameters corresponding to Cs. Note that once the strings are created the integrability of the system prevents further decay, thereby stabilizing the bound states [59, 162]. In chapter 2 we create Bethe stings in our experiment by ramping the interactions across the zero interaction point. Our data quantitatively agrees with the recently developed generalized hydrodynamics (GHD) theory [54, 55, 163]. In the next section, we look at the emergence of GHD and the main equations behind the theory.

1.6 Emergent hydrodynamics in closed quantum systems

Hydrodynamics, the macroscopic description of fluid-like behavior, has long been a cornerstone of classical physics. It provides a powerful framework for understanding the collective dynamics of large-scale systems, from turbulent flows in the atmosphere to the behavior of electrons in metal. Recently the principles of hydrodynamics have found renewed relevance in the study of closed quantum systems, where the interplay between quantum mechanics and statistical physics gives rise to novel emergent phenomena [165, 166].

In closed quantum systems, governed by unitary dynamics, the underlying microscopic equations are reversible. Yet, under certain conditions, the system exhibits emergent behavior that closely resembles classical hydrodynamics. This occurs because local conservation laws, such as those for energy, momentum, and particle number, impose constraints on the dynamics, leading to the formation of long-lived collective emergent collective behaviors. These collective behaviors dominate the system's evolution at late times, irrespective of the complexity of the underlying quantum interactions. As an example, consider the dynamics, specifically, the late-time dynamics, of a single classical particle on a lattice (Figure 1.14). Microscopically, the particle undergoes a random walk, whereas at the macroscopic level, its behavior can be described by a probability distribution whose late-time dynamics are governed by the classical diffusion equation. However, the situation changes

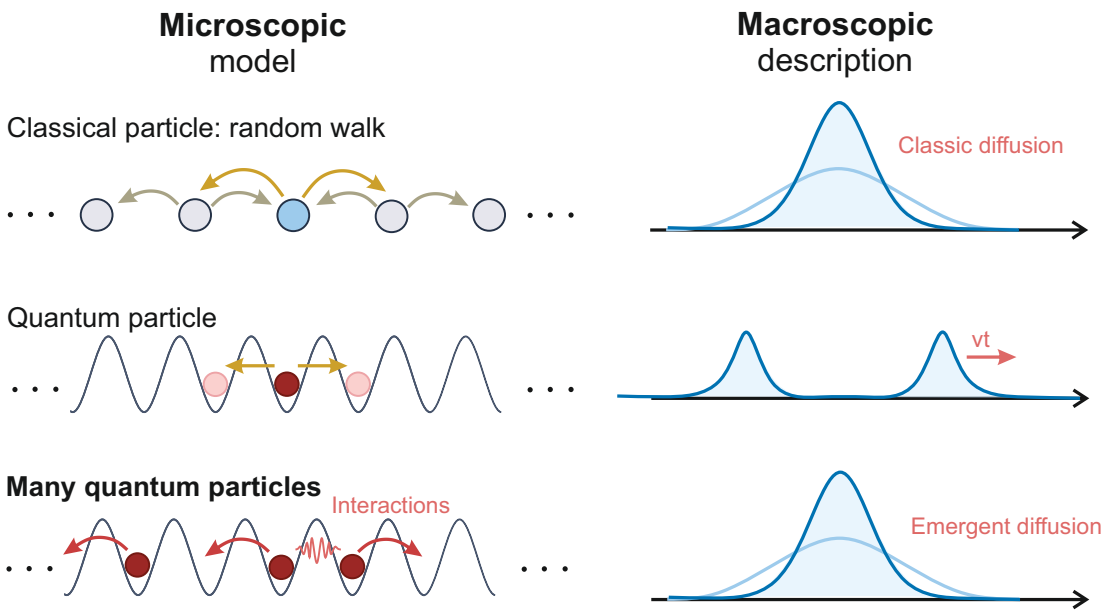

Figure 1.14: Emergent classical hydrodynamics in quantum systems. Comparing the microscopic model and the corresponding macroscopic description in the case of a quantum and a classical particle. For a classical particle on a lattice the microscopic description is given by a random walk, while the macroscopic description follows classical diffusion. A single-body quantum system, on the other hand, shows ballistic expansion behavior. In comparison, a many-body quantum system with interactions gives rise to emergent hydrodynamics at late times. This illustration is adopted from reference [164].

drastically when we consider a single quantum particle on a lattice. Instead of exhibiting diffusive behavior, the quantum particle displays ballistic dynamics. Once many particles are introduced, along with interactions between them, the system's long-term behavior typically reverts to being diffusive. This transition to classical diffusion-like behavior (in the long-term dynamics) of many-body quantum systems is closely linked to the thermalization of isolated systems, where different parts of the system effectively act as a bath for smaller subsystems [167].

For strongly interacting systems that are globally out of equilibrium, but locally in equilibrium, hydrodynamics has long been a valuable tool, relying on the local conservation of mass, momentum, and energy (continuity equation). However, for an integrable system, where there are an infinite number of conserved quantities, conventional hydrodynamics has proven to be insufficient [168–172]. The recently developed theory of GHD overcomes this problem by focusing on the evolution of the momenta of the quasi-particles, the rapidities [54]. It relies on two fundamental assumptions [173, 174]. First, it assumes that the system can modeled as a continuum of spatially homogeneous fluid cells, where each cell contains many particles and can be described by an integrable model. The second assumption is that the time variation is slow enough such that each fluid cell remains in a local equilibrium. Notably, due to the many conserved quantities an integrable system cannot relax to a thermal equilibrium. Instead it relaxes to a generalized Gibbs ensemble (GGE) [175–177], which includes all conserved quantities in the description. The generality of the assumptions used in the GHD theory also makes it applicable to

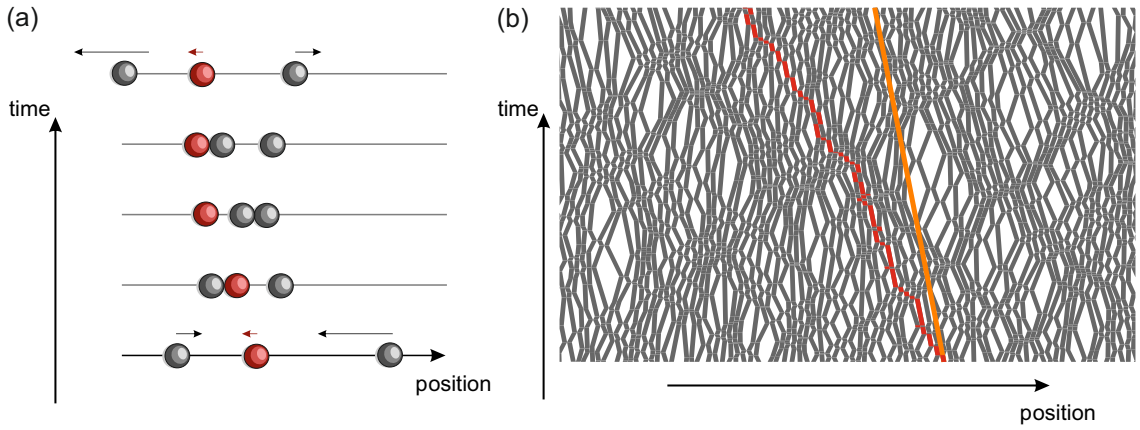

Figure 1.15: Illustration of a system of identical classical hard balls restricted along a single line of motion, which features GHD. (a) Elastic collisions between the balls result in an exchange of velocities. The red ball illustrates that the velocity of the balls can be indexed such that the bare velocity after each collision remains constant. (b) At large distances and over extended time scales, the effective velocity of the red ball (depicted by the red trajectory) differs from its "bare" velocity (shown in orange). This illustration is taken from reference [145].

other integrable models besides the 1D Bose gas.

1.6.1 Generalized hydrodynamics

We will now take a brief look at the equations behind GHD. For precise derivations and in general a more detailed overview of GHD see references [145, 174, 178]. In a nutshell, GHD describes the evolution of the quasi-particles density by solving a set of coupled equations known as the GHD equations. Firstly the GHD continuity equation or the transport equation for the quasi-particles is written as

$$\partial_t n(\lambda, x, t) + \partial_x (v^{\text{eff}}(\lambda, x, t) n(\lambda, x, t)) = 0, \tag{1.64}$$

where $n(\lambda, x, t)$ is the distribution or occupation function for quasi-particles with rapidity λ at position x and time t. $v^{\text{eff}}(\lambda, x, t)$ is the effective velocity of the quasi-particles, which is dependent on the interactions between the quasi-particles. The effective velocity is given by a second equation. It is determined by both the velocity of the quasi-particles without interactions, the bare velocity $v^{\text{bare}}(\lambda)$, as well as the interactions between the quasi-particles

$$v^{\text{eff}}(\lambda) = v^{\text{bare}}(\lambda) + \int \mathrm{d}\lambda' \Delta(\lambda' - \lambda) n(\lambda') (v^{\text{eff}}(\lambda') - v^{\text{eff}}(\lambda)). \tag{1.65}$$

Here $\Delta(\lambda' - \lambda)$ is the scattering kernel. The interaction term of Eq. (1.65) (the second term) describes the motion of the particle through the medium. Equation (1.65) describes the dressing of the velocities of particles that move through the system with the interaction with other particles [179–182]. This dressing incorporates physics similar to Wigner time delays (Eq. (1.42)) but in a many-body context. Rather than a simple sum of individual delays, the effective velocity emerges from a self-consistent solution where all quasi-particles mutually influence each other's motion

through the dynamical medium. In Figure 1.15 we show an illustration of this for a classical 1D hard gas system. The rapidities λ in these equations are precisely the same rapidity parameters that appear in the Bethe ansatz solution of the microscopic integrable model, with $n(\lambda, x, t)$ representing the continuous limit of the discrete rapidity distribution from the many-body Bethe wavefunction.

With the recently developed technique [149] providing experimental access to the rapidity distribution of a Bose gas, GHD has been successfully compared with experiments [183, 184]. To measure the rapidity distribution, we first quench the external longitudinal trapping potential to a flat-bottom and allow the gas to expand in 1D for time t_{1D} until it reaches the dilute regime. A subsequent 3D time-of-flight measurement then gives the momentum distribution of the dilute gas, which reflects the rapidity distribution of the original trapped sample. In chapter 2 we use this technique, as well as release energy measurements, to experimentally demonstrate the applicability of GHD to interaction changes and systems with bound states.

1.7 Adding a lonely impurity in a Lieb-Liniger gas

Even a small perturbation in a 1D gas, such as the introduction of a single impurity, can profoundly influence the behavior of the entire system, giving rise to dynamics that extend beyond the scope of standard Luttinger theory. The presence of an impurity in a 1D system can trigger a wide range of phenomena, including the formation of polarons [185], where the impurity becomes dressed by the medium's excitations, and the Kondo effect [186], where the impurity dramatically transforms the system's properties. Furthermore, it can lead to Anderson's orthogonality catastrophe [187], in which a single distinguishable particle alters the system's transport characteristics.

This section examines the behavior of an impurity interacting with a Bose gas. We discuss the celebrated Yang-Gaudin model [43, 44]. In particular, we look at the solution of the Yang-Gaudin model via the Bethe ansatz. We then discuss the emergence of anyonic correlations [188] in the finite-momentum ground state of such system. Finally, we turn to the out-of-equilibrium dynamics, discussing the relaxation of a mobile impurity injected in a Lieb-Liniger gas and the subsequent development of the so-called quantum flutter phenomenon [189, 190].

1.7.1 The Yang-Gaudin model (and emergent anyons)

The Yang-Gaudin model, independently developed by Michel Gaudin and Chen-Ning Yang, describes a two component 1D gas of fermions with contact interactions. The two components can either be seen as fermions with two different spins, spin up ($\uparrow$) and spin down ($\downarrow$), or alternatively as two-component bosons with with SU(2) symmetric interaction [64]. Here we discuss the specific case of the Yang-Gaudin model of a single mobile impurity immersed in a Tonks gas with the same mass. This specific case was first solved by McGuire [191, 192]. As previously discussed, the Tonks gas maps onto a gas of spin-polarized free fermions. In this case, all the observables related to the impurity are the same, whether the background is a Tonks gas or a gas free femions. Below, we will consider a free fermionic background gas that repulsively interacts with the impurity. We denote the impurity by $|\downarrow\rangle$ and

the host by $|\uparrow\rangle$. The Hamiltonian reads

$$\hat{H} = \sum_{j=1}^{N} \frac{\hat{P}_j^2}{2m} + \frac{\hat{P}_\downarrow^2}{2m} + g_{\uparrow\downarrow} \sum_{j=1}^{N} \delta(z_j - z_\downarrow), \tag{1.66}$$

where z_j ($\hat{P}_j$) denotes the coordinate (momentum) of the jth host gas particle, $j = 1...N$, and $z_\downarrow$ ($\hat{P}_{\text{imp}}$) is for the impurity, and $g_{\uparrow\downarrow}$ the impurity-host interaction strength. This Hamiltonian is integrable and can be solved via the Bethe ansatz [191–193]. Below, we will go through the Bethe ansatz solution. For the purpose of this discussion we will again set $\hbar = m = 1$.

We begin with a transformation from the laboratory to the mobile impurity reference frame. This is known as the Lee-Low-Pines (LLP), or the polaron, transformation [194]

$$\mathcal{O} \to \mathcal{O}_\mathcal{Q} = \mathcal{Q}\mathcal{O}\mathcal{Q}^{-1}. \tag{1.67}$$

where $\mathcal{O}$ is an arbitrary operator and

$$\mathcal{Q} = e^{i\hat{P}_\uparrow \hat{z}_\downarrow} \tag{1.68}$$

where, $\hat{P}_\uparrow$ is the total momentum of the host particles. The momentum of the impurity particles are changed by the LLP transform, while the momentum of the host particles remains unaffected

$$\hat{P}_{\uparrow\mathcal{Q}} = \hat{P}_\uparrow, \qquad \hat{P}_{\downarrow\mathcal{Q}} = \hat{P}_\downarrow - \hat{P}_\uparrow. \tag{1.69}$$

This leads to the following total momentum of the system in the mobile impurity reference frame

$$\hat{P}_\mathcal{Q} = \hat{P}_\downarrow. \tag{1.70}$$

We now apply $\mathcal{Q}$ to the wavefunction. Here it is important to remember that our system consists of fermions in a continuum and is therefore translationally invariant. The action of the momentum operator shifts all coordinates according to

$$e^{a\frac{d}{dz}} f(x) = f(z + a). \tag{1.71}$$

This results in

$$\begin{aligned} \mathcal{Q}\Psi_Q(z_\downarrow, z_1, \ldots, z_N) &= \Psi_Q(z_\downarrow, z_1 + z_\downarrow, \ldots, z_N + z_\downarrow) \\ &= e^{iQz_\downarrow}\Psi_Q(0, z_1, \ldots, z_N), \end{aligned} \tag{1.72}$$

where Ψ_Q is the wavefunction in the original frame, and the subscript Q corresponds to the total momentum of the system. Equation (3.31) can now be rewritten as

$$\begin{aligned} \Psi_Q(z_\downarrow, z_1, \ldots, z_N) &= e^{iQz_\downarrow}\Psi_Q(0, z_1 - z_\downarrow, \ldots, z_N - z_\downarrow) \\ &\equiv e^{iQz_\downarrow} f_Q(y_1, \ldots, y_N), \end{aligned} \tag{1.73}$$

where $y_j = z_j - z_\downarrow$, $j = 1, \ldots, N$, and $f_Q(y_1, \ldots, y_N)$ is the wavefunction of the system in the mobile impurity reference frame.

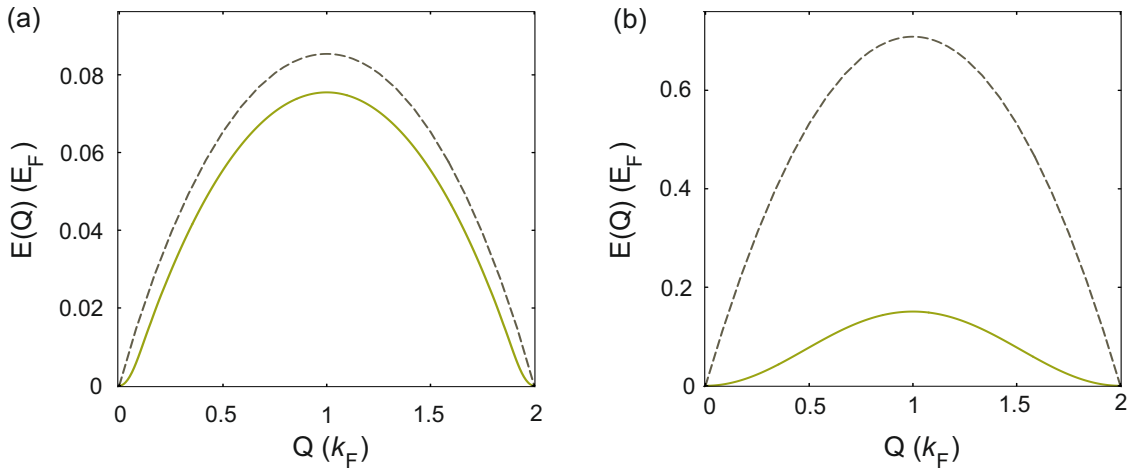

Figure 1.16: Excitation spectrum for different values of interactions. The solid line is the dispersion of bosons interacting with an impurity with $\gamma_{\uparrow\uparrow} = \gamma_{\uparrow\downarrow} = 0.1$, and 10 for (a) and (b) respectively. For comparison the dashed curve shows the dispersion of the Bose gas without impurity. This figure is adapted from reference [195].

We now return to the Hamiltonian (1.66). In the mobile impurity frame it reads

$$\hat{H}_Q = \frac{1}{2}\sum_{i=1}^{N} \hat{P}_i^2 + \frac{1}{2}(\hat{P}_\downarrow - \hat{P}_\uparrow)^2 + g_{\uparrow\downarrow}\sum_{i=1}^{N}\delta(y_i). \tag{1.74}$$

The wavefunctions in the impurity frame can be written in terms of the following Slater determinant [196]

$$f_Q(y_1,\ldots,y_N) = \frac{Y}{\sqrt{N!L^N}}\begin{vmatrix} e^{ik_1y_1} & \ldots & e^{ik_{N+1}y_1} \\ \vdots & \ddots & \vdots \\ e^{ik_1y_N} & \ldots & e^{ik_{N+1}y_N} \\ \nu(k_1) & \ldots & \nu(k_{N+1}) \end{vmatrix}, \qquad 0 \le y_j \le L, \tag{1.75}$$

where

$$\nu(q) = \frac{g_{\uparrow\downarrow}}{2}\frac{1}{q - g_{\uparrow\downarrow}(\Lambda + i)/2}. \tag{1.76}$$

Here the factor Y ensures the normalization condition and the set of quasi-momenta $k_1,\ldots,k_{N+1}$ satisfies a system of nonlinear equations

$$\cot\frac{k_jL}{2} = \frac{2k_j}{g_{\uparrow\downarrow}} - \Lambda, \qquad j = 1,2,\ldots,N+1, \tag{1.77}$$

where Λ is a free parameter. These are the Bethe equations. The free parameter Λ is fixed by the requirement that the sum of the quasi-momenta is equal to the total momentum of the system

$$Q = \sum_{j=1}^{N+1} k_j. \tag{1.78}$$

Finally the total energy of the system is

$$E_{\mathrm{F}} = \frac{1}{2}\sum_{j=1}^{N+1} k_j^2. \tag{1.79}$$

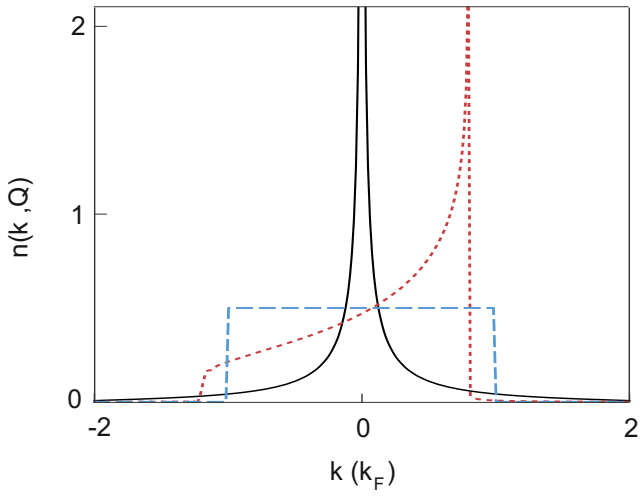

Figure 1.17: Momentum distribution of the impurity $n(k, Q)$ for large repulsive interactions $\gamma_{\uparrow\downarrow} = 10$, for different values of total momenta Q. Black, red, and blue curves correspond to $Q = 0\ k_{\mathrm{F}}$, $0.8\ k_{\mathrm{F}}$, and $1\ k_{\mathrm{F}}$, respectively. This figure has been adopted from [188].

We now turn to the excitation spectrum of the system. The introduction of an impurity changes the excitation spectrum drastically. Figure 1.16 shows the lower edge of the spectrum for two different interaction strengths $\gamma_{\uparrow\downarrow}$. The spectral edge decreases with increasing interactions. In contrast to the Lieb-Liniger model, where the dispersion relation is linear for small Q, for the case of an immersed impurity the edge of the excitation spectrum has a quadratic dependence

$$E(Q) \simeq \frac{Q^2}{2m_*}. \tag{1.80}$$

Here m_* is the effective mass of the impurity, which is always larger than m for any non-zero repulsive interaction [197]. This can be understood as the impurity getting dressed by the excitations of the background gas, thus the lower branch is called the polaron (or magnon) branch. The bare excitation spectrum of the background gas is also referred to as the exciton (or plasmon) spectrum in literature. In the thermodynamic limit for large $\gamma_{\uparrow\downarrow}$ the effective mass is given by

$$\frac{m}{m^*} = \frac{2\pi^2}{3\gamma_{\uparrow\downarrow}}, \qquad \gamma_{\uparrow\downarrow} \to \infty. \tag{1.81}$$

As $\gamma_{\uparrow\downarrow} \to \infty$, the effective mass m^* approaches the total mass of the system $(N + 1) \times m$. This has a clear physical interpretation: in the limit of infinite interactions, the impurity becomes impenetrable, so moving the impurity requires displacing the entire host gas collectively.
In the limit of infinite repulsion ($g_{\uparrow\downarrow} \to \infty$) the edge of the excitation spectrum flattens to zero. In this limit the Bethe equations (Eq. (3.36)) simplify to

$$\cot \frac{k_j L}{2} = -\Lambda, \qquad j = 1, 2, \ldots, N+1, \qquad g_{\uparrow\downarrow} \to \infty. \tag{1.82}$$

The quasi-momenta k_j are quantized as free fermion momenta with an additional shift

$$k_j = q_j + \frac{\mu}{L}, \qquad j = 1, 2, \ldots, N+1, \qquad g_{\uparrow\downarrow} \to \infty \tag{1.83}$$

where, $\mu = -2\tan(\Lambda)$ and q_j are free-fermion momenta

$$q_j = \frac{2\pi}{L} n_j, \qquad n_j = 0, \pm 1, \pm 2, \ldots. \tag{1.84}$$

The total momentum of the system is obtained by summing over all quasi-momenta

$$Q = \sum_{j=1}^{N+1} k_j. \tag{1.85}$$

The total momentum Q is also related to μ via

$$Q = k_{\mathrm{F}}(1 + \mu/\pi). \tag{1.86}$$

A remarkable feature of this system in this limit is that the momentum distribution of the impurity $n(k, Q)$ for a total momentum Q maps onto a system of 1D hard-core anyons as shown in Ref. [188]. Anyons [123, 124] are low-dimensional quasi-particles that are neither bosons nor fermions. Rather than gaining a phase factor of 0 or π upon exchange, such as for bosons and fermions, respectively, the wavefunction of anyons acquire an arbitrary phase factor $e^{i\theta}$ upon exchange, where θ is known as the statistical angle. For the infinitely repulsive impurity case, the total momentum of the system is related to the statistical angle via $\theta = \pi Q/k_{\mathrm{F}}$. This allows us to continuously tune the statistical angle from bosonic to fermionic by changing the total momentum of the system. As shown in Figure 1.17, $n(k, Q)$ is bosonic for $Q = 0\ k_{\mathrm{F}}$ and fermionic for $Q = k_{\mathrm{F}}$. For the intermediate case, $Q = 0.8\ k_{\mathrm{F}}$, $n(k, Q)$ is asymmetric and peaked at finite k. Such an asymmetic momentum distribution is a hallmark of an anyonic system. The mapping to an anyonic system can be understood in terms of spin-charge separation (see chapter 3).

1.7.2 Quantum flutter: the dance between a particle and a hole

So far we have discussed the ground state of an interacting impurity immersed in a 1D Bose gas. Equilibrium properties of polaronic excitations in ultracold atomic gases have been thoroughly studied both theoretically and experimentally [198]. However, the out-of-equilibrium transport properties of such impurities remain experimentally largely unexplored in these highly controllable cold atom platforms. In chapter 4, we will show experimental results on the relaxation dynamics of an impurity injected with constant velocity into a strongly interacting 1D Bose gas. Here we take a brief look at the theoretical description of a mobile impurity interacting with a free Fermi or a Tonks gas, following references [189, 190, 199]. Note that all the observables related to the impurity are the same, whether the impurity is immersed in a background gas of either Tonks gas or fully polarized fermions. The moving impurity is described by a plane wave with momentum Q and thus gives the following initial state of the system [189]

$$|\mathrm{in}\rangle = \hat{c}^{\dagger}_{Q\downarrow}|\mathrm{FS}\rangle, \tag{1.87}$$

where $|\mathrm{FS}\rangle$ is the wavefunction of the Fermi sea formed by the host particles and $\hat{c}^{\dagger}_{Q\downarrow}$ is the creation operator of an impurity with momentum Q. The time evolution

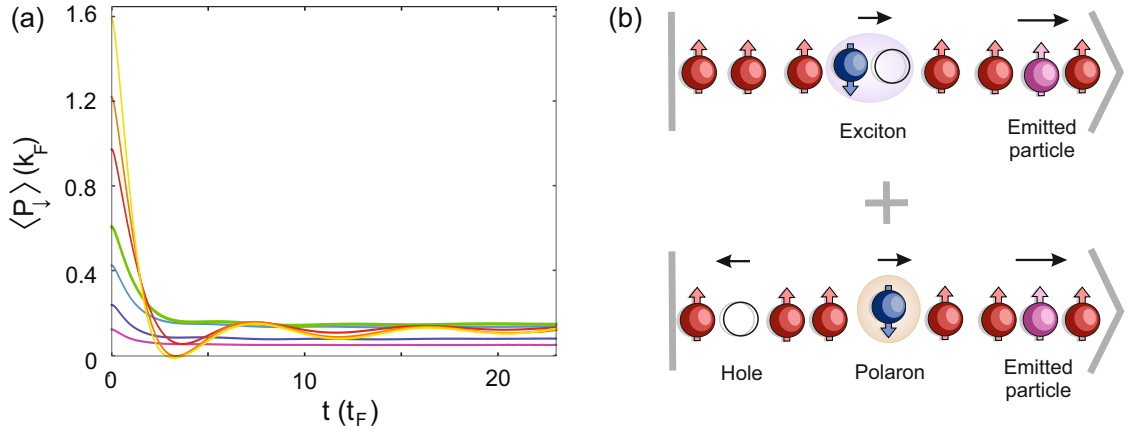

Figure 1.18: Quantum flutter. (a) Evolution of the mean impurity momentum for different initial momenta Q. For $Q < k_{\mathrm{F}}$ the evolution of the impurity momentum is a simple decay, while for $Q > k_{\mathrm{F}}$ The momentum exhibits long term coherent oscillations known a quantum flutter. (b) Illustration of the quantum flutter phenomena. For a supersonic impurity, a superposition of a polaron, (where the impurity and the hole travel independently) and an exciton state (where the impurity and the hole bind together and propagate in unison) leads to long lived coherent oscillations in the momentum of the impurity known as quantum flutter. During the initial collisions with the host, majority of the impurity momentum is imparted onto host particle resulting in an emitted wave packet. This figure has been adapted from reference [189].

of the state $|\mathrm{in}\rangle$ follows $|\mathrm{in}(t)\rangle = e^{it\hat{H}}|\mathrm{in}\rangle$, where $\hat{H}$ is the Yang-Gaudin Hamiltonian (Eq. (1.66)). Figure 1.18(a) shows the average momentum of the impurity $\langle \hat{P}_{\downarrow}(t)\rangle$ as a function of time for different values of Q. Two distinct observations can be made from this plot: first, the impurity never comes to a full stop and second, there is a notable difference in the subsonic ($Q < k_{\mathrm{F}}$) and the supersonic ($Q > k_{\mathrm{F}}$) impurity dynamics. In the subsonic case, the impurity sheds some of its momentum before reaching a steady state. In contrast, the momentum of a supersonic impurity shows damped oscillatory behavior after the initial decay. These oscillations result from a novel coherent quantum dynamical phenomenon known as quantum flutter. The amplitude of this long-lived oscillation increases with Q, while the frequency is independent of Q.

Intuitively this behavior can be understood as follows: upon interacting with the host, the majority of the impurity momentum is transferred to the host, creating a wave packet that carries away the excess momentum and leaves behind a hole deep inside the Fermi sea. From the initial collisions two possible states arise, as schematically illustrated in Figure 1.18(b). First, the impurity can bind itself with the hole forming an exciton-like (or plasmon-like) state. Alternatively, the impurity dresses itself with the excitations of the host forming a polaron-like (or magnon-like) state, which travels independently of the hole. The energy difference of the polaron and exciton state at $Q = k_{\mathrm{F}}$ is equal to the frequency of the flutter [189, 190], suggesting that the quantum flutter originates from an interplay between these two states. In other words, the flutter can be seen as a many-body correlated state that is a superposition of the lowest energy excitation of the host (dashed curve in Figure 1.16) and of the entire system (solid curve in Figure 1.16) around $Q = k_{\mathrm{F}}$, and has

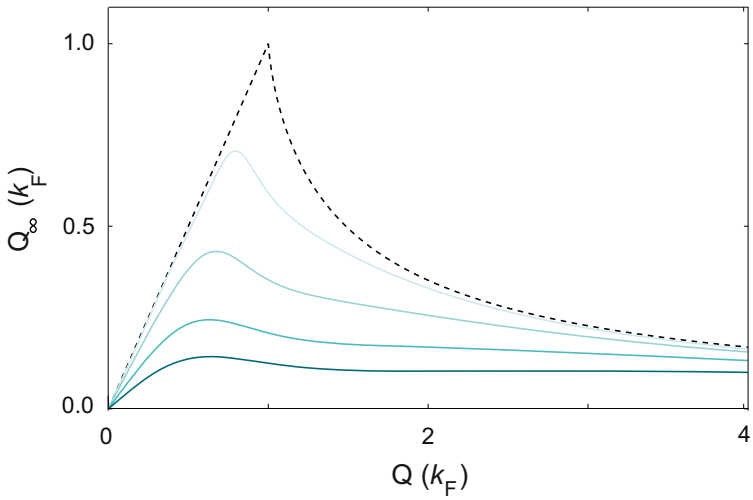

Figure 1.19: Exact solution of saturated momentum as a function of initial momentum of the impurity for different interaction strengths. The solid curves show the analytic results from reference [199] for the impurity-gas interaction strengths $\gamma_{\uparrow\downarrow} = 1, 3, 6$, and 10 for increasing shades of blue. The dashed curve corresponds to $\gamma_{\uparrow\downarrow} = 0$.

a group velocity close to zero (since for both excitation spectra $\partial E/\partial Q|_{Q=k_\mathrm{F}} = 0$). The frequency of the flutter matches the energy difference of the polaron and exciton state at $Q = k_\mathrm{F}$. A hand-waving argument for why it is a superposition at $Q = k_\mathrm{F}$ is that the highest density of states occurs at $Q = k_\mathrm{F}$. In order for this superposition between the two states to arise, and hence for the flutter oscillation to occur, the initial momentum of the impurity must necessarily be greater than or equal to k_F.

The second interesting feature of Figure 1.18(a), is that the impurity never comes to a complete stop, but instead eventually reaches a finite velocity. An intuitive interpretation of this is that after multiple collisions that carry away momentum, the impurity finally decays onto a finite momentum magnon state, which corresponds to the edge of the dispersion of the system. One curious effect that this explanation does not take into account is that the final velocity of the impurity has a dependence on the initial condition, specifically Q. In Figure 1.19 we show the saturated velocity Q_∞ of the impurity as a function of the initial injected velocity for different interaction strengths. For small initial velocities, Q_∞ is positively correlated with Q.

Finally it is worth noting that while the original paper on quantum flutter looked at an integrable model [189], this phenomena is persistent even if the integrability of Hamiltonian 1.66 is broken. In fact follow up simulations have shown that theoretically the flutter phenomena is very robust: when the impurity is immersed in a 1D Bose gas with finite γ and also in the presence of a integrability-breaking harmonic trap [190].

1.8 Conclusion and outlook

We have now reached the final part of the introductory chapter. Beyond this section each chapter of the thesis is comprised of one of four selected publications. Here

we will close this introductory chapter with few brief speculations about possible future experimental directions going beyond each of these publications. We end this section with the spin-dependent lattice, which was implemented during the course of this PhD and offers further promising directions for future research.

Bethe strings and GHD

In chapter 2, we present a study where we realize Bethe strings for the first time in a 1D attractive Bose gas by sweeping interactions from the repulsive to the attractive regime, passing through the non-interacting point. We characterize these strings via binding energy measurements, Tan's contact and momentum distribution after 1D-expansion. The implementation of an 808-nm flat trap, during this PhD, enabled us to expand the gas in 1D before taking 3D time-of-flight images. For repulsive interactions this measurement effectively maps onto the rapidities of the gas. While in the attractive regime this is not the case, the resulting distributions can still be directly compared with GHD. We find our results are in good agreement with the results of GHD.

The outlook for this project can be divided into two main categories: the Bethe strings themselves and the 1D-expansion technique. A follow up project of the Bethe strings measurements presented in this thesis, would be the study the size of the bound states that are populated with respect to the sweep rate. This could be carried out via release energy measurements. A significant step in a slightly different direction would be the direct imaging of the strings. Spectroscopic methods, such as radio-frequency (RF) or Bragg spectroscopy, are promising approaches to visualize these bound states and characterize their formation dynamics. Furthermore, the cesium quantum gas microscope, currently under construction in the adjacent laboratory, will increase the imaging resolution to the single-atom level, which will enable correlation measurements capable of directly detecting individual Bethe strings.

The second avenue of future research would be the ability to measure the rapidity of a system and directly compare it with GHD. This new technique opens up a whole range of experiments. The quantum Newton cradle experiment [144], for instance, demonstrated that 1D quantum systems do not reach thermal equilibrium. Despite its profound impact on the field, a comprehensive theoretical description of these observations has remained elusive. This new capability to measure the rapidity distribution offers an opportunity to directly compare the non-equilibrium dynamics of the Newton's cradle with GHD simulations. This comparison could finally provide a quantitative theoretical framework for understanding this paradigmatic experiment after more than a decade of theoretical and experimental efforts. Extension of GHD to multi-component gases represents another promising future direction. Two-component gases, while experimentally accessible, pose significant theoretical challenges due to their increased complexity.

Generalized hydrodynamics is a relatively new theoretical framework. Its limitations and domain of applicability still remain uncharacterized. The theory makes two critical assumptions. Firstly, the system consists of fluid cells that are spatially uniform, integrable and contain many particles. Secondly, local quantities evolve slowly enough that each cell equilibrates to a generalized Gibbs state. The latter can be tested via interaction ramps with varying ramp rates, and ultimately quenching the system. Furthermore the controlled breaking of integrability would

be another fundamental test of GHD's limitations. By introducing perturbations that break integrability, such as a lattice along the tubes, we can investigate the crossover from integrable to non-integrable dynamics.

Impurity dynamics

In chapters 3, and 4, we study in-, and out-, of-equilibrium dynamics of a system of 1D bosons with an injected impurity, respectively. In chapter 3 we find that the finite-momentum ground state of an impurity immersed in a system of 1D bosons can be mapped onto system of hard-core anyons with fully tunable statistical parameter. In chapter 4, we discuss the relaxation dynamics of a mobile impurity injected with a constant velocity into a Tonks gas. Due to the underlying properties of the Tonks gas, we observe distinctly different time scales in the relaxation for impurity injected with velocities above and below k_{F}.

Both of these projects have several promising directions for future investigations. For the publication presented in chapter 3, the continuous tuning of quantum statistics could be used to realize heat engines and quantum thermal machines [200–202]. For the work in chapter 4, we were unable to observe the long term quantum flutter phenomena. However, multiple experimental upgrades during this PhD, such as an improvement of the imaging setup, implementation of optical levitation and Bragg spectroscopy could make detection of the flutter now feasible. Optical levitation, for instance, allows for the simultaneous levitation of both the impurity and the host circumventing the need to go into the free fall frame and hence increasing the experimental observation time from approximately three milliseconds to hundreds of milliseconds. Furthermore, future implementation of a box potential would remove the inhomogeneous broadening of k_{F}, which would significantly improve our ability to detect small signals such as the quantum flutter oscillations. Looking forwards, these experiment could also be extended to two and three dimensions opening the investigation into the role that dimensions play in this setting.

Going from a repulsive to an attractively interacting impurity would also be an interesting direction of future study. Theoretically it has been shown that an attractively interacting impurity immersed in a Tonks gas does not experience friction [188]. This is in stark contrast to the repulsive impurity that comes to stop after only a few Fermi-times. Experimentally we can use the CIR for impurity-bath interactions near 50 G to realize such an a scenario. This effect is a direct consequence of integrability. When integrability is broken the frictionless transport is also broken. In our case the integrability relies on the equal mass of the impurity and the host. This can be tuned by using a spin-dependent lattice (see below), where one can effectively increase the mass of either the host or the impurity, and thereby moving away from the integrable point.

Utilizing the $(3, 2)$ BEC

In chapter 5, we for the first time, condense Cs in a non-ground state, the $(3, 2)$ state. We achieve a condensate around 40 G as well as 160 G where the $(3, 2) + (3, 3)$ scattering length is favorable. For both of these magnetic field regions we characterize the lifetime of a thermal sample and find a three-body spin-exchange resonance around 40 G.

The ability to condense Cs in the $(3, 2)$ state, presented in chapter 5, widens the range of usable magnetic field regions for the species. This could be of particular interest for future mixture experiments potentially making it more compatible with other atoms. Potassium-Cesium mixture, for example, is a promising candidate for highly dipolar molecules. Both of the two species have a rich spectrum of Feshbach resonances, but this also limits the possible magnetic field regions where they can be cooled simultaneously. Using Cs in the $(3, 2)$ state would open up a window at 160 G which would be much more favorable for Potassium in KCs we tried this. It works if the samples are kept apart but we see losses when they are overlapped. Most likely we are limited by two-body spin relaxations involving one particle of each specie. A BEC in the $(3, 2)$ state also expands the range of the tunability of interactions in impurity systems for Cs. In previous studies using Cs, the dynamics of an intentionally injected impurity revealed the underlying correlations of the 1D system. These studies were carried out with the bulk, and impurity, in the $(3, 3)$, and $(3, 2)$, states respectively. Consequently the bulk-bulk interactions were always greater than the impurity-bulk interactions. The $(3, 2)$ BEC provides a pathway to reverse the roles of the two magnetic spin states allowing the bulk-bulk interactions to be tuned, while maintaining a large constant bulk-impurity interactions. This serves as an ideal setting where a deliberately introduced impurity atom can act as a local probe of a many-body system in both static and dynamic cases. In particular, it can be used to probe phase transitions such as the pinning transition [14] and, more importantly, topological phase transitions, where there are no underlying order parameters, making them otherwise difficult to detect. Another property that distinguishes the $(3, 2)$ state from the $(3, 3)$ ground state is that it is exposed to two-body decay. The two-body dissipation can, on one hand, be viewed as a limitation to the coherence of the system. On the other hand, it could provide a promising platform for engineering and controlling quantum states in a dissipative environment [203, 204]. In particular, when combined with an external drive these systems could give rise to a novel class of many-body of states that do not have any equilibrium counterpart.

Spin-dependent lattice

The AC Stark shift causes the dipole potential experienced by an atom to depend on its internal state. In the case of two different spin states, specific wavelengths exist where the light shift of one spin state becomes negligible; this is known as a tune-out wavelength. There are also wavelengths where the light shifts of two states become either identical or exactly opposite, referred to as magic wavelengths and anti-magic wavelengths, respectively. For alkali atoms, the magic wavelength typically falls between the D_1 and D_2 lines. Importantly, off-resonant photon scattering, which leads to heating and atom loss, depends on both the depth of the dipole potential and the detuning from resonance, with the scattering rate decreasing as the detuning increases. Cesium, having the largest D_1 to D_2 transition frequency among the alkali atoms, is particularly well-suited for implementing this spin-dependent light. In Figure 1.20, we show the lattice depth as a function of wavelength for both the $(3, 3)$ and $(3, 2)$ states. During this PhD, a spin-selective lattice was implemented and tested for the $(3, 3)$ and $(3, 2)$ states. Figure 1.20 also presents measured momentum distributions of a BEC in both the $(3, 3)$ and $(3, 2)$ spin states exposed to a 50 μs lattice pulse. The pulse was tuned to the tune-out wavelengths of $(3, 3)$

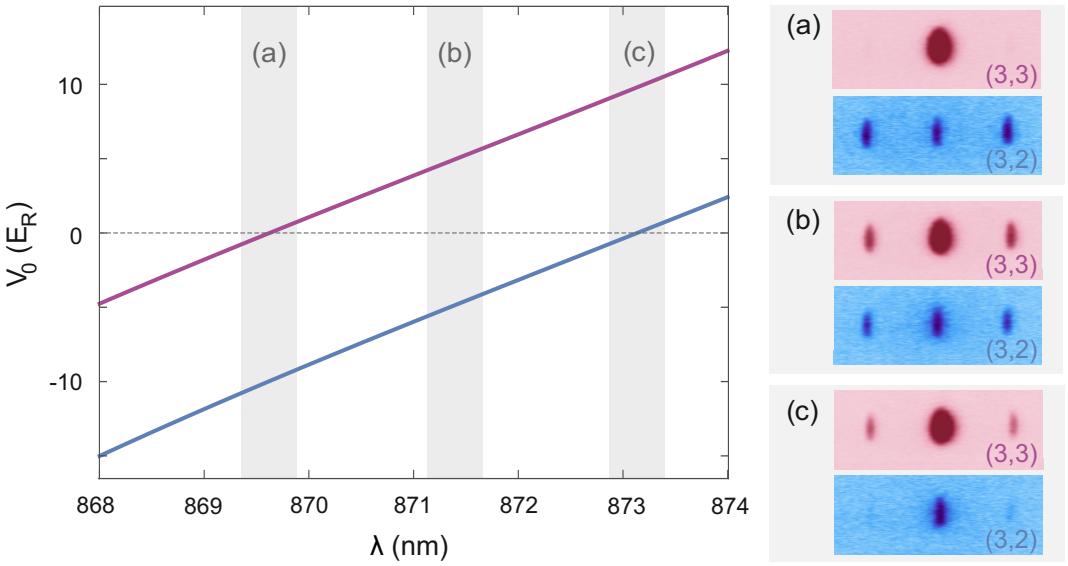

Figure 1.20: Lattice depth for $(3,3)$ and $(3,2)$ spin states as a function of wavelength. The solid purple and blue curves correspond to the $(3,3)$ and the $(3,2)$ states respectively. The dashed line indicates a lattice depth of 0 E_{R}. The gray regions correspond to the wavelengths used for insets (a), (b) and (c). Insets: Example experimental absorption images of an atomic cloud in the $(3,3)$ and $(3,2)$ state after being exposed to a lattice with a wavelength of 869.7 nm, 871.3 nm, and 873.1 nm, shown in (a), (b), and (c) respectively.

(Figure 1.20(a)) and $(3,2)$ (Figure 1.20(b)), as well as to the anti-magic wavelength for both spin states (Figure 1.20(c)).

The spin-dependent lattice is not discussed further in this thesis, as it was not used in any of the featured publications. However, it opens up opportunities for simulating extended Bose-Hubbard models, realizing frustrated spin systems, and exploring exotic phases of matter [205, 206]. Moreover, it could also be used in the proposed experiment probing the pinning transition [14] via an impurity. Pinning the host with a spin-dependent lattice would ensure that the impurity dynamics are influenced solely by the structure of the host, remaining entirely independent of the pinning lattice.

1.9 List of publications

- *Bose-Einstein condensation of non-ground-state caesium atoms*
  Milena Horvath, Sudipta Dhar, Arpita Das, Matthew D. Frye, Yanliang Guo, Jeremy M. Hutson, Manuele Landini, Hanns-Christoph Nägerl,
  Nature Communications **15**, 3739 (2024)

- *Observing Bethe strings in an attractive Bose gas far from equilibrium*
  Milena Horvath*, Alvise Bastianello*, Sudipta Dhar*, Rebekka Koch, Yanliang Guo, Jean-Sebastien Caux, Manuele Landini, and Hanns-Christoph Nägerl
  (*These authors contributed equally to this work)
  preprint at: arxiv.org/abs/2505.10550

- *Observing dissipationless transport of a correlated quantum state of an impurity in a strongly-interacting Bose gas*
  Milena Horvath*, Sudipta Dhar*, Elisabeth Wybo, Dimitrios Trypogeorgos, Yanliang Guo, Mikhail Zvonarev, Michael Knap, Manuele Landini and Hanns-Christoph Nägerl (*These authors contributed equally to this work)
  In preparation.

- *Observing anyonization of bosons in a quantum gas*
  Sudipta Dhar*, Botao Wang*, Milena Horvath*, Amit Vashisht, Yi Zeng, Mikhail B. Zvonarev, Nathan Goldman, Yanliang Guo, Manuele Landini, and Hanns-Christoph Nägerl (*These authors contributed equally to this work)
  Nature **642**, 53–57 (2025)

- *Observation of many-body dynamical localization*
  Yanliang Guo*, Sudipta Dhar*, Ang Yang*, Zekai Chen, Hepeng Yao, Milena Horvath, Lei Ying, Manuele Landini, Hanns-Christoph Nägerl (*These authors contributed equally to this work)
  Science **389**, 716-719 (2025)

- *Observation of the 2D-1D crossover in strongly interacting ultracold bosons*
  Yanliang Guo*, Hepeng Yao*, Satwik Ramanjanappa, Sudipta Dhar, Milena Horvath, Lorenzo Pizzino, Thierry Giamarchi, Manuele Landini, Hanns-Christoph Nägerl (*These authors contributed equally to this work)
  Nature Physics **20**, 934–938 (2024)

- *Anomalous cooling of bosons by dimensional reduction*
  Yanliang Guo*, Hepeng Yao*, Sudipta Dhar, Lorenzo Pizzino, Milena Horvath, Thierry Giamarchi, Manuele Landini, Hanns-Christoph Nägerl (*These authors contributed equally to this work)
  Science. Advances. **10**, 6-11 (2024)

CHAPTER 2

PUBLICATION I

Observing Bethe strings in an attractive Bose gas far from equilibrium

Milena Horvath[1,*], Alvise Bastianello[2,*], Sudipta Dhar[1,*], Rebekka Koch[4], Yanliang Guo[1], Jean-Sébastien Caux[4], Manuele Landini[1], and Hanns-Christoph Nägerl[1]

[1]*Institut für Experimentalphysik und Zentrum für Quantenphysik, Universität Innsbruck, Technikerstraße 25, Innsbruck, 6020, Austria*
[2] *Technical University of Munich, TUM School of Natural Sciences, Physics Department, 85748 Garching, Germany*
[3]*Munich Center for Quantum Science and Technology (MCQST), Schellingstr. 4, 80799 München, Germany*
[4]*Institute of Physics and Institute for Theoretical Physics, University of Amsterdam, PO Box 94485, 1090 GL Amsterdam, The Netherlands*
[*]These authors contributed equally to this work

Bethe strings are bound states of constituent particles in a variety of interacting many-body one-dimensional (1D) integrable quantum models relevant to magnetism, nanophysics, cold atoms and beyond. As emergent fundamental excitations, they are predicted to collectively reshape observable equilibrium and dynamical properties. Small individual Bethe strings have recently been observed in quantum magnets and superconducting qubits. However, creating states featuring intermixtures of many, including large, strings remains an outstanding experimental challenge. Here, using nearly integrable ultracold Bose gases, we realize such intermixtures of Bethe strings out of equilibrium, by dynamically tuning interactions from repulsive to attractive. We measure the average binding energy of the strings, revealing the presence of bound states of more than six particles. We find further evidence for them in the momentum distribution and in Tan's contact, connected to the correlated density. Our data quantitatively agree with predictions from generalized hydrodynamics (GHD).

Manipulating intermixtures of Bethe strings opens new avenues for understanding quantum coherence, nonlinear dynamics and thermalization in strongly-interacting 1D systems.

2.1 Introduction

Strong correlations present modern physics with both challenges and opportunities. In elementary cases, interactions merely renormalize bare excitations [207] or generate emergent collective hydrodynamic modes [10, 126]. A further (and far more exciting) possibility is for a non-perturbative overhaul of microscopic degrees of freedom to occur, invalidating any description of the many-body state from a non-interacting basis. The formation of bound states is a simple manifestation of this paradigm: Bardeen–Cooper–Schrieffer (BCS) pairs illustrate how bound states give rise to superconductivity [208], while quark confinement leads to the hadrons of high-energy physics [209]. Bosonic systems are potentially far richer than fermionic ones, since they accommodate large compounds of tightly-bound and thus strongly-correlated emergent particles. Realizing long-lived ensembles of attractive bosons, however, poses major practical challenges in analogy with the vacuum instability of attractive QED [210]. In bosonic systems, the absence of Pauli exclusion permits the formation of large complexes, which in turn collapse due to short-ranged molecular processes. Attractively interacting bosons have thus been observed only at weak interactions for a limited number of particles [211–213], or in one dimension for strong attractive interactions [17, 143, 214–216] where bound states are suppressed due to energetics. The realization of a system of strongly attractive bosons displaying hierarchies of large bound states has remained elusive due to these difficulties.

In 1D integrable quantum systems [168], attractive interactions do not necessarily induce collapse, but instead give rise to Bethe strings, multi-particle bound states predicted nearly a century ago [61]. They emerge as stable excitations in spin chains [168], cold atomic gases [217], and quantum magnets [137, 218]. Their stability stems from the characteristic absence of diffractive collisions in integrable systems [168], which prevents bound states from decaying into lower-lying states. Recent studies show that large Bethe strings determine anomalous transport properties of integrable spin chains and drive the emergence of the Kardar-Parisi-Zhang (KPZ) universality class [219–226]. Beyond traditional condensed matter systems, they are also relevant in high-energy physics and string theory [227]. A proper understanding of this wealth of manifestations requires the ability to create and manipulate dense intermixtures of Bethe strings of different sizes.

Bethe strings are expected to exist in the cold-atom Lieb-Liniger (LL) setting [59, 162]. Here, using ultracold attractively-interacting Cs atoms in 1D, we create a dense intermixture of strings by sweeping the interaction from repulsive to attractive, passing through the non-interacting point, as proposed in Ref. [139]. A fast and indiscriminate collapse of the gas is hindered by the approximate integrability [59, 162] of the system. Using a finite-rate sweep, we create a far-from-equilibrium state that exhibits multiple, including large, Bethe strings. Their typical size is set by the initial conditions, primarily the temperature and atomic cloud density. We detect their signature by comparing release measurements in 1D and 3D and by analyzing the momentum distribution and performing a measurement of Tan's contact [160]. Our data agrees well with the predictions [139, 228] from generalized

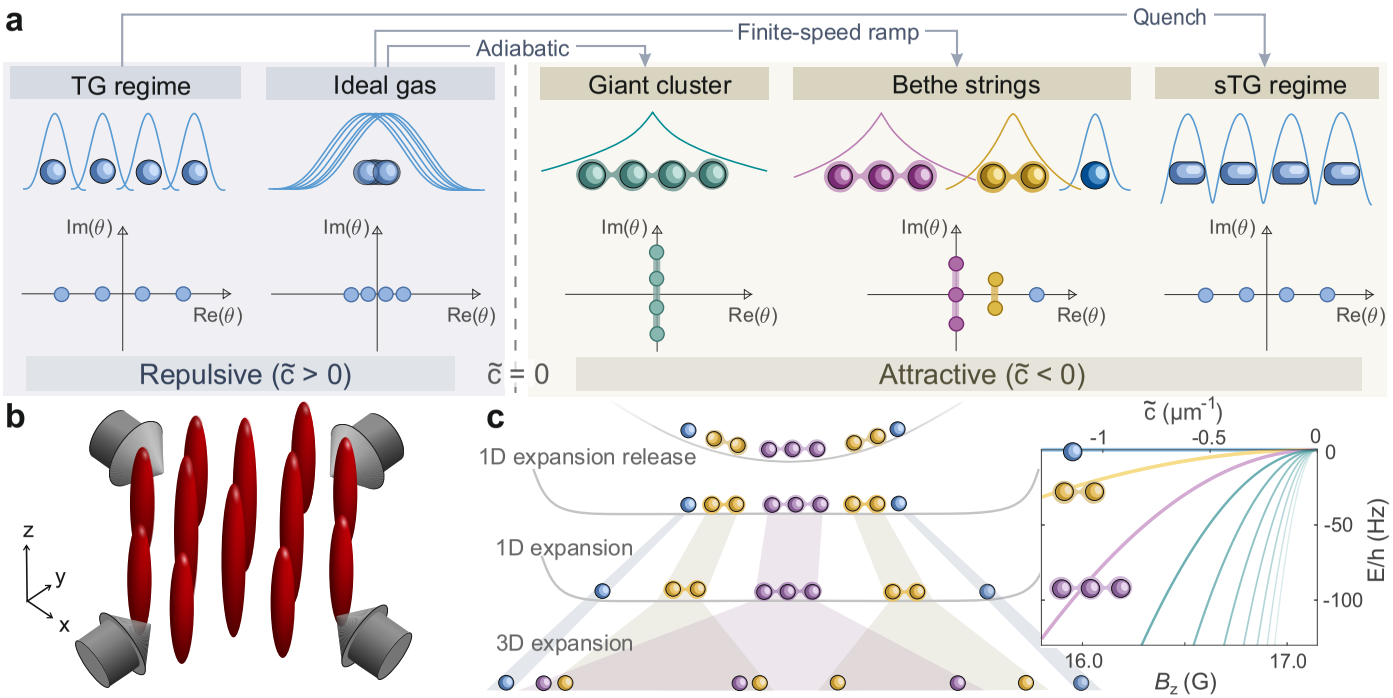

FIG. 2.1: **Bethe strings and their detection in 1D Bose gases.** **a**, Pictorial representation of the different interaction regimes of 1D Bose gases. Wavefunction correlation of the different states (top panel) and corresponding rapidity distribution θ (bottom panel). As the interaction parameter $\tilde{c}$ is increased from 0 (ideal gas) to $+\infty$ (TG regime) the gas fermionizes. The sTG regime can be accessed by quenching the interaction from the repulsive to the infinitely attractive regime. In contrast, adiabatically following the ground state of the system from positive to negative interactions $\tilde{c}$, and passing through $\tilde{c}=0$, results in a giant cluster. Sweeping $\tilde{c}$ from the strongly repulsive regime through the $\tilde{c}=0$ point with a finite rate realizes a non-equilibrium 1D gas composed of Bethe strings. Bound states with different number of particles are represented by different colours. **b**, Illustration of the experimental geometry. Horizontally propagating lattice beams (gray arrows) create an ensemble of independent 1D Bose gases (red tubes). **c**, Schematic of the 1D-3D expansion protocol used to probe Bethe strings. In the 1D the expansion, Bethe strings remain bound, breaking apart only upon the 3D release. Inset: Energy of different string states as a function of both $\tilde{c}$ and B_z, for bound states with up to ten particles.

hydrodynamics [54, 55].

Bethe strings arise as eigenstates of the celebrated LL Hamiltonian

$$\hat{H}_{\mathrm{LL}} = -\frac{\hbar^2}{2m}\sum_i \frac{\partial^2}{\partial z_i^2} + \frac{\hbar^2\tilde{c}}{2m}\sum_{i\neq j}\delta(z_i - z_j), \tag{2.1}$$

where the first term is the kinetic energy for the particles with mass m and the second term models the inter-particle interactions with strength $\tilde{c}$. The eigenstates, obtained by Bethe ansatz [59, 61], are labeled by a set of rapidities θ [168], which are generalized momenta of a set of emergent, stable quasiparticles. Figure. 2.1**a** shows a schematic representation of the different interaction regimes of the 1D Bose gas. For $\tilde{c} > 0$, the particles interact repulsively and the rapidities are real quantities. For sufficiently strong repulsive interactions, the bosons fermionize in the Tonks-Girardeau (TG) state [229, 230]. A quench to strong attractive interactions ($\tilde{c} < 0$) realizes an excited gaseous state, the super Tonks-Girardeau (sTG) state [17]. However, in the attractive regime, the rapidities are generally complex valued with non-zero imaginary parts. They are arranged in clusters that share the same real part $\lambda \equiv \mathrm{Re}(\theta)$, symmetrically placed along the imaginary axis with spacing $|\tilde{c}|$. These states are the Bethe strings [231]. An isolated Bethe string of size n has wavefunction $\psi(z_1 < ... < z_n) \propto \exp\left(i\sum_{j=1}^n \theta_j z_j\right)$, with rapidities $\theta_j = \lambda + i|\tilde{c}|(n + 1 - 2j)/2$. Its extent Δz_n can be estimated from the wavefunction decay as $\Delta z_n = 2[|\tilde{c}|(n-1)]^{-1}$, where the length scale is set by $|\tilde{c}|^{-1}$. The total energy E_n of the string is $E_{\mathrm{com;n}} - E_{\mathrm{b;n}}$, where $E_{\mathrm{com;n}} = n\hbar^2\ \lambda^2/(2m)$ is the center-of-mass energy and $E_{\mathrm{b;n}} = \hbar^2\tilde{c}^2 n(n^2-1)/(24m)$ is the binding energy [162]. The very ground state for N particles is a giant Bethe state with N constituents. Bethe strings with a lesser number of constituents have to be realized in a non-equilibrium situation [139, 232, 233], here realized with a finite-rate interaction ramp from the repulsive to the attractive phase, passing through the non-interacting point. The specifics of the initial state, the ramp rate, and the necessarily nonzero temperature will then determine the distribution of Bethe states in such a non-equilibrium situation.

2.2 Experimental protocol

Our experimental sequence starts with a 3D Bose-Einstein condensate (BEC) of Cs in a crossed-beam optical dipole trap, levitated against gravity by a magnetic force [234]. We control the atom number in the BEC within the range of 2×10^4 to 6×10^4, with an uncertainty of 10%, and the temperature between 10 nK to 35 nK, with a precision of 1 nK. A broad Feshbach resonance allows us to tune the 3D s-wave scattering length $a_{3\mathrm{D}}$ via an offset magnetic field B_z. Initially, B_z is set to 20.8(1) G, at which $a_{3\mathrm{D}} = 209(4)\ a_0$. The BEC is in the Thomas-Fermi regime. It is adiabatically loaded into two lattice beams that cross at 90° in the horizontal $x-y$ plane (see Fig. 2.1**b**). This results in approximately 4000 isolated 1D tubes with trapping frequencies of $\omega_\perp/2\pi = 10.5(1)$ kHz in the transversal and $\omega_z/2\pi = 29.3(1)$ Hz in the longitudinal direction for a lattice depth of 25 E_r, where, $E_\mathrm{r} = \pi^2\hbar^2/(2md^2)$ is the recoil energy and $d = 532.2$ nm is the lattice spacing set by the wavelength of the lattice light. This gives longitudinal and transversal harmonic oscillator lengths of $a_\mathrm{ho} = 1.6(2)\ \mu$m and $a_\perp = 83(4)$ nm, respectively. We tune the average number of atoms per tube N between 7 and 30 by varying the density of the initial BEC.

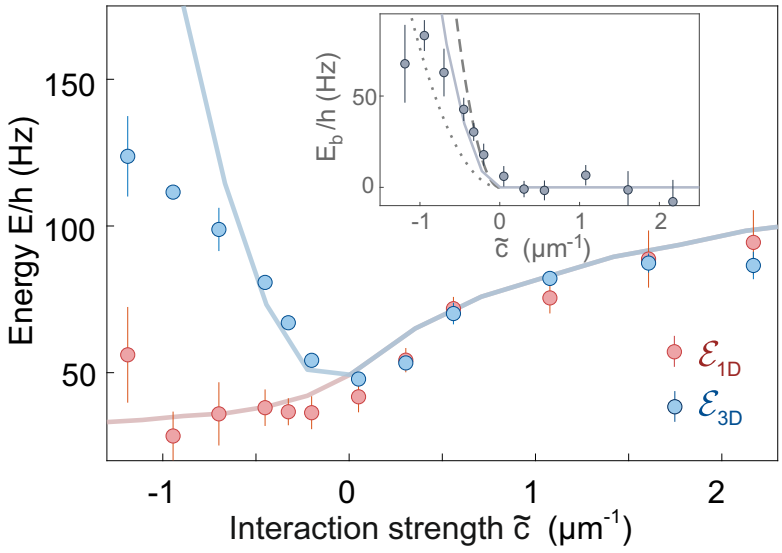

FIG. 2.2: **Evidence for Bethe strings from release measurements.** Release energy $\mathcal{E}_{1D}$ (red) and $\mathcal{E}_{3D}$ (blue) as a function of the interaction parameter $\tilde{c}$ at the end of the ramp. Each data point for the $\mathcal{E}_{1D}$ ($\mathcal{E}_{3D}$) energy is determined from a fit of the change of the second moment of the cloud as a function of t_{1D} (t_{3D}). The initial 1D temperature is estimated to be $T_{1D}=7$ nK (see Supplementary materials), and $N = 11$. Inset: The binding energy obtained via $E_b = \mathcal{E}_{3D} - \mathcal{E}_{1D}$. The dotted and dashed curves correspond to binding energy per particle of the Bethe strings of sizes $n = 6$ and 10 respectively. For both plots the standard error is given. The solid curves correspond to results from GHD.

In our 1D setting, the strength of the interaction is controlled via $\tilde{c} \simeq 4a_{3D}/a_\perp^2$ [132]. After lattice loading, we set the interaction strength to $\tilde{c}=3.4(1)$ μm^{-1}, putting our systems in the moderately interacting TG regime. The 1D temperature T_{1D} is set to values between 3 nK and 35 nK with an uncertainty of 20% (see Supplementary materials). We ramp the interaction parameter to lower and to negative values, crossing the non-interacting point, with a nearly constant rate of $\partial\tilde{c}/\partial t \approx -0.038$ μm^{-1}ms^{-1}. We expect that this procedure maps our system onto a distribution of Bethe strings as the interactions become attractive [139]. For our experiment, for an interaction strength of $\tilde{c}=-1$ μm^{-1}, a string of size $n=4$ has a bond length of about 0.67 μm. The binding energy of this string then is $h \times 190$ Hz $\approx k_B \times 9$ nK. Note that Bethe strings are only well defined when their bond length Δz_n is much larger than $a_\perp$. For short distances, loss through short-range molecular processes is expected. Such loss is not captured by the LL model.

We employ the rapidity measurement protocol [142, 143, 149, 184, 235], previously used in the absence of bound states, to probe our system. This protocol consists of a two-step expansion sequence: first, an expansion within the tubes for a time t_{1D}, followed by a free expansion into 3D space for time t_{3D} (see Fig. 2.1**c**). We ensure that t_{1D} is large enough so that the system enters a dilute regime, where the interparticle interactions become negligible (see Supplementary materials). In the repulsive regime, a subsequent absorption image yields the rapidity distribution of the gas. However, in the attractive regime the connection between the rapidity distribution and the absorption image becomes more intricate, as we explain below. Experimentally, the expansion in the tubes is achieved by simultaneously switch-

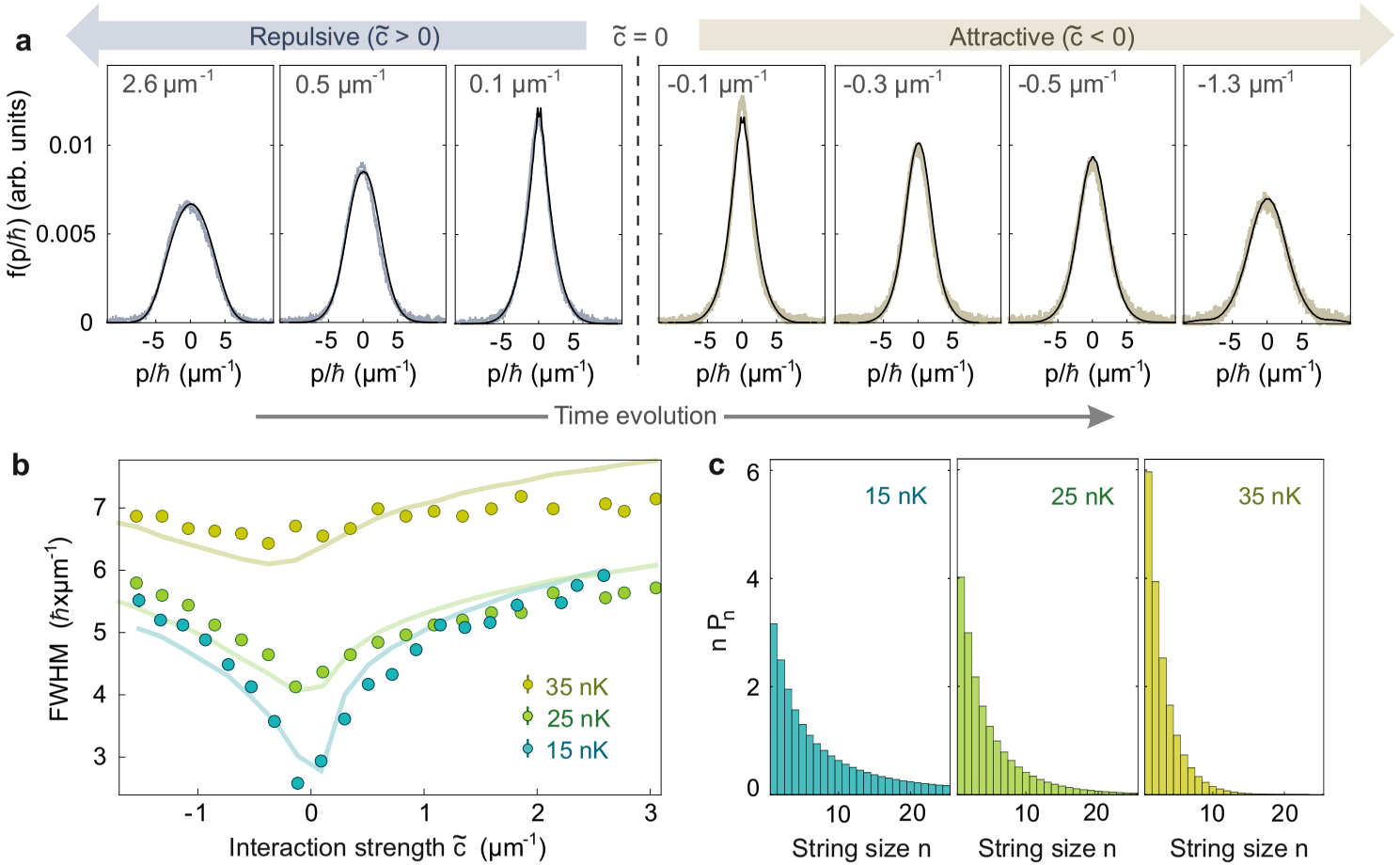

FIG. 2.3: **Evidence for Bethe strings from the momentum distribution via a comparison with the results of GHD a**, Momentum distribution after 1D expansion $f(p/\hbar)$ for various values of the interaction parameter $\tilde{c}$ at the end of the ramp as indicated, from the repulsive (left) to the attractive (right) regime. Each distribution is the mean of five repetitions and the shaded region corresponds to the standard error. The data is compared with the results from GHD (solid line), which assumes an initial 1D temperature of $T_{1D} = 15$ nK. **b**, FWHM of $f(p/\hbar)$ as a function of $\tilde{c}$ for three selected values of the T_{1D} as indicated. Each data point is the average of five repetitions. The standard error is given. **c**, Average number of atoms nP_n in each string of size n as predicted by theory for the temperatures as in Fig. 2.3**b**.

ing off the dipole traps and removing the residual longitudinal confinement created by the lattice beams by applying a 808-nm blue-detuned anti-trapping beam that flattens out the potential [119]. For the second expansion step, the expansion into 3D, we simply shut off the transverse confinement and simultaneously set $a_{3D} \simeq 0$ to avoid any interaction-induced broadening of the density distribution of the expanding cloud.

2.3 Release energy measurements

In the first experiment, we aim to find evidence of Bethe strings via measurements of the release energy. We extract the release energies $\mathcal{E}_{1D}$ and $\mathcal{E}_{3D}$ from the evolution of the second moment of the expanding cloud during 1D and 3D phases of our rapidity measurement protocol. $\mathcal{E}_{1D}$ is obtained by varying t_{1D} while keeping t_{3D} constant, and $\mathcal{E}_{3D}$ is obtained by varying t_{3D} while keeping t_{1D} constant (see Supplementary materials). Figure 2.2 shows $\mathcal{E}_{1D}$ and $\mathcal{E}_{3D}$ as a function of $\tilde{c}$. We find that for the repulsive case, $\mathcal{E}_{1D}$ and $\mathcal{E}_{3D}$ match within the error, and decrease from about $h \times 100$ Hz in the strongly repulsive side to approximately $h \times 60$ Hz close to the non-interacting point. In contrast, a clear difference can be detected for attractive interactions. While $\mathcal{E}_{1D}$ plateaus around $h \times 35$ Hz, $\mathcal{E}_{3D}$ increases to about $h \times 110$ Hz for $\tilde{c} = -1.0\ \mu\text{m}^{-1}$. This discrepancy between $\mathcal{E}_{1D}$ and $\mathcal{E}_{3D}$ for attractive interactions provides strong evidence for the presence of Bethe strings. During the 1D expansion, these bound states scatter, but remain intact, leading to a measured $\mathcal{E}_{1D}$ that remains low. However, upon release into 3D, the sudden removal of the confinement breaks the bound states, converting their binding into kinetic energy, which leads to a larger release energy, mainly in the z-direction. In the repulsive regime, on the other hand, the absence of bound states ensures that $\mathcal{E}_{1D}$ and $\mathcal{E}_{3D}$ are equal. In fact, in the repulsive regime, $\mathcal{E}_{1D} = \mathcal{E}_{3D} = U$, where $U = \langle \hat{H}_{LL} \rangle$ is the internal energy of the gas. In the attractive regime, $\mathcal{E}_{1D}$ is given by the average center-of-mass energy of the strings $\mathcal{E}_{1D} = \langle E_{com} \rangle$. In contrast, $\mathcal{E}_{3D}$ is the contribution from both the average center-of-mass energy of the strings and the binding energy $\mathcal{E}_{3D} = \langle E_{com} \rangle + \langle E_b \rangle$ (see Supplementary materials). The corresponding GHD simulations agree well with our measurements. In the inset of Fig. 2.2 we show the E_b as a function of $\tilde{c}$ obtained via $\mathcal{E}_{3D} - \mathcal{E}_{1D}$. In order to account for the observed value of $\langle E_b \rangle$, the system necessarily contains strings of size n^* or larger, where n^* is the largest integer such that $\langle E_b \rangle \geq E_{b,n^*}/n^*$. We estimate n^* to be six.

2.4 Temperature dependence

We find further evidence for Bethe strings by comparing the momentum distribution after 1D expansion $f(p/\hbar)$ with the predictions of GHD. For this we fix $t_{1D} = 10$ ms and $t_{3D} = 46.3$ ms. The momentum distribution is obtained from the longitudinal profile of the expanded cloud, converting position z to momentum as $p = mz/(t_{1D} + t_{3D})$. In Fig. 2.3**a** we show $f(p/\hbar)$ as the interaction strength $\tilde{c}$ is ramped from the repulsive to the attractive regime. At the beginning of the ramp $f(p/\hbar)$ is bell-shaped with a full width at half maximum (FWHM) $\hbar \times 6.0(1)\ \mu\text{m}^{-1}$ As $\tilde{c}$ decreases and approaches the non-interacting point, $f(p/\hbar)$ becomes more sharply peaked, with the FWHM narrowing to $\hbar \times 3.0(1)\ \mu\text{m}^{-1}$ at $\tilde{c} = 0.1\ \mu\text{m}^{-1}$.

After crossing the zero-interaction point, $f(p/\hbar)$ broadens, nearly doubling in size by the end of the ramp at $\tilde{c} = -2.0\ \mu\mathrm{m}^{-1}$. Next we compare our data with GHD. We estimate the best initial conditions for the simulations by optimizing the match with experimental data in the weakly repulsive regime, which is most sensitive to the initial parameters (see Supplementary materials). We find $T_{1\mathrm{D}} = 15$ nK. The GHD simulations accounts for finite time-of-flight (TOF) effects by simulating the entire 1D and 3D expansions performed in the experiment (see Supplementary materials). We find good agreement between the experimental data and the results from GHD. In the repulsive regime, $f(p/\hbar)$ corresponds to the rapidity distribution of the gas (see Supplementary materials). Therefore, the narrowing of the distributions for decreasing $\tilde{c} > 0$ is attributed to a reduction in the effective velocity of the quasiparticles. In contrast, for the attractive case $\tilde{c} < 0$, the quasiparticles bind together to form Bethe strings that broaden the distributions. An intuitive understanding based on Heisenberg's uncertainty principle suggests that a string with bond length Δz_n will release momentum within a window $\Delta p_n \sim \hbar/(2\Delta z_n)$. This broadening effect becomes more prominent for larger Bethe strings and for stronger attractive interactions.

We now examine how the temperature affects the formation of the bound states. In Fig. 2.3**b**, we show the FWHM of $f(p/\hbar)$ as a function of $\tilde{c}$ for three different values of $T_{1\mathrm{D}}$. Note that for the 15 nK dataset, we use a lattice depth of 20 $\mathrm{E_r}$ instead of 25 $\mathrm{E_r}$. As is already evident from Fig. 2.3**a** the distribution broadens away from $\tilde{c} = 0$. This effect diminishes for higher $T_{1\mathrm{D}}$. Results from GHD are in good agreement with our experimental data. Figure 2.3**c** shows the GHD prediction for the number of atoms nP_n participating in the n^{th} bound state. Here P_n is the average number of strings of size n. The probability of forming larger strings decreases with increasing $T_{1\mathrm{D}}$. For increasing temperature, the kinetic energy of the system dominates over the interaction energy. This reduces the probability of forming larger bound states, and in turn reduces the average binding energy per particle. This is reflected in Fig. 2.3**b**, where the FWHM of $f(p/\hbar)$ becomes less sensitive to the change of interaction at higher $T_{1\mathrm{D}}$.

The presence of Bethe strings significantly modifies the short-range correlations of the gas, notably the local pair correlations integrated over the trap G_2 [134, 236], which quantify the probability of finding two particles in the same place. This is directly proportional to Tan's contact $C = \tilde{c}^2 G_2$ [158, 160]. Tan's contact establishes a fundamental link between microscopic quantities and the thermodynamic properties of the system. At thermal equilibrium, the virial theorem [159] relates C to the internal energy U and the potential energy E_{V} of the harmonic trap as

$$C = \frac{2m\tilde{c}}{\hbar^2}(U - E_{\mathrm{V}})\,. \tag{2.2}$$

We find that Eq. (2.2) also generalizes to out-of-equilibrium scenarios described by stationary solutions for GHD (see Supplementary materials).

Experimentally, we obtain U from the 3D release-energy measurements described previously. While for repulsive interactions we can directly extract U from $\mathcal{E}_{3\mathrm{D}}$, for attractive regime this is not the case. As shown in Fig. 2.2, E_{com} plateaus within experimental uncertainty for attractive interactions. We therefore approximate E_{com} $(\tilde{c} < 0) \simeq \mathcal{E}_{3\mathrm{D}}$ $(\tilde{c} = 0)$. The binding energy $\langle E_{\mathrm{b}} \rangle$ is given by $\mathcal{E}_{3\mathrm{D}} - \mathcal{E}_{3\mathrm{D}}$ $(\tilde{c} = 0)$. We use this approximation to extract U for the attractive regime. The potential

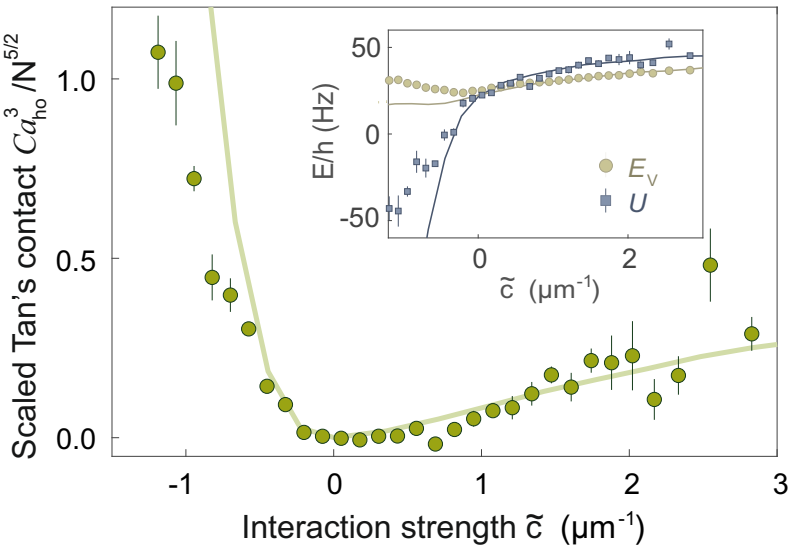

FIG. 2.4: **Interaction dependence of Tan's contact.** The scaled contact (circles) is extracted from experimental measurements of U and E_V via Eq. (2.2). Inset: The potential energy E_V (circles) and internal energy U (squares) as a function of $\tilde{c}$. The solid curves in both plots are results obtained from GHD. For these measurements $T_{1D} = 3$ nK and $N = 5$. The standard error is given.

energy is measured by imaging the spatial distribution of the atom cloud. We use a short TOF of 1.5 ms without 1D expansion in order to lower the optical density before imaging. The potential energy per particle is given by $E_V = (1/2)m\omega_z^2\langle z^2\rangle$, where $\langle z^2\rangle$ is the mean squared width of the cloud in the longitudinal direction. In Fig. 2.4 we plot the interaction dependence of the contact, determined from the measured U and E_V using Eq. (2.2) (see inset of Fig. 2.4). On the repulsive side, Tan's contact decreases as $\tilde{c}$ is reduced. Upon entering the attractive regime, Tan's contact increases dramatically. It is nearly six times higher on the attractive side at the same magnitude of the interaction $|\tilde{c}| = 1\ \mu\text{m}^{-1}$. The GHD predictions qualitatively describe experimental observations with very good agreement on the repulsive side. For $\tilde{c} < 0$, we attribute the discrepancy to finite-size effects, as theory predicts a substantial contribution from Bethe strings larger than the average number of particles in the tubes. Additional discrepancies stem from atom loss in the experiment, with approximately 20% of the atoms being lost during the ramp for the strongest attractive interaction (see Supplementary materials). Our data can be used to benchmark other theoretical methods for calculating Tan's contact in 1D [237–239].

2.5 Conclusion

In summary, we have used 1D attractive Bose gases to realize novel non-equilibrium states of quantum matter featuring dense intermixtures of Bethe strings. In our experiment, approximate integrability stabilizes these bound states, and bypasses the rapid collapse normally associated to attractive bosons [211–213]. We have experimentally characterized these bound states through measurements of the binding energy, Tan's contact, and the momentum distribution following 1D expan-

sion. Our results agree with predictions from GHD, showcasing the latter's validity beyond the previously-considered repulsive [183, 184, 235, 240–242] and sTG regimes [143]. Our results show that the presence of Bethe strings (somewhat similar to Efimov physics [243]) in correlated gases greatly enriches the landscape of achievable non-equilibrium states in the vicinity of integrability. Since Bethe strings display remarkable resilience to integrability breaking [138], they can alter transport properties [244], give rise to new interesting pre-thermal phases [245] and affect the emergent hydrodynamics and thermalization of nearly-integrable systems [241, 246–248]. Going further, it would be interesting to study their participation in the emergence of KPZ universality [249] or their fate under dimensional crossover [250].
Data availability. Experimental and simulation data are available on Zenodo [251].

Acknowledgments
The Innsbruck team acknowledges funding by a Wittgenstein prize grant under the Austrian Science Fund's (FWF) project number Z336-N36, by the European Research Council (ERC) under project number 789017, by an FFG infrastructure grant with project number FO999896041, and by the FWF's COE 1 and quantA. Y.G. is supported by the FWF with project number 10.55776/COE1. MH thanks the doctoral school ALM for hospitality, with funding from the FWF under the project number W1259-N27. AB acknowledges support from the Deutsche Forschungsgemeinschaft (DFG, German Research Foundation) under Germany's Excellence Strategy–EXC–2111–390814868. JSC and RK acknowledge support from the European Research Council under ERC Advanced grant 743032 DYNAMINT.

2.6 Supplementary notes

2.6.1 Estimating the populations of atoms in the tubes and fitting the initial conditions

Since the formation of Bethe strings in our protocol is a non-linear function of the density, having a good quantitative estimation of the distribution of atoms across the tubes is of key importance. Before the creation of the one-dimensional tubes, we assume the gas is at thermal equilibrium and it remains so until the dimensional cross-over: when the transverse trapping is strong enough, the tubes cannot exchange particles any longer and are effectively decoupled. Just before the tubes decouple, we approximate the gas as a collection of one-dimensional systems at thermal equilibrium, characterized by a unique temperature and a local chemical potential according to the shallow three dimensional trap [252]. We also approximate the one-dimensional interactions $\tilde{c}$ to be the same as the one at the end of the cross-over in one dimension. Below, we summarize in a table the relevant parameter for the tubes' loading.

Under these assumptions, we can tabulate the distribution of atoms using thermodynamic Bethe ansatz (see Supplementary Note 2.6.7), keeping $T_{\text{cross-over}}$ as a tunable parameter. Notice that during the dimensional crossover, the trapping frequency along the $z-$ direction smoothly changes from the loading frequency w_1 to the final 1D value: the thermodynamics of the 1D tubes at the dimensional crossover

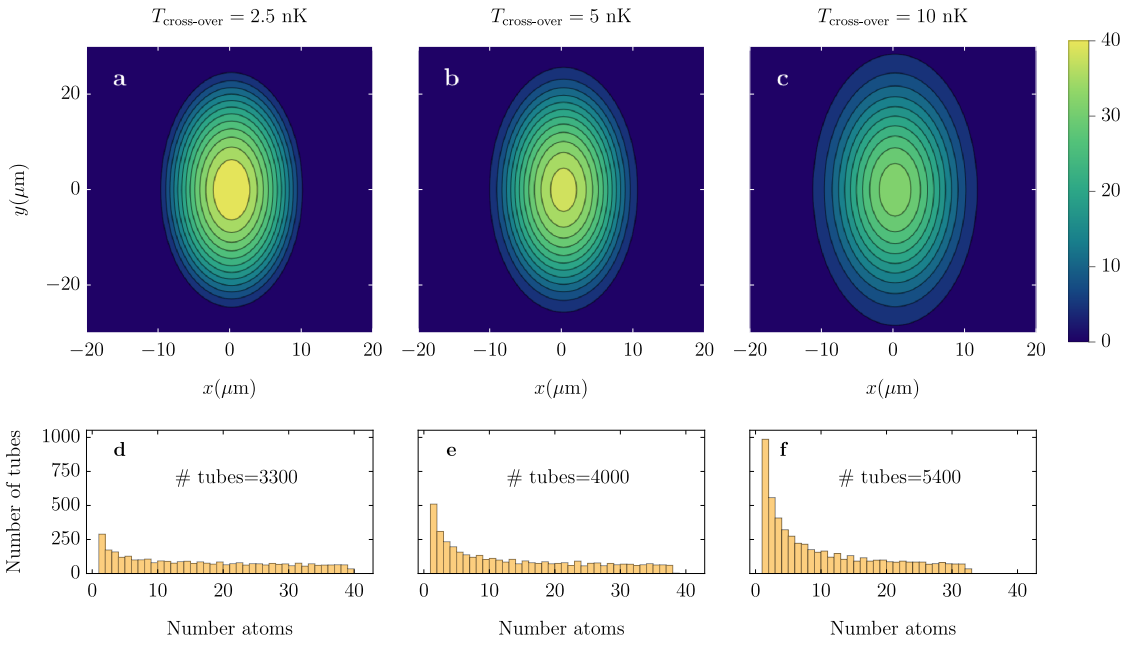

SUPPLEMENTARY FIG. 2.5: **Example of tubes' population varying $T_{\text{cross-over}}$.** As a concrete example, we show how tuning the dimensional crossover, the temperature changes the population of the tubes. In this example, we focus on the dataset of Fig. 2.3 corresponding to $T_{\text{1D}} = 15$ nK. From left to right, the three columns corresponds to the choices $T_{\text{cross-over}} = (2.5, 5, 10)$ nK: the choice that best fits the initial data is $T_{\text{cross-over}} = 5$ nK. In the first row (**a** to **c**), we show the spatial distribution of the tube population in the (x, y) plane, whereas the longitudinal tubes are oriented in the z direction. By increasing $T_{\text{cross-over}}$, more tubes are populated, but the average number of atoms in each of them decreases: this affects the creation of bound states when crossing to the attractive regime, as tubes with larger atom density populate larger bound states. In the second row (**d** to **f**), we show an histogram of the atom number population: tubes with less than one atom are not accounted for, and "# tubes" is the total the number of populated tubes in each case.

is computed using the loading frequency as the frequency of the 1D trap. An example of how different choices of $T_{\text{cross-over}}$ affect the tubes' population is provided in Fig. 2.5, a working code solving the thermodynamics of the one-dimensional tubes is provided on Zenodo [251]. From the dimensional cross-over to the true 1D regime, the transverse trap is further increased, but the number of atoms in each tube remains constant. As the system enters deeper in the 1D regime, it approaches the integrable limit hindering thermalization. We assume that at the end of the lattice loading protocol, each tube is still well-approximated by a thermal ensemble with a new temperature T_{1D}, assumed to be uniform across all the tubes. The validity of this assumption is a posteriori supported by the good agreement with experimental data. The parameters T_{1D} and $T_{\text{cross-over}}$ are estimated by matching as the experimental data in the weakly repulsive regime (see Supplementary Note 2.6.7). In Tab 2.6.1, we summarize the experimental parameters and the corresponding results from the simulations for each of the datasets presented in the main text.

	Experiment				Simulation			
	N_{BEC} ($\times 10^4$)	$(w_1, w_2, w_3)/2\pi$ (Hz)	$\omega_z/2\pi$ (Hz)	$\omega_\perp/2\pi$ (kHz)	$T_{\text{cross-over}}$ (nK)	T_{1D} (nK)	N	N_{cent}
Fig. 2	3.2	(25.1, 10.1, 27.1)	29.3	10.5	10	7	11	21
Fig. 3	5.7	(25.1, 10.1, 27.0)	28.8	9.0	5	15	25	41
	5.7	(25.1, 10.1, 27.0)	27.6	10.5	10	20	19	34
	5.7	(25.1, 10.1, 27.0)	27.1	10.5	10	35	19	34
Fig. 4	1.9	(10.3, 5.7, 11.7)	18.1	11.5	3	3	5	9

Tab. 2.1: **Experimental and theoretical parameters for each dataset presented in the main text**. For the experimental parameters, we give the the initial atom number in the BEC N_{BEC}, the lattice loading frequencies $(\omega_1, \omega_2, \omega_3)/2\pi$ in the z, x, y directions, respectively. After lattice loading, the longitudinal $\omega_z/2\pi$ and transversal $\omega_\perp/2\pi$ trapping frequencies in the tubes are also indicated. From the simulation, we estimate the cross-over temperature $T_{\text{cross-over}}$, the 1D temperature T_{1D}, and the average atom number per tube N and the central tube atom number N_{cent}.

2.6.2 Summary of generalized hydrodynamics

Here we provide a compact summary of GHD, overviewing the main equations and how theory describes the momentum measurement after 1D expansion. A more detailed discussion for the interested reader can be found in Supplementary Note 2.6.7. GHD [54, 55] is a non-perturbative kinetic theory for integrable systems, governed at the Euler scale by the main equation

$$\partial_t \rho_n(\lambda) + \partial_z[v_n^{\rm eff}(\lambda)\rho_n(\lambda)] + \partial_\lambda[F_n^{\rm eff}(\lambda)\rho_n(\lambda)] = 0\,. \tag{2.3}$$

The root density $\rho_n(\lambda) \to \rho_{n;t,z}(\lambda)$ is the phase-space density of Bethe strings of species n in the position-rapidity plane. For $\tilde{c} > 0$, $\rho_{n=1}$ is the only non-zero root density, since no bound states are present. The effective velocity $v_n^{\rm eff}$ [54, 55] is renormalized by interactions accounting for non-trivial scattering, while the weak integrability-breaking induced by the trap $\partial_z V \neq 0$ [253] and the effect of slow interaction changes $\tilde{c} \to \tilde{c}(t)$ [228] are captured by the effective forces $F_n^{\rm eff}$. Ref. [139] connects the GHD equations across $\tilde{c} = 0$ and determines the population of Bethe strings. Within GHD, the internal and potential energies of the gas are $U = \sum_n \int \mathrm{dzd}\lambda\, \mathrm{E_n}(\lambda)\rho_{\rm n}(\lambda)$ and $E_V = \sum_n \int \mathrm{dzd}\lambda\, \mathrm{V(z)n}\rho_{\rm n}(\lambda)$ respectively.

The combined 1D and 3D expansion of our protocol can be also described within GHD. After reaching the dilute regime upon expanding in 1D with $F_n^{\rm eff} = 0$, Bethe strings travel with their bare velocity $\hbar\lambda/m$. Then, the transverse trap is removed and interactions quenched to zero. Particles released from a Bethe string acquire new momenta p due to the converted binding energy, resuming the expansion and leading to a longitudinal density profile $d(z)$

$$d(z) = \sum_n \int \mathrm{d}\lambda\mathrm{dp}\, \delta\left(\mathrm{z} - \tfrac{\mathrm{t_{1D}}\hbar\lambda + \mathrm{t_{3D}p}}{\mathrm{m}}\right) \mathrm{C_n}\left(\tfrac{\mathrm{p}\hbar^{-1} - \lambda}{|\tilde{\mathrm{c}}|}\right) \tfrac{\mathrm{n}\bar{\rho}_{\rm n}(\lambda)}{|\tilde{\mathrm{c}}|}, \tag{2.4}$$

where $\bar{\rho}_n(\lambda)$ is the rapidity distribution integrated over the whole cloud. C_n are universal bell-shaped function describing the momentum distribution obtained from an isolated Bethe string quenched to zero interaction, see Supplementary Note 2.6.7 for details. For simplicity, in Eq. (2.4) we neglect the initial width of the cloud, and the short transient where the Bethe strings' velocity is renormalized by interactions: these effects are included simulating the 1D expansion with the GHD Eq. (2.3). In the repulsive phase, $d(z)$ maps to the rapidity distribution since $C_1(x) = \delta(x)$. This identification is lost in the attractive phase in the presence of Bethe strings. One can explicitly compute $\int \mathrm{dz\, x^2 C_n(x)} = \mathrm{n(n^2-1)/12}$ (see Supplementary Note 2.4), leading to a simple expression for the variance of the expanded density profile $\langle z^2\rangle \equiv \int \mathrm{dz\, z^2 d(z)} \Big/ \int \mathrm{dz\, d(z)}$

$$\langle z^2\rangle = \frac{2(t_{\rm 1D} + t_{\rm 3D})^2}{m}\langle E_{\rm com}\rangle + \frac{2t_{\rm 3D}^2}{m}\langle E_{\rm b}\rangle\,, \tag{2.5}$$

which we use to extract the average center of mass and binding energies upon varying the 1D and 3D expansions. The average of $E_{\rm com}$ and $E_{\rm b}$ is taken over the root densities, normalized to the particles number.

The pair correlation integrated over the trap is formally defined as $G_2 \equiv \left\langle \sum_{i\neq j} \delta(z_i - z_j)\right\rangle$. In Supplementary Note 2.6.7, we give an explicit formula for G_2 in terms of the root densities (2.13), and provide a more detailed overview of GHD and a discussion of finite expansion's time effects.

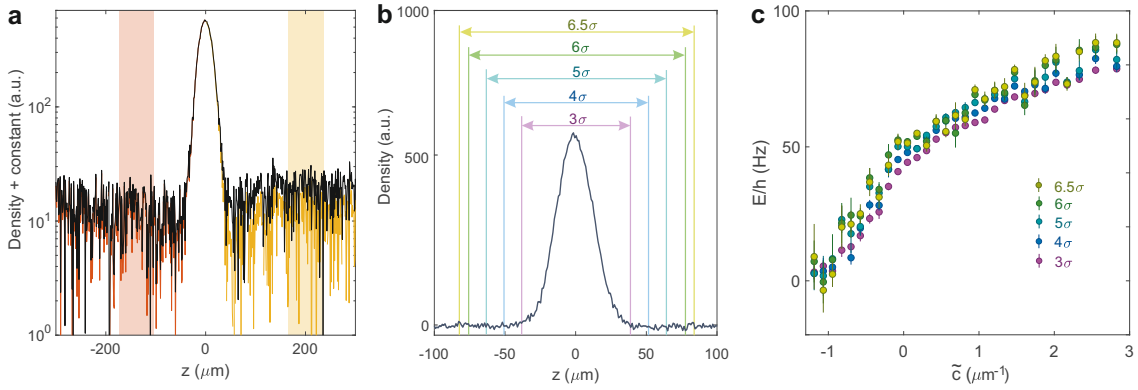

FIG. 2.6: **Convergence of energy extracted from the second moment of the distribution.** **a**, Typical TOF profile of the cloud in log-linear scale. z denotes the spatial position after TOF. For this plot, a small constant is added to TOF distribution in order to avoid negative values in logarithm. Different offsets are used on either side of the distribution in order to ensure that the second momentum converges for increasing regions of interest. Original data is shown in black and the colored curves correspond to the data after offset (mean over shaded region) has been applied. **b**, Typical TOF distribution indicating different region of interests used to obtain the internal energy U shown in **c**. **c**, Internal energy determined using the different region of interest shown in **b**.

2.6.3 Determining the release energies of the system via the second moment

We determine the release energies $\mathcal{E}_{1D}$ and $\mathcal{E}_{3D}$ by measuring the expansion rate of the second moment of the sample $\langle z^2 \rangle$ during the 1D and 3D expansion stages, respectively. For the measurement shown in Fig. 2.2, we scan t_{1D} (t_{3D}) from 6 to 11 ms (18 to 43 ms), while keeping $t_{3D} = 20.4$ ms ($t_{1D} = 8$ ms) fixed. For each experimental absorption image, we apply a background noise removal technique [254] to improve the accuracy in the determination of the second moment. In Fig. 2.6**a** we show a typical TOF density profile after noise removal. We find that far away from the signal, the distribution has a non-zero offset. Furthermore, this offset is different on either side of the distribution, which we attribute to the inhomogeneous profile of the imaging beam. Although the difference between the two offset values is less than 1%, it is crucial for determining the second moment $\langle z^2 \rangle$ of the distribution. In order to faithfully calculate the energy from $\langle z^2 \rangle$, we use different regions of interest (see Fig. 2.6**b**) and check for convergence in the estimated energy. As shown in Fig. 2.6**c**, we see a convergence in energy above 3σ region of interest, where σ is the gaussian width of the distribution. The energy is determined by fitting the evolution of $\langle z^2 \rangle$ as a function of expansion time. For the 1D release energy, we fit a parabolic function $a(t_{1D} + t_{fix})^2 + b$ to our 1D-expansion data, where a and b are fitting parameters, and t_{fix} is the fixed 3D expansion time. The fitting parameter a is related to $\mathcal{E}_{1D}$ via $\mathcal{E}_{1D} = 2a/m$ as given in Eq. 2.5. Similarly, for the 3D release energy, we use a parabolic fitting function $a(t_{3D} + t_{fix})^2 + b$ to our 3D-expansion data. Here, t_{fix} is the fixed 1D expansion time. We extract $\mathcal{E}_{3D}$ from the fit via $\mathcal{E}_{3D} = 2a/m$.

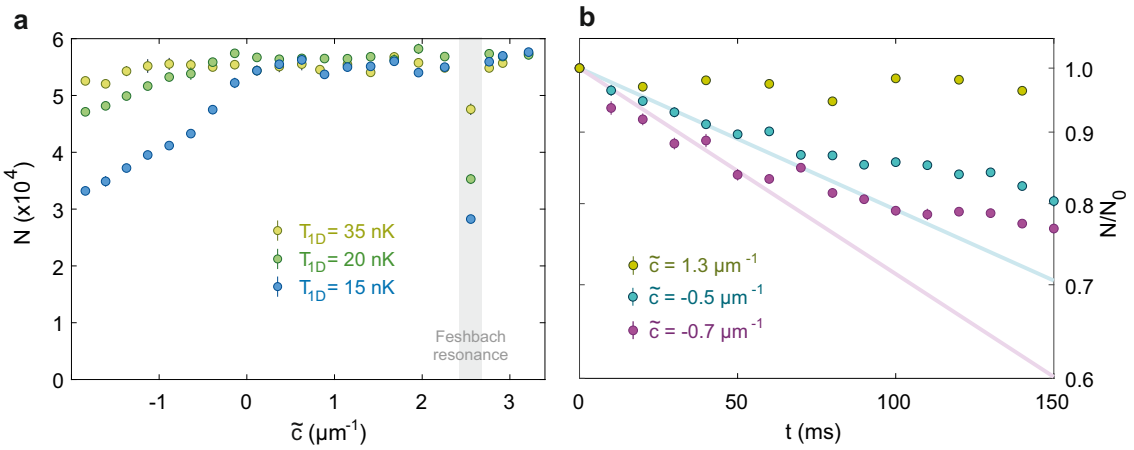

Figure 2.7: **Atom loss for different temperatures and interaction strengths.** **a**, Number of atoms after the interactions ramp as a function of $\tilde{c}$ for different temperatures. Blue, green, and yellow correspond to 1D temperatures T_{1D} of 15 nK, 20 nK, 35 nK, respectively. A Feshbach resonance is indicated by a gray shaded region. **b**, Evolution of normalized atom number for different values of $\tilde{c}$ at a temperature of 15 nK. Each data point in is an average of five repetitions and the displayed error is equal to the standard error. The solid curves are exponential fits up to 50 ms.

2.6.4 Atom loss and lifetime measurements

In our experiment, short-range molecular processes lead to atom loss. In Fig. 2.7**a** we show the atom losses during the interaction ramp corresponding to the measurements given in Fig. 2.3**b**. In the repulsive regime $\tilde{c} > 0$, the atom number remains stable, however we see losses for interactions below $\tilde{c} = 0$. We attribute this atom loss primarily to the formation of bound states, which enhance inelastic scattering processes not taken into account by the 1D Hamiltonian (2.1). Since we use Cs atoms in the lowest hyperfine ground state $|F, m_F\rangle = |3, 3\rangle$, two-body inelastic processes are suppressed. Therefore, these losses in our experiment primarily originate from the three-body inelastic scattering. The stability of the gas, depends both on the interaction strength and on the initial conditions of the protocol. The stronger the attraction, the tighter the bound states, with more frequent inelastic scattering. For a fixed $\tilde{c}$, the atom loss decreases at higher temperatures, as the probability of forming larger strings decreases at higher temperatures. While for T_{1D}=20 and 35 nK, the losses are less than 20%, for the coldest T_{1D}=15 nK, we observe losses around 40% for the strongest attractive interaction. Even with such high losses, the agreement between experimental data for the momentum distribution after 1D expansion (normalized with atom number) and GHD results as shown in Fig. 2.7**a** remains very good. Next, we measure the lifetime of the gas for different interaction strengths. In Fig. 2.7**b**, we show the normalized atom number as a function of hold time t after the completion of the $\tilde{c}$ ramp for three different $\tilde{c}$ target values: $\tilde{c} = 1.3, -0.5, -0.7\ \mu\text{m}^{-1}$. For these measurements, we set $t_{1D} = 0$ ms and $t_{3D} = 36$ ms. In the repulsive regime, we do not observe any significant atom loss, however, in the attractive regime, we observe around 20% atom loss over $t = 150$ ms. Here, the density of the gas increases, resulting in higher three-body losses. Here we refrain from fitting the decay measurements with a three-body loss function and instead use a simple exponential function up to 50 ms to estimate the lifetime. For $\tilde{c} = -0.5$

$\mu\mathrm{m}^{-1}$, and $-0.7\ \mu\mathrm{m}^{-1}$, we obtain lifetime of 75.6(252) ms, and 57.4(178) ms respectively. These lifetimes are longer than the typical 1D expansion times $t_{1\mathrm{D}}$ of 10 ms used in our experiment.

2.6.5 Simulating the Tonks-Girardeau regime

At strong repulsive interaction, the 1D Bose gas is well described by a gas of hard-core bosons, also known as Tonks-Girardeau (TG) regime and it is amenable of a straightforward theoretical treatment that we briefly recap [255]. Through a Jordan-Wigner transformation, hard-core bosons can be mapped into a system of free fermions. Hence, their hydrodynamics is that of free particles, satisfying the equation $\partial_t \rho_{t,z}(\lambda) + v(\lambda)\partial_z \rho_{t,z}(\lambda) - \partial_z V(z)\partial_k \rho_{t,z}(\lambda) = 0$, with $v(\lambda) = \partial_\lambda E(\lambda)$ and $E(\lambda) = \frac{\hbar^2\lambda^2}{2m}$ and $\rho_{t,z}(\lambda)$ being the local rapidity distribution. The initial condition to the hydrodynamic equations is given by thermal states, which we compute within the local density approximation $\rho_{t=0,z}(\lambda) = \frac{1}{2\pi}\left(1 + e^{\beta[E(\lambda)-\mu+V(z)]}\right)^{-1}$, with the inverse temperature β and the chemical potential μ being fitting parameters.

We compute the momentum distribution within a local density approximation (LDA). We fix the position z, and consider a homogeneous state described by the rapidity distribution $\rho_{t,z}(\lambda)$. On homogeneous states, one defines the fermionic correlator $F_z(\Delta z) = \int \mathrm{d}\lambda\, \mathrm{e}^{\mathrm{i}\lambda\Delta\mathrm{z}}\rho_{\mathrm{t,z}}(\lambda)$, from which the bosonic correlation $g_{1,z}(\Delta z) \equiv \langle\hat{\psi}^\dagger(z+\Delta z/2)\hat{\psi}(z-\Delta z/2)\rangle$ can be computed, where we conveniently introduced the creation-annihilation bosonic fields $\hat{\psi}^\dagger(z)$ and $\hat{\psi}(z)$ obeying canonical commutation relations $[\hat{\psi}(z), \hat{\psi}^\dagger(z')] = \delta(z-z')$. $g_{1,z}(\Delta z)$ is found within LDA by solving certain Fredholm integral equations [256] (see also Ref. [257] for our notation)

$$g_{1,z}(\Delta z) = \det[1 - 2\mathcal{F}_{(\Delta z,0)}]\left[\mathcal{F}_{(\Delta z,0)} * (1 - 2\mathcal{F}_{(\Delta z,0)})^{-1}\right](\Delta z, 0)\,, \tag{2.6}$$

where $\mathcal{F}_{(\Delta z,0)}$ is an operator acting on functions with support in $(\Delta z, 0)$ and with entries $\mathcal{F}_{(\Delta z,0)}(a,b) \equiv F_z(a-b)$. Its action on a test function f is defines as $[\mathcal{F}_{b\in(\Delta z,0)}](a) \equiv \int_{(\Delta z,0)} \mathrm{db}\, \mathcal{F}_{(\Delta\mathrm{z},0)}(\mathrm{a},\mathrm{b})\mathrm{f}(\mathrm{b})$. For brevity, we define the operator product on this space as $[A * B](a,b) \equiv \int_{y\in(\Delta z,0)} \mathrm{dy}\, \mathrm{A}(\mathrm{a},\mathrm{y})\mathrm{B}(\mathrm{y},\mathrm{b})$. In Eq. (2.6), after having computed the operator $\left[\mathcal{F}_{(\Delta z,0)} * (1 - 2\mathcal{F}_{(\Delta z,0)})^{-1}\right]$, one has to focus on its entries at the edge of the definition domain $\left[\mathcal{F}_{(\Delta z,0)} * (1 - 2\mathcal{F}_{(\Delta z,0)})^{-1}\right](\Delta z, 0)$

In practice, determinants and matrix inversions are computed by discretizing the operator on a finite grid (about 120 points in our simulations). Finally, the momentum distribution is obtained by Fourier transform. More specifically, we define the LDA position-dependent momentum distribution as

$$P_z(p) = \int \frac{\mathrm{d}\Delta\mathrm{z}}{2\pi}\, e^{-ip\Delta z} g_{1,z}(\Delta z)\,. \tag{2.7}$$

$P_z(p)$ describes the probability distribution in the momentum-space (p,z) phase space in the longitudinal direction obtained right after the release of the three dimensional optical lattice: the final comparison with experimental data is obtained by further propagating the particles for a finite three dimensional TOF, assuming that $P_z(p)$ describes the number of particles starting at z and with velocity $v(p) = \frac{\hbar p}{m}$.

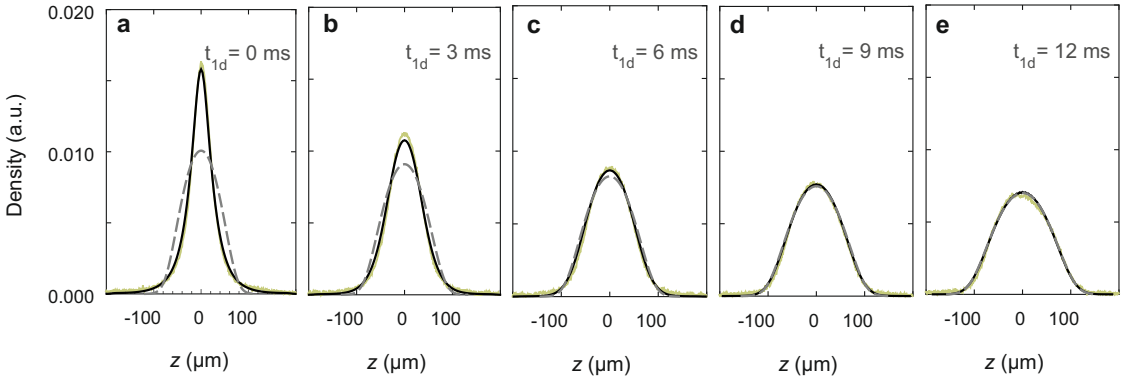

Figure 2.8: **1D expansion in TG regime. a** to **e**, TOF distributions of a TG gas following an expansion in 1D, with $t_{1D} = 0$ to 12 ms. z denotes the spatial position after TOF. The experimental data and simulation results are plotted in green, and black respectively. The black curve is the density profile obtained expanding the true momentum distribution, whereas the grey dashed curve is obtained approximating the momentum distribution with the rapidity distribution. Each experimental data is the average of five repetitions.

2.6.6 Characterizing the rapidity distribution in the Tonks-Girardeau regime

Theory predicts the longitudinal density profile of the expanded cloud after the system has entered a sufficiently dilute regime. Therefore, benchmarking the validity of this approximation is of key importance. In the repulsive regime, the momentum distribution of a dilute gas is approximated by the rapidity distribution, but at finite density, interactions spoil this identification. Computing the momentum distribution at finite density and for arbitrary interaction strength is theoretically challenging, but it is accessible in the TG regime (see Supplementary Note 2.6.5). We use this to benchmark our experimental results. We characterize our rapidity measurement protocol by first matching the experiment with the simulation in the TG regime for different 1D expansion times t_{1D}. In our experiment, after lattice loading, we ramp a_{3D} from 210 a_0 to approximately 750 a_0 in 150 ms. We then apply a 808-nm anti-trapping beam that flattens out the longitudinal harmonic trap. We estimate that the longitudinal confinement of the tubes is flattened for a region of approximately 80 μm around the center of the trap without affecting the transverse trapping. We allow the gas to expand in 1D for variable time t_{1D}, before taking a standard TOF absorption image. In Fig. 2.8, we show the TOF distribution of the gas after expansion in 1D for $t_{1D} = 0$ to 12 ms. Throughout the 1D expansion, we see good agreement with the simulation results. For $t_{1D} = 0$ ms, the momentum and rapidity distributions are strikingly different. As t_{1D} increases, the distributions broaden and approach the rapidity distribution. After $t_{1D} = 6$ ms, the TOF distributions coincide with the rapidity distribution of the gas.

2.6.7 Generalized hydrodynamics and simulations at finite interactions

To give quantitative theoretical predictions for the finite interactions, we employ thermodynamic Bethe ansatz (TBA) [168] to determine the initial state, and Generalized Hydrodynamics (GHD) to follow the time evolution. Throughout this section, we use for simplicity adimensional units rescaling coordinates z_i by a unit length $\ell = 1$ μm, in such a way the Bose gas Hamiltonian reads

$$\hat{H} = -\sum_i \frac{\partial^2}{\partial z_i^2} + c\sum_{i\neq j}\delta(z_i - z_j) + \sum_i V(z_i)\,, \tag{2.8}$$

with $c = \tilde{c}\,\ell$.

Summary of notation.

It is convenient to define a unified notation. In integrable models, interactions are captured by "dressing" bare quantities: for an arbitrary test function $\tau_n(\lambda)$, the dressing operation $\tau_n(\lambda) \to \tau_n^{\rm dr}(\lambda)$ is defined as the solution of the integral equation

$$\tau_n^{\rm dr}(\lambda) = \tau_n(\lambda) - \sum_{n'}\int \frac{{\rm d}\lambda'}{2\pi}\varphi_{n,n'}(\lambda-\lambda')\vartheta_{n'}(\lambda')\tau_{n'}^{\rm dr}(\lambda')\,. \tag{2.9}$$

Above, the integral over the rapidities is on the whole real axis, and the summation over the internal index n runs over the domain discussed below. In Eq. (2.9) one defines the filling fraction $\vartheta_n(\lambda) \equiv \rho_n(\lambda)/(2\pi(\partial_\lambda p_n(\lambda))^{\rm dr}$, with $p_n(\lambda)$ the bare momentum of the quasiparticle and $\varphi_{n,n'}(\lambda)$ the interaction-dependent scattering kernel. In the repulsive phase $c > 0$ one has only terms for $n = 1$, and $p_{n=1}(\lambda) = \lambda$, $\varphi_{n=1,n'=1}(\lambda) = -\frac{2c}{\lambda^2+c^2}$ and bare energy $E_{n=1}(\lambda) = \lambda^2$. In contrast, in the attractive case $n \in \mathbb{N}$ and one has $p_n(\lambda) = n\lambda$, $E_n(\lambda) = n\lambda^2 - \frac{c^2}{12}n(n^2-1)$ and scattering kernel $\varphi_{n,n'}(\lambda) = (1-\delta_{n,n'})a_{|n-n'|}(\lambda)+2a_{|n-n'|+2}(\lambda)+2a_{|n-n'|+4}(\lambda)...+2a_{n+n'-2}(\lambda)+a_{n+n'}(\lambda)$, with $a_j(\lambda) = -\frac{4jc}{c^2j^2+4\lambda^2}$. The thermodynamics and hydrodynamics of integrable models can be expressed in terms of these functions.

Thermodynamics.

The initial conditions of our experimental protocol within the repulsive phase are well-approximated by a thermal ensemble. Within the local density approximation, the filling function $\vartheta_{t=0,x}(\lambda)$ (where we suppress the $n-$label, since we focus on the repulsive phase $n = 1$) is obtained by solving the following integral equations from thermodynamic Bethe ansatz [168]

$$\log[1/\vartheta_{t=0,z}(\lambda)-1] = \beta[E(\lambda)-\mu_\parallel+V(z)] - \int\frac{{\rm d}\lambda'}{2\pi}\varphi(\lambda-\lambda')\log[1-\vartheta_{t=0,z}(\lambda')]\,. \tag{2.10}$$

When estimating the tube population in Supplementary Note 2.6.1, the chemical potential of each tube is renormalized by the transverse potential $\mu_\parallel \to \mu - V_\perp(x,y)$, where $V_\perp(x,y)$ is the transverse trapping potential in the $x-y$ plane. The global chemical potential μ and global inverse temperature β are then considered fitting parameters.

Hydrodynamics.

We simulate the evolution with GHD, expressed in the space of filling fractions [54, 55]

$$\partial_t \vartheta_n + v_n^{\rm eff}\partial_x \vartheta_n + F_n^{\rm eff}\partial_\lambda \vartheta_n = 0 \tag{2.11}$$

and equivalent to Eq. (2.3), where we omitted all the variables for compactness. The GHD equations in the fillings' space are more stable for numerical purposes. The effective velocity can be computed as $v_n^{\rm eff}(\lambda) = (\partial_\lambda E_n)^{\rm dr}/(\partial_\lambda p_n)^{\rm dr}$, while the effective force $F_n^{\rm eff}(\lambda) = \mathcal{F}_n^{\rm dr}(\lambda)/(\partial_\lambda p_n)^{\rm dr}$ combines the effect of the trap, and of interaction changes in time $\mathcal{F}_n(\lambda) = -n\partial_z V + \partial_t c \sum_{n'} \int \frac{{\rm d}\lambda'}{2\pi} \partial_c \Phi_{n,n'}(\lambda-\lambda')(\partial_{\lambda'} p_{n'})^{\rm dr}\vartheta_{n'}(\lambda')$, where one defines $\Phi_{n,n'}(\lambda) = \int^\lambda {\rm d}\lambda'\, \varphi_{\rm n,n'}(\lambda')$. The above GHD equations describe the hydrodynamic evolution within the repulsive or attractive phase separately, but for passing from one to another the proper boundary conditions are needed. Physically, they describe how particles form Bethe strings by passing from the repulsive to the attractive phase. Using a maximum-entropy argument valid in the regime of slow interaction changes, these equations have been derived in Refs. [139, 258]

$$\vartheta_{n;z}(\lambda)\Big|_{c\to 0^-} = 1 - \frac{\sinh(n\Omega_z(\lambda)/2)\sinh((n+2)\Omega_z(\lambda)/2)}{\sinh^2((n+1)\Omega_z(\lambda)/2)} \tag{2.12}$$

with $\Omega_z(\lambda)$ defined from the repulsive root density at vanishing interactions $\Omega_z(\lambda) = \lim_{c\to 0^+} \log\left[1 + 1/(2\pi\rho_{n=1;z}(\lambda))\right]$. During the evolution, the density and energy profiles are computed in local density approximation. An analytical expression for the local pair correlator has been obtained through the Hellmann-Feynmann theorem [228, 259]

$$\langle[\hat\psi^\dagger(z)]^2[\hat\psi(z)]^2\rangle = \sum_n \int {\rm d}\lambda \left\{\partial_{\rm c} {\rm E_n}(\lambda)\rho_{\rm n}(\lambda) + \frac{1}{2\pi}\partial_\lambda {\rm E_n}(\lambda)\vartheta_{\rm n}(\lambda){\rm f_n^{dr}}(\lambda)\right\}, \tag{2.13}$$

whereas the total integrated pair correlation is $G_2 \equiv \int {\rm dz}\, \langle[\hat\psi^\dagger({\rm z})]^2[\hat\psi({\rm z})]^2\rangle$. Above, $f_n(\lambda) = \sum_{n'} \int {\rm d}\lambda'\, \Phi_{\rm n,n'}(\lambda-\lambda')\rho_{\rm n'}(\lambda)$, where, using a local density approximation, the TBA expressions are evaluated on the root density in position z.

The momentum distribution after the 1D asymptotic expansion.

The analytical computation of the momentum-distribution of a dense Bose gas is a formidable challenge. However, in the approximation of a dilute gas obtained after a one-dimensional expansion from a dense gas, analytical results can be obtained. In the repulsive case, isolated particles are well separated and the spatially resolved momentum distribution $P_z(p)$ coincides with the rapidity distribution $P_z(p) \simeq \rho_z(p)$ [246]: to compare with the TOF experimental measurements, we assume that when the three dimensional optical trap is switched off, $P_z(p)$ is the density distribution of particles in position z and with momentum p, which further freely evolve during the three-dimensional expansion.

In the attractive regime, Bethe strings complicate the picture. We assume Bethe strings are spatially well-separated, and they independently contribute to the final momentum distribution. The momentum distribution of a single Bethe string is given by the modulus square of the overlap between the Bethe string's wavefunction

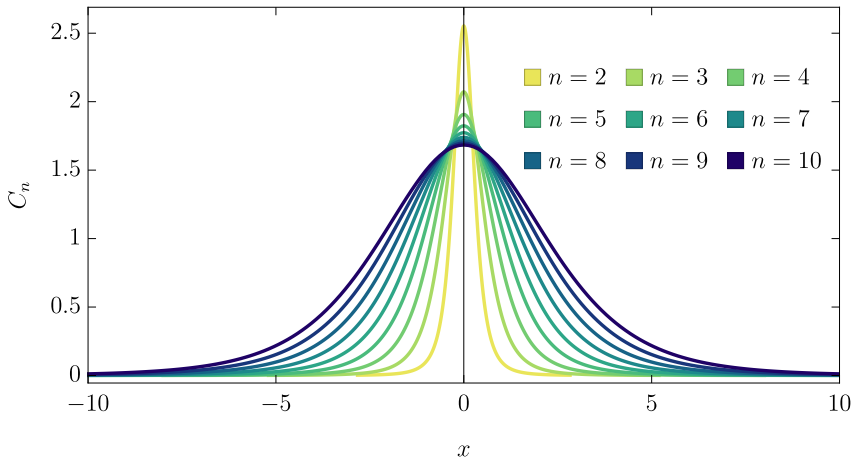

Figure 2.9: **The universal functions C_n.** We show the first universal functions appearing in the string-resolved momentum distribution after 1D expansion, see Eq. (2.14) and related discussion.

and plane waves. A Bethe string of rapidity λ and n particles has wavefunction $\psi_n(z_1 < z_2 < \cdots < z_n) \propto e^{i\sum_{j=1}^{n}(\lambda + i\frac{c}{2}(n+1-2j)z_j}$, and the wavefunction is symmetrically extended to other orderings of the coordinates. Taking advantage of Galilean invariance and the scaling with the interaction c, we can write the total spatially-resolved momentum distribution as

$$P_z(p) = \sum_{n=1}^{\infty} \int \mathrm{d}\lambda \frac{1}{|\mathrm{c}|} \mathrm{C_n}\left(\frac{\mathrm{p}-\lambda}{|\mathrm{c}|}\right) \rho_{\mathrm{n;z}}(\lambda)\,, \tag{2.14}$$

where the function C_n captures the contribution of each string, and it is defined as the modulus squared of the overlap of the Bethe string wavefunction with zero real rapidity and computed at unit interaction $c = -1$, which we call $\bar{\psi}_n$

$$C_n(x) = \int \mathrm{dz_1 e^{-ixz_1}} \int \mathrm{dz_{j>1}}\, \bar{\psi}^*_{\mathrm{n}}(0, \mathrm{z_2}, ..., \mathrm{z_n}) \bar{\psi}_{\mathrm{n}}(\mathrm{z_1}, \mathrm{z_2}, ..., \mathrm{z_n})\,. \tag{2.15}$$

Notice that above there is no restriction on the order of the coordinates. This integral can be simplified with some tedious combinatorics which can be carried over on a laptop and we overview below. Modulus getting a factor $(n-1)!$, we can assume $z_2 < z_3 < ... < z_n$ and the non-trivial permuations are now z_1 and 0 with respect to the other coordinates: we expand the integral by summing over these domains. In the end, everything requires computing integrals in the form $I_j[q_1, ..., q_j] = \int_{y_1<...<y_j<\infty} \mathrm{d^n y\, e^{i\sum_{a=1}^{j} q_j y_j}}$ with imaginary q_j: by explicitly integrating the rightmost coordinate y_j, a simple recursive equation is found $I_j[q_1, ..., q_{j-1}, q_j] = \frac{i}{q_j} I_{j-1}[q_1, ..., q_{j-1} + q_j]$, which eventually gives a quick tabulation of $C_n(z)$. A Mathematica commented notebook that tabulates C_n is provided on Zenodo [251]. In Fig. 2.9 we show the first universal functions $C_n(z)$: they are bell-shaped functions normalized to the number of particles in the Bethe string $\int \mathrm{dz\, C_n(z)} = \mathrm{n}$ and of increasing width for larger n.

While the full profile for $C_n(z)$ is tedious to recover analytically for large n, the variance is rather easy to compute. We consider directly the momentum variance $\langle p^2 \rangle_{n,\lambda}$ of a Bethe string of rapidity λ and n components. We can leverage on the

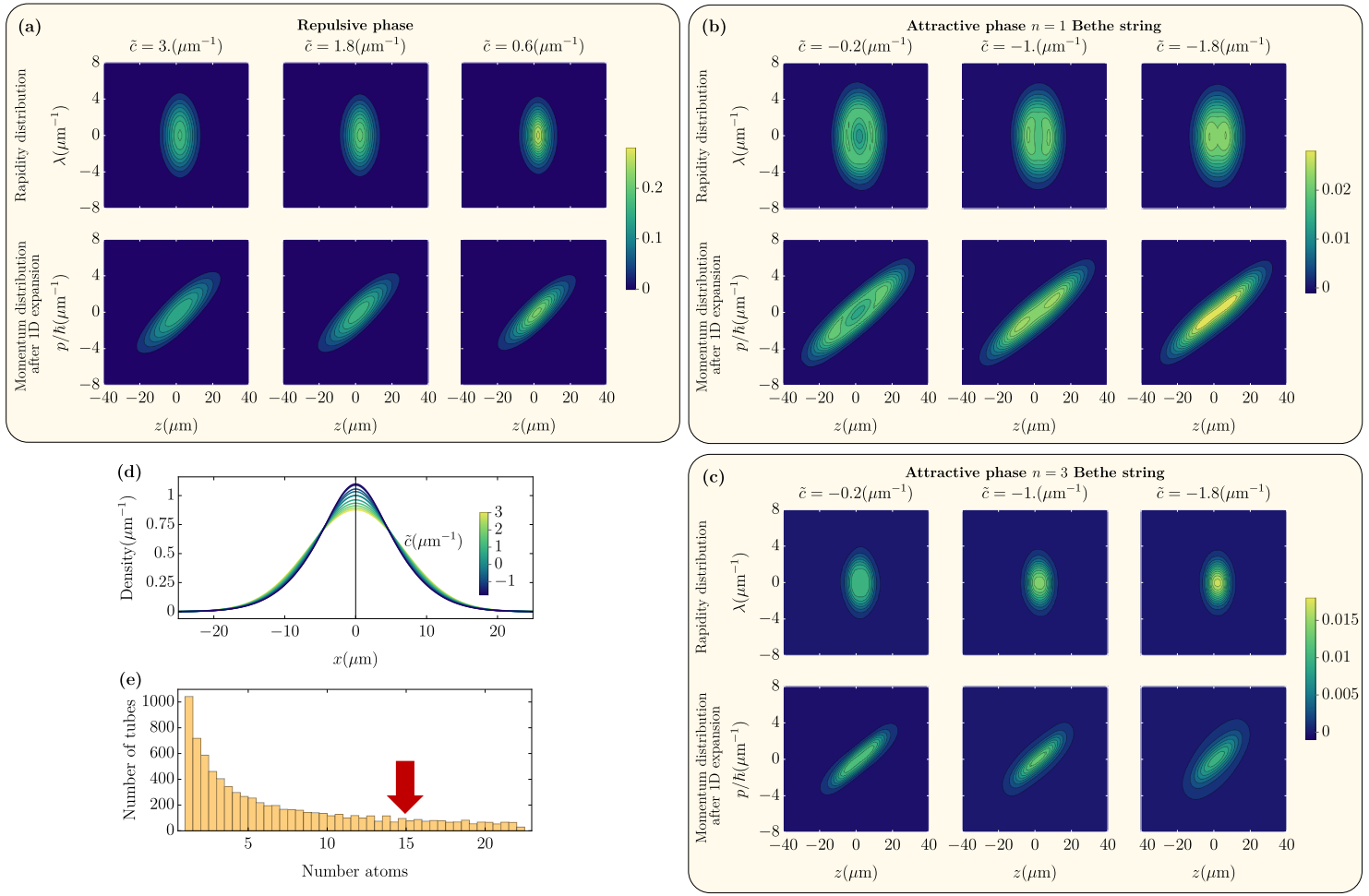

Figure 2.10: **Example of a typical evolution with GHD.** GHD evolution of a representative tube of 15 atoms in a harmonic trap with frequency 27.6 Hz, initially described by a thermal ensemble with temperature $T_{1\text{D}} = 20$ nK. **a** to **c**, phase space density of the rapidity (first row) and momentum distribution per particle after 1D expansion of 10ms (second row). **a** shows the repulsive phase at different interactions, **b** to **c** focus on the example of the $n = 1$ and $n = 3$ Bethe strings. **d**, density profile in the harmonic trap, for different interactions. **e**, estimated atom number populations in the one-dimensional tubes for a crossover temperature of 10 nK.

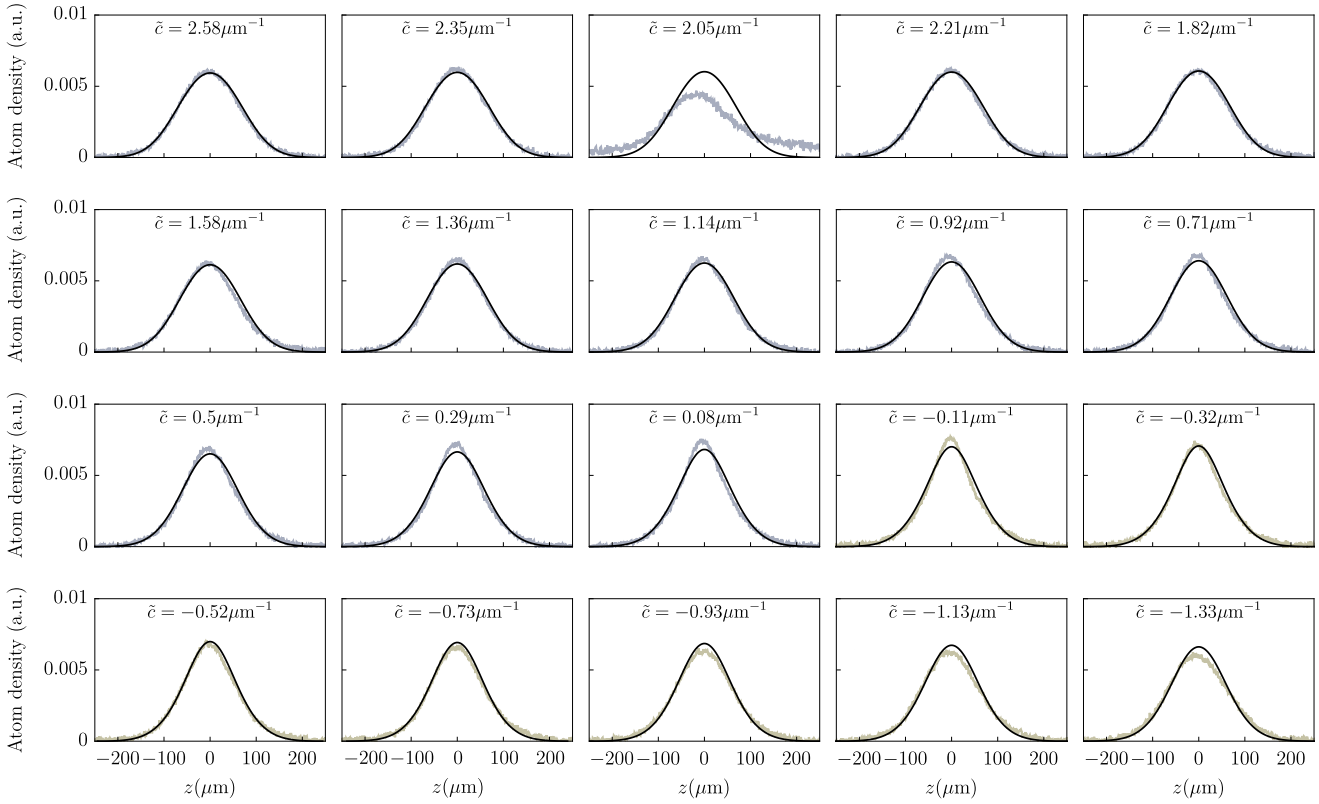

Figure 2.11: **Comparison of experimental data with GHD.** For completeness, we show the full dataset of experimental data compared with the results of GHD simulations, for the dataset of Fig. 2.3 corresponding to $T_{1D} = 15$ nK. See caption of Fig. 2.3 for details. We show the atom density after a longitudinal expansion of $t_{1D} = 10$ ms and $t_{3D} = 46.3$ ms in real space. Black solid lines are GHD curves, whereas colored lines are experimental data (repulsive: light blue, attractive: light green). The starting point of the interaction ramp is at $\tilde{c} = 2.58\,\mu\text{m}^{-1}$, which is then linearly changed in time. The discrepancy shown at $\tilde{c} = 2.05\,\mu\text{m}^{-1}$ is attributed to the fact that it is close to a Feshbach resonance. When ramping the magnetic field to reach less repulsive interactions and the attractive phase, we jump across the resonance to obtain a smooth interaction ramp. The small dents shown by GHD curves at the weakest repulsive and attractive interactions are numerical artifacts arising during the extraction of the 1D-expanded profile from the filling function. This can be reduced by improving the discretization.

knowledge of the energy of this state $E_n(\lambda) = \langle H \rangle_{n,\lambda} = n\lambda^2 - \frac{c^2}{12} n(n^2-1)$. From the Hellmann-Feynman theorem we know $\partial_c E_n(\lambda) = \langle \partial_c H \rangle_{n,\lambda}$, and with the explicit observation that $\partial_c H = \sum_{i \neq j} \delta(z_i - z_j)$ we observe

$$\langle p^2 \rangle_{n,\lambda} = \langle H - c \sum_{i,j} \delta(x_i - x_j) \rangle_{n,\lambda} = E_n(\lambda) - c\partial_c E_n(\lambda) = n\lambda^2 + \frac{c^2}{12} n(n^2-1)\,. \quad (2.16)$$

Specifying $\lambda = 0$ and $c = -1$, we connect with the functions C_n getting $\int \mathrm{dy\, C_n(y)} = \frac{1}{12}\mathrm{n(n^2-1)}$. The total variance of the momentum distribution after 1D expansion is obtained by summing over all the strings with the proper weight $\rho_n(\lambda)$.

Numerical discretization.

The filling functions appearing in the GHD equations (2.11) are discretized on a finite grid in the rapidity and real space. The main bottleneck for the simulations is the solution of the (discretized) integral equations defining the dressing operation, whose matrices grow with the number of strings times the number of points in the rapidity discretization. We use 100 points in the space discretization, 50 points in the rapidity's grid for a maximum number of 25 strings for Fig. 2.3, and increase it to 30 strings for Fig. 2.4 where we did not numerically expanded in 1D, but directly computed the energies from the GHD. For the time-evolution of GHD, we use the method of characteristics with the second order implementation described in Ref. [228]. In Fig. 2.10, we provide further details on a typical simulation focusing on theory only. For the sake of concreteness, we focus on one of the datasets discussed in Fig. 2.3, more precisely we consider the case $T_{1\mathrm{D}} = 20$ nK, and we focus on a single representative tube with 15 atoms. In Fig. 2.10**a** to **c**, we show density plots of the rapidity distribution in the harmonic trap, and the spatially-resolved momentum distribution after 1D expansion of 10 ms, for different interaction strengths. Figure 2.10**a** shows the repulsive side (no strings), whereas in Fig. 2.10**b** and **c**, we consider the attractive phase and focus, as an example, on the $n = 1$ Bethe string (one particle) and $n = 3$ Bethe string (three-particle bound state) respectively. As the interaction $\tilde{c}$ is changed from strongly to weakly repulsive, and then from weakly attractive to strongly attractive the rapidity distribution gets squeezed in the center of the trap. Upon 1D expansion, the momentum distribution in the repulsive branch and of the $n = 1$ Bethe string are simply a deformation of the rapidity distribution obtained ballistically propagating the particles in the z-direction, the magnitude of the velocity increases with the momentum giving the apparent rotation of the oval. For the $n = 3$ Bethe string, this effect is superimposed with the energy release upon breaking the bound states, that dilates the distribution in the vertical direction. This effect is stronger at larger values of attractive interaction. In Fig. 2.10**d**, we show the density profile within the harmonic trap, where the squeezing in the center of the trap is evident. Finally, in Fig. 2.10**e** we provide the estimated atom population across the tubes (see Supplementary Note 2.6.1). The dimensional-crossover temperature that best matches experimental data is 10 nK. For completeness, in Fig. 2.11 we show a full comparison of the experimental expanded cloud with results of GHD simulations for the dataset corresponding to $T_{1D} = 15$ nK shown in Fig. 2.3.

2.6.8 The virial theorem and generalized hydrodynamics

The virial theorem

$$2U - 2E_V - E_{\rm int} = 0 \tag{2.17}$$

is well-known for equilibrium states [159]. In this section, we prove its validity for non-equilibrium states that are stationary with respect to the GHD equations. We work in the adimensional units of Supplementary Note 2.6.7 and start by manipulating the TBA expression for the pair correlator (2.13). We consider the attractive phase, but the same calculations hold in the repulsive case considering the $n = 1$ case only. In the Lieb-Liniger model, the scattering kernel is not an independent function of λ and c, but a scaling function of their ratio $\partial_c \Phi_{n,n'}(\lambda) = -\frac{\lambda}{c}\partial_\lambda \Phi_{n,n'}(\lambda) = -\frac{\lambda}{c}\varphi_{n,n'}(\lambda)$. Using this fact, and the symmetry of the kernel and of the dressing function $\sum_n \int \mathrm{d}\lambda \vartheta_{\rm n}(\lambda)\mathrm{a_n}(\lambda)\mathrm{b_n^{dr}}(\lambda) = \sum_{\rm n}\int \mathrm{d}\lambda \vartheta_{\rm n}(\lambda)\mathrm{a_n^{dr}}(\lambda)\mathrm{b_n}(\lambda)$ for any function $a_n(\lambda)$ and $b_n(\lambda)$, with straightforward manipulations we can write

$$\begin{aligned}\langle[\hat\psi^\dagger(z)]^2[\hat\psi(z)]^2\rangle =& \frac{1}{c}\sum_n \int \mathrm{d}\lambda\, \left[\partial_{\rm c}\mathrm{E_n}(\lambda) + \lambda\partial_\lambda \mathrm{E_n}(\lambda)\right]\rho_{\rm n}(\lambda) \\ &+ \frac{1}{c}\sum_n \int \mathrm{d}\lambda\, \lambda\partial_\lambda \mathrm{p_n}(\lambda)(\partial_\lambda \mathrm{E_n})^{\rm dr}\vartheta_{\rm n}(\lambda)\,.\end{aligned} \tag{2.18}$$

We now use the explicit expressions for the energy and momentum in the Lieb-Liniger model, and notice $\partial_c E_n(\lambda) + \lambda\partial_\lambda E_n(\lambda) = 2E_n(\lambda)$ and $\lambda\partial_\lambda p_n(\lambda) = p_n(\lambda)$. Multiplying both sides by c and integrating over z, we recognize the total interaction energy $E_{\rm int} = c\int \mathrm{dz}\,\langle[\hat\psi^\dagger(\mathrm{z})]^2[\hat\psi(\mathrm{z})]^2\rangle$ and total internal energy $U = \int \mathrm{dz}\,\sum_{\rm n}\int \mathrm{d}\lambda\,\mathrm{E_n}(\lambda)\rho_{\rm n}(\lambda)$, where the $z-$dependence of the root density and filling fraction is left implicit for the sake of notation.

$$E_{\rm int} = 2U + \int \mathrm{dz}\sum_{\rm n}\int \mathrm{d}\lambda\,\mathrm{p_n}(\lambda)(\partial_\lambda \mathrm{E_n})^{\rm dr}\vartheta_{\rm n}(\lambda)\,. \tag{2.19}$$

So far we have not used the GHD equations yet, but only the local density approximation and symmetries of the TBA. The last step uses the GHD equations to further manipulate the remaining integral in Eq. (2.19). In particular, it is possible to show

$$\begin{aligned}\int \mathrm{dz}\sum_{\rm n}\int \mathrm{d}\lambda\,\mathrm{p_n}(\lambda)(\partial_\lambda E_n)^{\rm dr}\vartheta_n(\lambda) = -\langle z\partial_z V\rangle - \frac{\mathrm{d}}{\mathrm{dt}}\left(\sum_n \int \mathrm{dz}\int \mathrm{d}\lambda\,\mathrm{z p_n}(\lambda)\rho_{\rm n}(\lambda)\right) \\ + \partial_t c\int \mathrm{dz}\sum_{\rm n}\int\frac{\mathrm{d}\lambda}{2\pi}\mathrm{zn}\left(\sum_{\rm n'}\int \mathrm{d}\lambda'\partial_{\rm c}\Phi_{\rm n,n'}(\lambda-\lambda')\rho_{\rm n'}(\lambda')\right).\end{aligned} \tag{2.20}$$

The proof is technical and reported below. If the potential $V(z)$ is harmonic, then $z\partial_z V(z) = 2V(z)$ and one recovers the potential energy $\langle z\partial_z V\rangle = 2E_V$. In Eq. (2.20), the total derivative is reminiscent of the virial theorem for classical particles, and there is a further contribution coming from interaction changes. If we consider stationary states, then $\partial_t c = 0$ and the total derivative vanishes as well, thus we recover the virial theorem $E_{\rm int} - 2U + 2E_V = 0$. The virial theorem remains a good approximation for slowly evolving states. In our simulations, we explicitly checked that the interaction energy computed through the virial theorem agrees with the internal energy from (2.13), see Fig. 2.12, and both agree well with the experimental data as shown in Fig. 2.4.

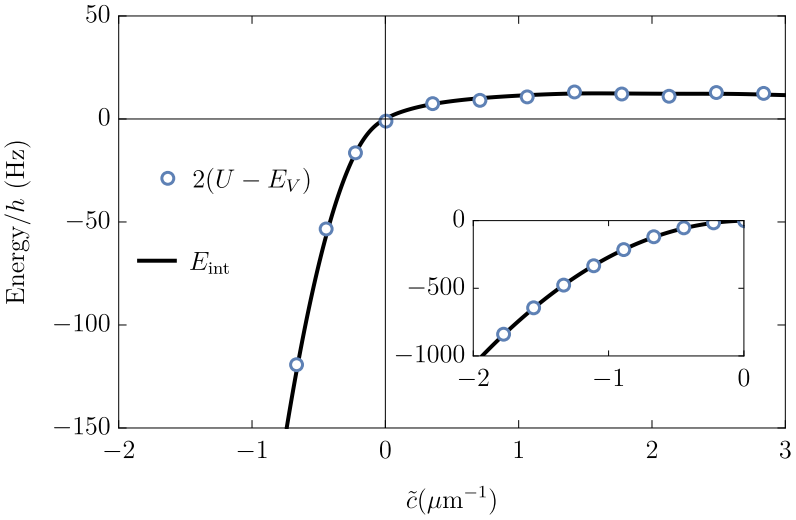

Figure 2.12: **Benchmark of the virial theorem in GHD simulations.** For the same dataset provided in Fig. 2.4, but focusing on theory only, we check that the corrections to the virial theorem due to the non-stationary nature of the state and to the interaction changes, as discussed in Eq. (2.20), are negligible. The black line shows the total interaction energy obtained in the local density approximation from Eq. (2.19). Markers are twice the difference between the internal and potential energies, and agree well with the interaction energy: the small oscillations shown in the repulsive phase are due to the corrections discussed in Eq. (2.20), and are negligible compared to the experimental uncertainty. In the inset, we focus on the strongly attractive regime, the axis of the inset are same of the main plot, but on a different scale: in this regime, the binding energy of Bethe strings dominates the virial theorem. In these simulations, we considered 20 strings, in contrast with Fig. 2.4 where 30 strings have been used. Since the virial theorem holds for any filling fraction stationary to the GHD equations, the truncation in the number of strings does not spoil the agreement between the two curves.

Proof of Eq. (2.20)

To prove Eq. (2.20), we first go through a convenient change of variables in the GHD equations. More precisely, we move from the (z, λ) plane to a pair of conjugated canonical variables $(z, \mathbf{p})$. We define

$$\mathbf{p}_n(\lambda) = p_n(\lambda) - \sum_{n'} \int \frac{\mathrm{d}\lambda'}{2\pi} \Phi_{n,n'}(\lambda - \lambda') \vartheta_{n'}(\lambda') (\partial_{\lambda'} p_{n'}(\lambda'))^{\mathrm{dr}} \tag{2.21}$$

$$\mathbf{e}_n(\lambda) = E_n(\lambda) + nV(z) - \sum_{n'} \int \frac{\mathrm{d}\lambda'}{2\pi} \Phi_{n,n'}(\lambda - \lambda') \vartheta_{n'}(\lambda') (\partial_{\lambda'} E_{n'}(\lambda'))^{\mathrm{dr}} \tag{2.22}$$

And consider the string-dependent change of variable $\lambda \to \mathbf{p} = \mathbf{p}_n(\lambda)$, likewise we define the filling fraction in the new space $\bar{\vartheta}_{n,z}(\mathbf{p})$ through the identity $\bar{\vartheta}_{n,z}(\mathbf{p}_n(\lambda)) = \vartheta_n(\lambda)$. We furthermore define $\mathcal{H}_n(z, \mathbf{p})$ as $\mathcal{H}_n(z, \mathbf{p}_n(\lambda)) = \mathbf{e}_n(\lambda)$, where the z-dependence is implicit in the integral (2.22).

We now rewrite the GHD equations in the filling fraction space (2.11) in terms of the new variables. Notice that $\partial_\lambda \mathbf{p}_n(\lambda) = (\partial_\lambda p_n)^{\mathrm{dr}}$ and $\partial_\lambda \mathbf{e}_n(\lambda) = (\partial_\lambda E_n)^{\mathrm{dr}}$,

therefore $\frac{1}{(\partial_\lambda p_j)^{\rm dr}}\partial_\lambda \to \partial_{\mathbf{p}}$ and $v_n^{\rm eff}(\lambda) \to \partial_{\mathbf{p}}\mathcal{H}_n(x,\mathbf{p})$. Using these identities in Eq. (2.11) one obtains $(\partial_t + \partial_t \mathbf{p}_j \partial_{\mathbf{p}})\bar{\vartheta}_n(\mathbf{p}) + \partial_{\mathbf{p}}\mathcal{H}_n \partial_x \bar{\vartheta}_n(\mathbf{p}) + \mathcal{F}^{\rm dr}\partial_{\mathbf{p}}\bar{\vartheta}_n(\mathbf{p}) = 0$, where it must be stressed that the change of variable $\lambda \to \mathbf{p}$ is time dependent since Eq. (2.21) depends on the evolving state. As a next step, one shows $\partial_t \mathbf{p}_n + \partial_z \mathbf{e}_n = -\mathcal{F}_n^{\rm dr}$ through straightforward manipulations. First, one takes the time and space derivatives of both sides of Eqs. (2.21) and (2.22) respectively, and sums the two equations. The GHD equations in the space of root densities $\partial_t[(\partial_\lambda p_n)^{\rm dr}\vartheta_n(\lambda)] + \partial_x((\partial_\lambda E_n)^{\rm dr}\vartheta_n(\lambda)] + \partial_\lambda[\mathcal{F}^{\rm dr}\vartheta_n(\lambda)] = 0$ (notice that $\rho_n(\lambda) = \frac{1}{2\pi}(\partial_\lambda p_n)^{\rm dr}\vartheta_n(\lambda)$) are used for further simplifications. With this last step, one obtains $\partial_t \mathbf{p}_n + \partial_z \mathbf{e}_n = -\mathcal{F}_n(\lambda) + \sum_{n'}\int {\rm d}\lambda'\, \Phi_{{\rm n},{\rm n}'}(\lambda-\lambda')\vartheta_{{\rm n}'}(\lambda')[-\mathcal{F}_{{\rm n}'}^{\rm dr}(\lambda')]$, and thus can identify $\partial_t \mathbf{p}_n + \partial_z \mathbf{e}_n = -\mathcal{F}_n^{\rm dr}$ as anticipated. Using now $\partial_z \mathbf{e}_n \to \partial_z \mathcal{H}_n(x,\mathbf{p})$, one can rewrite the GHD equations in an explicit symplectic form

$$\partial_t \bar{\vartheta}_{n,x}(\mathbf{p}) + \partial_{\mathbf{p}}\mathcal{H}_j(x,\mathbf{p})\partial_x\bar{\vartheta}_{n,x}(\mathbf{p}) - \partial_x\mathcal{H}_n(x,\mathbf{p})\partial_{\mathbf{p}}\bar{\vartheta}_{n,x}(\mathbf{p}) = 0\,. \tag{2.23}$$

These are the Liouville's equations [260] in the phase space $(z,\mathbf{p})$ for a particle evolving with classical Hamiltonian $\mathcal{H}_n(z,\mathbf{p})$. The evolution can be seen in two ways: either as a function evolving in a time-independent phase space, or as if the coordinates are evolving with a fixed density background $\bar{\vartheta}_{n;t,z(t)}(\mathbf{p}(t)) = \bar{\vartheta}_{n;t=0,z}(\mathbf{p})$, where coordinates obey the equations of motion $\dot{z} = \partial_{\mathbf{p}}\mathcal{H}_n$ and $\dot{\mathbf{p}} = -\partial_z\mathcal{H}_n$. To prove Eq. (2.20), the second interpretation is more convenient. Notice that the Liouville's theorem [260] guarantees that the phase-space volume ${\rm dzd}\mathbf{p}$ is constant in time. We consider the left-hand side of Eq. (2.20) and express it in the $(z,\mathbf{p})$ plane $\sum_n \int {\rm dzd}\mathbf{p}\, \frac{{\rm p_n}(\lambda_{\rm n}(\mathbf{p}))}{2\pi}\partial_{\mathbf{p}}\mathcal{H}_{\rm n}\bar{\vartheta}_{\rm n}(\mathbf{p})$, where $\lambda_n(\mathbf{p})$ denotes the inverse change of variable $\lambda \to \mathbf{p}$. We use $\partial_{\mathbf{p}}\mathcal{H}_n = \dot{z}$ and straightforward identities reaching

$$\begin{aligned}\int {\rm dz} \sum_{\rm n}\int {\rm d}\lambda\, {\rm p_n}(\lambda)(\partial_\lambda {\rm E_n})^{\rm dr}\vartheta_{\rm n}(\lambda) =& \frac{\rm d}{\rm dt}\left(\sum_n \int {\rm dzd}\mathbf{p}\, \frac{{\rm p_n}(\lambda_{\rm n}(\mathbf{p}))}{2\pi}{\rm z}\bar{\vartheta}_{\rm n}(\mathbf{p})\right)\\ &- \sum_n \int \frac{{\rm dzd}\mathbf{p}}{2\pi}\,\frac{{\rm dp_n}(\lambda_{\rm n}(\mathbf{p}))}{\rm dt} z\bar{\vartheta}_n(\mathbf{p})\,.\end{aligned} \tag{2.24}$$

We now use the chain rule to compute $\frac{{\rm dp_n}(\lambda_{\rm n}(\mathbf{p}))}{\rm dt} = \partial_t[p_n(\lambda_n(\mathbf{p}))]\Big|_{\text{fixed }\mathbf{p}} + \dot{\mathbf{p}}\partial_{\mathbf{p}}(p_n\lambda_n(\mathbf{p}))$, then we use $\dot{\mathbf{p}} = -\partial_z\mathcal{H}_n$ and move to time derivatives at fixed λ by using $\partial_t[p_n(\lambda_n(\mathbf{p}))]\Big|_{\text{fixed }\mathbf{p}} = \partial_t p_n(\lambda_n(\mathbf{p})) - \partial_t\mathbf{p}_n\partial_{\mathbf{p}}[p_n(\lambda_n(\mathbf{p}))]$. Therefore, we can write $\frac{{\rm dp_n}(\lambda_{\rm n}(\mathbf{p}))}{\rm dt} = \partial_t p_n(\lambda_n(\mathbf{p})) + \mathcal{F}_n^{\rm eff}(\lambda_n(\mathbf{p}))\partial_{\mathbf{p}}(p_n(\lambda_n(\mathbf{p})))$. We notice that, in the Lieb Liniger model, $\partial_t p_n(\lambda) = 0$. Using this last identity in Eq. (2.24) and rewriting it in terms of the rapidities, Eq. (2.20) follows.

CHAPTER 3

PUBLICATION II

Observing anyonization of bosons in a quantum gas

Sudipta Dhar[1,*], Botao Wang[2,3,*], Milena Horvath[1,*], Amit Vashisht[2,3], Yi Zeng[1], Mikhail B. Zvonarev[4],Nathan Goldman[2,3], Yanliang Guo[1], Manuele Landini[1], and Hanns-Christoph Nägerl[1]

[1]*Institut für Experimentalphysik und Zentrum für Quantenphysik, Universität Innsbruck, Technikerstraße 25, Innsbruck, 6020, Austria*
[2] *Center for Nonlinear Phenomena and Complex Systems, Université Libre de Bruxelles, CP 231, Campus Plaine, B-1050 Brussels, Belgium*
[3]*International Solvay Institutes, 1050 Brussels, Belgium*
[4]*Université Paris-Saclay, CNRS, LPTMS, 91405, Orsay, France*
[*]These authors contributed equally to this work

Anyons [123, 124] are low-dimensional quasiparticles that obey fractional statistics, hence interpolating between bosons and fermions. In two dimensions, they exist as elementary excitations of fractional quantum Hall states [261–263] and they are believed to enable topological quantum computing [264, 265]. One-dimensional (1D) anyons have been theoretically proposed, but their experimental realization has proven to be difficult. Here, we observe emergent anyonic correlations in a 1D strongly-interacting quantum gas, resulting from the phenomenon of spin-charge separation [266–268]. A mobile impurity provides the necessary spin degree of freedom to engineer anyonic correlations in the charge sector and simultaneously acts as a probe to reveal these correlations. Starting with bosons, we tune the statistical phase to transmute bosons via anyons to fermions and observe an asymmetric momentum distribution [231, 269–271], hallmark of anyonic correlations. Going beyond equilibrium conditions, we observe dynamical fermionization of the anyons [272]. Our work opens up the door to the exploration of non-equilibrium anyonic phenomena in a highly controllable setting [272–274].

3.1 Introduction

Quantum theory tells us that particles can be categorized into two distinct groups based on the phase θ that the quantum wavefunction accumulates when two particles are exchanged [275]. This phase is crucial to the collective behavior of ensembles of identical particles: bosonic particles, with $\theta = 0$, may pile up and condense into the same state, whereas fermions, with $\theta = \pi$, follow Pauli's exclusion principle and avoid each other. This has drastic consequences, e.g., forming the basis for the table of elements and assuring stability of neutron stars in the case of fermions, and giving rise to spectacular phenomena such as superfluidity, superconductivity, and laser emission for bosons. But in dimensions lower than three, more exotic possibilities exist. In the seminal works by Leinaas and Myrheim [123], and Wilczek [124], it was realized that a new type of particle, called anyon, with arbitrary values of θ is possible. Anyons behave neither as bosons nor as fermions. They obey fractional quantum statistics [276, 277] and are expected to show an intermediate correlation behavior, interpolating between bosons and fermions.

Two-dimensional anyons are found to exist as quasiparticles in topological states of matter, such as fractional quantum Hall states in solid-state systems [278, 279], and they can be engineered in superconducting quantum processors [280, 281], and trapped-ion processors [282]. Triggered by Haldane's fractional exclusion principle [276], which applies to arbitrary spatial dimensions, the existence of 1D anyons was revealed in the context of the Haldane-Shastry model [283], where spinon excitations were shown to exhibit fractional statistics. Since then, 1D anyons have attracted a lot of theoretical attention. A wealth of phenomena has been proposed, such as statistically induced phase transitions and fractional Mott insulators [284], anomalously bound pairs [285], the accumulation of Friedel oscillations with increasing θ [286], and dynamical fermionization and bosonization of anyons [272, 287]. Anyonic models in 1D have been studied both in the continuum [288, 289] and on discrete lattices [284, 290]. As a hallmark for the presence of anyonic correlations, an asymmetric momentum distribution [270, 271, 291] is expected. The theoretical underpinnings of 1D anyons have long intrigued the scientific community, yet their experimental realization and the observation of their dynamical behavior have remained elusive. A topological gauge theory, developed to describe 1D anyons, was realized using a weakly-interacting Bose-Einstein condensate [292, 293]. Recently, using a Floquet drive, 1D anyons have been realized in a two-atom lattice setting [294].

Here, we present a cold-atom realization of a many-body system with anyonic correlations in 1D. We use a degenerate gas of strongly interacting Cs atoms to simulate 1D hardcore anyons with an arbitrary statistical phase θ. Our system consists of a single spin impurity embedded in and strongly interacting with a Tonks-Girardeau (TG) [229, 230] host gas. The impurity serves a dual purpose in our study: it enables the generation of anyonic correlations in the system and acts as a probe to observe these correlations.

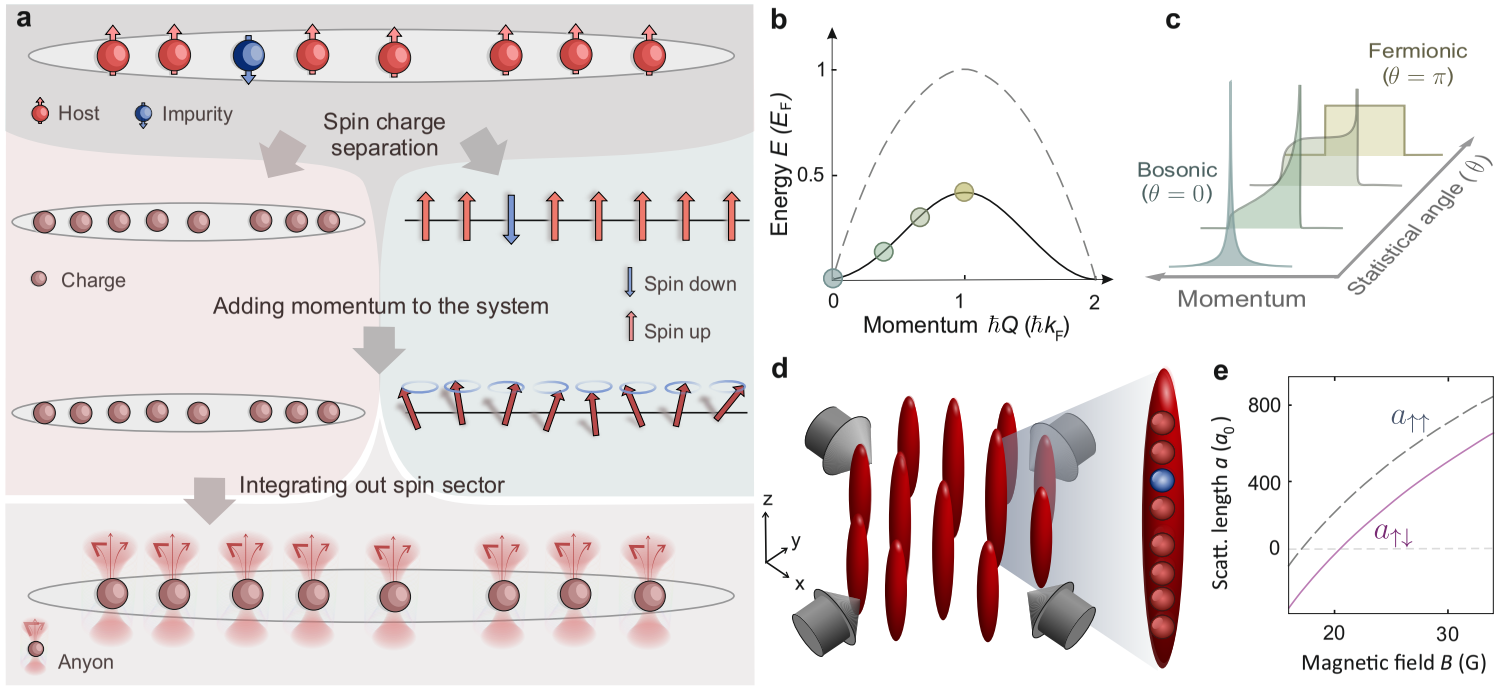

Fig 3.1: **Experimental realization of 1D anyons. a**, Illustration of the emergence of anyons from spin-charge separation. For strong interactions in 1D, the wavefunction factorizes into a charge part and a spin part. Note that, even though the illustration depicts a localized spin impurity, we create a delocalized impurity. The charge sector (left) depicts one possible positional arrangement of the particles, while the spin sector is one possible spin distribution in the squeezed space [295], both corresponding to the arrangement of the spinful particles in the top line. In the finite momentum ground state of the system, all the momentum is carried by the spin sector in the form of spin waves. Integrating out the spin degrees of freedom realizes an effective system of 1D hardcore anyons in the charge sector. The statistical phase θ of these emerging anyons is given by the momentum of the spin waves, see Methods. **b**, Edge of the excitation spectrum of a 1D Bose gas for charge excitation (dashed line) and spin excitation (solid line) [45]. **c**, Expected momentum distributions of anyons [296] for different values of the statistical phase θ as set by the momentum $\hbar Q$ and indicated in **b**. **d**, Experimental realization of an ensemble of 1D Bose gases in tubes formed by two retro-reflected laser beams. Each tube contains on average one impurity particle (blue sphere). The interaction between the impurity and the TG host gas (red spheres) can be tuned by means of a Feshbach resonance [45]. **e**, Host-host (dashed curve) and host-impurity (solid curve) scattering lengths $a_{\uparrow\uparrow}$ and $a_{\uparrow\downarrow}$ as a function of the magnetic field B.

3.2 Our system

For strong impurity-host interaction, spin-charge separation occurs in our system [266], see Fig. 3.1a, with the many-body wavefunction of N particles factorizing into a spatial $\varphi(x_1, x_2, .., x_N)$ and a spin part $\chi(\sigma_1, \sigma_2, .., \sigma_N)$, where $\sigma_i = \uparrow, \downarrow$ is the spin of the i-th particle. Anyonic correlations on φ arise from engineering a spin wavefunction with fractional exchange symmetry when we restrict to cyclic permutations. Intuitively, if χ is chosen such that a permutation results in a phase shift of $-\theta$, the spatial part φ is forced to have the opposite shift, in such a way that the combined wavefunction is still bosonic. For this, the spin wavefunction is prepared in eigenstates of the cyclic spin permutation operator $\hat{C}$, i.e., spin waves $|\theta\rangle$ with eigenvalue $e^{-i\theta}$, see Methods. We experimentally prepare the spin wave by adiabatically accelerating the impurity along the low-energy edge of the excitation spectrum to momentum $\hbar Q$, see Fig. 3.1b. In each particular state, the momentum of the spin wave fixes the effective phase shift resulting from an exchange of the impurity with one of the particles in the host gas. For $Q = 0$, the exchange results in no phase shift, akin to bosonic statistics, while for $Q = k_{\mathrm{F}}$, the resulting phase shift is π as expected from fermionic statistics (see Supplementary materials). For intermediate momenta, we expect that anyonic statistics is realized. Here, $k_{\mathrm{F}} = \rho\pi$ denotes the Fermi momentum of the TG gas, with ρ the 1D density.

A particular observable that is sensitive to the anyonic correlations and to the statistical phase θ is the momentum distribution of the impurity. Specifically, the one-body correlators of the impurity and for a hardcore anyon system are equal [295, 297],

$$(\langle\varphi| \otimes \langle\theta|)\hat{b}_{\downarrow}^{\dagger}(x)\hat{b}_{\downarrow}(y)(|\theta\rangle \otimes |\varphi\rangle) = \frac{1}{N}\langle\varphi|\hat{a}^{\dagger}(x)\hat{a}(y)|\varphi\rangle, \tag{3.1}$$

where $\hat{b}_{\downarrow}^{\dagger}$ ($\hat{b}_{\downarrow}$) is the bosonic creation (annihilation) operator of the impurity and $\hat{a}^{\dagger}$ ($\hat{a}$) is the anyonic creation (annihilation) operator, with $(\hat{a}^{\dagger})^2 = 0$ defining the hardcore condition. Equation (3.1) gives us direct access to the anyonic momentum distribution. Figure 3.1c illustrates the expected anyonic momentum distribution. As θ is varied, the evolution from a bosonic via a skewed to a fermionic distribution can clearly be seen.

3.3 Asymmetric momentum distributions

In the experiment, we prepare an array of about 6000 vertically oriented 1D Bose gases with a weighted average of 37(2) atoms by loading a weakly interacting 3D Bose-Einstein condensate of ^{133}Cs atoms [114] into a 2D optical lattice as illustrated in Fig. 3.1d. Initially, all the atoms are in the hyperfine state $|F, m_F\rangle = |3, 3\rangle$, which we denote by $|\uparrow\rangle$. A magnetic force levitates the atoms against gravity. We then tune the 1D interaction strength $g_{\uparrow} \propto a_{\uparrow\uparrow}$ by means of a Feshbach resonance for the scattering length $a_{\uparrow\uparrow}$ (see Fig. 3.1e) to bring the 1D Bose gases into the TG regime, setting the Lieb-Liniger parameter to $\gamma_{\uparrow\uparrow} \approx 14$, see Methods. A short radio-frequency pulse generates spin impurities in $|3, 2\rangle \equiv |\downarrow\rangle$ out of the host gas. On average, we create one impurity per 1D Bose gas, with the number set by the power and duration of the pulse. We handshake from pure magnetic levitation to a combination of magnetic and optical levitation to allow for a comparatively small

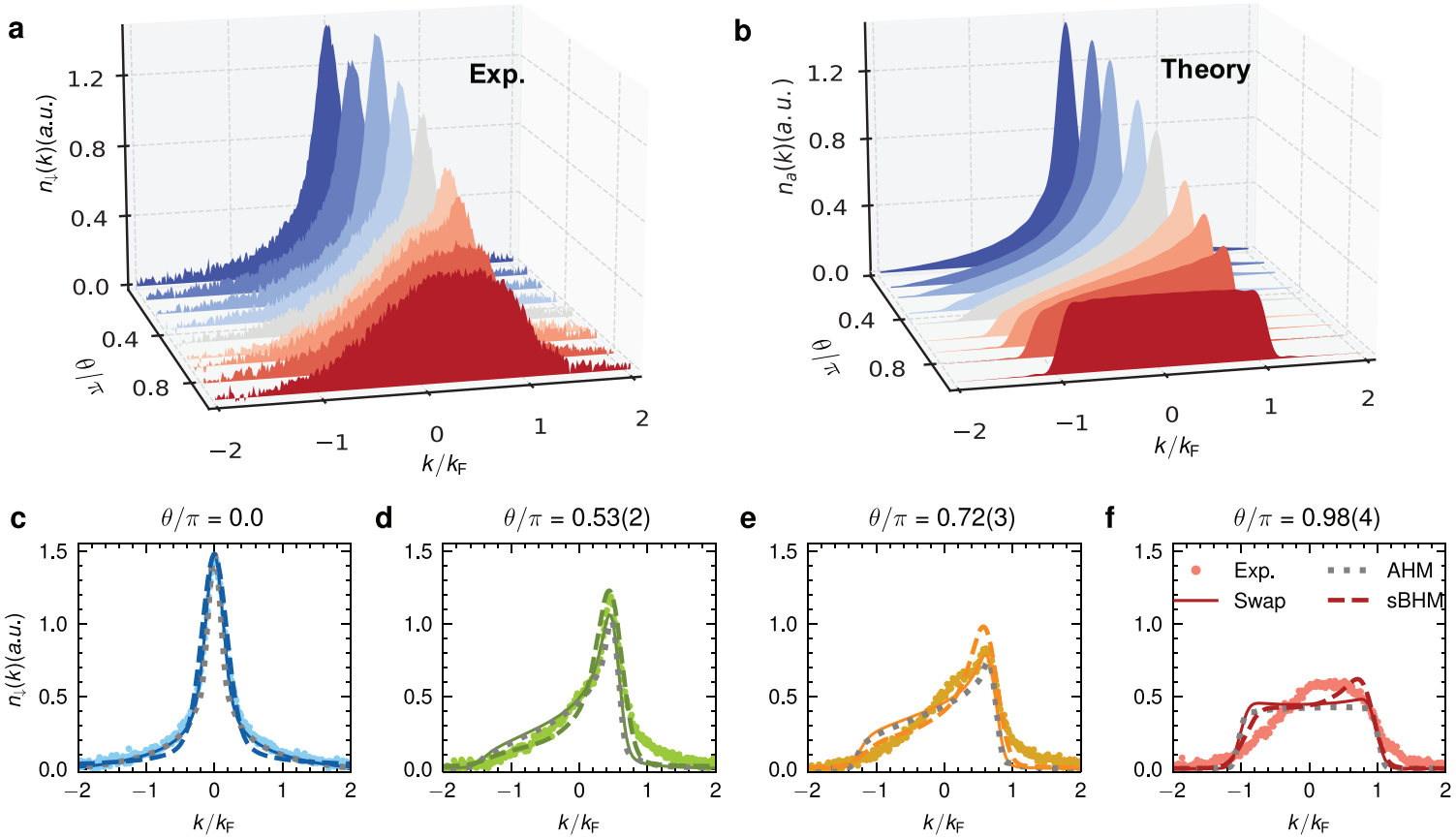

Fig. 3.2: **Momentum distribution of anyonized bosons.** **a**, Evolution of the measured impurity momentum distribution $n_\downarrow(k)$ for variable statistical phases θ, determined by the injected momentum $\hbar Q$, as indicated. Each distribution is the average of 7 experimental realizations. **b**, Numerical results of the anyonic momentum distribution $n_a(k)$ using the anyon-Hubbard model. **c-f**, Example distributions for θ/π equal to 0, 0.53(2), 0.72(3), 0.98(4), respectively. The error bars are smaller than the symbol sizes. The data is compared to numerical results of the ground states of the anyon-Hubbard model (dotted lines), the swap model (solid lines) and the time evolution governed by the spinful Bose-Hubbard model (dashed lines).

force of $F_\downarrow \approx mg/18$ on the impurities, while the host gas remains fully levitated. Here, m is the mass of ^{133}Cs atoms and g is the gravitational acceleration. The force must be kept small to ensure that the impurity adiabatically follows the lower edge of the excitation spectrum. During the evolution, the impurity experiences a host-impurity interaction strength of $\gamma_{\uparrow\downarrow} \approx 9$, as set by the host-impurity scattering length $a_{\uparrow\downarrow}$, see Fig. 3.1e and the Methods. Applying $F_\downarrow$ for a variable evolution time τ places the system at momentum $\hbar Q = F_\downarrow \tau$. Varying τ from zero to 3.5 ms sets the phase $\theta = Q/\rho = \pi Q/k_\mathrm{F}$ to values between zero and π. The inhomogeneities of our system affect the values of θ that we are able to prepare. We always indicate the mean value of the distribution, which we control to a few percent level. The distribution of densities and therefore θ values has an estimated rms spread of about 20% across the system. We finally measure the $|\downarrow\rangle$-momentum distribution $n_\downarrow(k)$ by switching $\gamma_{\uparrow\downarrow}$ to zero and imaging the $|\downarrow\rangle$ atoms after Stern-Gerlach separation and free time-of-flight (TOF) expansion. The results are presented in Fig. 3.2a. For $\theta = 0$, the impurity exhibits a momentum distribution $n_\downarrow(k)$ that is symmetric and sharply peaked at momentum $\hbar k = 0$. As θ is increased towards π, the distribution skews and the peak gradually disappears as the distribution broadens and flattens. At $\theta = \pi$ the distribution is flat-top, nearly filling the entire Brillouin zone from $-k_\mathrm{F}$ to k_F. In essence, the distribution evolves from a bosonic to a fermionic distribution with significant skewness in between.

The anyonic nature of such skewness behavior is confirmed by performing a quantitative analysis using several theoretical models. Our system is naturally described by a spinful Lieb-Liniger gas, for which an exact Bethe-ansatz solution is available [298] in the limit of a fermionized host gas and which allows an exact anyonic mapping of the impurity momentum distribution in the thermodynamic and hardcore limit [295, 296]. To properly capture finite-size effects and directly compare the theoretical prediction to the data, we make use of lattice models that we expect to reliably describe the system in the low lattice-filling regime, see Methods. We first turn to the anyon-Hubbard model (AHM)

$$\hat{H}_\mathrm{AHM} = -J \sum_\ell \hat{a}_\ell^\dagger \hat{a}_{\ell+1} + h.c. + \frac{U}{2} \sum_\ell \hat{n}_\ell (\hat{n}_\ell - 1) \tag{3.2}$$

in the hardcore limit with the on-site interaction $U \to \infty$. Here, J is the tunneling amplitude between nearest-neighboring sites, $\hat{a}_\ell$ is the anyonic annihilation operator at site ℓ, and $\hat{n}_\ell = \hat{a}_\ell^\dagger \hat{a}_\ell$ is the particle number operator. The prediction for the momentum distribution as calculated by a matrix product-state algorithm [299] is shown in Fig. 3.2b. The transition from a peaked bosonic distribution via a skewed to a box-like fermionic distribution can clearly be seen. A direct comparison with our data for selected values of θ is presented in Fig. 3.2(c-f), and we find reasonably good agreement. The second model we employ is the spinful Bose-Hubbard model (sBHM), aimed at describing the dynamics of a spinful Bose system when a force is applied. Additionally, we introduce a novel model, termed the swap model (see Supplementary materials), featuring swap interactions, whose ground state takes the form of the spin wave that we are targeting. The predictions from these models for a single-tube realization are included in Fig. 3.2(c-f). Given our finite momentum resolution that results from the inhomogeneous tube distribution (see Methods) of about $\pm 0.2\hbar k_\mathrm{F}$, these predictions agree well with our experimental data. Imperfect control of the impurity number also contributes to deviations.

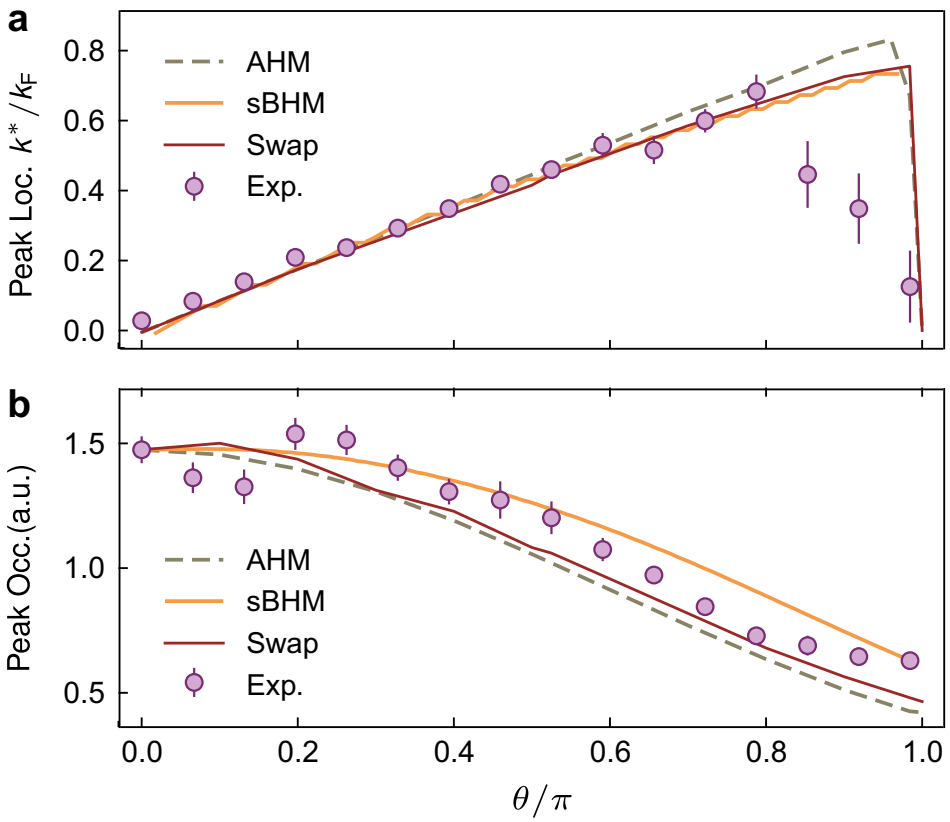

Fig. 3.3: **Characterization of the anyonic momentum distribution. a**, measured peak momentum k^* and **b**, peak occupation of the impurity momentum distribution $n_\downarrow(k)$ as a function of statistical phase θ. The experimental data (dots) is compared to the results of the simulations based on the various models as indicated. The error bars reflect the standard error.

The anyonic correlations are reflected in the asymmetric momentum distribution, exhibiting a shift of the peak of the momentum distribution and a variation of the peak value. In Fig. 3.3a we compare the observed peak position k^* and the peak value $n_\downarrow(k=k^*)$ with the calculated behavior of an anyonic system as θ is varied. For small θ, the peak momentum is proportional to θ. The slope of the linear dependence is expected to be proportional to the density ρ of the gas [270]. For large θ close to π, k^* sharply decreases, since $n_\downarrow(k)$ starts to transmute into a fermionic distribution. Simultaneously, the peak occupation $n_\downarrow(k=k^*)$ decreases as θ increases, as shown in Fig. 3.3b. These observations agree well with the results of the numerical calculations.

3.4 Dynamical fermionization

We next turn to the dynamical properties of our anyonized system. Specifically, we perform a rapidity measurement [300, 301], as has been used recently to study dynamical fermionization in TG gases [149]. The rapidities are the integrals of motion in a 1D integrable system, and they are expected to follow a fermionic distribution in the hard-core limit also for anyons [272]. As before, we prepare the system at momentum $\hbar Q$. We then set the force to $F_\downarrow=0$ and the atoms are allowed

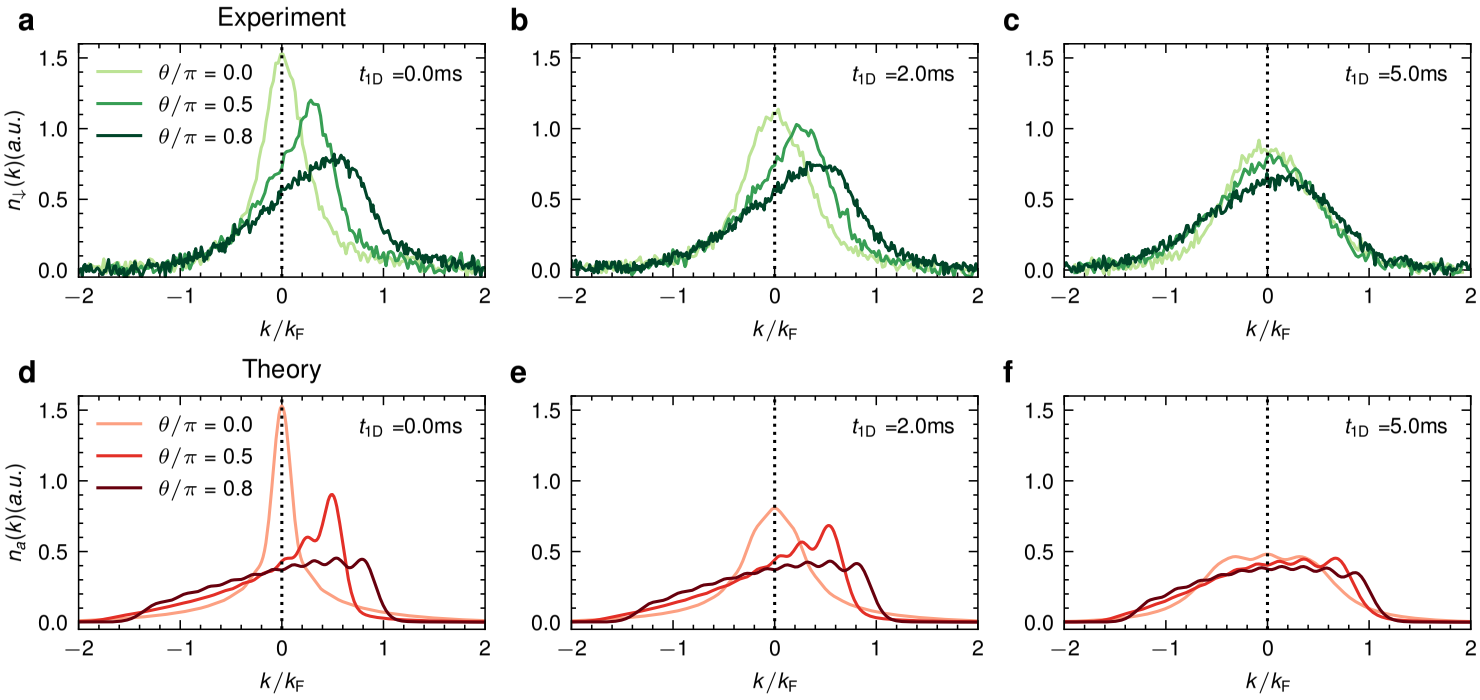

Fig. 3.4: **Dynamical fermionization of hardcore anyons. a-c**, Evolution of the impurity momentum distribution $n_\downarrow(k)$ after quenching the confinement to a flat-bottom trap and allowing 1D expansion for $t_{1D} = 0$, 2, 5 ms, for three different values of statistical phase θ as indicated. Each distribution is the average of 10 experimental realizations. **d-f**, Theoretical prediction for the evolution of the momentum distribution of hard-core anyons ($N = 10$) during 1D free expansion [272].

to expand in an approximately flat potential in 1D for a variable time t_{1D} by partially compensating the longitudinal harmonic confinement by means of a horizontally propagating blue-detuned anti-trapping laser beam. We then measure $n_\downarrow(k)$ as before. This procedure maps the rapidities onto momenta when t_{1D} is chosen to be long enough, typically 5 ms for our parameters, set by the longitudinal trap frequency and the average particle number (see Methods). The experimental results are shown in Fig. 3.4(a-c). In the case without 1D expansion ($t_{1D}=0$), as shown in Fig. 3.4a, the initial anyonic momentum distributions $n_\downarrow(k)$ for various values of θ differ greatly and exhibit the skewness behavior as discussed above. However, as t_{1D} is increased, the distributions converge to a similar asymptotic form. At $t_{1D}=2$ ms (Fig. 3.4b) the distributions still differ, but at $t_{1D}=5$ ms (Fig. 3.4c) they become almost equal. In particular, they have lost their skewness. This behavior is qualitatively captured by our numerical modeling, as shown in Fig. 3.4(d-e). We simulate the quench dynamics for $N=10$ anyons after suddenly releasing the harmonic trapping potential by solving the time-dependent Schrödinger equation (see Methods). The evolution from greatly differing distributions to nearly symmetric and identical distributions can clearly be seen. Note that the expected shape of the distribution in the long-time limit is set by the harmonic trapping potential [272, 302]. Only for box-shaped trapping one expects a box-shaped distribution. Future experiments with custom-shaped potentials will be able to probe this relationship.

3.5 Conclusion

In summary, we have realized a many-body system of 1D anyonized bosons with arbitrary statistical phase from a strongly interacting spinful bosonic system. Our approach relies on the intrinsic fractionalization of spin and charge degrees of freedom in 1D systems in the presence of strong interactions. The observed asymmetric momentum distributions, a hallmark of anyonic correlations, are in good agreement with theoretical predictions. Our findings demonstrate the ability to transmute between bosonic and fermionic behaviors by continuously varying the statistical phase, thus creating a flexible system that allows for the exploration of anyonic behavior in a controlled, low-dimensional environment. Moreover, the observed phenomenon of dynamical fermionization following a trap quench highlights the complex non-equilibrium dynamics that these systems can exhibit, providing insights into the interplay between quantum statistics and dynamical properties of 1D anyons.

A promising direction for future research will be the realization of tunable interactions between anyons [303, 304]. This will open up possibilities for the study of exotic quantum phases [305, 306] and phase transitions predicted for 1D anyonic systems [284, 307]. Our way of realizing density-dependent statistical angles provides a new opportunity to study intriguing dynamical phenomena due to the presence of a statistical interface [308]. Local control of the density distribution will be beneficial for precise tuning of the statistical phase. Generalizing our work beyond 1D to study topologically non-trivial states of matter is also an interesting avenue. Furthermore, our method of measuring non-local string-type correlators via impurities could be used to probe topological order in generic many-body systems [309–311].

Data Availability: The data shown in the main text is available via Zenodo [251].

Acknowledgments
We thank Philip Zechmann and Michael Knap for discussions and providing us at the early stage of this work with the results of simulations to understand the role of a finite force. We thank Xi-Wen Guan for insightful discussion about fractional statistics of an impurity immersed in spin polarized Fermi gases. **Funding:** The Innsbruck team acknowledges funding by a Wittgenstein prize grant under Austrian Science Fund (FWF) project number Z336-N36, by the European Research Council (ERC) under project number 789017, by an FFG infrastructure grant with project number FO999896041, and by the FWF's COE 1 and quantA. MH thanks the doctoral school ALM for hospitality, with funding from the FWF under the project number W1259-N27. Work in Brussels is supported by the ERC (LATIS project), the EOS project CHEQS, the FRS-FNRS Belgium and the Fondation ULB. Computational resources have been provided by the Consortium des Équipements de Calcul Intensif (CÉCI), funded by the Fonds de la Recherche Scientifique de Belgique (F.R.S.-FNRS) under Grant No. 2.5020.11 and by the Walloon Region.

3.6 Methods

3.6.1 Experiment

The experiment starts with an interaction-tunable 3D Bose-Einstein condensate (BEC) of $1.3{\times}10^5$ ^{133}Cs atoms [234] prepared in the lowest magnetic hyperfine state $|F, m_F\rangle = |3,3\rangle \equiv |\uparrow\rangle$, held in a crossed-beam dipole trap and levitated against gravity by a magnetic field gradient. The BEC is in the Thomas-Fermi regime with the 3D s-wave scattering length $a_{\uparrow\uparrow}$ tuned to $a_{\uparrow\uparrow} \approx 220\ a_0$ corresponding to an offset magnetic field of $B = 21.24(1)$ G. A 2D optical lattice, generated by two retro-reflected laser beams propagating in orthogonal directions, is gradually ramped up in 500 ms to a potential depth of $30E_\mathrm{r}$, with $E_\mathrm{r} = \pi^2\hbar^2/(2ma^2)$ the photon recoil energy, cutting the 3D system into an array of 1D tubes that are oriented along the vertical direction, as sketched in Fig. 3.1d. Here, $a = \lambda/2$ is the lattice spacing with $\lambda = 1064.5$ nm the wavelength of the lattice light. The longitudinal trapping frequency in the 1D tubes is 25.6(3) Hz. The magnetic field is then ramped up adiabatically to $B = 35.1$ G, tuning $a_{\uparrow\uparrow}$ to $a_{\uparrow\uparrow} \approx 750\ a_0$, setting the Lieb-Linger (LL) interaction parameter $\gamma_{\uparrow\uparrow} = mg_\uparrow/(\hbar^2\rho) \sim 14$, where $\rho = N/L \approx 1.33\ \mu\mathrm{m}^{-1}$ is the average 1D density and L is the average system length and the nominal value of the Fermi wavevector is given by $k_F = \pi\rho$. Here $g_\uparrow \approx 2\hbar\omega_\perp a_{\uparrow\uparrow}$ [45] and $\omega_\perp$ is the transversal trap frequency. For these values, the 1D systems are deeply in the fermionized TG regime [17, 230].

The impurities are Cs atoms that have been transferred to the Zeeman substate $|3,2\rangle \equiv |\downarrow\rangle$ by means of a short radio-frequency pulse. Power and duration are set such that on average one impurity per tube is created. The pulse duration (15 μs) is much shorter than the Fermi time ($t_\mathrm{F} = 120\ \mu$s), ensuring that the spatial profile of the impurity closely matches the one of the host gas. The number of impurities varies across the atomic density distribution. Because our detection is sensitive to only the impurity atoms, tubes with no impurities are irrelevant. For tubes with two impurities, the momentum distribution is not expected to be exactly anyonic, but the deviation is small, since the impurities are still the minority component.

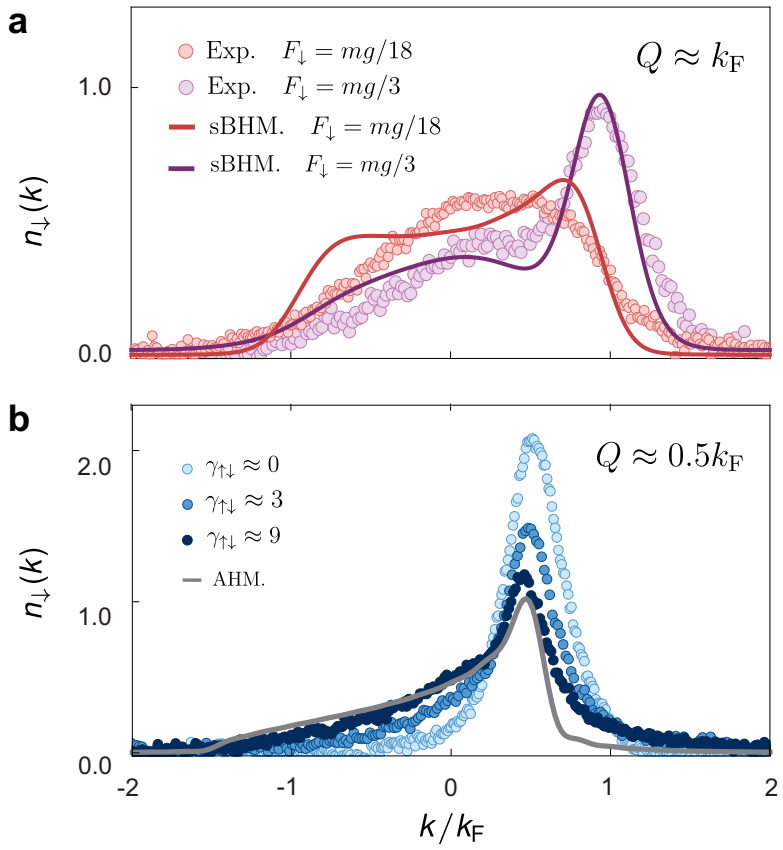

Fig. 3.5: **Role of finite force and finite interaction. a** Measured $n_\downarrow(k)$ at fixed total momentum Q and fixed interaction strength $\gamma_{\uparrow\downarrow}$ for two different values of the force $F_\downarrow$ as indicated. Each distribution is the average of 7 experimental realizations. The experimental data is compared to the results of the simulations based on the sBHM. **b** Measured $n_\downarrow(k)$ at fixed Q for different $\gamma_{\uparrow\downarrow}$. The solid line is the prediction from AHM.

The 3D scattering length between impurity and host atoms $a_{\uparrow\downarrow}$ also varies with B, see Fig. 3.1e. At $B = 35.1$ G the host-impurity LL parameter $\gamma_{\uparrow\downarrow}$ takes the value $\gamma_{\uparrow\downarrow} \sim 9$. The impurity atoms in $|\downarrow\rangle$ experience a smaller levitating force and would be accelerated by $F_\downarrow = mg/3$. Such a comparatively strong force would lead to a non-adiabatic time evolution [45], populating the continuous spectrum of the gapless quantum liquid and pulling the system away from its ground state (see below). To avoid this, we adiabatically turn on optical levitation in 100 ms. Specifically, a 1064-nm Gaussian beam with a $1/e^2$ waist of $\sigma_z \approx 210$ μm^{-1}, positioned $\sigma_z/2$ above the atoms, generates a nearly linear optical potential gradient. Approximately 10 W of laser power indiscriminately levitate the host and the impurity atoms when the magnetic force is off. A tunable force $F_\downarrow$ on the impurity atoms, while still fully levitating the host atoms, can then be generated by adjusting the fraction of optical vs. magnetic levitation.

3.6.2 Role of finite force and finite interaction

Here we study the role of the finite force and finite interaction in our system. In Fig. 3.5a, we show $n_\downarrow(k)$ at a fixed total momentum $\hbar Q \approx \hbar k_F$ for two different

values of force $F_\downarrow$. For strong force $F_\downarrow = mg/3$, the distribution $n_\downarrow(k)$ is skewed and has a peak around $k = k_\mathrm{F}$. In contrast, for a relatively small force $F_\downarrow = mg/18$, the distribution is more symmetric and flat-top as expected for a fermionic distribution. Simulations based on sBHM are in good agreement with our experimental data. The residual asymmetry in the theoretical curve is attributed to the finite $F_\downarrow$. The deviation between theory and experiment mainly results from inhomogeneities of the experimental system, in view of the distribution of k_F values for different tubes. We estimate an upper bound on the Fermi wavevector variation across the tubes from the observed broadening of the momentum distribution of the system. The rms width corresponds to 0.2 $\hbar k_F$, where k_F corresponds to the mean value. We next turn to the effect of finite interaction strength on the momentum distribution. In Fig. 3.5b we show $n_\downarrow(k)$ at a fixed $Q \approx 0.5k_\mathrm{F}$ for three different values of interaction strength $\gamma_{\uparrow\downarrow}$. Close to the non-interacting point $\gamma_{\uparrow\downarrow} \approx 0$, the distribution resembles a bosonic distribution peaked around $k = 0.5k_\mathrm{F}$ and does not show any skewness. As we increase the interaction strength to a moderate value of $\gamma_{\uparrow\downarrow} \approx 3$, the height of the peak decreases, and $n_\downarrow(k)$ broadens to the left. Only for sufficiently strong interaction, the distribution starts to agree with the prediction from AHM. This confirms that strong interactions are crucial for the emergence of anyonic correlations in our system. Note that the peak in the measured $n_\downarrow(k)$ is broader than the AHM predictions for a single tube. This we again attribute to the effect of inhomogeneities. Note that $\gamma_{\uparrow\uparrow}$ also varies when we change $\gamma_{\uparrow\downarrow}$, but it always stays above 3.

3.6.3 Exchange symmetry engineering

We now elaborate on the way in which the emergence of a spin wave in the system leads to the appearance of anyonic correlations on the original particles as expressed by Eq. (3.1). Due to the phenomenon of spin-charge separation, the exchange symmetry of the spatial part is dictated by the exchange symmetry of the spin part of the wavefunction. To obtain an exchange phase of θ in the spatial wavefunction, we need to have an exchange phase of $-\theta$ on the spin wavefunction. To describe the system, we will use the bosonic version of the approach described in ref. [295], where the spinful bosonic system is replaced by a spinless bosonic charge sector and a spin chain, describing the spin of each atom. The unitary pairwise spin-exchange operators $\hat{\mathcal{E}}_{\ell,\ell'}$ exchange spin ℓ with spin ℓ' in the spin chain. The set of $\hat{\mathcal{E}}$ operators generates the symmetric group of permutations S_N. A fully anyonic wavefunction should be a simultaneous eigenstate of all $\hat{\mathcal{E}}_{\ell,\ell'}$, with the eigenvalue $e^{-i\theta\mathrm{sgn}(\ell-\ell')}$.

This state cannot exist for various reasons. Since $\hat{\mathcal{E}}^2$ is the identity operator, the eigenvalues of $\hat{\mathcal{E}}$ are ± 1, corresponding to triplet (bosonic) and singlet (fermionic) wavefunctions. Furthermore, two exchange operators of the type $\hat{\mathcal{E}}_{\ell,\ell'}$ and $\hat{\mathcal{E}}_{\ell',\ell''}$ do not commute with each other, as can easily be verified. Simultaneous eigenstates of all pairwise exchange operators are therefore not easy to find, as a result of the fact that the group S_N for N larger than two is non-abelian. Nevertheless, certain observables in the form of correlation functions can be sensitive to only a subgroup of exchanges, as we will show in the following.

We will now try to find common eigenstates of just a subgroup of S_N, with the required form of eigenvalues. In this sense, even though this method cannot generate a fully anyonic wavefunction of the host-impurity system, it can at least give us direct access to specific observables of the anyonic gas. We are looking for a subgroup of

S_N whose elements can have complex eigenvalues. Cyclic subgroups are abelian and the eigenvalues of the different elements are given by the m-th roots of unity, if m is the size of the cycle. We will concentrate on the cyclic group of maximal order, C_N, as this is the most relevant for us. The group generator $\hat{C}$ performs a cyclic rotation of the spin chain configuration of the system $\hat{C}|\sigma_1, .., \sigma_N\rangle = |\sigma_N, \sigma_1, .., \sigma_{N-1}\rangle$. The eigenvalues are given by $e^{-i\theta}$, for $\theta = 2\pi n/N$, with $n = 0, .., N-1$ and the eigenstates are spin waves. Let us clarify the connection between the exchange phase and the eigenvalue of $\hat{C}$. One cyclic permutation corresponds to $N-1$ backwards binary exchanges. This can be seen by inspecting the effect of the operator on the state of the spin chain. To reproduce the behavior of anyons with forward exchange phase $-\theta$, the eigenvalue of $\hat{C}$ should correspond to $e^{i\theta(N-1)}$. This reduces to $e^{-i\theta}$, using the condition $\theta N = 2\pi n$, with $n \in \mathbb{Z}$, necessary to keep the wavefunction single-valued. The allowed values of θ are therefore discretized, but become dense in the thermodynamic limit. In our experiment, $N \simeq 37$, giving a discretization in steps of $\Delta\theta/\pi \simeq 0.03$, which is below our uncertainty due to inhomogeneities. For the case of a single impurity, the spin waves take the form

$$|\theta\rangle = \frac{1}{\sqrt{N}} \sum_{\ell=0}^{N-1} e^{i\theta\ell} \hat{C}^{\ell} |\downarrow, \uparrow, \uparrow .. \uparrow\rangle. \tag{3.3}$$

We want to identify correlation functions that are well described by the $\hat{C}$ operator. The simplest example of these is the one-body correlation function of the impurity, for the single-impurity case. To see this connection, consider the action of the operator $\hat{b}^{\dagger}_{\downarrow}(x)\hat{b}_{\downarrow}(y)$ on the spin configuration of the 1D system. The destruction operator is only non-zero if the spin down particle is found at position y, the creation operator then places it at position x. As a result, the spin configuration of the system has been shifted by exactly the amount $\hat{N}(x) - \hat{N}(y)$, taking $x > y$. Here $\hat{N}(x) = \int_{-\infty}^{x} \hat{n}(y)dy$ counts the number of particles to the left of x. This corresponds to the application of the operator $\hat{C}^{\hat{N}(x)-\hat{N}(y)}$. We can therefore rewrite

$$\hat{b}^{\dagger}_{\downarrow}(x)\hat{b}_{\downarrow}(y) = \hat{b}^{\dagger}(x)\hat{b}(y)\hat{C}^{\hat{N}(x)-\hat{N}(y)}\hat{\Pi}_{\downarrow}(\hat{N}(y)), \tag{3.4}$$

where $\hat{b}$ is the destruction operator of spinless hardcore bosons in the charge sector and $\hat{\Pi}_{\downarrow}(\hat{N}(y))$ is the projector operator on spin down for the spin at position $\hat{N}(y)$ in the spin chain. If the spin state $|\theta\rangle$ is prepared, we get

$$\begin{aligned}\langle\theta|\hat{b}^{\dagger}_{\downarrow}(x)\hat{b}_{\downarrow}(y)|\theta\rangle =& \frac{1}{N} e^{-i\theta\hat{N}(x)}\hat{b}^{\dagger}(x)\hat{b}(y)e^{i\theta\hat{N}(y)} = \\ &= \frac{1}{N}\hat{a}^{\dagger}(x)\hat{a}(y),\end{aligned} \tag{3.5}$$

where in the last equivalence we used the Jordan-Wigner transformation $\hat{a} = \hat{b}e^{i\theta\hat{N}}$. The factor $1/N$ results from the mean value of $\hat{\Pi}_{\downarrow}$ on the spin wave. It is easy to see how this argument can be generalized to the multi-impurity case, giving a family of anyonic correlation functions that can be exactly simulated with this method. Their explicit expression is given by

$$\begin{aligned}&\hat{b}^{\dagger}_{\sigma}(x_1)...\hat{b}^{\dagger}_{\sigma}(x_m)\hat{b}_{\sigma}(x_1+d)...\hat{b}_{\sigma}(x_m+d) \propto \\ &\hat{a}^{\dagger}(x_1)...\hat{a}^{\dagger}(x_m)\hat{a}(x_1+d)...\hat{a}(x_m+d),\end{aligned} \tag{3.6}$$

where the number m of creation (destruction) operators should match the number of spin σ particles in the spin wave. This demonstrates how, whenever the spin-wave state is realized, we can find correlation functions of the original spinful gas that map exactly onto correlation functions of a system of N anyons, explaining why it is possible to access the momentum distribution of the anyons with measurements on the original spinful bosons. Making use of this equivalence in practice requires the control of the spin state of the system, but it is completely independent of the state in the charge sector. It is therefore possible to directly measure dynamics of the anyonic correlation functions, assuming the spin wavefunction remains in a spin-wave state during the evolution. In our system, we prepare a spin wave as the eigenstate of momentum with lowest energy by slowly accelerating the impurity.

3.6.4 Emergence of anyons via spin-charge separation

We now turn to a lattice model in order to understand how the charge sector can be mapped onto an anyonic gas, when the spinful hardcore bosons are prepared in a finite-momentum ground state. We consider the Hamiltonian $\hat{H}_{\text{lat}}$ describing a gas of N spinful hardcore bosons,

$$\hat{H}_{\text{lat}} = -J \sum_{\ell=1,\sigma}^{L_S-1} \hat{b}^\dagger_{\sigma\ell}\hat{b}_{\sigma\ell+1} - J\sum_{\sigma} \hat{b}^\dagger_{\sigma L}\hat{b}_{\sigma 1} + h.c. \tag{3.7}$$

Here, $\hat{b}^\dagger_{\sigma\ell}$ ($\hat{b}_{\sigma\ell}$) are bosonic creation (annihilation) operator at site ℓ and $\sigma=(\uparrow,\downarrow)$ is the spin index and J is the hopping amplitude, whose value will be specified below. We assume to be in the low density limit $N/L \ll 1$, where $L\ N/L_S \ll 1$, where L_S is the number of lattice sites, and we impose periodic boundary conditions so that conservation of momentum is assured. The operators $\hat{b}^\dagger_{\sigma\ell}$ ($\hat{b}_{\sigma\ell}$) are assumed to satisfy a no-double-occupancy (NDO) constraint, $\sum_\sigma \hat{b}^\dagger_{\sigma\ell}\hat{b}_{\sigma\ell} \leq 1$. Under this NDO constraint, spin and charge degrees of freedom separate, *i.e.*, the wavefunction $|\Psi\rangle$ can be written as $|\Psi\rangle = |\varphi\rangle \otimes |\chi\rangle$. Here, $|\varphi\rangle$ and $|\chi\rangle$ denote the wavefunction for the charge and the spin part, respectively. The Hamiltonian $\hat{H}_{\text{lat}}$ can be written in spin-charge separated form as [312]

$$\hat{H}_{\text{sc}} = -J \sum_{\ell=1}^{L_S-1} \hat{f}^\dagger_\ell \hat{f}_{\ell+1} - J(-1)^{N-1}\hat{f}^\dagger_{L_S}\hat{f}_1\hat{C}^\dagger + h.c., \tag{3.8}$$

where $\hat{f}^\dagger_\ell$ ($\hat{f}_\ell$) is the spinless fermionic creation (annihilation) operator at site j and $\hat{C}$ is the previously introduced spin permutation operator. Note that a bosonic description of the charge sector, with hardcore constraint, is also possible, but has the disadvantage that the bosonic particles are still interacting so that diagonalization is not straightforward. The spin permutation operator $\hat{C}$ and the spinless fermionic operators can be diagonalized separately as they are independent of each other. The eigenstates of $\hat{C}$ are spin waves of the form

$$|\psi_\nu\rangle = \frac{1}{\sqrt{N_\nu}} \sum_{j=0}^{N_\nu-1} e^{i\theta j}\hat{C}^j|\sigma_1,..,\sigma_N\rangle, \tag{3.9}$$

where $|\sigma_1,..,\sigma_N\rangle$ is an arbitrary configuration of the spin chain, ν enumerates all possible disconnected spin blocks and N_ν corresponds to the total number of distinct

elements of the form $\hat{C}^j|\sigma_1,...,\sigma_N\rangle$ in the ν-th block. The eigenvalues of $\hat{C}$ are given by $e^{-i\theta}$, for $\theta = 2\pi n/N_\nu$, with $n = 0,..,N_\nu - 1$. In the case of a single impurity $N_\downarrow = 1$, the eigenstates take the form of Eq. (3.3). By projecting $\hat{H}_{\rm sc}$ on the eigenspace of $\hat{C}$, we get an effective Hamiltonian for the charge sector

$$\hat{H}_{\rm eff} = -J\sum_{\ell=1}^{L_S-1}\hat{f}_\ell^\dagger\hat{f}_{\ell+1} - J(-1)^{N-1}e^{i\theta}\hat{f}_{L_S}^\dagger\hat{f}_1 + h.c. \tag{3.10}$$

Here we see that the fermionic charge sector acquires an overall flux. This spin-generated flux is a collective effect, imposed by the spin waves onto the charge degrees of freedom. Note that the original Hamiltonian $\hat{H}_{\rm lat}$ does not break time-reversal symmetry (TRS). However, TRS is broken for the $\hat{H}_{\rm eff}$ governing the charge sector. This is a result of the projection onto a specific spin-wave subspace. Finally, we perform an anyonic transformation

$$\hat{a}_\ell = \hat{f}_\ell e^{i(\theta+\pi)\hat{N}_\ell} \qquad \text{with} \quad \hat{N}_\ell = \sum_{j=1}^{\ell-1}\hat{n}_j \tag{3.11}$$

The phase factor in the boundary term vanishes, $(-1)^{N-1}e^{i\theta}e^{i(\theta+\pi)(N-1)} = 1$, and the Hamiltonian $\hat{H}_{\rm eff}$ can be mapped onto a system of hardcore anyons with a periodic boundary condition

$$\hat{H}_{\rm AHM} = -J\sum_{\ell=1}^{L_S-1}\hat{a}_\ell^\dagger\hat{a}_{\ell+1} - J\hat{a}_{L_S}^\dagger\hat{a}_1 + h.c. \tag{3.12}$$

As one can see, the anyonic model does not contain any concatenated flux. The transformation Eq.(3.11) is a generalized Jordan-Wigner transformation [313] and the anyons can be understood as composite particles in the charge sector [314, 315]. Each spin wave selects a specific value for the statistical phase. In the thermodynamic limit, this result also holds for any choice of boundary conditions. This justifies the use of fixed boundary conditions in the numerics.

Next, we turn to anyonic observables that can be measured experimentally. The real-space density of these anyons can be extracted by measuring the total density of the gas $\langle\varphi|\hat{a}_\ell^\dagger\hat{a}_\ell|\varphi\rangle = \langle\varphi|\hat{f}_\ell^\dagger\hat{f}_\ell|\varphi\rangle = \sum_\sigma\langle\Psi|\hat{b}_{\sigma\ell}^\dagger\hat{b}_{\sigma\ell}|\Psi\rangle$, where Ψ is the many-body wavefunction of the whole system. However, for hardcore anyons the real-space density is independent of θ. The one-body correlator $\langle\hat{a}_i^\dagger\hat{a}_j\rangle$, on the other hand, is very sensitive to θ. The Fourier transform of this gives the anyonic momentum distribution, which can be measured by measuring the momentum distribution of the impurity in our system via equation (3.1). Note that Hamiltonian (3.10) can be diagonalized exactly [312]. The momenta of the fermions correspond to the rapidities of the system.

3.6.5 Anyon-Hubbard model

To benchmark the anyonic behavior realized in the experiment, we next elaborate on the anyonic correlations of the paradigmatic AHM, which can be effectively simulated by using a bosonic model with density-dependent tunneling. By using a

fractional version of the Jordan-Wigner transformation, i.e., the anyon-boson mapping

$$\hat{a}_\ell = \hat{b}_\ell e^{i\theta \hat{N}_\ell}, \quad \hat{N}_\ell = \sum_{j=1}^{\ell-1} \hat{n}_j, \tag{3.13}$$

the anyon-Hubbard model from Eq. (3.2) can be expressed in terms of bosonic operators as

$$\hat{H}^{\mathrm{B}}_{\mathrm{AHM}} = -J \sum_{\ell=1}^{L_S-1} \left(\hat{b}^\dagger_\ell \hat{b}_{\ell+1} e^{i\theta \hat{n}_\ell} + h.c. \right) + \frac{U}{2} \sum_\ell \hat{n}_\ell \left(\hat{n}_\ell - 1 \right). \tag{3.14}$$

Here, $\hat{b}_\ell$ are the bosonic annihilation operators at site ℓ.

Different from the the bosonic one-body density correlation $\langle \hat{b}^\dagger_\ell \hat{b}_{\ell'} \rangle$, the correlator of anyons $\langle \hat{a}^\dagger_\ell \hat{a}_{\ell'} \rangle$ can be expressed as

$$\langle \hat{a}^\dagger_\ell \hat{a}_{\ell'} \rangle = \langle \hat{b}^\dagger_\ell e^{i\theta(\hat{N}_{\ell'} - \hat{N}_\ell)} \hat{b}_{\ell'} \rangle. \tag{3.15}$$

For the data shown in Fig. 3.2 and Fig. 3.3, we have assumed $N = 10$ anyons in $L_S = 40$ lattice sites in the hard-core limit with open boundary condition. The effect of the boundary condition is negligible for large system sizes. The use of a reduced atom number speeds up considerably the numerics. We find a consistent and satisfactory agreement with the experimental data by considering large system size at low filling (see Supplementary materials).

3.6.6 Dynamical evolution with sBHM

In practice, a spin wave can be generated by slowly accelerating the impurity. In order to efficiently simulate such a dynamical process, we consider a spinful Bose-Hubbard model (sBHM) on a 1D lattice,

$$\begin{aligned} \hat{H}_{\mathrm{sBHM}} = &- J \sum_{\ell=1}^{L_S-1} \left(\hat{b}^\dagger_{\uparrow\ell} \hat{b}_{\uparrow\ell+1} + \hat{b}^\dagger_{\downarrow\ell} \hat{b}_{\downarrow\ell+1} + h.c. \right) \\ &+ U_{\uparrow\downarrow} \sum_\ell \hat{n}_{\uparrow\ell} \hat{n}_{\downarrow\ell} - \sum_\ell F_\downarrow a\ell \hat{n}_{\downarrow\ell}. \end{aligned} \tag{3.16}$$

Here, $\hat{b}_{\uparrow\ell}$ and $\hat{b}_{\downarrow\ell}$ are the annihilation operators of host particles and an impurity at site ℓ, respectively, with their hopping strength being denoted by J. We consider the hardcore limit of the intra-component interaction, i.e., $U_{\uparrow\uparrow} \to \infty$ and $U_{\downarrow\downarrow} \to \infty$. The on-site interaction between host particles and the impurity is denoted by $U_{\uparrow\downarrow}$. A constant force $F_\downarrow$ is applied only to the impurity. We define the dimensionless force $\mathcal{F} = \frac{F_\downarrow m}{\hbar^2 \rho^3}$. In the low filling limit, any lattice model reduces to a continuum model with the effective mass given by

$$m = \frac{\hbar^2}{2Ja^2}. \tag{3.17}$$

By setting the value of the effective mass to be equal to the particle's mass, we fix the value of Ja^2. By defining the filling factor in a lattice $n = N/L_{\mathrm{S}}$ and $a = L/L_{\mathrm{S}}$

being the lattice constant, one obtains the following mapping between quantities,

$$\frac{U}{J} = \frac{g_{\uparrow\downarrow}}{a}\frac{2ma^2}{\hbar^2} = 2\gamma_{\uparrow\downarrow}\frac{N}{L_{\mathrm{S}}}, \tag{3.18}$$

$$\frac{F_{\downarrow}a}{J} = F_{\downarrow}a\frac{2ma^2}{\hbar^2} = 2\mathcal{F}\left(\frac{N}{L_{\mathrm{S}}}\right)^3. \tag{3.19}$$

In our simulation, the initial impurity distribution is defined by the ground state of the Hamiltonian (3.16) with $F_{\downarrow} = 0$ and a harmonic trapping potential V applied only for the impurity. At $t = 0$, we suddenly remove the traps and switch on the constant force $F_{\downarrow}$. We simulate the quench dynamics by solving the time-dependent Schrödinger equation associated with the Hamiltonian (3.16) by using the time-dependent variational principle (TDVP) based on matrix product states implemented using ITensors [299, 316]. The results are presented in Fig. 3.2 and Fig. 3.3. The parameters have been chosen as $L_S = 40, N_{\downarrow} = 1, N_{\uparrow} = 20, U/J = 9.1$ and $F_{\downarrow}a/J = 0.15$ for numerical convenience. A more costly simulation by using a larger system size (e.g., $L_S = 120$) at lower filling (e.g. $N_{\uparrow}/L_S = 0.25$) gives very similar results (see Supplementary materials).

3.6.7 Swap model

Inspired by the central role of the spin wave in the emergence of anyonic behavior of our system, we develop a toy model whose ground state encodes the spin wave we are targeting,

$$\begin{aligned}\hat{H}_{\mathrm{swap}} = &- J\sum_{\ell=1}^{L_S-1}\hat{b}^{\dagger}_{\uparrow\ell}\hat{b}_{\uparrow\ell+1} - J\sum_{\ell=1}^{L_S-1}\hat{b}^{\dagger}_{\downarrow\ell}\hat{b}_{\downarrow\ell+1} \\ &- J_{\mathrm{ex}}e^{-i\theta}\sum_{\ell=1}^{L_S-1}\hat{b}^{\dagger}_{\uparrow\ell}\hat{b}^{\dagger}_{\downarrow\ell+1}\hat{b}_{\downarrow\ell}\hat{b}_{\uparrow\ell+1} + h.c.,\end{aligned} \tag{3.20}$$

with $\hat{b}_{\uparrow\ell}$ and $\hat{b}_{\downarrow\ell}$ being the annihilation operators of host particles and the impurity at site ℓ, respectively, and their hopping strength denoted by J. In the strongly interacting regime, the swapping strength J_{ex} is expected to be of the order of $J^2/U_{\uparrow\downarrow}$.Importantly, we encode the spin-wave information by assigning the factor $e^{-i\theta}$ to the swapping terms. The ground state of the swap model is expected to effectively describe the lowest energy state of the spinful system for momentum $\hbar Q = \hbar\rho\theta$ [317].

In a spin-charge separated representation, the one-body correlation function $\langle\hat{b}^{\dagger}_{\downarrow\ell}\hat{b}_{\downarrow\ell'}\rangle$ of the single impurity can be implemented by hopping of spinless particles and swapping $\hat{\mathcal{E}}$ on the spin chain [295, 318]. Taking $\ell' \geqslant \ell$ as an example, we have

$$\begin{aligned}\langle\hat{b}^{\dagger}_{\downarrow\ell}\hat{b}_{\downarrow\ell'}\rangle = &\sum_{m',m}\langle\varphi|\hat{b}^{\dagger}_{\ell}\hat{b}_{\ell'}\delta_{m,\hat{N}_l}\delta_{m',\hat{N}_{l'}}|\varphi\rangle \\ &\times\langle\chi|\hat{\mathcal{E}}_{m,m+1}\cdots\hat{\mathcal{E}}_{m'-1,m'}|\chi\rangle,\end{aligned} \tag{3.21}$$

Here, the Kronecker δ operators ensure that the ℓ'-th site is occupied the m'-th spin, and after hopping, the ℓ-th site is occupied by the m-th spin. In the case of a

single impurity, the product of swap operators is related to the $\hat{C}$ operator as shown previously, giving rise to a spin wave, which leads to the one-body correlator of the impurity shown in Eq. (3.1). Calculating the Fourier transform of the one-body correlator of the impurity and using the parameters $L_S = 120, N_\downarrow = 1, N_\uparrow = 30$ and $J_{\rm ex}/J = 0.01$, we obtain the quasi-momentum distribution of the impurity shown in Fig. 3.2 and Fig. 3.3. Note that the small value of swapping strength $J_{\rm ex}$ is related to the strong host-impurity interaction and the agreement with experimental data is found for a wide parameter regime (see Supplementary materials).

3.6.8 Rapidity of anyons in 1D

In Fig. 3.4(d-f), we present the results of the simulation of the quench dynamics of anyonic gases after suddenly removing the harmonic trap in 1D. The momentum distribution as a function of evolution time is expressed as

$$n_{\rm a}(k,t) = \frac{1}{2\pi}\iint {\rm d}x{\rm d}y e^{ik(x-y)}\rho_{\rm HCA}(x,y;t), \tag{3.22}$$

with the single-particle density matrix of hardcore anyons $\rho_{\rm HCA}(x,y;t)$. Following Ref. [272], it can be efficiently computed as

$$\rho_{\rm HCA}(x,y;t) = \sum_{m,n=0}^{N-1} \phi_m^*(x,t) A_{mn}(x,y;t)\phi_n(y,t), \tag{3.23}$$

where $A_{mn}(x,y;t)$ are the matrix elements of $\mathbf{A}(x,y;t) = (\mathbf{P}^{-1})^T {\rm det}\mathbf{P}$, and the elements of matrix $\mathbf{P}(x,y;t)$ are $P_{mn}(x,y;t) = \delta_{mn} - \left(1 - e^{-i\theta {\rm sgn}(y-x)}\right){\rm sgn}(y-x)\int_x^y dz \phi_m^*(z,t)\phi_n(z,t)$. Here, $\phi_n(x,0)$ are the single-particle wavefunctions of the 1D harmonic oscillator, and $\phi_n(x,t)$ fulfill the time-dependent Schrödinger equation

$$i\hbar\frac{\partial\phi_n(x,t)}{\partial t} = \left(-\frac{\hbar^2}{2m}\frac{\partial^2}{\partial x^2} + \frac{m\omega_0^2 x^2\Theta(-t)}{2}\right)\phi_n(x,t), \tag{3.24}$$

with Heaviside step function $\Theta(t)$, which models a sudden quench $\omega(t) = \omega_0\Theta(-t)$. The solution is found to be $\phi_n(x,t) = \phi_n(x/b(t),0)e^{imx^2\dot{b}/2b\hbar - iE_n\tau(t)/\hbar}/\sqrt{b(t)}$, with the scaling factor $b(t) = \sqrt{1+\omega_0^2 t^2}$, $\tau(t) = \int_0^t dt'/b^2(t')$ and $E_n = \hbar\omega_0(n+1/2)$. In the experiment, the trapping frequency is set to $\omega_0 = 2\pi \times 25.6(3)$ Hz, and the average Fermi time is $t_{\rm F} = 2m/\hbar k_{\rm F}^2 \approx 0.12$ ms. Due to the finite size of the optical levitation beam, the expansion time $t_{\rm 1D}$ is limited to about 5 ms in the experiment.

3.7 Supplementary materials

3.7.1 Exact solution via Bethe ansatz

Here, we consider the problem of an impurity interacting with a one-dimensional TG gas via a short-ranged δ-function potential of arbitrary strength $g_{\uparrow\downarrow}$. The TG gas can be mapped to a gas of spin-polarized free fermions. The system is governed by the Hamiltonian [189]

$$\hat{H} = \frac{1}{2m}\sum_{i=1}^{N}\hat{P}_i^2 + \frac{1}{2m}\hat{P}_\downarrow^2 + g_{\uparrow\downarrow}\sum_{i=1}^{N}\delta(x_i - x_\downarrow), \tag{3.25}$$

where x_i and $\hat{P}_i$ are the position and momentum of the i-th background particle, respectively. The position and momentum of the impurity are denoted by $x_\downarrow$ and $\hat{P}_\downarrow$, respectively. All particles are assumed to have the same mass m. The dimensionless LL interaction strength is given by $\gamma_{\uparrow\downarrow} = \frac{mg_{\uparrow\downarrow}}{\hbar^2\rho}$, where $\rho = \frac{N}{L}$ is the density of the background gas and L is the system-size. The Fermi momentum, defined as $k_{\mathrm{F}} = \pi\rho$, is directly proportional to the 1D density ρ. This model (3.25) is integrable for any value of $g_{\uparrow\downarrow}$ and can be solved via Bethe ansatz [298]. Some calculations are easier in the mobile impurity reference frame. This frame is accessed via the Lee-Low-Pines (LLP) transformation [194], sometimes called the polaron transformation, which is frequently used in polaron physics. For simplicity, we set $g_{\uparrow\downarrow} \equiv g$ and $\hbar = m = 1$ in the following.

3.7.2 Lee-Low-Pines transformation

The key object is the operator

$$\mathcal{Q} = e^{i\hat{P}_\uparrow \hat{x}_\downarrow}. \tag{3.26}$$

Here, $x_\downarrow$ is the position of the impurity and $P_\uparrow$ is the total momentum of the host particles. The transformation of an arbitrary operator $\mathcal{O}$ from the laboratory to the mobile impurity reference frame is given by

$$\mathcal{O} \to \mathcal{O}_\mathcal{Q} = \mathcal{Q}\mathcal{O}\mathcal{Q}^{-1}. \tag{3.27}$$

The LLP transformation does not affect the momentum of the host particles but changes the momentum operator of the impurity

$$\hat{P}_{\uparrow\mathcal{Q}} = \hat{P}_\uparrow, \qquad \hat{P}_{\downarrow\mathcal{Q}} = \hat{P}_\downarrow - \hat{P}_\uparrow. \tag{3.28}$$

Therefore, the total momentum of the system in the mobile impurity reference frame reads

$$\hat{P}_\mathcal{Q} = \hat{P}_\downarrow. \tag{3.29}$$

Let us apply $\mathcal{Q}$ to the wavefunction. Recall that

$$e^{a\frac{d}{dx}} f(x) = f(x+a). \tag{3.30}$$

As a result,

$$\mathcal{Q}\Psi_Q(x_\downarrow, x_1, \ldots, x_N) = \Psi_Q(x_\downarrow, x_1 + x_\downarrow, \ldots, x_N + x_\downarrow) = e^{iQx_\downarrow}\Psi_Q(0, x_1, \ldots, x_N). \tag{3.31}$$

Here Ψ_Q is the wavefunction in the original frame, the subscript Q indicates the value of the total momentum of the system. Note that we work with fermions in the continuum, hence our system is translationally invariant. The shift of all coordinates is achieved by the action of the momentum operator as follows from Eq. (3.30). This is how we got the right hand side of Eq. (3.31). We can rewrite Eq. (3.31) as

$$\Psi_Q(x_\downarrow, x_1, \ldots, x_N) = e^{iQx_\downarrow}\Psi_Q(0, x_1 - x_\downarrow, \ldots, x_N - x_\downarrow) \equiv e^{iQx_\downarrow} f_Q(y_1, \ldots, y_N), \tag{3.32}$$

where $y_j = x_j - x_\downarrow$, $j = 1, \ldots, N$.

The function $f_Q(y_1, \ldots, y_N)$ is the wavefunction of the system in the mobile impurity reference frame. Working with its first-quantized representation, we aim at doing an exact calculation for finite N. Hence, we impose periodic boundary conditions to take into account finite-size effects. For the following calculations, we consider the case where N is odd.

3.7.3 Bethe ansatz solution for arbitrary coupling

The Hamiltonian 3.25 in the mobile impurity frame transforms to,

$$\hat{H}_Q = \frac{1}{2}\sum_{i=1}^{N}\hat{P}_i^2 + \frac{1}{2}(\hat{P}_\downarrow - \hat{P}_\uparrow)^2 + g\sum_{i=1}^{N}\delta(y_i). \tag{3.33}$$

Thus, any gas particle in the impurity frame is scattered by the impurity particle positioned at the origin. The wavefunctions of the problem in the impurity frame look particularly simple. They are just Slater determinants [319]

$$f_Q(y_1,\ldots,y_N) = \frac{Y}{\sqrt{N!L^N}}\begin{vmatrix} e^{ik_1y_1} & \ldots & e^{ik_{N+1}y_1} \\ \vdots & \ddots & \vdots \\ e^{ik_1y_N} & \ldots & e^{ik_{N+1}y_N} \\ \nu(k_1) & \ldots & \nu(k_{N+1}) \end{vmatrix}, \qquad 0 \le y_j \le L, \tag{3.34}$$

where

$$\nu(q) = \frac{g}{2}\frac{1}{q - \frac{g}{2}(\Lambda + i)}. \tag{3.35}$$

The factor Y ensures the normalization condition. The set of quasi-momenta $k_1,\ldots,k_{N+1}$ satisfies a system of nonlinear equations (Bethe equations)

$$\cot\frac{k_jL}{2} = \frac{2k_j}{g} - \Lambda, \qquad j = 1,2,\ldots,N+1. \tag{3.36}$$

Here Λ is a free parameter, whose value is fixed by requiring

$$Q = \sum_{j=1}^{N+1} k_j. \tag{3.37}$$

That is, the sum of the quasi-momenta give the total momentum (which is an observable). In the system with finite number of particles the total momentum is quantized as usual,

$$Q = \frac{2\pi}{L}n, \qquad n = 0, \pm1, \pm2, \ldots. \tag{3.38}$$

The energy of the state is

$$E_{\mathrm{F}} = \frac{1}{2}\sum_{j=1}^{N+1} k_j^2. \tag{3.39}$$

Let us recall how Eqs. (3.36) are obtained. The function (3.34) has to be continuous,

$$f_Q(y_1,\ldots,y_N)\Big|_{y_j=0}^{y_j=L} = 0. \tag{3.40}$$

Its first derivative should experience a jump such that the second derivative generates the terms $g\delta(y_j)$:

$$-\partial_{y_j} f_Q(y_1,\ldots,y_N)\Big|_{y_j=0}^{y_j=L} = g f_Q(y_1,\ldots,y_j=0,\ldots,y_N). \tag{3.41}$$

Substituting the function (3.34) into these two equations we get the desired equations (3.36).

The form (3.34) is valid when all y_j are contained in the interval from zero to L. The expression, for example, for y_j in the interval from L to $2L$ is not given by Eq. (3.34). We discuss how to extend Eq. (3.34) from the interval $0 \le y_j \le L$ for the particular case $g \to \infty$ in the next section.

Bethe ansatz solution in the limit of infinite repulsion

The form of Eq. (3.34) further simplifies in the limit of infinite repulsion, $g \to \infty$. There, the function (3.35) becomes momentum-independent,

$$\nu(q) = -\frac{1}{\Lambda + i}, \qquad g \to \infty \tag{3.42}$$

and the wavefunction (3.34) takes the form

$$f_Q(y_1, \ldots, y_N) = \frac{\tilde{Y}}{\sqrt{N! L^N}} \begin{vmatrix} e^{ik_1 y_1} & \ldots & e^{ik_{N+1} y_1} \\ \vdots & \ddots & \vdots \\ e^{ik_1 y_N} & \ldots & e^{ik_{N+1} y_N} \\ 1 & \ldots & 1 \end{vmatrix}, \qquad g \to \infty \tag{3.43}$$

in the domain $0 \le y_j \le L$. The Bethe equations (3.36) also simplify a lot:

$$\cot \frac{k_j L}{2} = -\Lambda, \qquad j = 1, 2, \ldots, N+1, \qquad g \to \infty. \tag{3.44}$$

We see that the quasi-momenta k_j are quantized like free fermions plus a shift, same for all k_js from a given set:

$$k_j = q_j + \frac{\mu}{L}, \qquad j = 1, 2, \ldots, N+1, \qquad g \to \infty, \tag{3.45}$$

where $\mu = -2\tan(\Lambda)$ and q_j are free-fermion momenta

$$q_j = \frac{2\pi}{L} n_j, \qquad n_j = 0, \pm 1, \pm 2, \ldots. \tag{3.46}$$

We therefore have

$$f_Q(y_1, \ldots, y_N) = \frac{\tilde{Y}}{\sqrt{N! L^N}} \prod_{j=1}^{N} e^{i\mu y_j / L} \begin{vmatrix} e^{iq_1 y_1} & \ldots & e^{iq_{N+1} y_1} \\ \vdots & \ddots & \vdots \\ e^{iq_1 y_N} & \ldots & e^{iq_{N+1} y_N} \\ 1 & \ldots & 1 \end{vmatrix}, \qquad g \to \infty \tag{3.47}$$

in the domain $0 \le y_j \le L$.

It is worth mentioning that the function f_Q remains far from trivial even in the $g \to \infty$ limit, despite the seemingly "free-fermion" form of the expressions (3.43) and (3.47). This is because each plane wave, $e^{ik_j y}$, still does not satisfy periodic boundary conditions, that is, $e^{ik_j L} \neq 1$.

It is important to keep in mind that the function (3.43) is defined in the domain $0 \le y_j \le L$ (which means that the gas particles are positioned to the right of the impurity). Let us now extend the definition to the case where some particles are placed to the left of the impurity, that is, we tackle the domain $-L \le y_j \le L$ by defining the function extension as $\tilde{f}_Q$. We require periodicity of $\tilde{f}_Q$ on a ring of circumference L:

$$\tilde{f}_Q(y_1, \ldots, y_j - L, \ldots, y_N) = \tilde{f}_Q(y_1, \ldots, y_j, \ldots, y_N), \quad j = 1, \ldots, N. \tag{3.48}$$

Having Eq. (3.43) and using Eq. (3.48) we propose

$$\tilde{f}_Q(y_1,\ldots,y_N)=\frac{\tilde{Y}e^{-i\frac{\mu}{2}\prod_{j=1}^{N}\mathrm{sgn}(y_j)}}{\sqrt{N!L^N}}\begin{vmatrix} e^{ik_1y_1} & \ldots & e^{ik_{N+1}y_1}\\ \vdots & \ddots & \vdots \\ e^{ik_1y_N} & \ldots & e^{ik_{N+1}y_N}\\ 1 & \ldots & 1\end{vmatrix},\qquad g\to\infty. \tag{3.49}$$

It is the factor containing the sign functions that ensures the validity of Eq. (3.49) in the whole domain $-L\le y_j\le L$. Coming back to the laboratory frame we get for this wavefunction

$$\Psi_Q(x_\downarrow,x_1,\ldots,x_N)=\frac{\tilde{Y}e^{-i\frac{\mu}{2}\prod_{j=1}^{N}\mathrm{sgn}(x_j-x_\downarrow)}}{\sqrt{N!L^N}}\times\begin{vmatrix} e^{ik_1x_1} & \ldots & e^{ik_{N+1}x_1}\\ \vdots & \ddots & \vdots \\ e^{ik_1x_N} & \ldots & e^{ik_{N+1}x_N}\\ e^{ik_1x_\downarrow} & \ldots & e^{ik_{N+1}x_\downarrow}\end{vmatrix},\qquad g\to\infty. \tag{3.50}$$

valid in the domain $-L/2\le x_j\le L/2$, $j=1,\ldots,N,\downarrow$. Recall that Eqs. (3.49) and (3.50) are connected by the transformation (3.31). The function (3.50) is antisymmetric with respect to any permutation of the host particles.

At this point, let us summarize our knowledge about the wavefunctions and about the spectrum in the $g\to\infty$ limit. Equation (3.50) is a Slater determinant. This way, the impurity problem at infinite repulsion behaves just as the free fermion one. Indeed, if any two of the coordinates from the set $x_1,\ldots,x_N,x_\downarrow$ take the same value, the determinant vanishes regardless of the values of the quasi-momenta $k_1,\ldots,k_{N+1}$. This is how fermions should behave. The function (3.50) is antisymmetric with respect to any permutation of the host particles. What is really amazing about Eq. (3.50) is its periodicity, that is, Ψ takes the same values at $x_j=-L/2$ and $x_j=L/2$, $j=1,\ldots,N,\downarrow$ in the case of $k_1,\ldots,k_{N+1}$ quantized according to the Bethe equations (3.44) and (3.38), despite the fact that each plane wave is not periodic in this interval, $e^{ik_jL}=e^{i\mu}$. We now reformulate the problem in the language of the second quantization.

Anyon-fermion mapping of the $g\to\infty$ problem and second quantization

The parameter μ is related to the total momentum $\hbar Q$ as $Q=k_{\mathrm{F}}(1+\frac{\mu}{\pi})$. The wavefunction for each value of μ can be written in the second-quantized form as follows

$$|\Psi_Q\rangle=\frac{1}{\sqrt{N!}}\int_0^L dx_\downarrow dx_1\cdots dx_N\Psi_Q(x_\downarrow,x_1,\ldots,x_N)\psi_{\mathrm{A}}^\dagger(x_\downarrow)\psi^\dagger(x_1)\cdots\psi^\dagger(x_N)|0\rangle. \tag{3.51}$$

Here, ψ is the fermion destruction operator and ψ_{A} behaves as an impenetrable anyon with respect to ψ,

$$\psi_{\mathrm{A}}(x_\downarrow)\psi(x)-e^{-i(\mu+\pi)\mathrm{sgn}(x_\downarrow-x)}\psi(x)\psi_{\mathrm{A}}(x_\downarrow)=0, \tag{3.52}$$

while the host particles behave with respect to each other as free fermions. The impurity-host exchange phase is zero for Q=0 and π for $Q=k_{\mathrm{F}}$ as anticipated in the main text. Note that the momentum distribution of the impurity $n_\downarrow(k)$ is the same whether the host particles are free fermions or a TG gas and $n_\downarrow(k)$ can be expressed through a correlation function of 1D impenetrable anyons [296].

3.7.4 Anyon-Hubbard model in a nutshell

In this section, we briefly review the properties of the above-mentioned anyon-Hubbard model, which is a paradigmatic model to describe anyons in 1D lattices [270, 284],

$$\hat{H}_{\mathrm{AHM}} = -J\sum_{\ell}\left(\hat{a}_{\ell}^{\dagger}\hat{a}_{\ell+1} + h.c.\right) + \frac{U}{2}\sum_{\ell}\hat{n}_{\ell}\left(\hat{n}_{\ell}-1\right), \tag{3.53}$$

where J and U denote the tunneling amplitude and the on-site interaction between anyons, respectively, and $\hat{n}_{\ell} = \hat{a}_{\ell}^{\dagger}\hat{a}_{\ell}$ is the number operator at site ℓ. The *anyonic* operators $\hat{a}_{\ell}$ obey the generalized commutation relations

$$\hat{a}_j^{\dagger}\hat{a}_k - e^{-i\theta\mathrm{sgn}(j-k)}\hat{a}_k^{\dagger}\hat{a}_j = \delta_{jk}, \quad \hat{a}_j\hat{a}_k - e^{-i\theta\mathrm{sgn}(j-k)}\hat{a}_k\hat{a}_j = 0. \tag{3.54}$$

The above relations can be obtained by means of a fractional version of the Jordan-Wigner transformation, i.e., via the anyon-boson mapping

$$\hat{a}_{\ell} = \hat{b}_{\ell}e^{i\theta N_{\ell}}, \quad \hat{N}_{\ell} = \sum_{j=1}^{\ell-1}\hat{n}_j, \tag{3.55}$$

where $\hat{b}_{\ell}$ are bosonic operators and obey the bosonic commutation relation $[\hat{b}_j, \hat{b}_k^{\dagger}] = \delta_{jk}, [\hat{b}_j, \hat{b}_k] = 0 = [\hat{b}_j^{\dagger}, \hat{b}_k^{\dagger}]$. Note that the above transformation gives the same number operators, i.e., $\hat{n}_{\ell} = \hat{a}_{\ell}^{\dagger}\hat{a}_{\ell} = \hat{b}_{\ell}^{\dagger}\hat{b}_{\ell}$.

Combining the anyon-boson mapping (3.55) with Eq. (3.53), the anyon-Hubbard Hamiltonian can be expressed in terms of bosonic operators as

$$\hat{H}_{\mathrm{AHM}}^{\mathrm{B}} = -J\sum_{\ell}\left(\hat{b}_{\ell}^{\dagger}\hat{b}_{\ell+1}e^{i\theta\hat{n}_{\ell}} + h.c.\right) + \frac{U}{2}\sum_{\ell}\hat{n}_{\ell}\left(\hat{n}_{\ell}-1\right). \tag{3.56}$$

Here, we will be interested in the quasi-momentum distribution. One has to distinguish the quasi-momentum distribution in terms of bosonic operators from that using anyonic operators,

$$\langle\hat{n}_k^{\mathrm{b}}\rangle = \frac{1}{L}\sum_{\ell\ell'}e^{ik(\ell-\ell')}\langle\hat{b}_{\ell}^{\dagger}\hat{b}_{\ell'}\rangle, \tag{3.57}$$

$$\langle\hat{n}_k^{\mathrm{a}}\rangle = \frac{1}{L}\sum_{\ell\ell'}e^{ik(\ell-\ell')}\langle\hat{a}_{\ell}^{\dagger}\hat{a}_{\ell'}\rangle. \tag{3.58}$$

In the hardcore limit, the bosonic Hamiltonian (3.56) will be independent of the statistical angle θ, i.e.,

$$\hat{H}_{\mathrm{AHM}}^{\mathrm{B}} \overset{U\to\infty}{\longrightarrow} \hat{H}_{\mathrm{AHM}}^{\mathrm{B}} = -J\sum_{\ell}\left(\hat{b}_{\ell}^{\dagger}\hat{b}_{\ell+1} + h.c.\right). \tag{3.59}$$

Thus, computing the quasi momentum of bosons $\langle\hat{n}_k^{\mathrm{b}}\rangle$ would give a θ-independent quasi-momentum distribution [270].

However, the anyonic nature can be revealed by computing the anyonic quasi-momentum distribution $\langle\hat{n}_k^{\mathrm{a}}\rangle$, because the anyonic correlation $\langle\hat{a}_{\ell}^{\dagger}\hat{a}_{\ell'}\rangle$ are modified

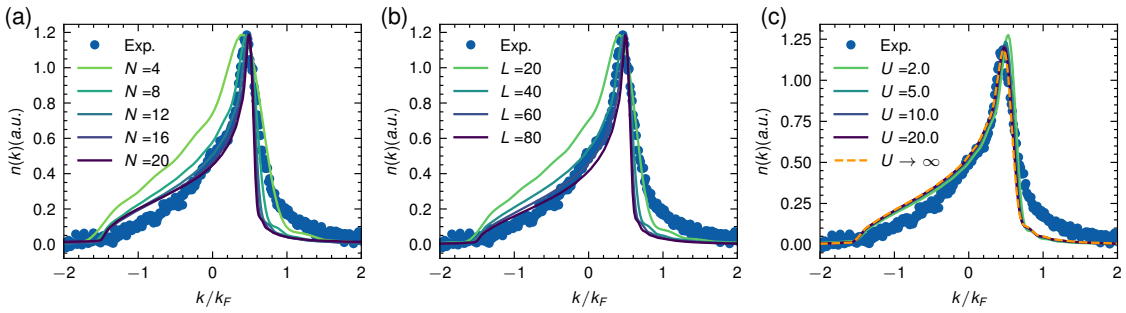

Figure 3.6: **Benchmarking the experimental data by the AHM.** (a) Effect of total host particle number at $L = 40$ and $U \to \infty$. (b) Effect of the system size at filling 1/4 at $U \to \infty$. (c) Effect of the on-site interaction U at $L = 40, N = 10$. The blue dots are the experimental data for $\theta/\pi = 0.53(2)$; the solid lines are the prediction from the AHM. Note that in (a,b), the peak has been rescaled to match the amplitude of the experimental data.

by the Jordan-Wigner transformation. To clarify this, we can explicitly write the anyonic correlation as

$$\langle \hat{a}_\ell^\dagger \hat{a}_{\ell'} \rangle = \langle \hat{b}_\ell^\dagger e^{i\theta(\hat{N}_{\ell'} - \hat{N}_\ell)} \hat{b}_{\ell'} \rangle = \begin{cases} \langle \hat{b}_\ell^\dagger \hat{b}_{\ell'} e^{i\theta(\hat{N}_{\ell'} - \hat{N}_\ell)} \rangle, & \ell' \geq \ell \\ \langle \hat{b}_\ell^\dagger \hat{b}_{\ell'} e^{i\theta(\hat{N}_{\ell'} - \hat{N}_\ell + 1)} \rangle, & \ell' < \ell. \end{cases} \tag{3.60}$$

Here, $\langle \bullet \rangle \equiv \langle \Psi | \bullet | \Psi \rangle$ represents the expectation value with respect to the ground state $|\Psi\rangle$ of the Hamiltonian (3.56), which can be expressed in the Fock state basis $\{|\psi_i\rangle\}$ as

$$|\Psi\rangle = \sum_j c_j |\psi_j\rangle, \qquad |\psi_j\rangle = |n_1^j, n_2^j, \cdots, n_L^j\rangle \tag{3.61}$$

with complex coefficients c_i, $n_\ell^i = \{0, 1\}$ in the hard-core limit, and L being the total site number of the chain. In this case, the above anyonic correlation (3.60) can be rewritten as

$$\langle \hat{a}_\ell^\dagger \hat{a}_{\ell'} \rangle = \begin{cases} \sum_{i,j} c_i^* c_j \langle \psi_i | \hat{b}_\ell^\dagger \hat{b}_{\ell'} | \psi_j \rangle e^{i\theta(N_{\ell'}^j - N_\ell^j)}, & \ell' \geq \ell, \\ \sum_{i,j} c_i^* c_j \langle \psi_i | \hat{b}_\ell^\dagger \hat{b}_{\ell'} | \psi_j \rangle e^{-i\theta(N_\ell^j - N_{\ell'}^j - 1)}, & \ell' < \ell. \end{cases} \tag{3.62}$$

with $N_\ell^j = \sum_j$. Here, the (N-dependent) phase factors in Eq. (3.60) and (3.62) are attributed to the contribution from the Jordan-Wigner transformation, which transfers the bosonic correlation $\langle \hat{b}_\ell^\dagger \hat{b}_{\ell'} \rangle$ to be the anyonic one $\langle \hat{a}_\ell^\dagger \hat{a}_{\ell'} \rangle$.

To benchmark the anyonic correlations from the AHM with the experiment, we consider the experimental impurity momentum distribution at $\theta/\pi = 0.53(2)$ as an example. As shown in Fig. 3.6, the agreement between the experimental data and the anyonic momentum distribution obtained from the AHM improves for large system sizes and low filling.

3.7.5 Ground-state properties of the swap model $\hat{H}_{\text{Swap}}$

Next, we investigate the effect of various system parameters of the swap model, specifically the number of host particles $N_\uparrow$, the length of the system chain L,

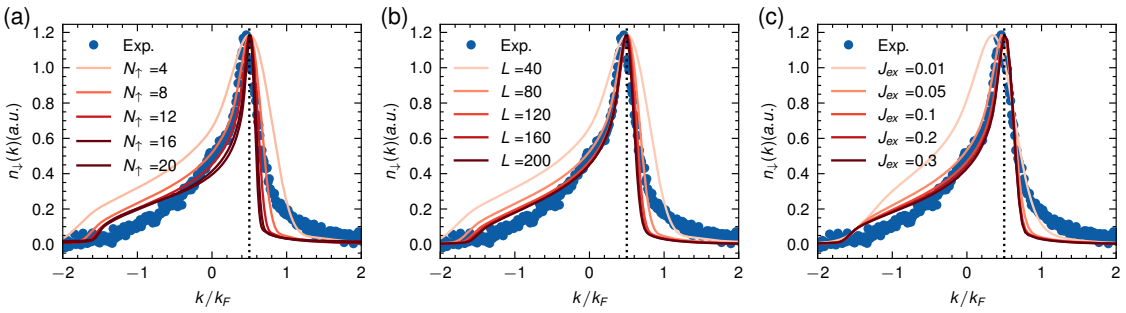

Figure 3.7: **Effect of different system parameters of the swap model.** (a) Quasi-momentum distribution for the impurity for varying number of host particles $N_\uparrow$ with $J_{\rm ex} = 0.1, L = 40$; (b) Quasi-momentum distribution of impurity for varying system size L with $J_{\rm ex} = 0.1, N_\uparrow/L = 0.1$; (c) Quasi-momentum distribution of impurity for varying $J_{\rm ex}$ with $N_\uparrow = 12, L = 120$. The black dotted lines in (a-c) show the location of the peak, which is given by $k_{\rm peak}/k_{\rm F} = \theta/\pi$. Note that the peak has been rescaled according to the experimental data.

and the swapping strength $J_{\rm ex}$. As shown in Fig. 3.7, changes in these parameters lead to similar behavior, in the sense that larger values give rise to a narrower quasi-momentum distribution (less uncertainty in momentum space). Note that the height of the theoretical quasi-momentum distribution results are rescaled by the experimental data.

Now we fix the system length to $L = 120$, and tune the parameters $J_{\rm ex}$ and $N_\uparrow$. By computing the residuals $\delta = \sum_i |y_i - f(x_i)|$ between experimental data y_i and the model $f(x_i)$, one can see that low values of δ appear in a wide parameter regime, as shown in Fig. 3.8(b). Similar results can be obtained by using either low filling (e.g. $n = 0.1$) with $J_{\rm ex} = 0.1$ or higher filling (e.g. $n = 0.25$) but lower $J_{\rm ex} = 0.02$, see Fig. 3.8(a). This trend indicates that in the thermodynamic limit ($N_\uparrow \to \infty$), the optimal value of $J_{\rm ex}$ would tend to 0. The behavior of anyionization in a finite system with open boundary conditions is well captured by using a finite $J_{\rm ex}$ in our swap model.

3.7.6 Dynamical evolution governed by $\hat{H}_{\rm sBHM}$

As mentioned in the main text, a strong host-impurity interaction and a weak force are necessary to achieve anyonization in our system. In the following, we present simulations for which we relax these requirements. We simulate the dynamical evolution by solving the time-dependent Schrödinger equation associated with the spinful Bose-Hubbard Hamiltonian (sBHM). For this simulation, the initial state of the impurity is set to the ground state of $\hat{H}_{\rm sBHM} + \frac{V}{2}\sum_\ell \ell^2 \hat{n}_{\downarrow\ell}$, where V quantifies the strength of the impurity harmonic trapping. For weak interactions, the impurity hardly feels the presence of the host particles and drifts away, see the spatio-temporal distribution of the impurity shown in Fig. 3.9(a). As a result, the quasi-momentum of the impurity is simply shifted from the initial state, in Fig. 3.9(d) to the final state in Fig. 3.9(e). In contrast, in the strongly-interacting regime, the impurity hardly moves, i.e., the density is not affected, see Fig. 3.9(b). The asymmetry in the momentum distribution survives in a wide range of values for the impurity-bath interaction U, which suggests the robustness of the protocol. As the spin wave is a

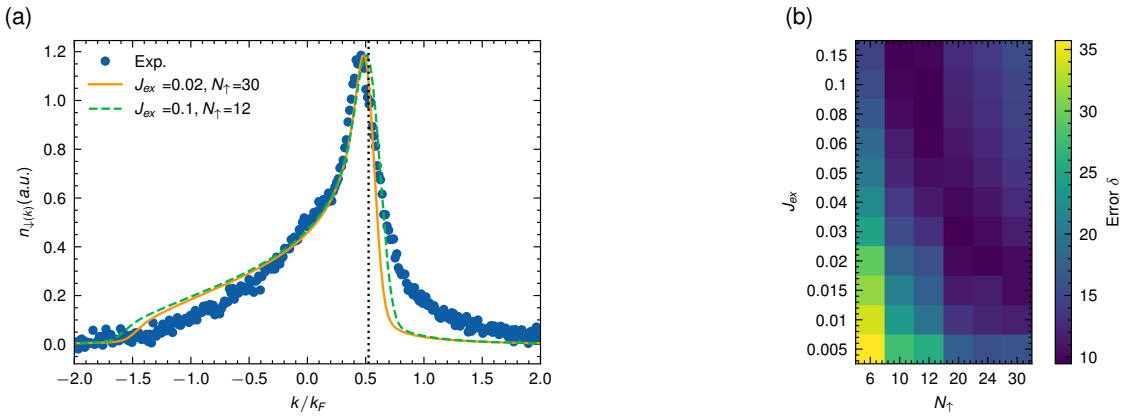

Figure 3.8: **Comparison between experiment and the predictions of the swap model for different values of J_{ex} and $N_\uparrow$.** (a) Comparison between experimental data (blue dots) and the quasi-momentum distribution obtained by using the swap model for optimal values of the parameters. (b) Residuals between the data and the model as a function of J_{ex} and $N_\uparrow$.

low energy excitation, the force should remain weak to properly prepare it. Indeed, as shown in Fig. 3.9(c), applying a strong force will result in Bloch oscillations of the impurity [45]. In Fig. 3.9(f) we see that the force $F_\downarrow a/J$ needs to be kept significantly smaller than 1 to properly reproduce the momentum distribution data.

We next investigate the effect of the impurity's initial density distribution by subjecting it to a hard-wall confinement of width W (in unit of lattice constant a). Namely, we start with the ground state of the sBHM with an initial hard-wall potential felt only by the impurity and using different values for W. The confinement is then removed for $t \geq 0$. For $W = 1$, which corresponds to the impurity initially localized at a single site, i.e., a single Wannier state, the spatial density distribution of the impurity shown in Fig. 3.10(a) exhibits a decaying breathing pattern. In this case, it is difficult to observe a consistent anyonic feature. For large values of W, the impurity has a broad spatial distribution (see Fig. 3.10(c)), which thus allows for a proper generation of a spin wave, and the quasi-momentum distribution gets closer to the experimental data; see Fig. 3.10(d,e). Note that for a long chain ($L = 120$) and wide enough initial hard-wall potentials, the time-evolved quasi-momentum distribution agrees with the experimental data, see Fig. 3.10(e). For a shorter chain ($L = 40$), as shown in Fig. 3.10(e), using a higher host particle density gives rise to similar results.

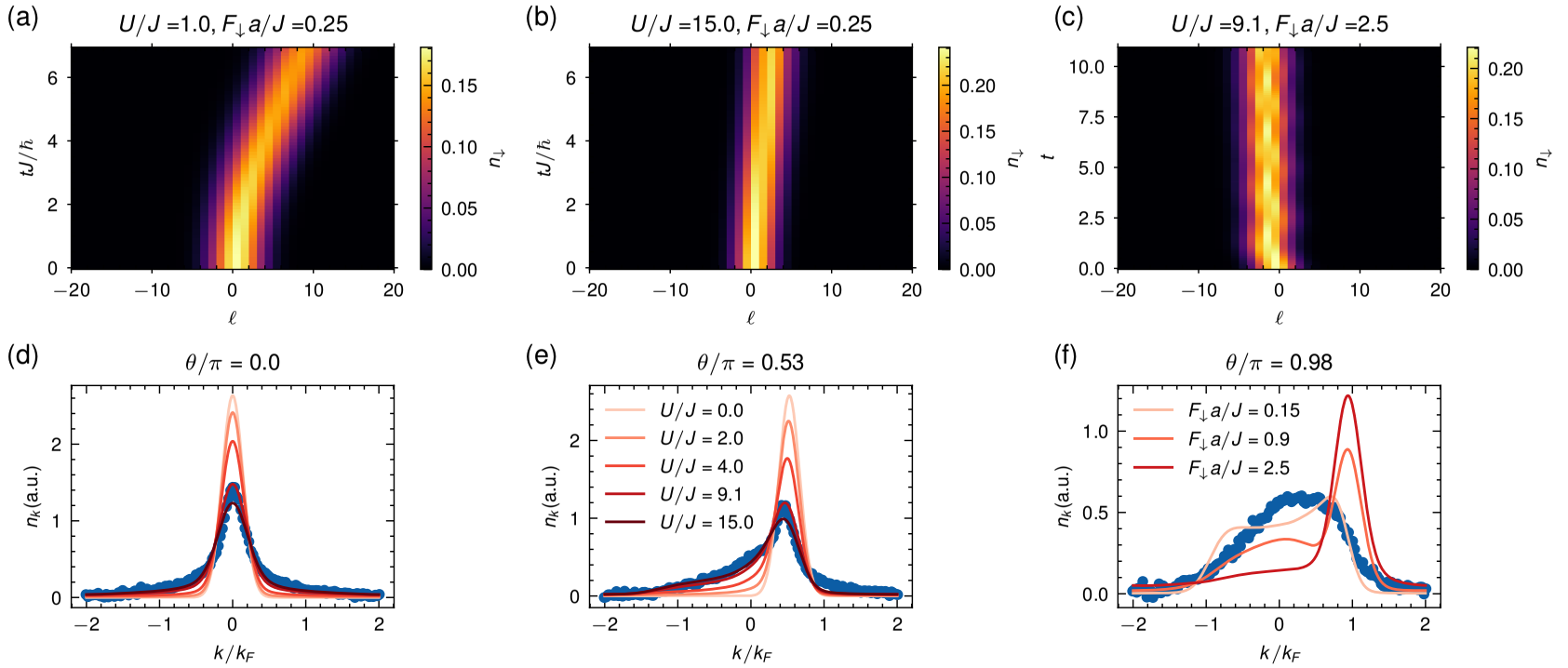

Figure 3.9: **Effect of the impurity-host interaction U and applied force $F_\downarrow$ as calculated from the sBHM.** (a-c) Spatio-temporal density distribution of the impurity as a function of time for (a) $U/J = 1, F_\downarrow a/J = 0.25$, (b) $U/J = 15, F_\downarrow a/J = 0.25$ and (c) $U/J = 9.1, F_\downarrow a/J = 2.5$. Effect of the impurity-bath interaction in the quasi-momentum distribution of the impurity at (d) $\theta = 0$, (e) $\theta = 0.53\pi$ The same legend applies for (d) and (e). (f) Effect of the force on the quasi-momentum distribution of the impurity at $\theta = 0.98\pi$. Blue dots are experimental data from Fig.2 in the main text and the solid lines are the numerical results. Other parameters are $N_\uparrow = 20, L = 40$ and the initial state is chosen as the ground state of the sBHM with harmonic trap $V/J = 0.02$ applied to the impurity.

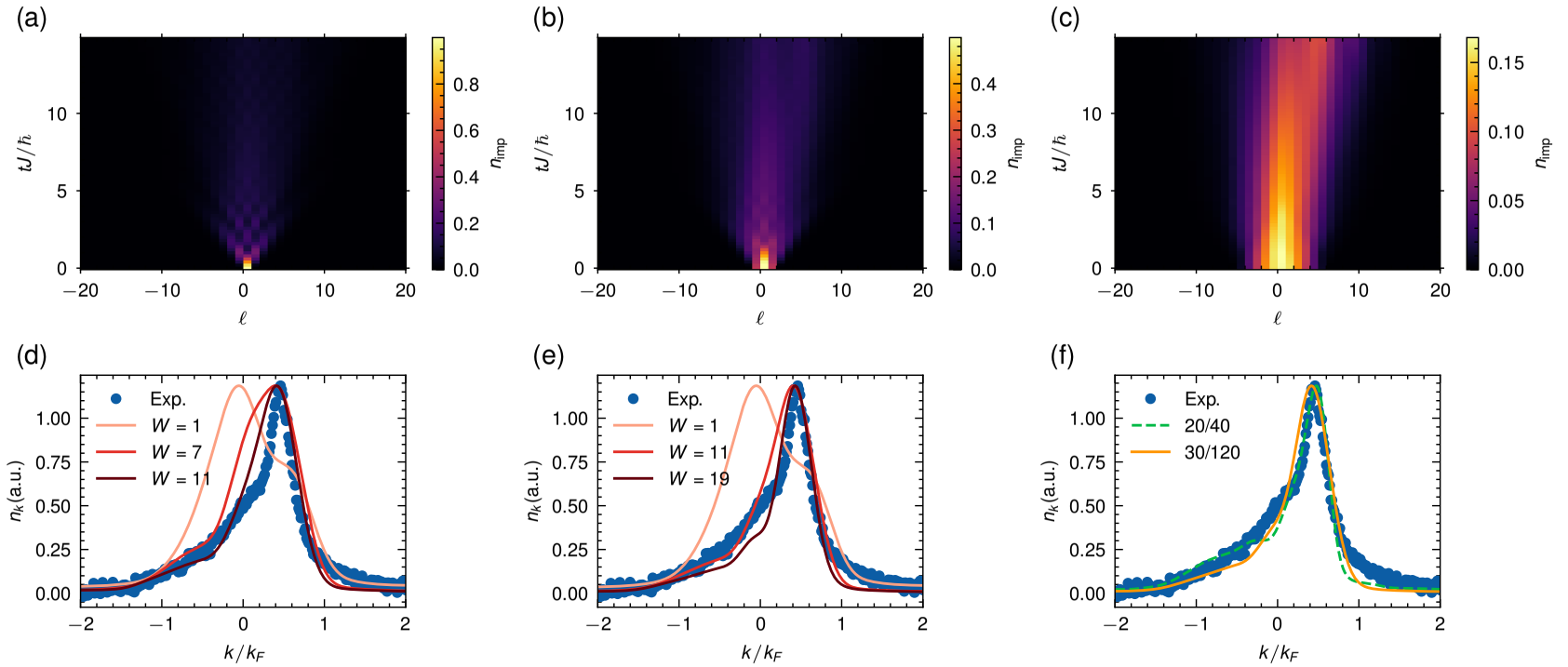

Figure 3.10: **Effect of the initial density distribution of the impurity determined by a hard-wall confinement.** (a-c) Spatio-temporal density distribution of the impurity for various values of the hard-wall width (a) $W=1$, (b) $W=3$ and (c) $W=11$ in the case of $N_\uparrow=10$ and $L=40$. (d) Comparison of quasi-momentum distribution between the experimental data (blue dots) and the results obtained by using the sBHM (solid lines) for various values for W. (e) Same as (d), but using $N_\uparrow=30$ and $L=120$. (f) Comparison of the quasi-momentum distribution between experimental data (blue dots) and the results obtained from the dynamical evolution governed by the sBHM. The analysis suggests that a decrease in system length can be compensated by considering a larger number of host particles. The other parameters are set to $U/J=4.55$ and $F_\downarrow a/J=0.03125$. Note that in (d-f) the peak has been rescaled according to the experimental data.

CHAPTER 4

PUBLICATION III

Observing dissipationless transport of a correlated quantum state of an impurity in a strongly-interacting Bose gas

Milena Horvath[1,*], Sudipta Dhar[1,*], Elisabeth Wybo[2,3], Dimitrios Trypogeorgos[4] Yanliang Guo[1], Mikhail Zvonarev[5], Michael Knap[2,3], Manuele Landini[1] and Hanns-Christoph Nägerl[1]

[1]*Institut für Experimentalphysik und Zentrum für Quantenphysik, Universität Innsbruck, Technikerstraße 25, Innsbruck, 6020, Austria*
[2] *Technical University of Munich, TUM School of Natural Sciences, Physics Department, 85748 Garching, Germany*
[3]*Munich Center for Quantum Science and Technology (MCQST), Schellingstr. 4, 80799 München, Germany*
[4]*Institute of Nanotechnology, Consiglio Nazionale delle Ricerche (CNR-Nanotech), via Monteroni 165, 73100, Lecce, Italy*
[5]*Université Paris-Saclay, CNRS, LPTMS, 91405, Orsay, France*
[*]These authors contributed equally to this work

The frictionless motion of an obstacle through a fluid medium is commonly viewed as a hallmark of superfluidity. Landau's seminal insight into superfluidity provided a microscopic criterion for this dissipationless transport. According to Landau, kinematic constraints prohibit superfluid behavior in one-dimensional (1D) Bose gases. Here using ultracold atoms, we show how a microscopic impurity can propagate through a strongly interacting Bose gas without any friction at odds with Landau's paradigm. Fast and precise control of interactions between atoms allows us to prepare the impurity with initial velocity ranging from subsonic to supersonic regimes and subsequently track the non-equilibrium dynamics of the system generated by an interaction quench. We find that the injected impurity

never comes to a full stop, at odds with conventional expectations of relaxation. Instead, the impurity forms a strongly correlated state with the quantum liquid and reaches a steady state that propagates at a reduced velocity. We further measure the full momentum distribution of the impurity and extract the timescale associated with momentum transfer from the impurity to its environment as a function of initial velocity of the impurity and interaction strength with the many-body bath. In particular, for strong interactions, we find that a supersonic impurity relaxes within Fermi time whereas for subsonic impurities the relaxation time is inversely proportional to its velocity. Our findings demonstrate the emergence of long-lived entangled quasiparticle states and provide key insights into transport and coherence in low-dimensional quantum fluids.

4.1 Introduction

Classical mechanics tells us that an impurity moving through a fluid medium experiences friction arising from countless microscopic collisions with surrounding particles. Each collision transfers energy and momentum away from the impurity, creating a dissipative force [321] that brings the moving impurity to a complete stop. This classical picture of ever-present multiple collisions suggests that a friction force always acts on the impurity in the case of its directed motion. The advent of quantum mechanics introduced a radical departure from this view. The phenomenon of superfluidity, first observed in helium-4 illustrates how quantum fluids can behave collectively in such a way that dissipation can vanish entirely [322, 323].

In 1941, Landau's seminal insight into superfluidity provided a microscopic criterion for this dissipationless transport [324]. A way to understand the superfluidity phenomenon is to regard all particles of a quantum fluid as an entity responding collectively to the motion of an external object through it. The dispersion [58], which is the relation between the energy and momentum of the excitations of this entity, could be such that the object moving with a velocity v below some non-zero critical value v_c cannot excite them at all, otherwise total energy and momentum conservation laws are violated. The condition $v < v_c$ deduced in this way is Landau's criterion for superfluidity. Over the past eight decades, this criterion has underpinned our understanding of superfluidity, guiding both theoretical developments [74] and experimental tests ranging from vortex nucleation [27, 325–327] to drag measurements [328, 329] in ultracold quantum gases. Landau's criterion assumes that the object is sufficiently massive to be treated classically, essentially as a macroscopic obstacle whose dynamics is largely decoupled from the quantum nature of the medium. When applied to interacting one-dimensional (1D) Bose gases, the critical velocity $v_c = 0$. That is, according to Landau, any macroscopic object moving through a 1D Bose gas should ultimately come to rest [330].

In this work, we show that this conclusion does not hold when the object is no longer macroscopic but instead a microscopic quantum impurity. Here, recoil due to interactions with the background gas can not be neglected, yielding novel physics beyond the kinematic picture [331–333]. The quantum flutter phenomena provides one such example where a finite-mass impurity forms an entangled state propagating through a many-body system and remaining coherent for long times [189, 190]. Experiments with ultracold atoms have served as a powerful platform for studying impurity physics [198], ranging from the observation of Fermi [334–336] and Bose

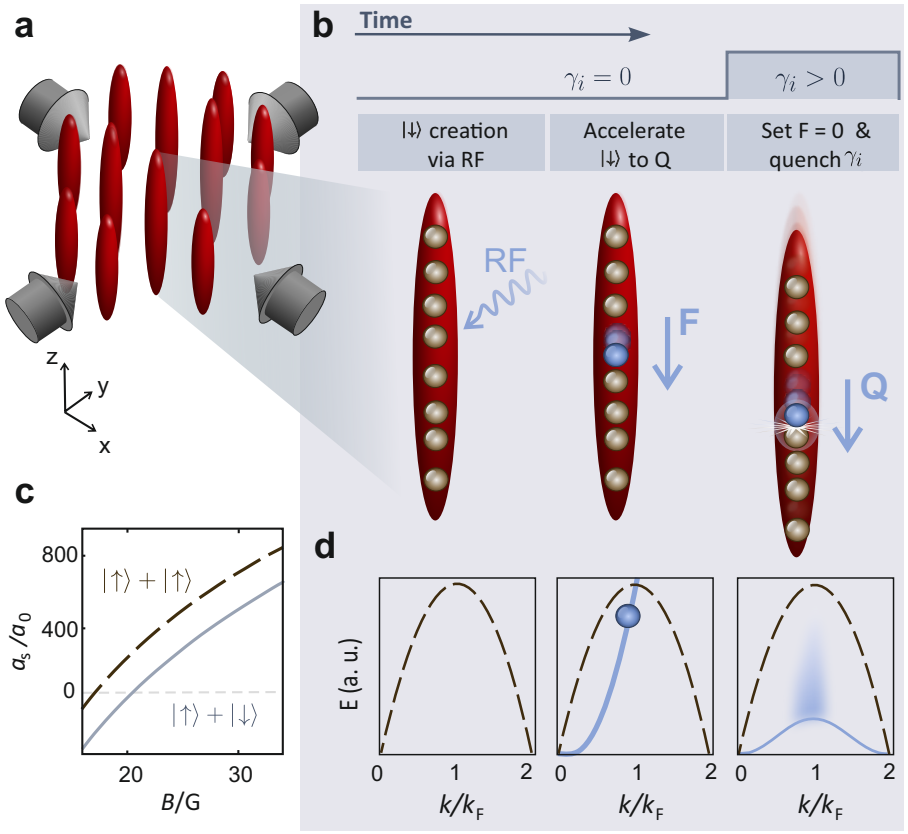

Figure 4.1: **Experimental procedure.** **a**, Experimental realization of an array of 1D Bose gases in tubes formed by two retro-reflected laser beams. **b**, Pictorial representation of the experimental sequence. Top panel: Interaction strength γ_i throughout the experimental sequence. Middle panel: On average one impurity particle (blue sphere) per tube is created from a strongly correlated host gas (brown spheres) via a radio-frequency pulse. The impurity initially does not interact with the host gas. After its creation the impurity is accelerated to the desired momentum Q. Subsequently the entire system is dropped and the interactions between the impurity and the host are turned on. **c**, Magnetic field dependence of the scattering length a_s for collisions between atoms in the host gas (dashed line) and between impurity and host atoms (solid line) [320]. **d**, Edge of the excitation spectrum of a 1D Bose gas without impurity - plasmon branch (dashed line) and with one impurity - magnon branch (solid line). For both cases, it is a $2k_F$ periodic function of the total momentum of the system $\hbar k$. The blue parabola corresponds to the energy-momentum relation of a single non-interacting impurity.

polarons [337, 338] to the study of polaron spectrum and the non-equilibrium dynamics of impurities [45, 339, 340]. Despite these recent progress, the experimental realization of a moving polaron is still lacking.

Here, using ultracold Cs atoms, we investigate the dynamics of an equal-mass impurity injected with a constant velocity into a strongly interacting 1D Bose gas. Taking advantage of the tunability of interactions offered by Cs, we prepare the impurity with initial velocities ranging from subsonic to supersonic regimes. Initially, the impurity is non-interacting with the surrounding many-body bath. Subsequently, we quench the interaction between the impurity and the many-body bath

to the strongly interacting and repulsive regime and study the relaxation dynamics of the system. Our main observations are twofold. First, we look at the dependence of the relaxation time-scale on the initial velocity of the impurity as well as on the interaction strength between the impurity and host. Our results show different relaxation mechanisms depending on whether the injected impurity was subsonic or supersonic. While for the subsonic case, we find that the momentum transfer from the impurity to the host strongly depends on the initial velocity of the impurity, for the supersonic case, we find that the relaxation occurs within the Fermi time, the fastest possible collective response time of the many-body system. Second, we find that in the long-time limit the impurity never comes to a full stop, at odds with conventional expectations of relaxation. Instead, the impurity forms a strongly correlated state with the quantum liquid and reaches a steady state that propagates at a reduced velocity. For small initial momentum, this correlated state can be interpreted as a moving Bose polaron. However, for impurity injected with momentum above the Fermi momentum, the polaron picture breaks down, and our experiment qualitatively agrees with the phenomenon of quantum flutter [189].

We consider strongly interacting 1D bosons, prepared in an array of tubes formed by a pair of retro-reflected laser beams (see Fig. 4.1**a**). Each of the individual 1D systems represents atoms that interact through a local repulsive potential whose strength is characterized by a dimensionless parameter γ [132]. Experiments in strong interaction regime, $\gamma \gg 1$, demonstrate transmutation of quantum statistics [17, 229, 341]: The excitation spectrum of the system becomes identical to that of the polarized Fermi gas [342]. The time scale governing interparticle collisions is thus determined by the Fermi time, $t_{\mathrm{F}} = 2m/(\hbar k_{\mathrm{F}}^2)$, where $k_F = \pi n_{1\mathrm{D}}$ is the Fermi wave-vector and $n_{1\mathrm{D}}$ is the 1D density. The excitations of the host gas are referred to as the plasmons, and the impurity of mass m interacting with the gas through a repulsive local potential of strength γ_i leads to a magnon-like branch of the excitation spectrum (see Fig. 4.1**d**, and Supplementary materials for detail).

4.2 Experimental procedure

We start the experiment by adiabatically loading an optically trapped, interaction-tunable Cs BEC [234] into an array of vertically oriented 1D tubes formed by a 2D optical lattice as illustrated in Fig. 4.1**a**. The atoms are initially in the magnetic hyperfine sublevel $(F, m_{\mathrm{F}}) = (3, 3)$ and they are levitated against gravity by means of a magnetic field gradient of $|\nabla B_z| \approx 31.1$ G/cm along the vertical direction. With about 1.5×10^5 atoms in the initial BEC, we fill approximately 5700 tubes with an average filling of 39 atoms per tube (see Supplementary materials). The offset magnetic field B_z is initially set to $B_z = 20.6(1)$ G, at which $a_s = 199(4)$ a_0, see Fig. 4.1**c**. With a 1D density of $n_{1\mathrm{D}} = 1.6(1)/\mu$m, this gives $\gamma = 2.5(2)$ in view of some weak harmonic trapping along the tube direction with a trap frequency of 17.0(1) Hz. The average Fermi time is $t_{\mathrm{F}} = 166$ μs. The impurity particles are created by transferring on average one atom per tube to the sublevel $(3, 2)$ by means of a short, 20-μs radio-frequency (RF) pulse (see Supplementary materials). The atoms in $(3, 3)$, constituting the majority fraction, now serve in each tube as the background host gas in which the impurity atoms move about. Initially, at $B_z = 20.6(1)$ G, the impurity-host interactions are zero (see Fig. 4.1**c**) making the host gas transparent for the impurity with $\gamma_i = 0$. Immediately after their creation, the impurity particles,

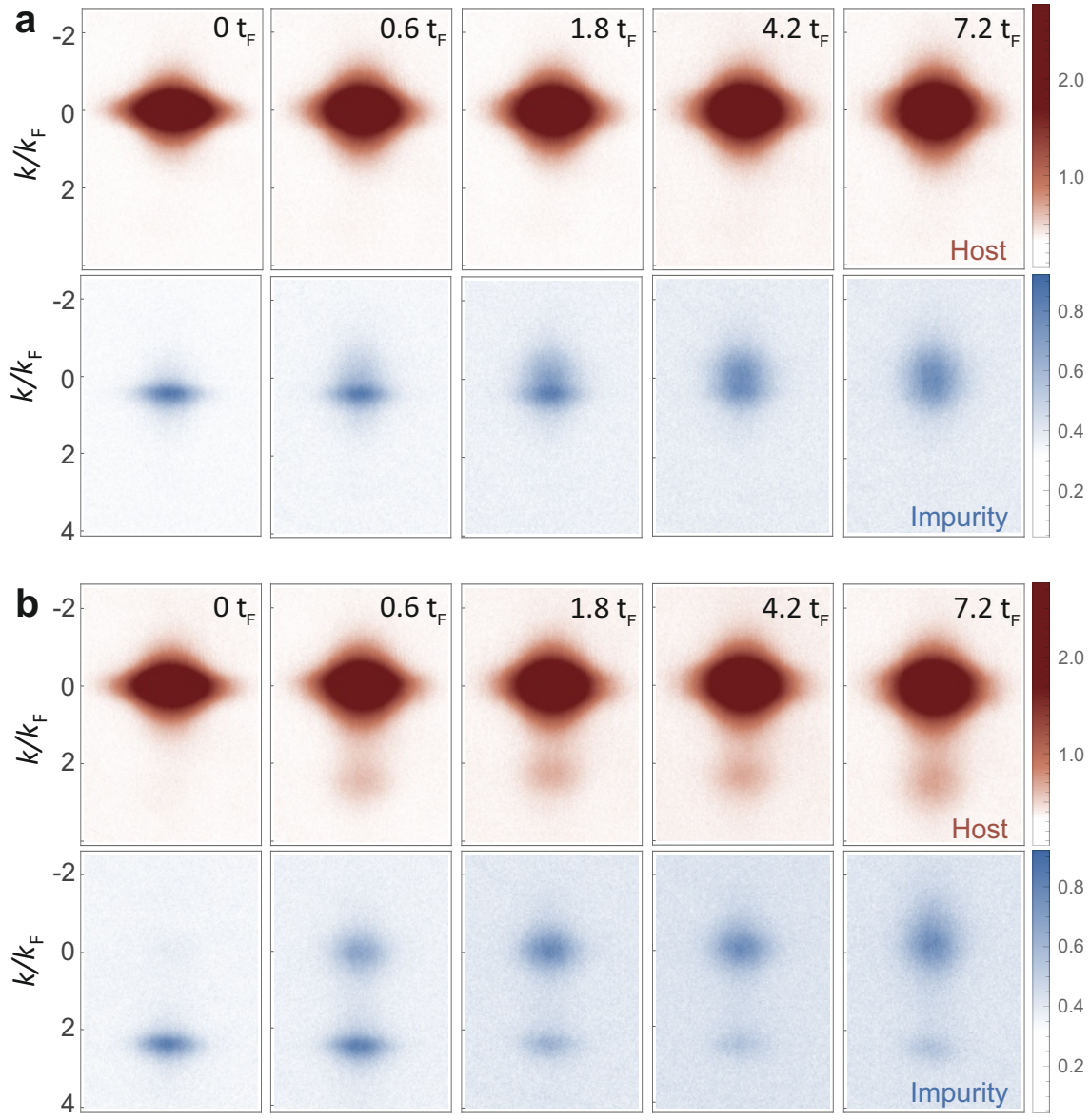

Figure 4.2: **Subsonic versus supersonic dynamics.** Example experimental absorption images of host (top panel, red) and impurity (bottom panel, blue) during the relaxation process. The interaction strengths after quench are $(\gamma_i, \gamma) = (2.6(3), 5.9(3))$. The evolution time $t = 0$ to $t = 7.2\ t_{\mathrm{F}}$ is indicated on the top right hand corner of the host images. Each image is an average of 10 experimental realizations. The vertical axis in each image is converted in momentum scale. **a**, Initial impurity momentum in subsonic regime $\hbar Q = 0.4\ \hbar k_{\mathrm{F}}$. **b**, supersonic case $\hbar Q = 2.3\ \hbar k_{\mathrm{F}}$.

given their lower magnetic moment, are accelerated by 1/3 of the gravitational force. When the impurities have reached the desired mean momentum $\hbar Q$, i.e., after about 0.70 ms for $Q = k_{\mathrm{F}}$, the levitation field is switched off, releasing the host gas and the impurities into free fall inside their respective 1D tubes. Simultaneously, within 50 μs, the impurity-host interaction strength γ_i is set to the desired value, in the range of 0 to 20 with a precision of 2. The system is subsequently evolved for times t up to 12 t_{F}. Note that these times are much shorter than the time scale associated with

the longitudinal harmonic trapping. The host and the impurity particles are finally imaged simultaneously after release into 3D and 20-ms levitated time-of-flight (tof). For a faithful measurement of the impurities' momentum distribution the impurity-host interactions γ_i are switched back to zero. The presence of the levitation field during tof separates the host and the impurity particles.

4.3 Supersonic vs. subsonic impurity

Typical absorption images of the relaxation process are shown in Fig. 4.2 for the case of $Q < k_\mathrm{F}$ and $Q > k_\mathrm{F}$. For the former, both the impurity and host distributions remain singly peaked and broaden throughout the evolution. In contrast, for $Q > k_\mathrm{F}$, two distinct momentum peaks emerge in both distributions within t_F. For the impurity this second distribution appears near $Q = 0$, while for the host it emerges around $Q \approx 2.3\ k_\mathrm{F}$. Moreover, we find that the particle numbers in these distributions are equal. Surprisingly this relaxation dynamics occurs within the first few collisions, at a timescale of t_F. Within $t = 2t_\mathrm{F}$ 90% of the impurities are transferred to the second peak. We attribute the impurities remaining at 2.3 k_F to a finite size effect. Consistent with the phenomena of quantum flutter [189], this suggests that upon collision between the impurity and the host, a wave packet is emitted from the host, carrying away most of the momentum Q.

We now turn to a more detailed evolution of the impurity momentum distribution for fixed strong interactions $\gamma_i = 11.0(7)$ and $\gamma = 18.5(12)$. Experimental results are shown in Fig. 4.3 for three selected values of Q that exemplify the subsonic, the supersonic, and the intermediate case. For each case the distribution broadens and relaxes as population is transferred to lower momenta within the first Brillouin zone. Specifically, for the subsonic case with $Q = 0.20(1)\ k_\mathrm{F}$ the distribution develops a shoulder on the low-momentum side. The rms width increases by a factor of 2.4(1). While the mean momentum changes to $0.09(2)\ \hbar k_\mathrm{F}$, the most probable momentum remains near $0.20(1)\ \hbar k_\mathrm{F}$. In the intermediate regime, with $Q = 0.80(4)\ k_\mathrm{F}$, the initial narrow distribution relaxes to a comparatively broad distribution with a mean at $0.06(2)\ \hbar k_\mathrm{F}$ and an rms width of $1.5(1)\ \hbar k_\mathrm{F}$. Yet, the initial and the final distributions partially overlap. This is different for the supersonic case $Q = 1.10(6)\ k_\mathrm{F}$. Here the initial and the final distributions are clearly separate, with a transient doubly-peaked distribution around $t = t_\mathrm{F}$. Subsequently, the population in the initial peak nearly fully goes to zero on the timescale of t_F. The rms width of the final distribution within the Brillouin zone is $1.2(1)\ k_\mathrm{F}$.

Our experimental findings are qualitatively supported by numerical simulations based on matrix product states. These simulations model a single 1D system governed by the many-body Hamiltonian

$$\hat{H} = \hat{H}_\mathrm{LL}(g_\mathrm{1D}, \{z_n\}) + \frac{P_\downarrow^2}{2m} + g_\mathrm{i} \sum_{n=1}^{N} \delta(z_n - z). \tag{4.1}$$

where $\hat{H}_\mathrm{LL}$ represents the Lieb-Liniger Hamiltonian, which describes a gas of N bosons with coordinates z_n, interacting via repulsive contact interactions of strength $g_\mathrm{1D} = \hbar^2 \gamma n_\mathrm{1D}/m$. The second term corresponds the kinetic energy of the impurity, with momentum $P_\downarrow$, while the last terms describe the interaction between

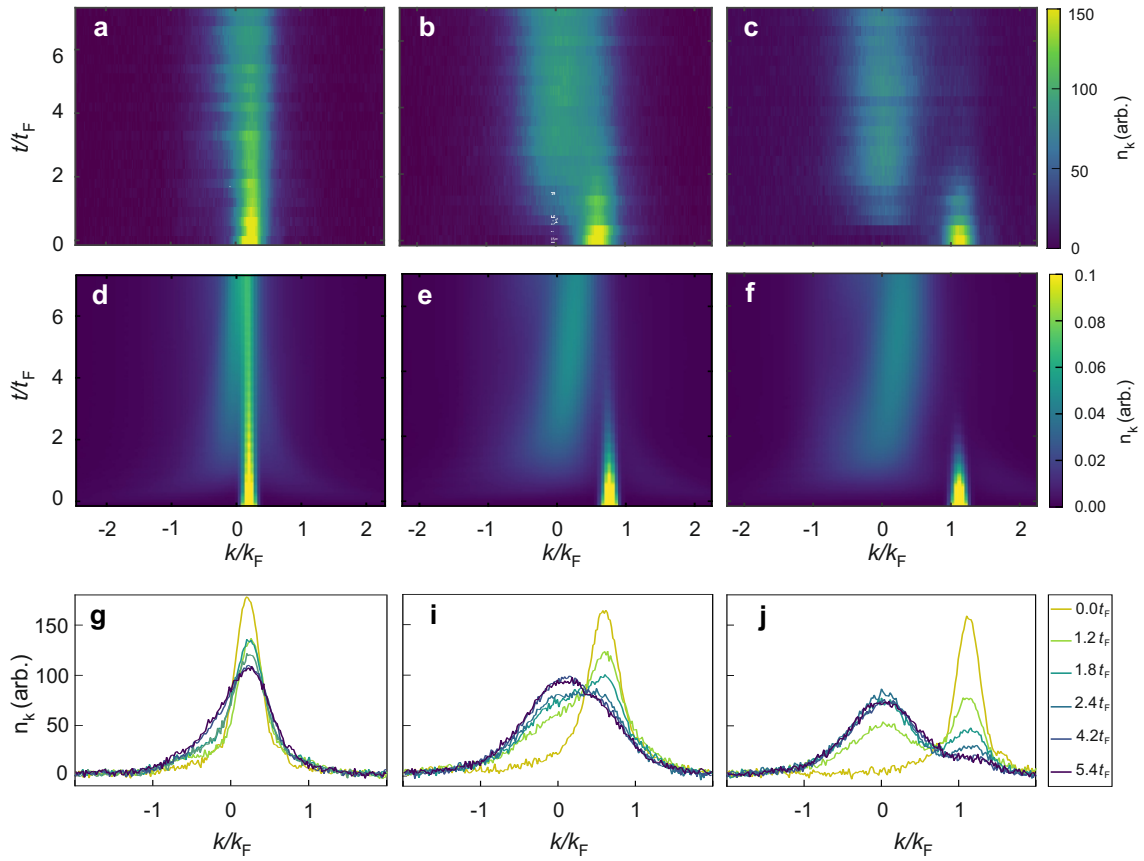

Figure 4.3: **Time evolution of the impurity momentum distribution $n(k)$. a, b, c**, Experimental $n(k)$ for $(\gamma_i, \gamma) = (11.0(7), 18.5(12))$ and selected values of the initial impurity momentum $\hbar Q$ as indicated for times up to $t = 7\ t_{\mathrm{F}}$ in time steps of $0.6\ t_{\mathrm{F}}$. **d, e, f**, Numerical results as discussed in the text. **g, i, j**, Selected experimental distributions for some specific evolution times from $t = 0$ to $t = 5.4\ t_{\mathrm{F}}$ as indicated. Each experimental data is the average of 10 realizations.

the impurity and the host particles, where the interaction strength is given by $g_i = \hbar^2 \gamma_i n_{1\mathrm{D}}/m$. At $t = 0$ the impurity is introduced into the host gas as a plane wave with well-defined momentum Q. Similar to the experiment the γ_i, and γ, are quenched from 0 to 11.0, and 2.5 to 18.5, respectively after the creation of the impurity. The subsequent time evolution of the impurity momentum distribution (see Fig. 4.3**d** to **f**) agrees well with the experimental data (see Fig. 4.3**a** to **c**). However, we do observe minor quantitative differences. Specifically, for large Q. In the experiment, a systematically larger fraction of $n(k)$ propagates freely through the host gas compared to the theoretical predictions. We attribute this deviation to contributions from outer tubes containing only a few particles. At large Q, impurities are accelerated out of these shorter tubes before host-impurity interactions are quenched on. The distribution of tube lengths has the further consequence that in the experiment since there is not a single k_{F} for the entire system, but rather a distribution. The defined Brillouin zone thus varies across the sample. One further noteworthy difference between the experiment and the simulations lies in the injection protocol of the impurity. While in the experiment the impurity is created out of the host via the aforementioned RF pulse, in the simulations, the impurity is

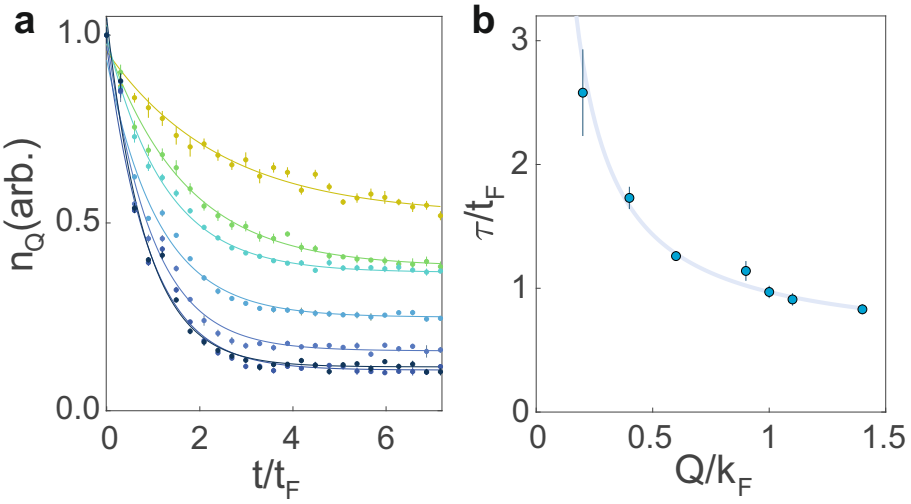

Figure 4.4: **Momentum-dependent impurity relaxation**. **a**, Decay of initial momentum occupation n_Q as a function of initial impurity momenta $\hbar Q$ for $\gamma_i = 11.0$. From slowest to fastest decay $Q = 0.2, 0.4, 0.6, 0.9, 1.0, 1.1, 1.4\ k_\mathrm{F}$, respectively. Each data point represents 10 repetitions. The solid curves correspond to exponential fits. **b**, Time constant extracted from the exponential fits in **a,** as a function of initial momentum. The solid curve is a $a/Q + c$ fit of the $\gamma_i = 11.0$ dataset and serves as a guide to the eye. The error corresponds to the standard fitting error.

injected into the sample as a plane wave.

In both experiment and simulations, the relaxed momentum distribution for $Q < k_\mathrm{F}$ is asymmetric, while for any $Q > k_\mathrm{F}$ it becomes symmetric about $Q = 0$. The momentum distribution of the impurity in the finite-momentum ground state of the system also shows an asymmetric distribution for $0 < Q < k_\mathrm{F}$. At $Q = k_\mathrm{F}$ the momentum distribution is that of a system of free fermions, i.e., again symmetric. This behavior can be understood by looking at the impurity evolution as a series of collision events. The impurity transfers its momentum to the host system through density wave excitations until it reaches a minimal energy state. This minimal energy state is the magnon state indicated in Fig. 4.1**d** . The emergence of a steady state signals the formation of a polaron state. For $Q < k_\mathrm{F}$, the momentum distribution of the impurity in polaron state is always asymmetric. This is reflected in our relaxed momentum distribution. However, for any $Q > k_\mathrm{F}$ the impurity favorably decays to a magnon state close to $Q = k_\mathrm{F}$ where the density of states is the largest.

4.4 Relaxation timescales

Evidently, relaxation happens quicker for higher initial Q. To quantify this, we track the evolution of the momentum population $n_Q \equiv n(k = Q)$ at the location Q of the peak of the initial distribution, averaged over $\pm 0.1\ k_\mathrm{F}$ around Q (see Fig. 4.3**g** to **j**). The results are shown in Fig. 4.4**a** for varying Q. A clear trend can be seen: for higher Q the initial peak is depleted more quickly. Exponential fits to the data provide time constants τ for varying Q as presented in Fig. 4.4**b**. Around $Q = k_\mathrm{F}$ the relaxation time scale settles to values near t_F.

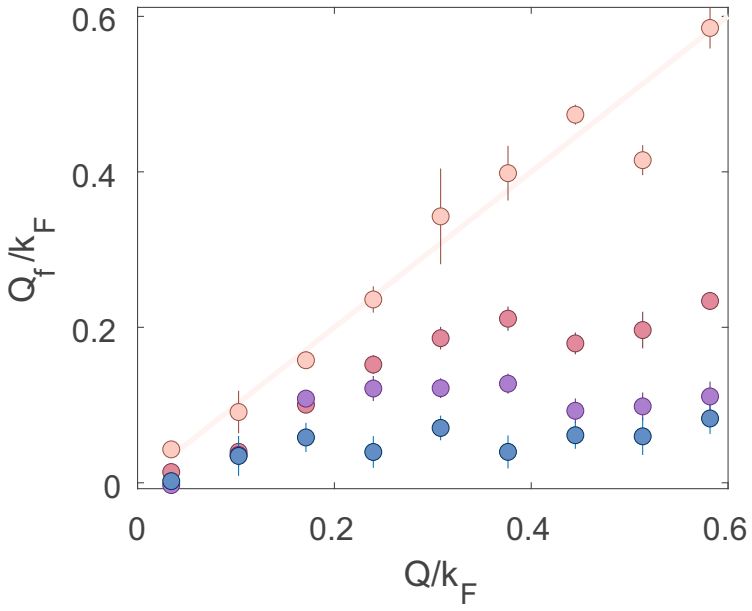

Figure 4.5: **Final impurity momentum after relaxation.** The mean steady state momenta of the impurity $\hbar Q_\mathrm{f}$ as a function of its initial momenta $\hbar Q$, for different values interaction strengths γ_i. Pink, red, purple and blue correspond to $\gamma_i = 0, 2.1, 4.1, 6.2$, respectively. Each data point is an average of 10 repetitions except for the non-interacting case ($\gamma_i = 0$) corresponding to 3 repetitions. The error is the standard error. The solid curve corresponds to the predicted momenta of a non-interacting particle.

4.5 Steady-state momentum

We now examine the steady-state momentum of the impurity in the long-time limit, denoted as $\hbar Q_\mathrm{f}$. To determine $\hbar Q_\mathrm{f}$, we calculate the mean momentum within a region of $\pm 1.5\ \hbar k_\mathrm{F}$ centered around $k = 0$ of the impurity momentum distribution, after the impurity has been evolved for $t = 10\ t_\mathrm{F}$. Figure 4.5 presents Q_f as a function of the initial impurity wavevector Q for four different interaction strengths: $\gamma_i = 0, 2.1, 4.1, 6.2$. In the non-interacting limit, our results agree well with the expected momentum evolution of a freely falling impurity. For finite interactions ($\gamma_i \neq 0$), we observe that Q_f initially increases before saturating at a finite asymptotic value. At strong coupling (γ_i large), Q_f reaches a plateau for initial momenta $Q > 0.2\ k_\mathrm{F}$. As the interaction strength decreases, this plateau shifts to higher values of Q. The average impurity velocity in this plateau increases with weaker coupling. The end velocity has a dependence on the initial velocity of the impurity, signaling that the system does not thermalize but rather forms a steady state.

The finite terminal velocity can be understood as a consequence of polaron formation, where the cosine-shaped excitation spectrum determines the asymptotic velocity through its derivative

$$v = \left.\frac{\partial \varepsilon_\mathrm{m}(k)}{\partial k}\right|_{k=Q} \tag{4.2}$$

where, ε_m is the energy of the magnon relative to the zero-momentum ground state energy. These observations align with the magnon spectrum picture: while impuri-

ties with small initial momentum Q eventually relax to low-momentum states, those with $Q > k_{\mathrm{F}}$ relax to momenta near k_{F}. Increasing γ_i pushes the magnon branch toward zero energy, which manifests as the reduced saturated values of Q_{f} observed at strong coupling. Furthermore, the extended rise before plateau at weaker coupling suggests a magnon spectrum with enhanced curvature. It is important to note that the finite end velocity is not merely an artifact of integrability, but goes beyond integrable systems. For an impurity with a different mass to the host, for example, the finite steady state velocity is expected to persist. In the limit of infinite impurity mass its behavior can be described by Landau's criteria for superfluidity.

4.6 Conclusion

In conclusion, we show how a microscopic impurity can propagate through a strongly interacting Bose gas without any friction at odds to Landau's paradigm. Our findings demonstrate the emergence of long-lived entangled quasiparticle states and provide key insights into transport and coherence in low-dimensional quantum fluids. Quantum entanglement between microscopic impurity and strongly correlated host gas can give rise to new physics that goes beyond the hydrodynamic picture of relaxation.

Acknowledgments
The Innsbruck team acknowledges funding by a Wittgenstein prize grant under Austrian Science Fund (FWF) project number Z336-N36, by the European Research Council (ERC) under project number 789017, by an FFG infrastructure grant with project number FO999896041, and by the FWF's COE 1 and quantA. MH thanks the doctoral school ALM for hospitality, with funding from the FWF under the project number W1259-N27.

4.7 Supplemenatary materials

4.7.1 Superfluidity theory: how Landau criterion interplays with dimensionality of the system and finite impurity mass

In this Section, we elaborate how possible outcome of collision of an impurity with the surrounding gas is determined by kinematic (that is, stemming from energy and momentum conservation laws) restriction. They come from an interplay of quantum statistics and interaction effects constrained by the 1D geometry of our problem.

We illustrate in Fig. 4.6 an excitation spectrum of indistinguishable quantum particles constrained to one spatial dimension. Several crucial features remain in this picture regardless of particle statistics and the strength of interparticle repulsion [58]. The first is the presence of the exact nonzero lower bound (or edge), $\varepsilon_{\min}(k)$, of the particle-hole continuum, shown by a solid curve in Fig. 4.6, as well as in Fig. 4.1 of the main text. Recall that momentum p is related to wave number k by equation $p = \hbar k$, where $\hbar$ is Planck's constant. All possible excitations of the quantum gas stay above this curve. The second is the fact that the edge energy at zero momentum

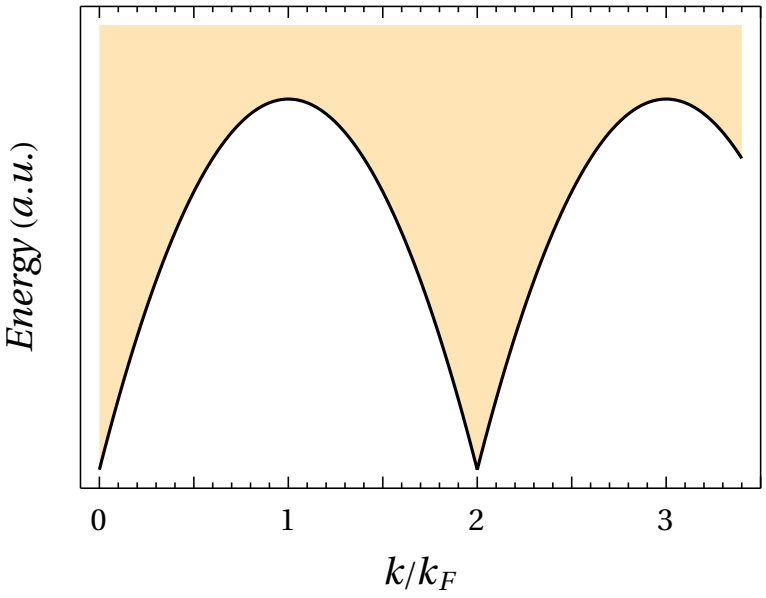

Figure 4.6: **Possible excitation energy of a 1D gas as a function of its total momentum**. The shaded area shows where excitations are possible. Dashed black line shows exact lower bound (edge) of this excitation spectrum.

has the same value as at $k = 2k_F$, independent of the interaction strength and quantum statistics of the constituent particles (this is referred to as the Luttinger theorem). Here, k_F is the Fermi momentum, defined through the density ρ of the gas as $k_F = \pi\rho$. The third is the $2k_F$-periodicity of the edge (in the infinite system). This periodicity is the reason for the frequent usage of the term "first Brillouin zone" for the interval $0 < k < 2k_F$ even in *continuous* quantum 1D systems. The fourth is a particular shape of the edge near $k = 0$: it has a linear slope.

$$\varepsilon_{\min}(k) = \hbar v k, \qquad k \to 0. \tag{4.3}$$

The low energy and momentum excitations in such a system are, therefore, sound waves whose velocity is

$$v = \left.\frac{\partial \varepsilon_{\min}(k)}{\partial k}\right|_{k=0}. \tag{4.4}$$

Because these excitations propagate through the system by causing the density fluctuations (or charge fluctuations in the case of charged particles), they are often referred to as plasmons in the literature.

Next, we present in brief the arguments why the 1D system, having the excitation spectrum shown in Fig. 4.6, cannot be superfluid. Let us briefly recall the Landau criterion of superfluidity. Assume that the liquid moves through a pipe with velocity $\mathbf{v}$ uniformly and steadily at a given time moment. Landau argues that a change in the macroscopic state (velocity $\mathbf{v}$ in our case) is caused by the emergence of elementary excitations in the liquid (however, a single elementary excitation causes only infinitesimal change in the macroscopic state). Consider a single excitation with momentum $\mathbf{p}$ and energy $\varepsilon(p)$ emerging in the reference frame of the liquid

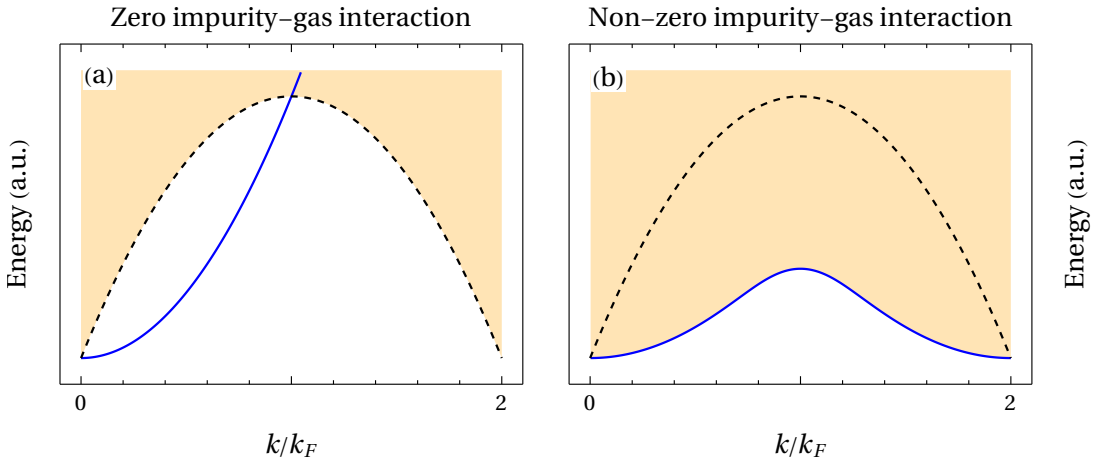

Figure 4.7: **Emergence of the magnon spectrum due to impurity-gas interaction**. Left panel: free impurity travels through 1D gas. Particle-hole excitations of the 1D gas lie in the shaded area, above dashed black line. The dispersion of the free impurity, given by Eq. (4.9), is shown by solid blue line. Right panel: Impurity interacts (repulsively) with 1D gas.

(that is, where the liquid is initially at rest). Then, ideally, all the energy and momentum of this excitation are converted into the kinetic energy of the liquid, $E_0 \equiv P_0^2/(2M) = \varepsilon(p)$, and the momentum $\mathbf{P}_0 = \mathbf{p}$, respectively. Here, M in the mass of the liquid and p is the length of the vector $\mathbf{p}$. Now, let us turn to the laboratory frame. There, the momentum of the liquid is

$$\mathbf{P}_{\text{lab}} = \mathbf{P}_0 + M\mathbf{v}, \tag{4.5}$$

and the energy is

$$E_{\text{lab}} = \frac{(\mathbf{P}_0 + M\mathbf{v})^2}{2M} = \varepsilon + \mathbf{pv} + \frac{Mv^2}{2}. \tag{4.6}$$

The term $\varepsilon + \mathbf{pv}$ in E_{lab} is due to the assumption that a kinetic energy is converted into an elementary excitation energy. Elementary excitations can only emerge if

$$\varepsilon + \mathbf{pv} \leq 0, \tag{4.7}$$

because the kinetic energy of the liquid cannot increase while this liquid flows through the steady pipe. Given p, the minimum v to satisfy the inequality (4.7) is reached when $\mathbf{p}$ and $\mathbf{v}$ are antiparallel, $\varepsilon - pv \leq 0$, that is,

$$v \geq \frac{\varepsilon(p)}{p} \qquad \text{Landau criterion} \tag{4.8}$$

at least for some value of p. The inequality (4.8) is Landau criterion of superfluidity. If inequality (4.8) is satisfied for some value of p, energy and momentum conservation *do not prohibit* the emergence of excitations with dispersion $\varepsilon(p)$ at the expense of kinetic energy, and the liquid is not superfluid. This is evidently the case for 1D systems, whose excitation spectrum, illustrated in Fig. 4.6, contains excitations with a momentum of about $2k_F$ and arbitrarily low energy.

Non-superfluid means for a 1D quantum gas to dissipate energy and momentum upon collision with *macroscopic* obstacles. The motion of the *microscopic* impurity through this gas can be dissipationless. This is what we confirmed experimentally in our work, and here we give some theory details not included in the main text. The energy of the free impurity of mass m is related to its momentum p by the law of classical mechanics:

$$\varepsilon_{\text{imp}} = \frac{p^2}{2m}. \tag{4.9}$$

This dispersion law is shown on top of the energy spectrum of the 1D gas of particles of mass m in Fig. 4.7(a), as well as in Fig. 4.1 of the main text. The impurity dispersion lies below the edge of the excitation spectrum of the 1D gas at a sufficiently small k, because the former is quadratic, Eq. (4.9), and the latter is linear around $k = 0$, Eq. (4.3). The excitation spectrum of a system containing an impurity that interacts with the 1D gas is shown in Fig. 4.7(b). Notably, the edge of the spectrum has the same functional form at low energy and momentum as given by Eq. (4.9):

$$\varepsilon_{\text{pol}} = \frac{p^2}{2m_*}. \tag{4.10}$$

This shape of the edge represents a polaron particle, which is the impurity "dressed" by particle-hole excitations in the gas (the polaron mass m_* is normally greater than the bare impurity mass m due to this dressing). The very existence of the 1D polaron ensures the possibility of dissipationless motion of the impurity through the 1D gas at equilibrium. Indeed, the polaron state (which encompasses the moving impurity) has a lower energy than any phonon state (which encompasses the gas particles without the impurity) at a small but non-zero momentum. Hence, a finite mass impurity may have a nonzero velocity in the steady state of a 1D interacting quantum system. We stress that this result is valid regardless of the details of the interaction potential in the gas and between the gas and the impurity particle.

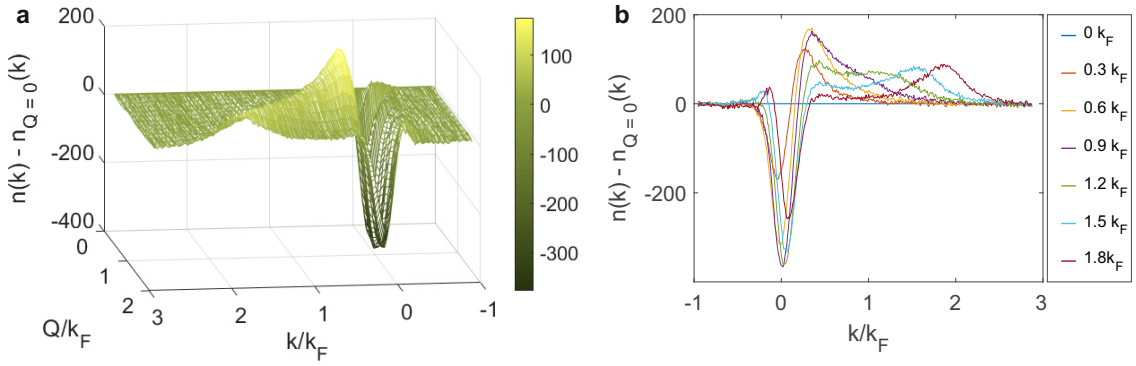

Figure 4.8: **Wavepacket emission in the host momentum distribution.** Change of momentum distribution of host $n_Q(k) - n_{Q=0}(k)$ as a function of Q after a fixed evolution time. **a**, Full evolution. **b**, Distribution for selected values of Q. Corresponding values of Q are indicated on the right-hand legend. Each distribution is the mean of ten repeats.

4.7.2 Momentum distribution of host

In Fig. 4.8 we show the change of the momentum distribution of the host as a function of Q for $\gamma = 3$. We find that for $Q \simeq k_{\mathrm{F}}$ an ejected wavepacket develops which carries away most of the initial momenta of the impurity. Since for $\gamma = 3$ the speed of sound of the medium is approximately $0.4\ \hbar k_{\mathrm{F}}/m$, this suggests that the saturation behavior observed in Fig. 4.4 is a consequence of the large density of states in the excitation spectrum around the k_{F}. In the ground state the impurity momentum distribution is symmetric at k_{F} and thus has a mean momenta of zero. If the impurity decays to the finite momentum ground state around k_{F} it must therefore transfer all of its momenta to the host, leading to an ejected host wavepacket that carries most of the momentum.

4.7.3 Interaction dependence

In the main text the discussion focuses on the strongly interacting case with $\gamma_i = 11(7) \gg 1$ for which the bosons are expected to be fully fermionized. We now turn to the intermediate regime as the interactions are tuned in the range $1 \leq \gamma_i \leq 10$. In Fig. 4.9 we show experimental results for the relaxation dynamics for five different interaction strengths ($\gamma_i = 1.7, 2.9, 4.1, 6.6$, and 9.1) and for $Q = 0.2, 0.6$ and $1.1\ k_{\mathrm{F}}$. We find that the behavior of the relaxation timescales with respect to γ_i is similar for different Q: the relaxation time decreases for increasing γ_i, saturating to the values shown in Fig. 4.4 for high γ_i. For small Q, the relaxation time is longer.

4.7.4 Preparation of 1D tubes

The experiment starts with a 3D interaction-tunable BEC consisting of approximately 1.5×10^5 Cs atoms in the absolute ground state $(F, m_{\mathrm{F}}) = (3, 3)$, confined in a crossed-beam dipole trap. The dipole traps have trapping frequencies of $(\omega_x, \omega_y, \omega_z)/2\pi = (5.7(1), 11.8(1), 10.3(1))$ Hz giving a Thomas Fermi radii of $(21.4(2), 16.0(1), 16.9(1))$ μm. The sample is adiabatically loaded into an array of 1D tubes created by a 2D optical lattice. The laser beams forming the lattice propagate in the horizontal x-y plane at right angle to each other, and their power is ramped up in 500 ms to give a lattice depth of $30E_{\mathrm{r}}$, where $E_{\mathrm{r}} = \pi^2\hbar^2/2md^2$ is the

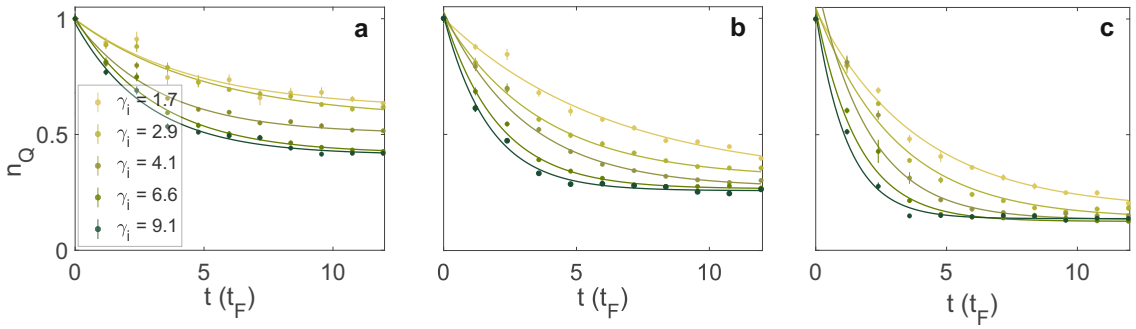

Figure 4.9: **Evolution of n_Q for different interaction strengths. a, b, c**, n_Q as a function of time for $Q = 0.2$, 0.6, and $1.1\ k_{\mathrm{F}}$ respectively. For each Q, the decay of n_Q is measured for $\gamma_i = 1.7$, 2.9, 4.1, 6.6, and 9.1, as indicated. The solid curves are exponential fits of the data. Each data point represents 5 to 10 repetitions.

recoil energy. Here, $d = \lambda/2 = 532.5$ nm is the lattice spacing set by the wavelength λ of the lattice light. At this depth, tunneling between the tubes are fully suppressed, and the tubes can be considered as independent. Due to the underlying dipole trap during the lattice loading, the resulting array of tubes have a distribution of number of atoms. We have on average 39 atoms per tube. Additionally, the Gaussian profile of the lattice beams results in weak harmonic trapping with trap frequency $\omega_z/2\pi = 17.0(1)$ Hz along the tubes' direction.

4.8 Experimental system parameters

In our experiment we control interactions in the host gas via the scattering length a_s. This in turn sets the 1D coupling constant $g_{1\mathrm{D}}$ [17, 132],

$$g_{1\mathrm{D}} = 2\hbar\omega_\perp a_s \left(1 - 1.0326\frac{a_s}{a_\perp}\right) \tag{4.11}$$

where $a_\perp = \sqrt{\hbar/m\omega_\perp}$ is the radial oscillator length. Similarly the scattering length for collisions between impurity and host atoms a_s^i sets the coupling constant g_i. In order to determine the dimensionless interaction strengths γ and γ_i we further require the density of the host gas $n_{1\mathrm{D}}$ and hence the atom number $N_{j,k}$ for the tube (i, j). Assuming that the interactions are sufficiently small during the adiabatic loading of the lattice, such that all of the tubes are in the Thomas-Fermi regime the atom number $N_{j,k}$ for the tube can be computed iteratively from the global chemical potential. For further detail see [252]. We then calculate the average number of atoms per tube $N = \frac{1}{N_{tot}} \sum_{j,k} N_{j,k}^2$, where $N_{\mathrm{tot}} = \sum_{j,k} N_{j,k}$ is the total number of atoms. The 1D density distribution $n(z)$ depends on the interaction regime in which the gas is in. Here, we calculate $n(z)$ by exactly solving the Lieb-Liniger model with local density approximation (LDA) [59, 343]. We then calculate the average 1D density $n_{1\mathrm{D}} = \frac{1}{N}\int n(z)^2 dz$. The average interaction strengths are calculated as,

$$\gamma = \frac{m g_{1\mathrm{D}}}{\hbar^2 n_{1\mathrm{D}}}, \qquad \gamma_i = \frac{m g_{\mathrm{i}}}{\hbar^2 n_{1\mathrm{D}}} \tag{4.12}$$

4.8.1 Impurity creation via RF transfer

The vertical magnetic gradient field ∇B gives rise to a position dependent resonance for transfer of the host atoms to the $(3, 2)$ state. The creation of the impurity can thus be made spatially selective along the tube. A 20 μs RF pulse is used to create the impurity. From the length of the RF pulse we estimate the spread of the impurity wavepacket to be $\sigma_z \sim 6.5$ μm. This corresponds to $\sigma_{\mathrm{k}} \sim 0.05$ k_{F} in momentum space. Note that the measured width of the impurity in momentum space at $t = 0$ t_{F} in Fig. 4.2 in the main text is $\sim 0.3 k_{\mathrm{F}}$, which reflects the coherence length of the host gas.

CHAPTER 5

PUBLICATION IV

Bose-Einstein condensation of non-ground-state caesium atoms

Milena Horvath[1], Sudipta Dhar[1], Arpita Das[2], Matthew D. Frye[3], Yanliang Guo[1], Jeremy M. Hutson[3], Manuele Landini[1], and Hanns-Christoph Nägerl[1]

[1]*Institut für Experimentalphysik und Zentrum für Quantenphysik, Universität Innsbruck, Technikerstraße 25, Innsbruck, 6020, Austria*
[2] *Durham-Newcastle, Durham University, Durham DH1 3LE, United Kingdom*
[3]*Department of Chemistry and Joint Quantum Centre (JQC) Durham-Newcastle, Durham University, Durham DH1 3LE, United Kingdom*

Bose-Einstein condensates of ultracold atoms serve as low-entropy sources for a multitude of quantum-science applications, ranging from quantum simulation and quantum many-body physics to proof-of-principle experiments in quantum metrology and quantum computing. For stability reasons, in the majority of cases the energetically lowest-lying atomic spin state is used. Here we report the Bose-Einstein condensation of caesium atoms in the Zeeman-excited $m_f = 2$ state, realizing a non-ground-state Bose-Einstein condensate with tunable interactions and tunable loss. We identify two regions of magnetic field in which the two-body relaxation rate is low enough that condensation is possible. We characterize the phase transition and quantify the loss processes, finding unusually high three-body losses in one of the two regions. Our results open up new possibilities for the mixing of quantum-degenerate gases, for polaron and impurity physics, and in particular for the study of impurity transport in strongly correlated one-dimensional quantum wires.

5.1 Introduction

Ultracold atomic gases have proven to be a fruitful testbed for few- and many-body quantum physics, in part due to their high degree of controllability [12]. A very

powerful tool for the ultracold-atom platform is the ability to tune the interactions between the atoms via Feshbach resonances [88]. One atomic element that has been very successful in this regard is Cs [114, 344]. The hyperfine ground state of Cs is enriched by an abundance of broad and narrow Feshbach resonances, and interaction tuning has been instrumental to a diverse series of seminal results on a wide range of topics. These include Bose-Einstein condensation (BEC) [114], Efimov physics [104, 115], ultracold molecules [116–118], strongly correlated one-dimensional (1D) physics [14, 17, 45], long-range tunneling dynamics [120] and density-induced tunneling [345], scale invariance [346], matter-wave jets [121], and, recently, cooling by dimensional reduction [347] and the 1D-2D crossover [250]. These results have all been obtained by making use of one particular hyperfine Zeeman sublevel of Cs, the state $(f=3, m_f=3)$, which is the energetically lowest-lying Zeeman state.

BEC of atoms in excited states offers additional possibilities. Such condensates have been produced with excited Zeeman states, metastable electronic states and atoms in higher bands of optical lattices. They have been used to create spinor quantum gases [348], to observe quantum droplet states [349] and to study unconventional superfluidity in excited lattice orbitals [350]. Early attempts to condense Cs in excited Zeeman sublevels were hindered by uncontrolled losses [109–113]. Later experiments using the sublevel $(3, 3)$ benefited from the absence of inelastic two-body processes, but care was needed to avoid detrimental three-body collisions [104, 105, 114].

Here we report the achievement of a tunable Cs BEC in a state other than the absolute ground state, namely in the Zeeman-excited state $(f = 3, m_f = 2)$. We identify one particular window around a magnetic field of $B \approx 160$ G in which two- and three-body processes are sufficiently suppressed that pure condensates can reliably be produced with 3×10^4 atoms. In a second window around $B \approx 40$ G partial condensation is possible. We find surprisingly high three-body losses in this window, most likely due the opening up of a new decay channel. Our work is guided by state-of-the-art coupled-channel calculations to determine the two-body scattering properties.

The attainment of BEC requires that the ratio of good to bad collisions is sufficiently high while effective one-body processes such as background-gas collisions and inelastic light scattering are negligible. Elastic collisions are needed to drive the evaporation and thermalization process, while two-body inelastic collisions and three-body recombination reduce the cooling efficiency, possibly to the point that BEC cannot be reached. With peak number densities in the range between 1×10^{11} and 1×10^{13} atoms/cm^3 during the cooling process, this translates into concrete values for the s-wave scattering length and into acceptable upper bounds for the two- and three-body loss-rate coefficients.

We have carried out coupled-channel calculations of the two-body scattering properties as a function of magnetic field, as described in Ref. [108]. The calculations use the interaction potential of Ref. [351] and a basis set including partial-wave quantum numbers L up to 4. For collisions involving excited-state atoms, the scattering length is complex, $a = \alpha - \mathrm{i}\beta$, and the 2-body loss-rate coefficient at limitingly low energy is $k_2 = (4g\pi\hbar/\mu)\beta$, where μ is the reduced mass and g is 1 (2) for distinguishable (indistinguishable) particles. Figure 5.1 shows the real parts of the s-wave scattering lengths $a_{m_{f1},m_{f2}}$ for the three possible combinations of atoms initially in $m_f=3$ and $m_f=2$, and the corresponding rate coefficients k_2 for two-body inelastic

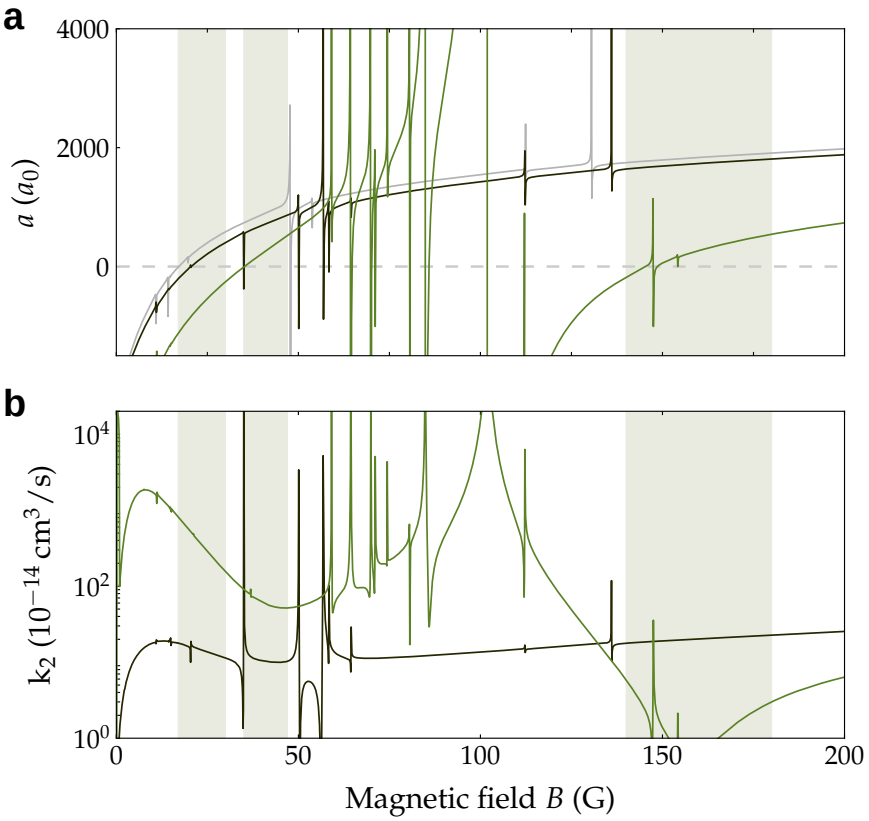

Fig. 5.1: **Two-body scattering properties of the Cs states of interest from coupled-channel calculations.** **a**, The real parts of the scattering lengths $a_{3,3}$ (grey), $a_{3,2}$ (black), and $a_{2,2}$ (green) and **b**, the two-body loss-rate coefficients k_2 for collisions of $(3,3)$ with $(3,2)$ (black) and $(3,2)$ with $(3,2)$ (green) as a function of the magnetic field B. The regions of interest for this work are indicated by the grey shadings.

loss (which cannot occur for two atoms with $m_f = 3$). As is well known, the Cs scattering lengths are strikingly field-dependent, featuring overlapping broad and narrow Feshbach resonances. The state $(3,3)$ features a comparatively gentle zero crossing near 17 G, and BEC in this state has been achieved in a narrow window around 21 G [114]. The state $(3,2)$ exhibits a broad s-wave resonance centred at 102 G and two gentle zero crossings near 35 G and 148 G. Its magnetic-field dependence is scarred by a multitude of narrow d-wave ($L = 4$) and g-wave ($L = 6$) Feshbach resonances. In fact, the zero crossing near 148 G is split in two by a narrow d-wave resonance. The two-body loss-rate coefficient k_2 is strictly zero for the state $(3,3)$. This is not so for the state $(3,2)$, but even here spin-exchange collisions, which conserve $m_{f1} + m_{f2}$, are energetically forbidden at low energies. The two-body loss rates in Fig. 1 are due entirely to spin-relaxation collisions, driven by the magnetic dipole-dipole interaction and second-order spin-orbit coupling [108, 352], and there are windows near 40 G and 160 G where the values for (3,2)+(3,2) are small or even negligible. It is these windows on which we will concentrate in this work.

5.2 BEC of Cs in the state (3,2).

The procedure used to achieve a condensate in the state $(3, 2)$ makes use of some of the tricks that have previously been used to create a BEC in the ground state $(3, 3)$ [344]. We start by loading about 2.5×10^8 atoms into a six-beam magneto-optical trap (MOT) within 4 s from a Zeeman-slowed atomic beam. Subsequent Raman-sideband cooling in the presence of a near-detuned optical lattice for a duration of 6.9 ms brings the atoms to temperatures below 1 μK and spin-polarizes them into the state $(3, 3)$. The sample, now with about 5×10^7 atoms, is loaded into a large-volume "reservoir" dipole trap by gradually switching off the lattice light as a levitating magnetic quadrupole field of 31.1 G/cm is turned on while the magnetic field B is ramped to $B = 160.3$ G, at which $a_{3,3} = 1500a_0$. The stability of the magnetic field is approximately 30 mG. The trap is generated by two horizontally propagating laser beams at 1064.5 nm, intersecting at nearly a right angle. The sample is held for 500 ms to allow plain evaporation at a trap depth of about 2.6(2) $\mu\mathrm{K}\times k_\mathrm{B}$. We now have about 6.5×10^6 atoms. To transfer the atoms into the state $(3, 2)$ we use a radio-frequency sweep across a range from 54.6 to 54.2 MHz with a duration of 1.45 ms. The levitating field is increased during the sweep to 46.65 G/cm to levitate the atoms in the state $(3, 2)$. The state-transfer efficiency that we can obtain is about 75 %. We attribute this to the motional excitation of the atoms as they see changing forces, leading to some heating and hence loss in the finite-depth optical trap. We now have about 4.9×10^6 atoms at a temperature of around 1 μK with a peak density of $8.2(1) \times 10^{10}$ atoms/cm^3. We estimate the peak elastic collision rate to be 2.8/s, with $a_{2,2} = 274\ a_0$ at $B = 160.3$ G. The geometrically averaged trap frequency is $\bar{\nu} = 8.1(5)$ Hz.

Next, as the final step towards BEC in $(3, 2)$, the sample is loaded into a tighter "dimple" trap generated by two orthogonally intersecting 1064.5-nm laser beams with estimated $1/e^2$-waist sizes of 40 and 150 μm, respectively, one propagating horizontally along the same axis as one of the reservoir beams, and the other propagating vertically. The loading process is completed after 1.5 s, and we then carry out forced evaporative cooling for 6.0 s by lowering the power of both dimple-trap beams in an approximately exponential manner. At the beginning of the evaporation process, the scattering length is tuned to $a_{2,2} = 255\ a_0$, by ramping the offset field to $B = 159.1$ G. At this value, a minimum for the loss is found, similar to the Efimov minimum for the state $(3, 3)$ [104]; it is crucial to utilize this minimum for optimal performance of the cooling process. The phase transition to a BEC occurs at a critical temperature of about 82(1) nK with 9.5×10^4 atoms after approximately 3 s of forced evaporation. Absorption images and horizontally integrated density profiles across the transition are shown in Fig. 5.2 **a**. The evolution via a characteristic bimodal distribution can clearly be seen. The images are taken after 46 ms of time-of-flight (TOF) with nulled interactions upon release [114] by means of the zero crossing in $a_{2,2}$ near 148 G, due to a Feshbach resonance near 102 G. At the end of the evaporation ramp, we obtain an essentially pure BEC with approximately 3.0×10^4 atoms. The condensate fraction is above 90 %. At this point, the dimple trap has trapping frequencies $(\nu_x, \nu_y, \nu_z) = (4.2(3), 6.5(2), 4.9(1))$ Hz, with a trap depth of $V = 8.0(2)$ nK$\times k_\mathrm{B}$. The peak density in the Thomas-Fermi (TF) regime is estimated to be $3.6(1) \times 10^{12}$ atoms/cm^3, and the TF radii are calculated to be $(R_x, R_y, R_z) = (18.5(2), 15.5(1), 17.4(1))$ μm. The BEC is comparatively stable, with

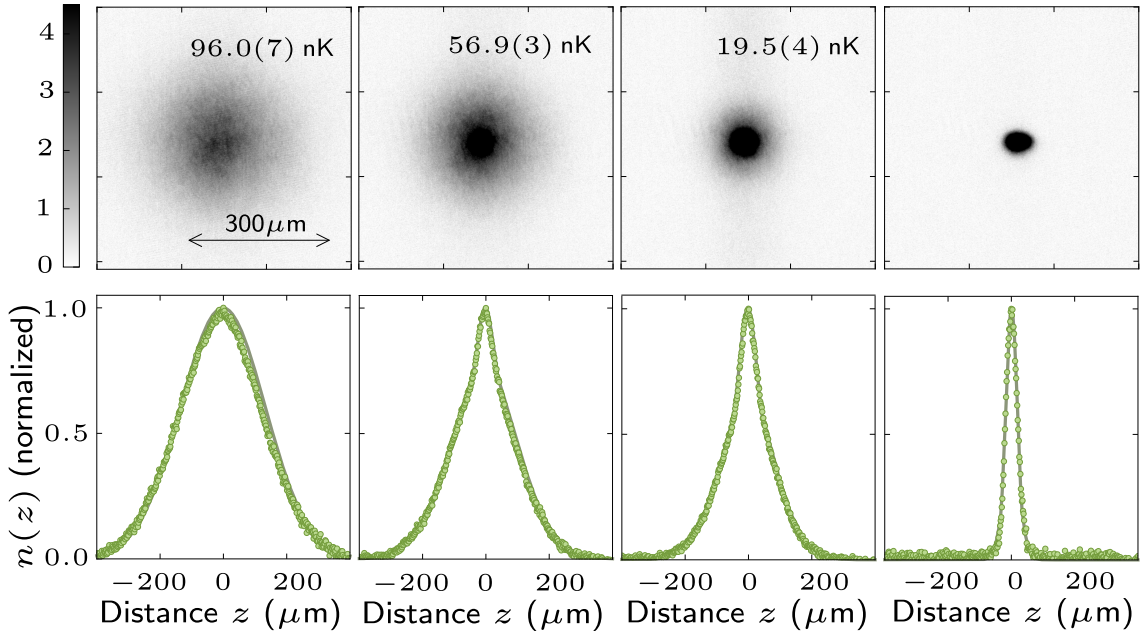

Fig. 5.2: **Formation of a BEC in (3, 2) at 160.** Absorption images at 160 G (left column), and the resulting horizontally integrated density profiles (right column), for different times during the evaporation ramp as indicated. The images are taken after release from the trap and subsequent 46 ms of TOF with nulled interactions. Each image is an average of five realizations. Bimodal fits to the normalized density profiles give the temperatures as indicated. The final BEC contains about 3.0×10^4 atoms.

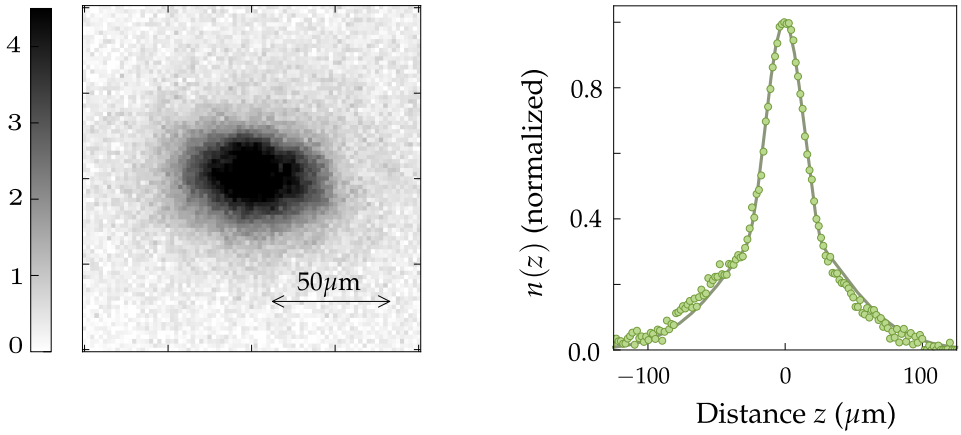

Fig. 5.3: **Formation of partial BEC at 40 G.**, Absorption image of the partial BEC at 40 G (left), and, normalized vertical density profile (right) fitted with a bimodal distribution, after a TOF of 96 ms. The sample has an atom number of $N = 7\times10^3$ with a BEC fraction of approximately 30 %. These measurements are the averages of four repetitions. We attribute the slight asymmetry that can be observed in the integrated z-profile to spilling of atoms into the vertically propagating dipole-trap beam.

an atom-number $1/e$-lifetime of around 30 s, most likely limited by slightly imperfect vacuum conditions and residual trap-light scattering. Overall, the BEC in $(3,2)$ performs nearly as well as the BEC in $(3,3)$. The cycle time for creating the BEC is 20 s.

We now turn to the window near 40 G. We have not been able to create a BEC in this window by means of the sequence outlined above, with the difference that the magnetic offset field B is ramped to this window at the beginning of the reservoir-trap stage; this is due to the losses discussed below. However, we are partially successful by implementing the lattice trick: The BEC in state $(3,2)$, created by the sequence above, is adiabatically loaded into a 3D optical lattice at 1064.5 nm with a depth of 25 E_r, where E_r is the photon-recoil energy. The lattice is the same as in some of our previous works; see Ref. [14, 45]. By adjusting the confinement via the dimple-trap beams we create a Mott insulator with predominant single-site occupancy. The lattice shields the atoms from collisions as the bias field is ramped from 160 G to a value near 40 G in 0.5 ms. Atom loss and sample heating are found to be negligible during the ramp, but they immediately set in when the lattice is unloaded and the atoms are released into the 3D dimple trap. Nevertheless, further evaporative cooling yields BECs of around $7.0{\times}10^3$ atoms with condensate fractions of up to 30%, as seen in Fig. 5.2 **b**. The lattice trick can be similarly implemented to transfer a BEC in the state $(3,3)$ to the state $(3,2)$ at 40 G directly, but without improving the BEC fraction.

5.3 Exploring the zero crossing around 148 G.

With a BEC in $(3,2)$ at hand we now explore the magnetic tunability of the state $(3,2)$. We focus on the zero crossing of $a_{2,2}$ around $B = 148$ G, which is caused by the broad resonance at 102 G. This zero crossing is of particular interest, not just because of its shallow nature, but also because of the existence of a narrow resonance in its close vicinity. This resonance is decayed, so does not produce a pole in the scattering length [353]; instead, it produces a sharp oscillation in the scattering length and an asymmetric peak in the two-body loss rate centred at $B_\mathrm{res} = 147.44$ G, as shown in Fig. 5.4. It thus gives rise to two zero crossings. We have characterised this resonance from coupled-channel calculations using the methods of Ref. [354], and obtain amplitude $a_\mathrm{res} = 5.8{\times}10^6\ a_0$ and strength $a_\mathrm{bg}\Delta = 54$ G a_0; see Supplementary Note 5.7.1 for further details. This setting provides an ideal playground to quench a non-interacting system into a highly interacting one in a fast but controlled manner.

For the measurements we start with pure BEC in $(3,2)$ at $B = 160.3$ G with a calculated scattering length $a_{2,2} = 274\ a_0$. We switch off the optical trap to initiate TOF while keeping the levitating field on. Within 0.2 ms B is ramped to the target value, where we allow the sample to expand for another 110 ms. All magnetic fields are switched off and 6 ms later an absorption image is taken, from which we determine the number of remaining atoms N and the cloud width σ_z of the atomic sample along the vertical direction z. The results are shown in Fig. 5.4. Both data sets show sharp features due to Feshbach resonances, on top of a varying background. Significant atom loss happens for values of B below about 146 G and in the vicinity of the resonances; the resonant loss peaks are centred at 147.62(3) G and 154.13(1) G.

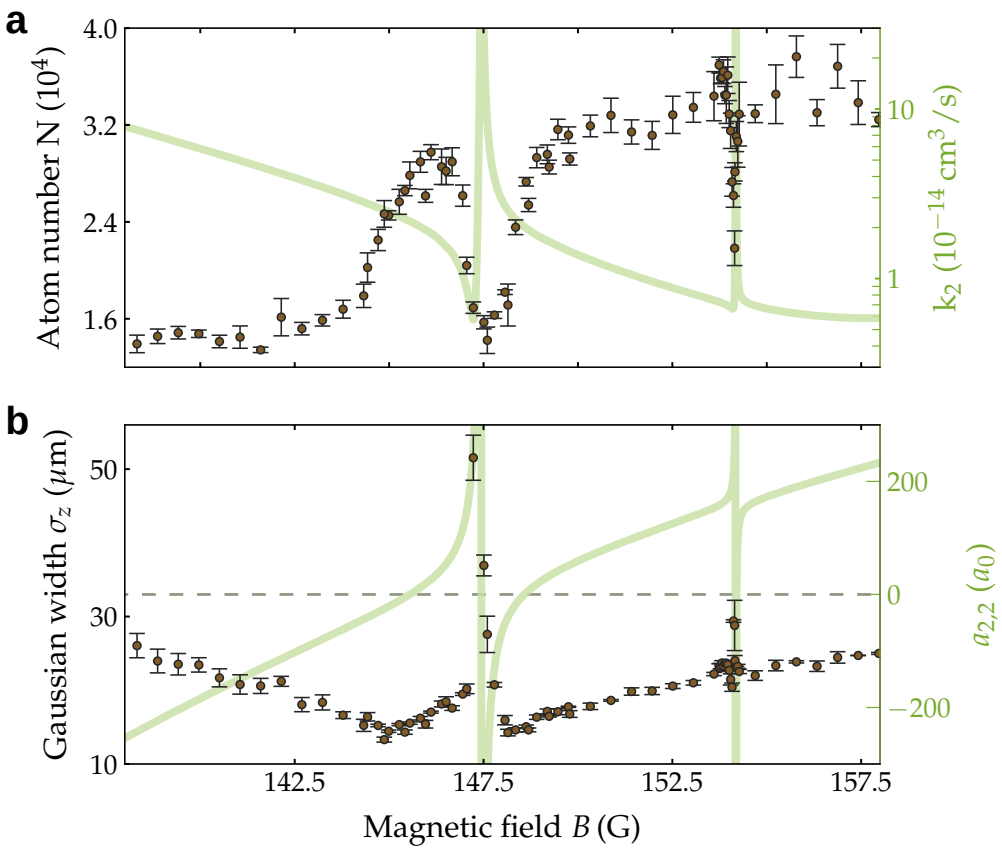

Fig. 5.4: **Exploring the vicinity of the zero crossing near 148 G with the BEC in $(3, 2)$.** **a**, Number of atoms N (circles) and **b**, the Gaussian cloud width σ_z (circles) of the BEC after TOF for different values of the magnetic field B. The experimental results in **a**, and **b**, are overlayed by the calculated two-body loss-rate coefficient k_2 (on a log scale) and scattering length $a_{2,2}$, respectively (green lines). Each data point is the average of at least three measurements and the error bars give the standard error.

The d-wave resonance causes two zero crossings in the calculated scattering length, at 145.5 and 148.6 G. The BEC shows the highest stability when the value of $a_{2,2}$ is non-zero and positive, as expected from mean-field theory. However, for negative values of $a_{2,2}$ mean-field theory predicts a collapsing BEC. In fact, below the zero crossing at 145.5 G, as B is lowered and $a_{2,2}$ becomes more negative, we observe more loss and increased sample widths. The presence of the two zero crossings is reflected in two minima in the cloud widths at 144.9(1) G and 148.1(1) G. These are at slightly lower fields than the zero crossings, i.e. at slightly negative scattering lengths. Evidently, slightly attractive interactions lead to reduced widths in expansion. This we attribute to the fact that the atom clouds contract for small attractive interactions, but do not fully collapse. The increased loss close to the resonances is caused by a combination of resonantly enhanced two-body and resonantly enhanced three-body losses. To sort out which of these dominates near the resonances would need a separate investigation.

Fitting the two resonant loss features with simple Gaussians gives resonance positions at 147.62(3) G and 154.13(1) G. These values are in good agreement with

the predictions. Further, more narrow resonant features, which do not appear in Fig. 5.4 because of the finite resolution of the scan over B, are discussed in the Supplementary Note 5.7.2.

5.4 Measurement of loss-coefficients.

The usability of a BEC in $(3,2)$ in future experiments is in part determined by the extent to which the BEC is compromised by losses. We therefore investigate the loss dynamics of ultracold non-condensed samples of atoms in $(3,2)$ for different values of $a_{2,2}$ in the regions around both 160 G and 40 G. Atoms in the state $(3,2)$ are exposed to both two-body and three-body decay channels. Two local minima in k_2 are predicted around 40 G and 160 G, as seen in Fig. 5.1. The value for the minimum at 160 G is calculated to be nearly two orders of magnitude lower than that for the minimum near 40 G. A distinct difference in the inelastic scattering behavior around 40 G and 160 G is clearly reflected by the fact that a pure BEC can be achieved at 160 G, but not near 40 G. For three-body recombination there are no precise predictions for these regions. Our lifetime measurements as discussed in this section provide an experimental estimate for both the two- and three-body coefficients in these regions.

We first focus on the region around 160 G. On the way to condensation we stop the evaporation process and create non-condensed samples in the state $(3,2)$ in the crossed dimple trap at a depth of approximately 3.1 μK. At this stage the samples have a temperature of 500 nK. For loss measurements away from the "sweet spot" with $B = 159.1$ G and $a_{2,2} = 274\ a_0$ discussed above, we further use "tilt" cooling [355] to decrease the temperature of the sample to around 150 nK without significantly affecting the trap curvature. Tilting the trap back gives such a deep trap that evaporative losses are minimized during the loss measurements, increasing our sensitivity for a potential measurement of k_2. With trapping frequencies of $(\nu_x, \nu_y, \nu_z) = (111.0(19), 118.1(38), 40.3(6))$ Hz, we get an initial peak density of the cloud in the range of $1.2 - 1.6 \times 10^{13}$ cm^{-3} for typically 5×10^4 atoms. We ensure that the sample remains above the BEC phase-transition temperature in order to simplify the modelling of our measurements. In the experiment, we hold the sample for a variable hold time t and then determine atom number and temperature. The results are presented in Fig. 5.5 a) and b) for hold times up to 2 s and for 4 different values of B from 151.1 to 177.7 G. Particle loss and sample heating are evident. For comparison, we add a data set that is taken at the sweet spot ($B = 159.1$ G and $a_{2,2} = 274\ a_0$) without using the tilt method, but just by stopping the evaporation sequence shortly before condensation. Here, some loss can be seen, but no heating. The loss is most likely evaporative loss, and possible heating is balanced by plain evaporative cooling, given the rather shallow trap. For the other data sets, there is an obvious trend that larger values of $a_{2,2}$ result in faster loss and more rapid temperature increase. However, we find fast loss also for lower values of $a_{2,2}$ away from the sweet spot, as can be seen from the data set with 88 a_0.

To model the loss, we assume that the samples remain in thermal equilibrium throughout the whole process. The number N of remaining atoms evolves according to the rate of change of the density, $\dot{n}(\mathbf{r},t) = -\sum_i k_i n(\mathbf{r},t)^i$, where $i = 1$, 2, and 3 denote the one-, two-, and three-body loss processes, respectively, with k_i the

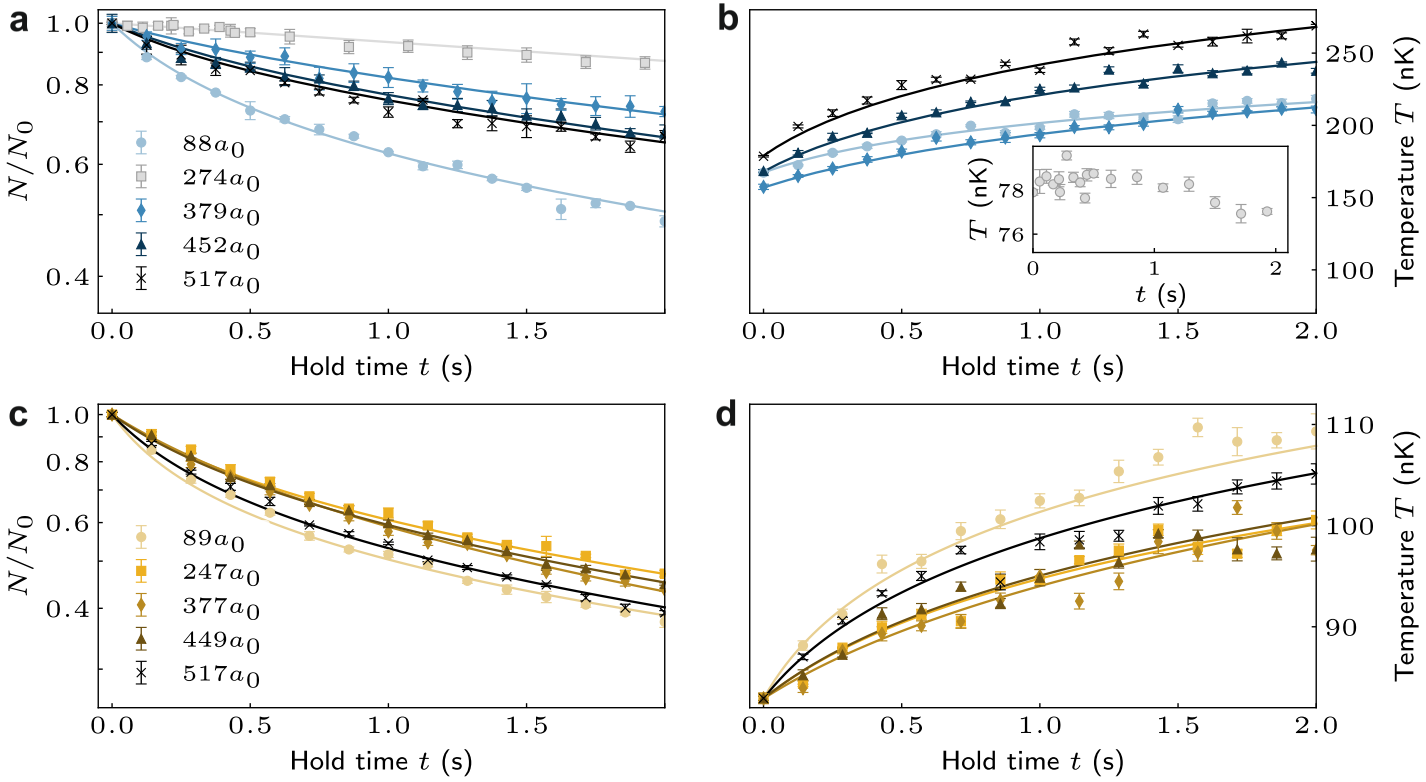

Fig. 5.5: **Atom-loss and temperature measurements for non-condensed samples in state $(\mathbf{3},\mathbf{2})$. a**, (and **c**,) Normalized number of remaining atoms N and **b**, (and **d**,) temperature T for varying hold time t in the region around 160 G (40 G). For **a**, and **b**, the scattering length $a_{2,2}$ is set to 88 a_0 (circles), 274 a_0 (squares), 379 a_0 (diamonds), 452 a_0 (triangles), and 517 a_0 (crosses) for $B = 151.1$ G, 160.3 G, 167.0 G, 172.4 G, and 177.7 G, respectively. The inset in b) shows the measured temperature for the sweet spot with $a_{2,2} = 274$ a_0. For **c**, and **d**, $a_{2,2}$ is set to 89 a_0 (circles), 247 a_0 (squares), 377 a_0 (diamonds), 449 a_0 (triangles), and 517 a_0 (crosses) for $B = 37.1$ G, 40.7 G, 43.7 G, 45.4 G and 47.0 G, respectively. Each data point is equal to the mean of three to five repeats, and the error bars reflect the standard error. The solid lines are fits to the data as discussed in the main text. The loss-rate coefficients obtained from the fits are given in Tab. 5.4.

coefficient of the collision rate for i-body loss. The rate of change for the atom number is obtained by integrating $\dot{n}(\mathbf{r},t)$, $\dot{N}(t) = \int \dot{n}(\mathbf{r},t)d^3\mathbf{r}$. As is well known [105], the atom loss from the trap induces heating via two dominant processes. These are known as anti-evaporation and recombination heating. Following Ref. [105] we incorporate the latter by an additional temperature parameter T_h in the three-body heating term of the rate equation. To obtain the loss-rate coefficients the data points are then fitted by the numerical solution of the resulting coupled rate equations (Eq. 5.1 and Eq. 5.2 of the Methods). The fits are shown along with the experimental data in Fig. 5.5, and the loss-rate coefficients obtained are summarized in Table 5.4. The model fits the data reasonably well, with the two-body loss rate being negligible and the loss thus dominated by three-body recombination. The one-body loss rate coefficient k_1 is ~ 0.05 s^{-1} for all the data sets. In cases where the fitted values of k_2 are close to zero, we fix them to the corresponding theoretical value to avoid overfitting. Note that the value for k_1 is significantly larger than we obtain for a pure BEC, where we use a much lower laser power for the dipole trap. We attribute the need for a higher value of k_1 here to increased losses due to inelastic light scattering. Otherwise, the values obtained for k_3 for a given value of $a_{2,2}$ are similar to the ones from previous work using the sublevel $(3,3)$ [104, 105].

We now turn to the region around 40 G. The measurements here have a surprise for us. This region is again reached using the lattice trick. The trap depth is approximately 800 nK, with an initial temperature of the samples between 80 and 90 nK and with peak densities of around 1.5×10^{12} cm^{-3}. Note that this time the density is a factor 10 lower than in the previous measurements. Figure 5.5 **c** and **d** show the resulting loss and heating, together with fits similar to those above. First of all, no sweet spot can be identified. For the plot, the values for B were chosen such that the values for $a_{2,2}$ are the same as for the measurements in the region around 160 G. Evidently, accounting for the lower density, the loss and heating observed is significantly greater than in the region around 160 G. The decay curves lie closer together, i.e., the loss does not depend so much on the value of $a_{2,2}$. All this is reflected by the fit results. When testing the fits, we find that both two- and three-body loss are significant. However, leaving all parameters, i.e. k_1, k_2, k_3 and T_h, as free parameters makes our model prone to overfitting. We fix $k_1 = 0.068$/s and we omit the contribution of T_h from the fits as it appears to be negligible. Then, letting k_2 and k_3 vary freely, we find values for k_2 of about 5×10^{-13} cm^3 s^{-1} and for k_3 between about 0.5×10^{-24} cm^6 s^{-1} and 3.2×10^{-24} cm^6 s^{-1}. The specific values are added to Table 5.4. The values for k_2 agree reasonably well with the theoretical values, but the values for k_3 are nearly two orders of magnitude larger than we obtained from the measurements in the region around 160 G or from measurements involving the state $(3,3)$ [104, 105], at given values for the relevant scattering length away from the sweet spots (which are at 160 G for $(3,2)$ and at 21 G for $(3,3)$).

Such high values for k_3 are a surprise, and we can only speculate about the origin of such high three-body loss. A simple calculation (given in Supplementary Note 5.7.3) shows that there is a possible three-body recombination process that flips the spin of one atom to $(3,1)$ while forming a molecule in the least-bound state of the channel $(3,3) + (3,2)$. This process becomes energetically resonant near $B = 45$ G due to the second-order Zeeman effect. Three-body recombination processes assisted by spin exchange are believed to be important for ^{7}Li [356, 357] and ^{39}K [358, 359], but not for ^{87}Rb [360, 361] and ^{85}Rb [362]. We note that this process does not

seem to play a role in the window near 160 G. To discuss the likelihood of this explanation further, we consider the energy mismatch between three free particles and the products of the three-body recombination. In ref. [356], the presence of an additional spin channel, with an energy mismatch of approximately 0.25 E_{vdW} was proposed as the cause of a discrepancy of about two orders of magnitudes in the measured k_3. Here E_{vdW} is the typical energy scale for the van der Waals interaction between the two atoms [88]. The energy mismatch in our case is significantly smaller, in the range of 0 to 0.05 E_{vdW}.

5.5 Discussion

In summary, for the first time, a BEC of Cs has been obtained in a spin state other than the absolute ground state $(3, 3)$. We have identified two windows where this is possible: In a region around 160 G, two-body losses are negligible and three-body losses are sufficiently suppressed. Here, a pure BEC with 3.0×10^4 atoms in $(3, 2)$ can be formed.

The situation is different in a region around 40 G. We have not been able to achieve BEC by direct evaporation in this region. However, creating a BEC first near 160 G and then transferring it in a lattice to 40 G allows us to produce BECs at that field value. Losses are strong, reducing the purity of the BEC and limiting its lifetime to around 0.5 s. Interestingly, three-body rather than two-body losses are the limiting factor. We have not been able to find a sweet spot where three-body recombination is sufficiently suppressed. In fact, the three-body loss-rate coefficient is close to two orders of magnitude larger than we had expected; the high value may be the result spin-flip-aided three-body recombination. This process merits further investigation. One signature would be the direct detection of atoms in $(3, 1)$ produced in the recombination process. We note that the losses in this region set in only when the atoms are released from the lattice into the 3D trap. The losses are nearly fully suppressed when the atoms are kept in, e. g., 1D tubes, as has been done previously in various experiments in our group [17, 363].

More than 20 years after the first attainment of a Cs BEC in $(3, 3)$ [114], BEC in $(3, 2)$ is not merely an academic achievement. While Cs spinor BECs remain out of reach, BEC in $(3, 2)$ opens up new possibilities for impurity and polaron physics. Specifically, for experiments in the context of strong bulk-bulk and impurity-bulk correlations in 1D [45], the strengths of the bulk-bulk and the impurity-bulk interactions can be interchanged, potentially allowing the impurity to serve as a matter-wave probe of the pinning transition [14] through the phase transition point. Precision tests of the underlying quantum field theory, the sine-Gordon model [41], are thus possible. Further uses of $(3, 3)$ as a strongly interacting probe (instead of $(3, 2)$) will enhance experiments on topological phase transitions [309]. In addition, being able to condense Cs in $(3, 2)$ opens new possibilities in quantum-gas mixture setups, e.g., for the production of ultracold and possibly quantum-degenerate samples of heteronuclear molecules such as KCs [364] and RbCs [365, 366].

Data availability Data supporting this study are openly available from Zenodo at [367].

		Experiment			Theory
B (G)	$a_{2,2}$ (a_0)	k_1 (s^{-1})	k_2 ($10^{-14}\,cm^3\,s^{-1}$)	k_3 ($10^{-26}\,cm^6\,s^{-1}$)	k_2 ($10^{-14}\,cm^3\,s^{-1}$)
37.1	89	-	18.2(49)	323.2(108)	73.2
40.7	247	-	35.5(25)	179.9(47)	59.2
43.7	377	-	88.7(30)	52.9(55)	47.0
45.4	449	-	49.5(27)	135.2(53)	51.8
47.0	517	-	39.4(26)	156.5(44)	51.6
151.1	88	0.040(11)	2.1(12)	4.56(22)	1.2
167.0	379	0.057(12)	1.2 (fixed)	0.50(10)	1.2
172.4	452	0.062(1)	1.8 (fixed)	1.11(2)	1.8
177.7	517	0.054(4)	2.3 (fixed)	1.86(5)	2.3

Tab. 5.1: **Experimentally determined and theoretically predicted values of loss-rate coefficients in the windows around 40 G and 160 G.** The errors in the experimental values are determined from the fit.

Acknowledgements
We thank R. Grimm for discussions and for pointing out to us the possible loss mechanism in the region near 40 G. The Innsbruck team acknowledges funding by a Wittgenstein prize grant under the Austrian Science Fund's (FWF) project number Z336-N36, by the European Research Council (ERC) under project number 789017, and by an FFG infrastructure grant with project number FO999896041. MH thanks the doctoral school ALM for hospitality, with funding from the FWF under the project number W1259-N27. The theoretical work was supported by the UK Engineering and Physical Sciences Research Council (EPSRC) Grant Nos. EP/P01058X/1, EP/V011677/1 and EP/W00299X/1.

5.6 Materials and methods

5.6.1 Fitting of loss measurements

For our fitting procedure we use a coupled fit of the atom number and the temperature evolution [105, 366]

$$\dot{N}(t) = -k_1 N(t) - k_2\beta\frac{N(t)^2}{2^{3/2}T(t)^{(3/2)}} - k_3\beta^2\frac{N(t)^3}{3^{3/2}T(t)^3}, \tag{5.1}$$

$$\dot{T}(t) = k_2\beta\frac{N(t)}{2^{7/2}T(t)^{(1/2)}} + k_3\beta^2\frac{N(t)^2(T(t)+T_\mathrm{h})}{3^{5/2}T(t)^3}, \tag{5.2}$$

where $\beta = (m\bar{\omega}^2/2\pi k_\mathrm{B})^{3/2}$ with the mass m of the Cs atom, and $\bar{\omega} = 2\pi \times \bar{\nu}$ is the geometrically averaged trap frequency. Applying the standard approach of the least-square fit method we minimize the function

$$\chi^2 = \sum_i \left(\frac{r_\mathrm{N}(i)}{\sigma_\mathrm{N}(i)}\right)^2 + \sum_i \left(\frac{r_\mathrm{T}(i)}{\sigma_\mathrm{T}(i)}\right)^2. \tag{5.3}$$

Here $r_\mathrm{N} = (N_\mathrm{exp} - N_\mathrm{mod})$ ($r_\mathrm{T} = (T_\mathrm{exp} - T_\mathrm{mod})$) are the residual of the number of atoms (temperature), N_exp (T_exp) is the measured atom number (temperature), and N_mod (T_mod) are the corresponding values obtained from Eq. 5.1 (Eq. 5.2). The weighted error of the atom loss (temperature) measurements is $\sigma_\mathrm{N}(i)$ ($\sigma_\mathrm{T}(i)$). For the region near 160 G we use k_1, k_3 and T_h in Eqs. 5.1 and 5.2 as free parameters. Additionally using k_2 as a free parameter yields non-zero values of k_2 only for the data set at 151.1 G. We hence leave k_2 as a free parameter for this particular data set and set it to the corresponding theoretical values for the others. In the region near 40 G, we leave k_3 and k_2 as free parameters and restrict $k_1 = 0.068$/s and $T_\mathrm{h} = 0$ μK to avoid overfitting. Note that for all of these fits the correlation coefficients between the loss coefficients are above 0.9. The fitting parameters listed in Tab. 5.4 include the standard error, which is derived from the diagonal elements of the variance-covariance matrix.

$B_{\rm res}$ (G)	Δ (mG)	$a_{\rm bg}$ (a_0)	$a_{\rm res}$ (a_0)
134.28	−0.0076	−402	2.5×10^4
136.96	−0.12	−293	3.3×10^4
141.10	−0.47	−147	1.7×10^6
144.99	−4.1	−21.3	107
147.73	−2.9	−154	5.9×10^6

SUPPLEMENTARY TABLE 5.2: Parameters of i-wave Feshbach resonances between 130 and 150 G, from coupled-channel calculations with $L_{\rm max}=8$.

5.7 Supplementary notes

5.7.1 Calculated resonance parameters

We locate and characterise resonances in our coupled-channel calculations using the methods of Ref. [354]. We use the regularised scattering length procedure, which is suitable for the weak background inelasticity that is present for the resonances here. Characterising the d-wave resonance in Fig. 5.4 near 147.5 G is complicated by the significant variation of the background scattering length $a_{\rm bg}$ across its width. We therefore subtract off a field-dependent reference $a_{\rm ref}(B) = (B-147.5\ {\rm G})\times 25\ a_0\ {\rm G}^{-1}$ before fitting to obtain the parameters given in the main text. The field-variation of the background means it is not possible to define the resonance width Δ as usual, but the strength $a_{\rm bg}\Delta$ is nonetheless well defined. The g-wave resonance shown in Fig. 5.4 is narrower and simpler to fit, giving parameters $B_{\rm res} = 154.18$ G, $\Delta = 20$ mG, $a_{\rm bg} = 160\ a_0$, and $a_{\rm res} = 3.2 \times 10^6\ a_0$.

The resonances described in Supplementary Note 5.7.2 are harder to assign and characterise. The coupled-channel calculations described in the main text use the interaction potential of Berninger *et al.* [351] with a basis set limited by $L_{\rm max} = 4$. This is appropriate because the potential was fitted to experimental results using this basis set, so that the potential itself accounts (in an averaged way) for the absence of basis functions with $L > 4$. However, these calculations show only the two resonances discussed above in the region of interest. We therefore carry out further calculations with $L_{\rm max} = 6$ and 8. These calculations reveal several additional narrow resonances in this region, due to i-wave ($L = 6$) states; their parameters are listed in Table 5.2. In each case there is at least one i-wave resonance within 3 G of the observed loss feature, but there is no clear mapping between the individual calculated resonances and experimental loss peaks. Specific assignments of the loss peaks would require refitting the entire interaction potential, using a more accurate form for the shorter-range part of the interaction potential than in Ref. [351]. This is outside of the scope of the present work.

5.7.2 Resonances in the range of $B = 138$ to 145 G

We carry out an atomic loss spectroscopy measurement in the magnetic field region between 138 and 145 G by holding a non-condensed sample of atoms in $(3, 2)$ in the dipole trap for 2 s and recording the number of remaining atoms N as B is varied. The results are plotted in Supplementary Fig. 5.6. We find three loss features within this region, at 139.80(1), 144.48(1) and 144.65(1) G.

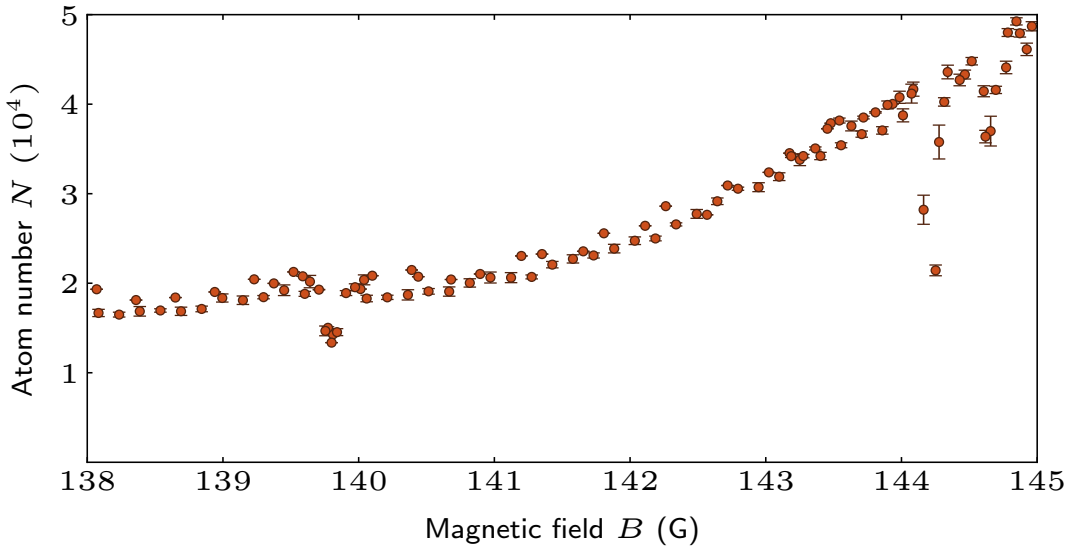

SUPPLEMENTARY FIG. 5.6: **Search for additional Feshbach resonances.** Loss spectroscopy performed with a non-condensed cloud in the dipole trap between 138 G and 145 G. For this measurement the sample is held in the trap for 2 s before imaging via the standard TOF technique. Each data point is an average of up to five repetitions.

5.7.3 Three-body recombination processes assisted by spin exchange

As a possible collision process accounting for the large three-body loss measured in the magnetic field region around 40 G, we consider three-body recombination assisted by a spin-exchange process. We begin with three atoms in the $(3,2)$ state, each with energy E_2, undergoing a spin-exchange collision that produces one atom in each of the states $(3,3)$, $(3,2)$ and $(3,1)$, with corresponding energy E_{m_f}. Between 40 and 50 G, the Zeeman energy, mostly dominated by the quadratic Zeeman shift, results in an excess energy of approximately 50 to 100 kHz for this spin-exchange process. This is of the same order of magnitude as the binding energy $E_{\mathrm{b},m_{f1},m_{f2}}$ of a weakly bound dimer in the channel $(3,3)+(3,2)$ in this region of field. In Supplementary Fig. 5.7 we show the energy difference between the excess Zeeman energy and the binding energy of weakly bound dimers in the spin channels $(3,3)+(3,2)$, $(3,3)+(3,1)$, and $(3,2)+(3,1)$, respectively. The binding energies of the dimers are calculated using

$$E_{\mathrm{b},m_{f1},m_{f2}} = -\hbar^2/(2\mu(a_{m_{f1},m_{f2}} - \bar{a})^2), \tag{5.4}$$

where μ is the reduced mass of the atom pair and $\bar{a} \approx 96.56a_0$ is the mean scattering length of Cs. From Supplementary Fig. 5.7 we see that at 45 G the formation of a molecule in the $(3,3)+(3,2)$ channel becomes energetically resonant. This suggests that three-body recombination via a spin-exchange collision is the likely cause of the large values of k_3 that we measure in this region. Interestingly we further find from Supplementary Fig. 5.7 that molecular channels $(3,2)+(3,1)$ and $(3,3)+(3,1)$ also have resonant features above 55 G.

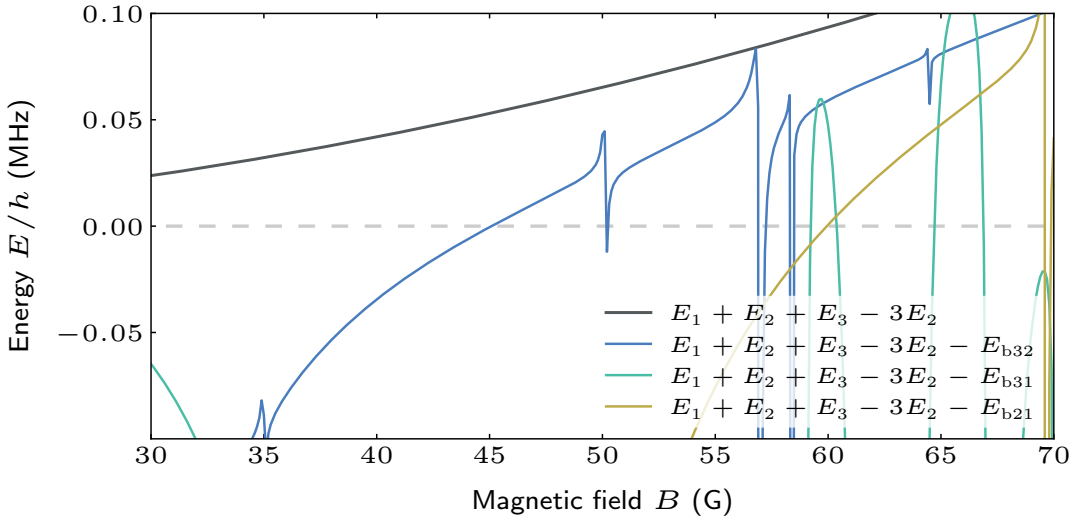

SUPPLEMENTARY FIG. 5.7: **Energies of possible decay channels for spin-exchange-assisted three-body recombination around 40 G.** Excess Zeeman energy required for the spin-exchange process $(3,2)+(3,2) \rightarrow (3,3)+(3,1)$ (black). Energy difference between the excess Zeeman energy and the binding energy of a weakly bound dimer in $(3,3)+(3,2)$ (blue), $(3,3)+(3,1)$ (green) and $(3,2)+(3,1)$ (yellow). In the legend the Zeeman shift and the binding energies are labeled as E_{m_f} and $E_{\mathrm{b},m_{f1},m_{f2}}$, respectively. The dashed line shows zero energy separation.

This process differs from a typical three-body recombination collision, where the molecular binding energy is carried away by the collision products. Here most of the binding energy is absorbed by the excess Zeeman energy, so the products do not gain significant kinetic energy.

CHAPTER 6

ADDITIONAL PUBLICATIONS

Observation of many-body dynamical localization

Yanliang Guo,[1,*] Sudipta Dhar,[1,*] Ang Yang,[2,*] Zekai Chen,[1] Hepeng Yao,[3] Milena Horvath,[1] Lei Ying,[2,†] Manuele Landini,[1] and Hanns-Christoph Nägerl[1,‡]

[1] *Institut für Experimentalphysik und Zentrum für Quantenphysik, Universität Innsbruck, Technikerstraße 25, Innsbruck, 6020, Austria*
[2] *School of Physics, Zhejiang University, Hangzhou 310027, China*
[3] *DQMP, University of Geneva, 24 Quai Ernest-Ansermet, Geneva, CH-1211, Switzerland*

(Dated: December 22, 2023)

The quantum kicked rotor is a paradigmatic model system in quantum physics. As a driven quantum system, it is used to study the transition from the classical to the quantum world and to elucidate the emergence of chaos and diffusion. In contrast to its classical counterpart, it features dynamical localization, specifically Anderson localization in momentum space. The interacting many-body kicked rotor is believed to break localization, as recent experiments suggest. Here, we present evidence for many-body dynamical localization for the Lieb-Liniger version of the many-body quantum kicked rotor. After some initial evolution, the momentum distribution of interacting quantum-degenerate bosonic atoms in one-dimensional geometry, kicked hundreds of times by means of a pulsed sinusoidal potential, stops spreading. We quantify the arrested evolution by analysing the energy and the information entropy of the system as the interaction strength is tuned. In the limiting cases of vanishing and strong interactions, the first-order correlation function exhibits a very different decay behavior. Our results shed light on the boundary between the classical, chaotic world and the realm of quantum physics.

Chaos is a phenomenon that is found almost everywhere in our daily life and it plays a central role in many of the sciences. Nonlinear complex systems, as they appear abundantly in mathematics, physics, biology, ecology, meteorology, economics, and other fields, are generally subject to chaotic dynamics [1]. The long-time evolution sensitively depends on the initial conditions and is inherently unpredictable. Chaos, although it has a negative connotation, is often very useful. It is intimately connected to ergodicity, and dense sampling of the available phase space drives many of the important physical processes, from thermodynamics to biology [2]. However, this behavior is in stark contrast to what one expects from quantum physics [3, 4]. The evolution of a closed (non-relativistic) quantum system is subject to the Schrödinger equation and it is unitary, i.e., in principle fully reversible and non-chaotic, at least to the point of measurement. The central questions are hence: Where is the boundary between the quantum coherent and the classical chaotic world? Which processes, apart from the measurement process, break the non-chaotic dynamics in a quantum system? Do particle-particle interactions necessarily lead to chaotic dynamics, in particular for strong interactions?

A minimal physical system to study chaotic behavior is a rotating object periodically kicked by an external force. A transition from integrable to chaotic motion is found as the kick strength crosses a critical value. Its quantum version, known as quantum kicked rotor (QKR), is a paradigmatic example in which quantum coherence can prevent the system from falling into the regime of quantum chaos even in the strong-driving regime, in stark contrast to the classical counterpart. This counter-intuitive phenomenon can be understood as Anderson localization in momentum space [5–7]. It is termed dynamical localization (DL) and has been demonstrated experimentally in dilute ultracold atomic gases [8–10].

The QKR is a highly idealized single-particle model system. Realistic systems consist of many particles that interact with each other. Interactions almost always lead to a randomization of the many-body dynamics [11, 12]. Nevertheless, recent theoretical and experimental work has identified various dynamical quantum many-body systems for which ergodicity is broken. Examples include many-body localized cold atoms in lattices [13], many-body scar states of interacting Rydberg atom arrays [14], and prethermalized samples of bosons in low dimension [15, 16]. Driving an interacting quantum many-body system further increases the complexity. For the case of the many-body QKR a breakdown of DL has been proposed using meanfield approaches [17–19], and in fact recent cold-atom experiments with either weakly interacting one-dimensional (1D) [20] or strongly interacting 3D gases [21] align with these proposals. However, recent theoretical work [22–26] suggests that DL may persist in an interacting, even strongly interacting many-body quantum system. Specifically, interacting 1D bosonic gas as an ideal Lieb-Lininger QKR is proposed to support many-body dynamical localization (MBDL). Driving a strongly correlated interacting system surprisingly may not have to end up in chaotic dynamics.

Here we report the observation of MBDL in interaction-tunable 1D Bose gases. Using quantum-degenerate samples of Cs atoms, we realize the Lieb-Liniger quantum kicked rotor, a paradigmatic model

* These authors contributed equally to this work.
† leiying@zju.edu.cn
‡ christoph.naegerl@uibk.ac.at

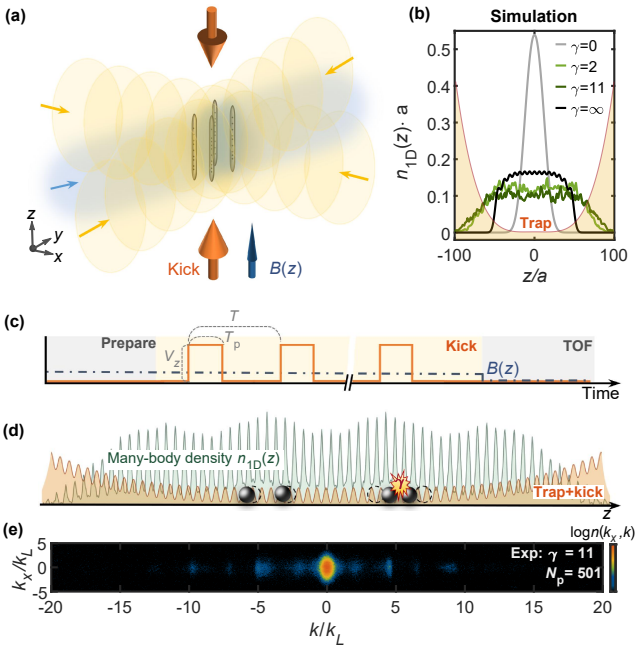

Figure 1. **Experimental implementation of MBDL.** (a) Sketch of the 3D BEC loaded into an array of 1D tubes generated by the 2D optical lattice (yellow) and partially compensated by a blue-detuned optical anti-trap (blue). The QKR lattice propagates along the vertical z-direction. (b) Calculated ground-state many-body 1D spatial density $n_{1D}(z)$ for the flat-bottom trap in units of a^{-1} for various values of the interaction parameter γ. The data for $\gamma = 2$ and $\gamma = 11$ is obtained from a quantum Monte Carlo calculation at a temperature of 2 nK, while the data for $\gamma = 0$ and $\gamma = \infty$ are the zero-temperature results from a one-cycle Floquet map and fermionization method [27, 28]. (c) Schematic of the experimental QKR sequence with N_p pulses sandwiched between the preparation and TOF-imaging procedures. (d) Illustration of $n_{1D}(z)$ (green) for 4 interacting atoms in a cosine standing-wave potential in the flat-bottom trap (orange) for $\gamma = \infty$. The anti-nodes of $n_{1D}(z)$ register with the nodes of the kick potential. The envelope of $n_{1D}(z)$ with the 4 bumps reflects the presence of 4 atoms. (e) Typical absorption image for $\gamma = 11$ after $N_p = 501$ kicks showing the spatial density in color coding after TOF and integrated along the line-of-sight.

for the simulation of driven interacting quantum many-body systems. We tune the interaction strength from the non-interacting regime to the Tonks-Girardeau (TG) regime [29–31] and find signatures of MBDL in a freezing of the momentum distribution and in a saturation of the energy and the entropy as the 1D Bose gases are kicked hundreds of times. The first-order correlation function exhibits a strikingly different decay in the two limiting cases of zero and strong interactions. Our results are in agreement with recent proposals [22–24] and are captured qualitatively by our modeling.

The experiment starts by loading a Bose-Einstein condensate (BEC) of Cs atoms [32] into an array of narrow 1D tubes created by a 2D optical lattice as illustrated in Fig. 1(a). The laser beams forming the lattice propagate in the horizontal x-y plane at right angle to each other, and their power is adiabatically ramped up to give a lattice depth of $30E_r$, where $E_r = \pi^2\hbar^2/(2ma^2)$ is the recoil energy. Here, $a = \lambda/2 = \pi/k_L = 532.25$ nm is the lattice spacing with the wavenumber k_L that is set by the wavelength λ of the lattice light. At this depth, tunneling between the tubes is fully suppressed, and the tubes can be considered as independent. A magnetic field B along the vertical z-direction controls the inter-atomic interaction [33] as quantified by γ, the dimensionless 1D Lieb-Liniger interaction parameter [34]. By choosing values between $\gamma = 0$ and $\gamma = 11$ we cover the range from the non-interacting, single-particle regime well into the strongly interacting TG regime in which the bosons have fermionized. The atoms are levitated against gravity by means of a gradient of B. The finite transversal extent of the lattice beams results in weak harmonic trapping with trap frequency $\nu_z = 14.7(3)$ Hz along the tubes' direction. We partially compensate this trap by means of a horizontally propagating blue-detuned anti-trap laser beam. This forms a flat-bottom potential, as illustrated in Fig. 1(b). Typically, we fill about 10^4 tubes, with a weighted average of 18 atoms per tube. At this stage, the 1D systems are in equilibrium with a temperature around 2 nK, which is estimated by the thermometry method demonstrated in Refs. [35, 36]. Calculated 1D density distributions $n_{1D}(z)$ for various values of γ are included in Fig. 1(b).

We next implement the QKR procedure. A longitudinal standing wave with lattice spacing a and depth V_z is periodically pulsed on with period T and square-pulse duration T_p for a number of N_p pulses as illustrated in Fig. 1(c). We choose $T = 60\,\mu$s and 80μs, $T_p = 10\,\mu$s, and $V_z = 20E_r$, resulting in a dimensionless kick strength $K = 3.3$ and $K = 4.4$ respectively, see below and Supplemental Material. For values of N_p between 1 and 1101, the entire pulse sequence takes up to 66 ms and 88 ms, respectively. Fig. 1 (d) illustrates the many-body wavefunction during the kicking procedure. We obtain the longitudinal momentum distribution $n(k)$ by a 20-ms time-of-flight (TOF) absorption-imaging technique. A typical absorption image is shown in Fig. 1 (e) and $n(k)$ is obtained as a probability distribution by integration along the transversal direction and normalizing by the atom number. For a faithful measurement of $n(k)$ the particle interaction is switched off via a Feshbach-resonance's zero crossing [33] during TOF. From $n(k)$ we subsequently compute the kinetic energy E, the information entropy S, and the one-body correlation function G.

We model the system by the explicitly time-dependent Lieb-Liniger QKR Hamiltonian. For N interacting bosons with mass m moving in a 1D tube at zero tem-

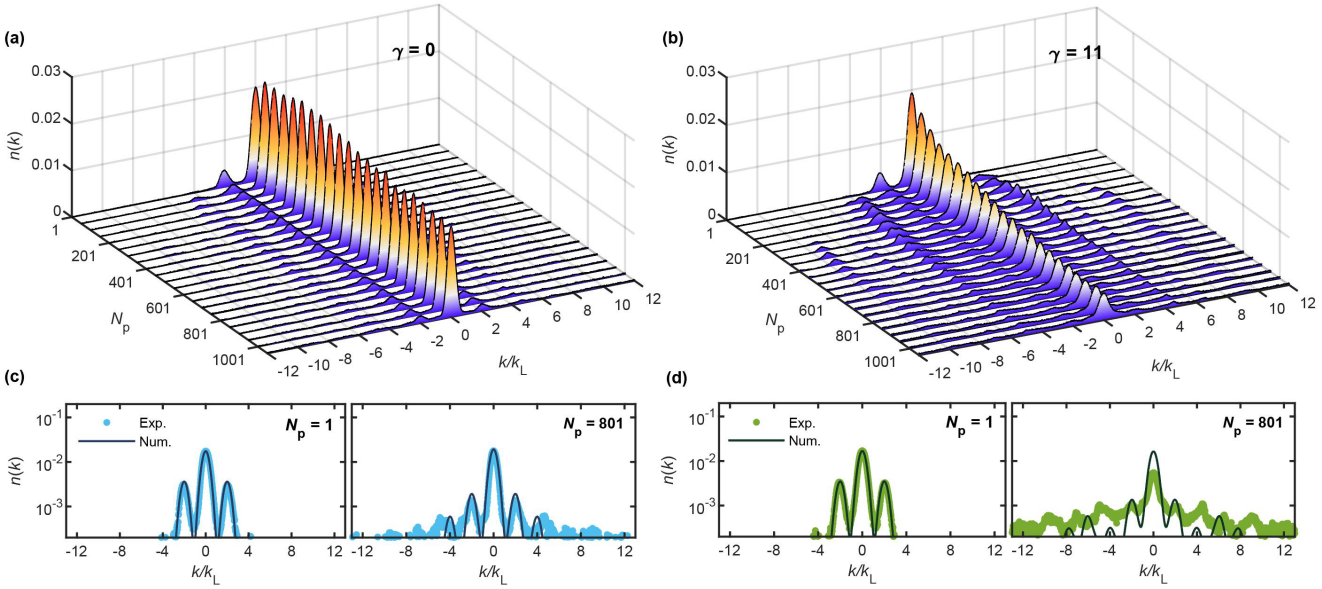

Figure 2. **Evolution of the 1D momentum distribution.** Measured $n(k)$ for the non-interacting (a) and strongly-interacting case (b) for a kick strength $K=3.3$. In (a) and (b) the number of kicks N_p is increased from 1 to 1101 in steps of 50. Example distributions are shown in (c) and (d) for $N_\mathrm{p}=1$ and 801 for $\gamma=0$ and $\gamma=11$, respectively. The data is compared to numerically calculated distributions for $\gamma=0$ and $\gamma=\infty$. In view of the finite TOF duration these are convoluted by Gaussians whose waist is half of the flat-bottom length. All experimental distributions are the average of three realizations.

perature, it reads [22, 24]

$$H(t)=\sum_{i=1}^{N}\left[\frac{P_i^2}{2m}+\hbar\kappa\cos\left(2k_L z_i\right)\sum_{N_\mathrm{p}}\delta_{T_\mathrm{p}}\left(t-N_\mathrm{p}T\right)+V_\mathrm{ext}\left(z_i\right)\right]+g_\mathrm{1D}\sum_{i<j}^{N}\delta(z_i-z_j). \tag{1}$$

Here, $\hbar\kappa=V_z T_\mathrm{p}/2$ sets the kick strength $K=8TE_\mathrm{r}\kappa/\hbar$. The first three terms represent the QKR for a single particle at position z_i moving in the trap potential V_ext. The last summand models the δ-type pairwise contact interaction whose strength g_1D is related to γ via $\gamma=mg_\mathrm{1D}/n_\mathrm{1D}\hbar^2$. Details of our modeling are given in Supplemental Materials (SM).

We first turn to the evolution of the momentum distribution as N_p is increased. Fig. 2 presents the experimental results of $n(k)$ for two limiting values of the interaction strength, namely for vanishing ($\gamma=0$) and for very strong interactions ($\gamma=11$). In the former case, the system is in the single-particle regime, in the latter it is deeply in the TG regime. Starting with the first kick, higher momentum states are populated, primarily the ones with $\pm2\hbar k_\mathrm{L}$. For the non-interacting case, some of the population is subsequently transferred to higher momentum states, but evidently further transfer is halted and the distribution becomes stationary, as can be seen from comparing the data sets with $N_\mathrm{p}=301$ and $N_\mathrm{p}=1001$. The system is dynamically localized [9, 10, 21]. In the interacting case, the change in the momentum distribution from $N_\mathrm{p}=1$ to about $N_\mathrm{p}=301$ is much more pronounced. However, the subsequent evolution, in particular from $N_\mathrm{p}=501$ to $N_\mathrm{p}=1101$, appears to have stopped. Examples of $n(k)$ after the first kick and in the localized state after $N_\mathrm{p}=801$ for the non-interacting and the strongly interacting cases are shown in Fig. 2 (c) and (d), respectively. As we will argue below, the interacting system, after some initial evolution towards a broadened distribution, has entered the regime of MBDL.

We utilize the Jensen-Shannon divergence J to quantitatively study the evolution of $n(k)$. It is a measure of the overlap of two probability distributions [37] with values between $J=0$ (full overlap) and $J=1$ (no overlap), see SM. Fig. 3(a) presents the time evolution of J for both the non-interacting and the strongly interacting scenarios as N_p is stepped in units of 50. Initially, as the distributions still change, the value for J is large compared to the noise floor. But quite quickly, J drops towards the noise level. For the non-interacting case, the noise level is reached already after the first step, and overlap cannot be distinguished from noise beyond $N_\mathrm{p}=300$. The system has undergone dynamical localization. For the interacting case, this takes about $N_\mathrm{p}=450$ kicks. Afterwards, the change in the distributions is minimal and cannot be distinguished from the noise anymore. The system has undergone MBDL. This can also be seen from a direct comparison of two typical distributions taken at $N_\mathrm{p}=701$ and $N_\mathrm{p}=1001$ as shown in the inset of Fig. 3(a). Within the error bars the two structured distributions are the same, and also the slight shifts away from the multiples of $2\hbar k_\mathrm{L}$ are well reproduced. This is remarkable, as the

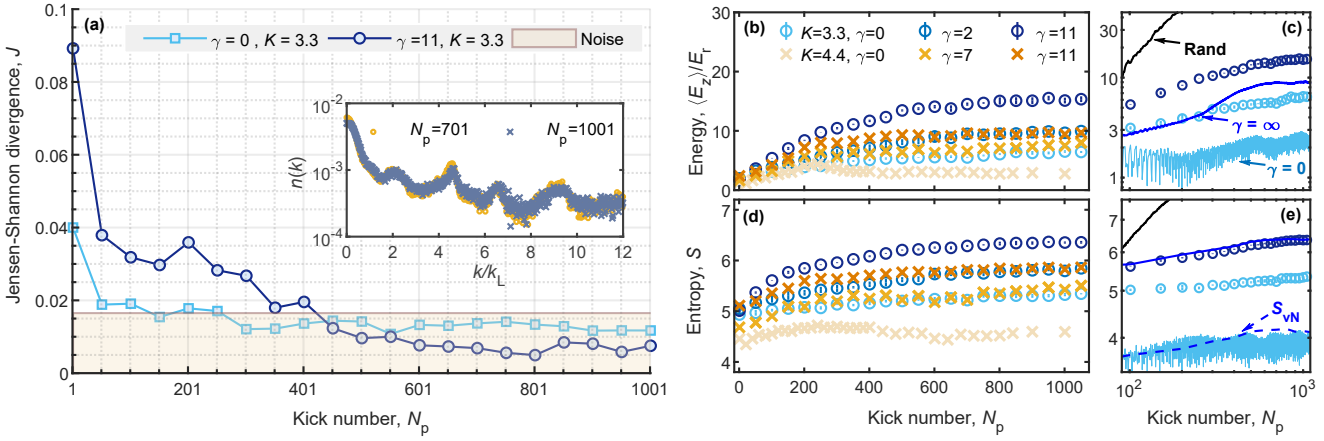

Figure 3. **Evidence for MBDL.** (a) Jensen-Shannon divergence J between the momentum distributions at N_p and $N_\mathrm{p}+100$ as N_p is stepped in units of 50, for the non-interacting ($\gamma=0$, light blue squares) and the strongly interacting ($\gamma=11$, dark blue circles) cases. The orange shaded area indicates the typical shot-to-shot noise determined by comparing 3 repeats at $N_\mathrm{p}=501$. Inset: Comparison of $n(k)$ at $N_\mathrm{p}=701$ and at $N_\mathrm{p}=1001$ for the strongly interacting case $\gamma=11$. (b-e) Time evolution of the kinetic energy $\langle E_z\rangle$ (b) and of the information entropy S (d) for various values of the 1D interaction strength γ as indicated and for two values of the kick strength $K=3.3$ ($T=60\,\mu$s, circles) and $K=4.4$ ($T=80\,\mu$s, crosses). (c) and (e): Comparing the energy (c) and entropy (e) calculated for the non-interacting (light blue solid line) and infinitely interacting cases (dark blue solid line) to the data with $\gamma=0$ (light blue circles) and $\gamma=11$ (dark blue circles) for the case of $K=3.3$ on a log-log scale. Fast oscillations for the theory data for $\gamma=0$ are not resolved. For comparison, the time evolution of a non-interacting system with random kicks is presented (black line, average over 10 realizations). Additionally, the calculated von-Neumann entropy S_vN for infinite interactions is shown (dashed line). The statistical error in (b) through (e) is smaller than the symbol size.

interacting system has been kicked 300 times more for the later measurement. Evidently, the interplay of quantum coherence and strong interactions prevents the breaking of localization.

We further quantify the behavior observed above by analyzing the longitudinal kinetic energy $\langle E_z\rangle \propto \langle k^2\rangle$ and the information entropy $S=-\sum_k n(k)\log[n(k)]$ for various values of γ. The former is measure of the absorbed energy, and the latter relates to the degree of chaos in the system. The data is taken for two values of the kick strength, $K=3.3$ and $K=4.4$, and, next to the previous choice of $\gamma=0$ and $\gamma=11$, for intermediate values of γ. The experimental results are shown in Fig. 3(b) and (d), For any choice of γ, both observables, after an initial rise, settle to constant values after a few hundred kicks. Evidently, the evolution has stopped. The limiting values depend on γ: The larger γ, the larger the localization energy and the localization entropy for a given K. The limiting values also depend on K. One can see a clear difference for the data taken for $\gamma=11$, with a smaller kick strength giving larger localization values. We note that for a time evolution up to $N_\mathrm{p}=1001$, atom loss is small and transversal excitations are negligible. Stronger interactions lead to slightly higher atom loss, but losses remain below 25%. We also note that we can increase γ to values that are much larger than the ones used here, e.g., to $\gamma=86$. For this choice we find increased atom loss and pronounced transversal excitations. These become evident already after about 100 kicks. Details on loss and transversal excitations are discussed in SM.

In Fig. 3(c) and (e) we compare the results for vanishing and very strong interactions to our theory data, obtained in the two limiting cases $\gamma=0$ and $\gamma\to\infty$, for which calculations can be carried out. While the experimental data lie above the theory predictions, the growth trend for the energy and the entropy for experiment and theory agree reasonably well. In particular, theory confirms the onset of localization after around 500 kicks. The theory allows us to also calculate the von-Neumann entropy $S_\mathrm{vN}=-\mathrm{Tr}[\rho\log\rho]$, where ρ is the one-particle density matrix (see SM) [27, 38]. It is a measure of the entanglement generated in the system. It also settles to a constant value, and its growth trend is almost the same as for the information entropy. All this behavior is in stark contrast to what happens when the system is subject to random kicks. In that case energy and entropy increase diffusively without bounds, analogous to the case of classical chaos.

We now turn to the quantum coherence of our kicked many-body system. It is contained in the one-particle density matrix $\rho(z,z')=\langle\hat\Psi^\dagger(z')\hat\Psi(z)\rangle$, where $\hat\Psi$ is the many-body field operator. It governs the functional form of the one-body correlation function via $G^{(1)}(z)\propto\int\rho(z,z')dz'$. In practice, one gets $G^{(1)}(z)$ from the Fourier transform of $n(k)$ [29, 36]. The experimental results for $G^{(1)}(z)$ of the QKR are presented in Fig. 4 for the TG regime and the non-interacting regime for two kick strengths and for consecutive values of N_p in the localized regime. As a consequence of the frozen momentum distribution, $G^{(1)}(z)$ does not depend on N_p

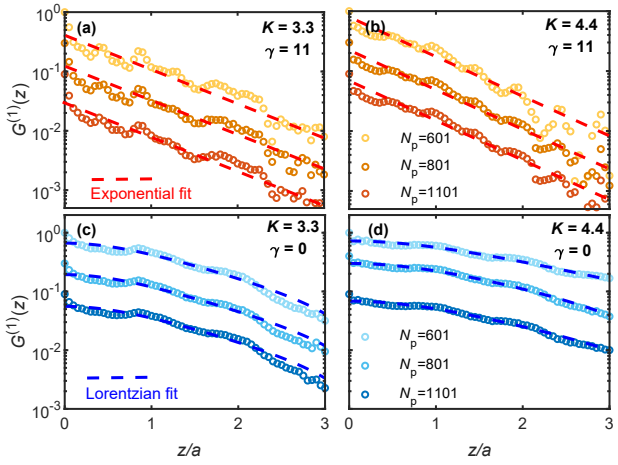

Figure 4. **Decay of the one-body correlation function for DL and MBDL.** (a) and (b): One-body correlation function $G^{(1)}(z)$ for strong interactions ($\gamma = 11$) and two kick strengths and for $N_\mathrm{p} = 601$, 801, and 1101, as indicated. The different datasets have been offset for better visibility. Exponential fits to the data for the range $z/a = 0.25$ to 2.5 are indicated by the dashed lines. (c) and (d): Same as above, but for the non-interacting case ($\gamma = 0$). Lorentzian decays have been fit to the experimental data over the full range (dashed lines).

after MBDL has occurred. The decay for the strongly interacting case is well fit by an exponential for intermediate distances. A frozen correlation length is considered to be a property of the effectively thermalized TG gas in MBDL phase, as predicted for trapping-free systems [24, 25]. The exponential fit is not expected to cover $G^{(1)}$ for very short distances, which via Fourier transform correspond to the region of large momenta. This is compatible with a predicted algebraic-like decay for large momenta in the MBDL phase [23–25]. Our data is in fact consistent with a $n(k) = \mathcal{C}_\mathrm{th} k^{-4}$ behavior. Here, the weight $\mathcal{C}_\mathrm{th}$ is Tan's contact of the effectively thermalized TG gas [24, 39, 40], see details in SM. Contrary to the TG case, for the non-interacting system $G^{(1)}(z)$ exhibits a Lorentzian decay behavior. This implies an exponential decay in momentum space, signalling Anderson-like localization [5]. While the one-body correlation function for the MBDL phase requires more theoretical studies, especially for finite interactions and for trapped systems, the change in the behavior of the correlation function from one regime to the other highlights the many-body effect in the MBDL dynamics.

In summary, we have observed and analyzed a novel many-body phase termed MBDL by periodically kicking a TG gas confined in a flat-bottom trap. Our observation reveals a remarkable phenomenon: The momentum distribution of a strongly correlated system freezes despite the periodic kicks and preserves its characteristic interference structure. The kinetic energy and the information entropy show suppressed growth and saturation. Evidently, the quantum many-body system does not fall into the regime of chaos. The differences for the momentum distributions and the correlation functions between the non-interacting scenario and the strongly interacting one highlight the impact of the many-body effect under the periodic driving. Our findings raise a series of interesting questions to experiment and theory: What mechanisms could break MBDL in our Lieb-Liniger setting and how does chaos emerge from it? What happens for intermediate interactions in the presence of inhomogeneous trapping for which integrability is expected to be broken? As interactions for our system are short-ranged in real space and hence necessarily long-ranged in momentum space, is there a mapping to real-space localized states for the case of long-range real-space interactions [41, 42]? How is the relation to other many-body localized states that are, e.g., found in a lattice setting [43] for which localization happens in real space? The observation of MBDL, in view of recent theoretical research [22–25], opens the door to a further exploration of the emergence of chaos in a many-body setting and provides new directions to investigate the boundary between the classical, chaotic world and the quantum realm, in particular for the strongly interacting scenario.

Acknowledgments

The Innsbruck team acknowledges funding by a Wittgenstein prize grant under Austrian Science Fund (FWF) project number Z336-N36, by the European Research Council (ERC) under project number 789017, by an FFG infrastructure grant with project number FO999896041, and by the FWF's COE 1 and quantA. MH thanks the doctoral school ALM for hospitality, with funding from the FWF under the project number W1259-N27. The team at Zhejiang University is supported by the National Natural Science Foundation of China (Grant No. 12375021) and the National Key R&D Program of China (Grant No. 2022YFA1404203). HY is also supported by the Swiss National Science Foundation under grant number 200020-188687. The numerical calculations make use of the ALPS scheduler library and statistical analysis tools [44–46].

Data Availability

The data that support the findings of this study are made publicly available from Zenodo by the authors at [47].

[1] S. H. Strogatz, *Nonlinear dynamics and chaos with student solutions manual: With applications to physics, biology, chemistry, and engineering* (CRC press, 2018).

[2] G. L. Baker and J. P. Gollub, *Chaotic dynamics: an introduction* (Cambridge university press, 1996).

[3] F. Haake, *Quantum signatures of chaos* (Springer, 1991).

[4] H.-J. Stöckmann, *Quantum Chaos, an introduction* (Cambridge University Press, 1999).

[5] P. W. Anderson, Absence of diffusion in certain random lattices, Phys. Rev. **109**, 1492 (1958).

[6] S. Fishman, D. R. Grempel, and R. E. Prange, Chaos, quantum recurrences, and Anderson localization, Phys. Rev. Lett. **49**, 509 (1982).

[7] D. R. Grempel, R. E. Prange, and S. Fishman, Quantum dynamics of a nonintegrable system, Phys. Rev. A **29**, 1639 (1984).

[8] F. L. Moore, J. C. Robinson, C. F. Bharucha, B. Sundaram, and M. G. Raizen, Atom optics realization of the quantum δ-kicked rotor, Phys. Rev. Lett. **75**, 4598 (1995).

[9] I. Manai, J.-F. Clément, R. Chicireanu, C. Hainaut, J. C. Garreau, P. Szriftgiser, and D. Delande, Experimental observation of two-dimensional Anderson localization with the atomic kicked rotor, Phys. Rev. Lett. **115**, 240603 (2015).

[10] G. Lemarié, J. Chabé, P. Szriftgiser, J. C. Garreau, B. Grémaud, and D. Delande, Observation of the Anderson metal-insulator transition with atomic matter waves: Theory and experiment, Phys. Rev. A **80**, 043626 (2009).

[11] M. Srednicki, Chaos and quantum thermalization, Phys. Rev. E **50**, 888 (1994).

[12] M. Rigol, V. Dunjko, and M. Olshanii, Thermalization and its mechanism for generic isolated quantum systems, Nature **452**, 854 (2008).

[13] P. Bordia, U. Lüschen, H. aand Schneider, M. Knap, and I. Bloch, Periodically driving a many-body localized quantum system., Nature Physics **13**, 460 (2017).

[14] D. Bluvstein, A. Omran, H. Levine, A. Keesling, G. Semeghini, S. Ebadi, T. T. Wang, A. A. Michailidis, N. Maskara, W. W. Ho, S. Choi, M. Serbyn, M. Greiner, V. Vuletić, and M. D. Lukin, Controlling quantum many-body dynamics in driven Rydberg atom arrays, Science **371**, 1355 (2021).

[15] Y. Le, Y. Zhang, S. Gopalakrishnan, M. Rigol, and D. S. Weiss, Observation of hydrodynamization and local prethermalization in 1d Bose gases, Nature **618**, 494 (2023).

[16] D. Abanin, W. De Roeck, W. W. Ho, and F. Huveneers, A rigorous theory of many-body prethermalization for periodically driven and closed quantum systems, Communications in Mathematical Physics **354**, 809 (2017).

[17] S. Lellouch, A. Rançon, S. De Bièvre, D. Delande, and J. C. Garreau, Dynamics of the mean-field-interacting quantum kicked rotor, Phys. Rev. A **101**, 043624 (2020).

[18] D. L. Shepelyansky, Delocalization of quantum chaos by weak nonlinearity, Phys. Rev. Lett. **70**, 1787 (1993).

[19] J. D. Bodyfelt, S. Flach, and G. Gligoric, Interactions destroy dynamical localization with strong & weak chaos, Europhysics Letters **96**, 30004 (2011).

[20] J. See Toh, K. McCormick, X. Tang, S. Ying, X.-W. Luo, C. Zhang, and S. Gupta, Many-body dynamical delocalization in a kicked one-dimensional ultracold gas, Nature Physics **18**, 1297 (2022).

[21] A. Cao, R. Sajjad, H. Mas, E. Q. Simmons, J. L. Tanlimco, E. Nolasco-Martinez, T. Shimasaki, H. E. Kondakci, V. Galitski, and D. M. Weld, Interaction-driven breakdown of dynamical localization in a kicked quantum gas, Nature Physics **18**, 1302 (2022).

[22] C. Rylands, E. B. Rozenbaum, V. Galitski, and R. Konik, Many-body dynamical localization in a kicked Lieb-Liniger gas, Phys. Rev. Lett. **124**, 155302 (2020).

[23] R. Chicireanu and A. Rançon, Dynamical localization of interacting bosons in the few-body limit, Phys. Rev. A **103**, 043314 (2021).

[24] V. Vuatelet and A. Rançon, Effective thermalization of a many-body dynamically localized bose gas, Phys. Rev. A **104**, 043302 (2021).

[25] V. Vuatelet and A. Rançon, Dynamical many-body delocalization transition of a Tonks gas in a quasi-periodic driving potential, Quantum **7**, 917 (2023).

[26] M. Fava, R. Fazio, and A. Russomanno, Many-body dynamical localization in the kicked bose-hubbard chain, Phys. Rev. B **101**, 064302 (2020).

[27] M. Rigol and A. Muramatsu, Ground-state properties of hard-core bosons confined on one-dimensional optical lattices, Phys. Rev. A **72**, 013604 (2005).

[28] J. M. Wilson, N. Malvania, Y. Le, Y. Zhang, M. Rigol, and D. S. Weiss, Observation of dynamical fermionization, Science **367**, 1461 (2020).

[29] B. Paredes, A. Widera, V. Murg, O. Mandel, S. Fölling, I. Cirac, G. V. Shlyapnikov, T. W. Hänsch, and I. Bloch, Tonks–girardeau gas of ultracold atoms in an optical lattice, Nature **429**, 277 (2004).

[30] T. Kinoshita, T. Wenger, and D. S. Weiss, Observation of a one-dimensional Tonks-Girardeau gas, Science **305**, 1125 (2004).

[31] E. Haller, M. Gustavsson, M. J. Mark, J. G. Danzl, R. Hart, G. Pupillo, and H.-C. Nägerl, Realization of an excited, strongly-correlated quantum gas phase, Science **325**, 1224 (2009).

[32] T. Kraemer, J. Herbig, M. Mark, T. Weber, C. Chin, H.-C. Nägerl, and R. Grimm, Optimized production of a cesium Bose–Einstein condensate, Applied Physics B **79**, 1013 (2004).

[33] T. Weber, J. Herbig, M. Mark, H.-C. Nägerl, and R. Grimm, Bose-Einstein condensation of Cesium, Science **299**, 232 (2003).

[34] M. A. Cazalilla, R. Citro, T. Giamarchi, E. Orignac, and M. Rigol, One dimensional bosons: From condensed matter systems to ultracold gases, Rev. Mod. Phys. **83**, 1405 (2011).

[35] Y. Guo, H. Yao, S. Dhar, L. Pizzino, M. Horvath, T. Giamarchi, M. Landini, and H.-C. Nägerl, Cooling bosons by dimensional reduction, arXiv:2308.04144 (2023).

[36] Y. Guo, H. Yao, S. Ramanjanappa, S. Dhar, M. Horvath, L. Pizzino, T. Giamarchi, M. Landini, and H.-C. Nägerl, Experimental observation of the 2d-1d dimensional crossover in strongly interacting ultracold bosons, arXiv:2308.00411 (2023).

[37] J. Lin, Divergence measures based on the Shannon entropy, IEEE Transactions on Information Theory **37**, 145 (1991).

[38] M. Thamm, H. Radhakrishnan, H. Barghathi, B. Rosenow, and A. Del Maestro, One-particle entanglement for one-dimensional spinless fermions after an interaction quantum quench, Phys. Rev. B **106**, 165116 (2022).

[39] S. Tan, Generalized virial theorem and pressure relation for a strongly correlated Fermi gas, Annals of Physics **323**, 2987 (2008).

[40] H. Yao, D. Clément, A. Minguzzi, P. Vignolo, and L. Sanchez-Palencia, Tan's contact for trapped Lieb-Liniger bosons at finite temperature, Phys. Rev. Lett. **121**, 220402 (2018).

[41] R. M. Nandkishore and S. L. Sondhi, Many-body localization with long-range interactions, Phys. Rev. X **7**, 041021 (2017).

[42] N. Defenu, T. Donner, T. Macrì, G. Pagano, S. Ruffo, and A. Trombettoni, Long-range interacting quantum systems, Rev. Mod. Phys. **95**, 035002 (2023).

[43] D. A. Abanin, E. Altman, I. Bloch, and M. Serbyn, Colloquium: Many-body localization, thermalization, and entanglement, Rev. Mod. Phys. **91**, 021001 (2019).

[44] M. Troyer, B. Ammon, and E. Heeb, Parallel object oriented Monte Carlo simulations, Lect. Notes Comput. Sci. **1505**, 191 (1998).

[45] A. F. Albuquerque, F. Alet, P. Corboz, P. Dayal, A. Feiguin, S. Fuchs, L. Gamper, E. Gull, S. Gürtler, A. Honecker, *et al.*, The alps project release 1.3: Open-source software for strongly correlated systems, Journal of Magnetism and Magnetic Materials **310**, 1187 (2007).

[46] B. Bauer, L. Carr, H. G. Evertz, A. Feiguin, J. Freire, S. Fuchs, L. Gamper, J. Gukelberger, E. Gull, S. Guertler, *et al.*, The alps project release 2.0: open source software for strongly correlated systems, Journal of Statistical Mechanics: Theory and Experiment **2011**, P05001 (2011).

[47] Data set is available from Zenodo at doi: 10.5281/zenodo.10375982.

[48] H. Buljan, R. Pezer, and T. Gasenzer, Fermi-Bose transformation for the time-dependent Lieb-Liniger gas, Phys. Rev. Lett. **100**, 080406 (2008).

[49] W. Xu and M. Rigol, Universal scaling of density and momentum distributions in Lieb-Liniger gases, Phys. Rev. A **92**, 063623 (2015).

[50] D. M. Ceperley, Path integrals in the theory of condensed helium, Rev. Mod. Phys. **67**, 279 (1995).

[51] M. Boninsegni, N. Prokof'ev, and B. Svistunov, Worm algorithm for continuous-space path integral Monte Carlo simulations, Phys. Rev. Lett. **96**, 070601 (2006).

[52] M. Boninsegni, N. V. Prokof'ev, and B. V. Svistunov, Worm algorithm and diagrammatic Monte Carlo: A new approach to continuous-space path integral Monte Carlo simulations, Phys. Rev. E **74**, 036701 (2006).

[53] S. Tan, Large momentum part of a strongly correlated Fermi gas, Annals of Physics **323**, 2971 (2008).

Supplementary Materials

CONTENTS

References 5

S1. Experimental sequence 8

S2. Supplementary experimental data 8
A. MBDL with stronger interactions 8
B. Evidence of algebraic k^{-4} tail during the kicking process 9
C. Many-body QKR model and fermionization of bosons 9

S3. Numerical methods 10
A. Details of exact numerics 10
B. Quantum Monte Carlo simulation 11
C. Calculation of Jensen-Shannon divergence 11

S4. Additonal numerical results 11
A. Localization for various trapping conditions 11
B. Convergence of the energy with basis size 12
C. MBDL for different atom numbers 12
D. Momentum and $G^{(1)}$ evolution 12

S1. EXPERIMENTAL SEQUENCE

The experiment starts with a 3D interaction-tunable Bose-Einstein condensate (BEC) consisting of approximately 1×10^5 Cs atoms prepared in the lowest magnetic hyperfine state $|F, m_F\rangle = |3, 3\rangle$, held in a crossed-beam dipole trap and levitated against gravity by a gradient of the magnetic field $B(z)$ [32]. The BEC is prepared in the Thomas-Fermi regime with a 3D s-wave scattering length of $a_{3D} \approx 190a_0$, where a_0 is Bohr's radius. A 2D optical lattice is gradually ramped up within 600 ms to $30E_r$, cutting the 3D system in the horizontal x-y plane into an array of 1D tubes oriented along the vertical z-direction. After loading the atoms into the lattice, the initial crossed-beam trap is ramped down within 300 ms. The offset magnetic field is then ramped up adiabatically to a desired value between $B \approx 17$ G and 40 G to set a_{3D} in the range between $a_{3D} \approx 0a_0$ and $620a_0$, with $3a_0$ precision. After holding the atoms for an additional time of 100 ms, the 1D tubes are periodically kicked by a pulsed one-dimensional optical lattice propagating along the longitudinal direction z. After the kicks, all trapping fields are switched off and the atoms perform a 20-ms TOF, during which, importantly, the inter-particle interaction is turned off to avoid any residual interaction effects by switching a_{3D} to zero. This allows us to obtain the momentum distribution $n(k)$ as the various experimental parameters are varied via absorption imaging and integration over the transverse direction.

The horizontally propagating lattice beams cause weak harmonic trapping along the longitudinal direction of the tubes with a trap frequency of about 14.7 Hz as a result of their finite beam size. We use an additional laser beam with a wavelength of 808 nm, which is blue detuned to the laser-cooling transition and which propagates horizontally, to create an anti-trap in the z-direction. The waist of this beam is 135 µm, whereas the lattice beams have a waist of 300 µm. This results in a flat-bottom potential with a length of around 50 µm. The detuning of the anti-trap beam is sufficiently large to not cause any noticeable heating from spontaneous light scattering.

S2. SUPPLEMENTARY EXPERIMENTAL DATA

A. MBDL with stronger interactions

We have taken similar data as shown in Fig. 3 for an even stronger interaction strength $\gamma = 86$. The experimental results are presented in Fig. S1. For both two kick strengths, the qualitative evolution of the kinetic energy and of the entropy for $\gamma = 86$ does not differ from the previous results in main text. However, the stronger interaction leads to more atom losses and to significant transversal excitations, as shown in Fig. S2. Particularly for the case of $\gamma = 86$ with $K = 3.3$, the transversal waist increases substantially as a function of the kick number. These results indicate the situation that the gas enters into a regime of the dimensional crossover from 1D to 3D, which requires further exploration.

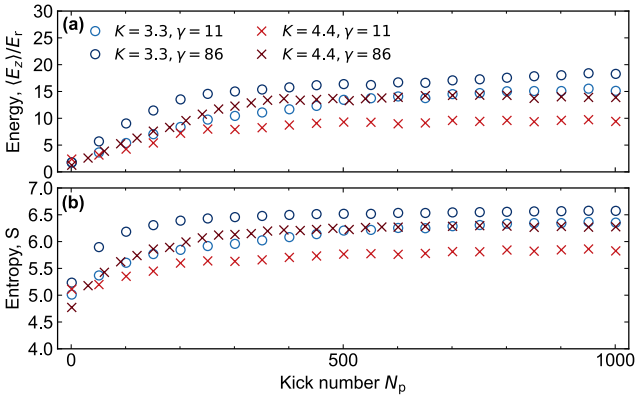

Figure S1. Evolution of the kinetic energy (a) and of the information entropy (b) for $\gamma = 11$ (same data as is shown in Fig. 3 of the main text) and $\gamma = 86$ for two kick strengths, $K = 3.3$ ($T = 60$ µs) and $K = 4.4$ ($T = 80$ µs).

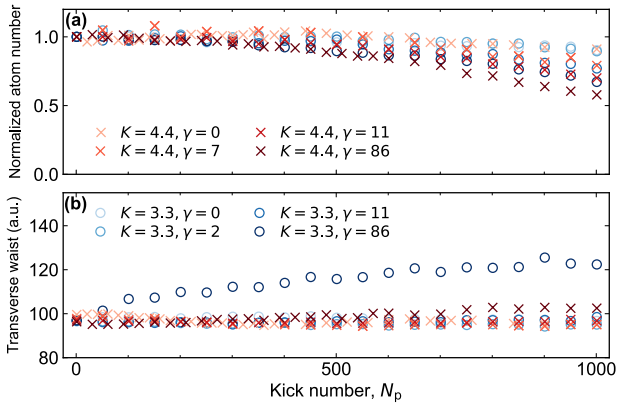

Figure S2. Evolution of the atom number and the transverse waist during the kicking process. (a) Atom number normalized to the initial one as a function of the kick number. (b) Evolution of the extracted Gaussian waist from the transverse momentum distribution of the main peak within $[-k_{\mathrm{L}}, k_{\mathrm{L}}]$. The data in (a) and (b) is shown for all cases from this work as indicated.

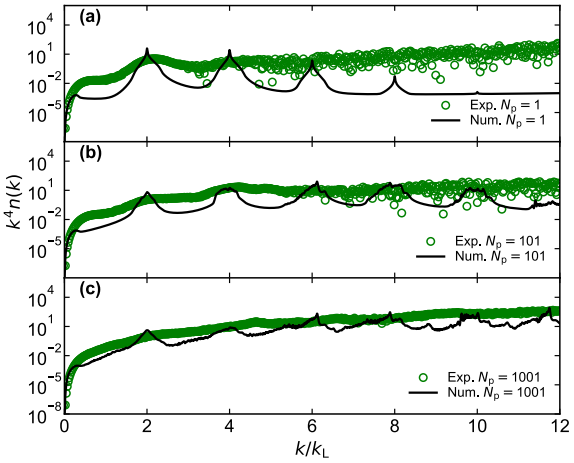

Figure S3. Distribution of $k^4 n(k)$ for $\gamma = 11$ (green circles) with $K = 3.3$ at kick numbers $N_{\mathrm{p}} = 1$ (a), 101 (b), and 1001 (c). The black solid lines show the corresponding numerical predictions for $\gamma \to \infty$.

B. Evidence of algebraic k^{-4} tail during the kicking process

In the MBDL phase, the momentum distribution of an untrapped kicked TG gas is expected to exhibit an algebraic-like decay at large momenta, namely $n(k) = \mathcal{C}_{\mathrm{th}} k^{-4}$, where the weight $\mathcal{C}_{\mathrm{th}}$ is expected to be Tan's contact of the effectively thermalized TG gas [24]. Figure S3 shows the distribution of $k^4 n(k)$ of the kicked TG gas for different kick numbers for a probing of Tan's contact $\mathcal{C}_{\mathrm{th}}$. After 1 kick, the quantity $k^4 n(k)$ increases especially for $k > 6k_{\mathrm{L}}$, whereas the numerical predictions show a clear plateau (see also Fig. S7(c)). When $N_{\mathrm{p}} = 101$, at a point in time at which the energy and entropy are still increasing, we find that the measured $k^4 n(k)$ fluctuates around a constant at large momenta. As the kick number increases into the localized regime, the measured $k^4 n(k)$ presents a growth trend at small momenta while it nearly approaches a plateau for momenta beyond $6k_{\mathrm{L}}$, in agreement with the corresponding numerical predictions. This possibly indicates that the momentum distribution in the MBDL phase exhibits a power-law decay $\mathcal{C}_{\mathrm{th}} k^{-4}$ at large momenta. This requires further investigations.

C. Many-body QKR model and fermionization of bosons

Our numerical calculations are based on the Hamiltonian of Eq. (1) in the main text. We introduce a set of dimensionless parameters to rewrite the Hamiltonian [10]:

$$\begin{aligned} \zeta &= 2k_{\mathrm{L}} z, \quad p = \frac{2k_{\mathrm{L}} TP}{m}, \quad \tau = \frac{t}{T}, \\ \hbar_{\mathrm{eff}} &= \frac{8TE_{\mathrm{r}}}{\hbar}, \quad K = \hbar_{\mathrm{eff}}\kappa, \quad g = \frac{8k_{\mathrm{L}}^3 T^2 g_{1\mathrm{D}}}{m}, \end{aligned} \tag{S1}$$

where $E_{\mathrm{r}} = \hbar^2 k_{\mathrm{L}}^2 / 2m$ is the recoil energy and $\hbar_{\mathrm{eff}}$ denotes the effective Planck constant. This scaling makes $p = \hbar_{\mathrm{eff}}$ corresponding to $P = 2\hbar k_{\mathrm{L}}$, which allows us to take k_{L} as the unit of momentum. Then, the dimensionless Hamiltonian with δ-function kicks is written as

$$\begin{aligned} \mathcal{H}(\tau) = &\sum_{i}^{N} \left(\frac{p_i^2}{2} + \mathcal{V}_{\mathrm{ext}}(\zeta_i) + K\cos(\zeta_i) \sum_{N_{\mathrm{p}}} \delta(\tau - N_{\mathrm{p}}) \right) \\ &+ g \sum_{i<j}^{N} \delta(\zeta_i - \zeta_j). \end{aligned} \tag{S2}$$

As g is proportional to the Lieb-Liniger parameter γ, we use γ to quantify the interaction strength throughout the paper.

For the non-interacting scenario, the Hamiltonian is simplified to $\mathcal{H}_{\mathrm{QKR}}(\tau) = \mathcal{H}(\tau, \gamma = 0)$. After evolving the ground state $|\psi\rangle$ of bosons in the external trap potential $\mathcal{V}_{\mathrm{ext}}$, we use a split-step fast Fourier transform method to alternate between the real-space basis and the momentum-space basis. Here, space is discretized before the stroboscopic evolution and the Floquet operator over one period is written as

$$U = \exp\left\{ -i \left(\frac{\hbar_{\mathrm{eff}} k^2}{2} + \frac{\mathcal{V}_{\mathrm{ext}}(\zeta)}{\hbar_{\mathrm{eff}}} \right) \right\} \exp\left\{ -i \frac{K}{\hbar_{\mathrm{eff}}} \cos(\zeta) \right\}, \tag{S3}$$

which generates the stroboscopic evolution $|\psi(\tau + 1)\rangle = U|\psi(\tau)\rangle$. Applying U repeatedly, we obtain the long-time dynamic observables of the ensemble of bosons, in particular, the momentum distribution $n(k, \tau)$ and the averaged kinetic energy $\langle k^2(\tau) \rangle$.

The kick above is an ideal delta pulse, denoted by $\delta(t - N_{\mathrm{p}} T)$. In our experiments and numerics, we apply a

square pulse with finite pulse duration $T_{\rm p}$:

$$\delta_{T_{\rm p}}(t-N_{\rm p}T)=\begin{cases}\frac{1}{T_{\rm p}} & |t-N_{\rm p}T|\le T_{\rm p},\\ 0 & |t-N_{\rm p}T|>T_{\rm p}.\end{cases} \tag{S4}$$

Thus, the dimensionless Floquet operator over one period can be written as

$$\begin{aligned}U=&\exp\left\{-i\left(\frac{\hbar_{\rm eff}k^2}{2}+\frac{\mathcal{V}_{\rm ext}(\zeta)}{\hbar_{\rm eff}}\right)\frac{T-T_{\rm p}}{T}\right\}\\ &\times\exp\left\{-i\frac{K}{\hbar_{\rm eff}}\cos(\zeta)-i\left(\frac{\hbar_{\rm eff}k^2}{2}+\frac{\mathcal{V}_{\rm ext}(\zeta)}{\hbar_{\rm eff}}\right)\frac{T_{\rm p}}{T}\right\}.\end{aligned} \tag{S5}$$

For the scenario of strong interactions in the TG regime ($\gamma\to\infty$), the strong local repulsion leads to the situation that only one particle can occupy one point in space z. Utilizing the Bose-Fermi mapping, we can straightforwardly compute the exact time-dependent many-body wavefunction of bosons $\Psi_B(\{\zeta\},\tau)$ at positions $\{\zeta\}=\{\zeta_1,\zeta_2,\ldots,\zeta_N\}$ [25, 48]

$$\Psi_B(\{\zeta\},\tau)=\prod_{i<j}\mathrm{sgn}(\zeta_i-\zeta_j)\Psi_F(\{\zeta\},\tau), \tag{S6}$$

where $\Psi_F(\{\zeta\},\tau)=\det[\psi_i(\zeta_j,\tau)]/\sqrt{N!}$ is the many-body wavefunction of free fermions expressed in terms of the Slater determinant of single-particle wavefunctions $\psi_i(\zeta_j,\tau)$.

We then calculate the one-particle density matrix [24, 25],

$$\begin{aligned}\rho(\zeta,\zeta',\tau)=N\int d\zeta_2\ldots d\zeta_N\Psi_B(\zeta,\zeta_2\ldots\zeta_N,\tau)\times\\ \Psi_B(\zeta',\zeta_2\ldots\zeta_N,\tau),\end{aligned} \tag{S7}$$

to obtain the density and momentum distributions of the fermionized Bose gas. The diagonal part of the matrix is the spatial density and the momentum distribution is given by

$$n(k,\tau)=\int d\zeta d\zeta' e^{ik(\zeta-\zeta')}\rho(\zeta,\zeta',\tau). \tag{S8}$$

Furthermore, the correlation function $G^{(1)}(z)$ is defined as average of $\rho(\zeta',\zeta'')$ over all distances [24, 49], and it is written as

$$\begin{aligned}G^{(1)}(\zeta)=\frac{1}{L_z}\Bigg[&\int_0^{L_z}\rho(\zeta',\zeta'+\zeta)\,d\zeta'\\ &+\int_0^{L_z}\rho(\zeta''+\zeta,\zeta'')\,d\zeta''\Bigg],\end{aligned} \tag{S9}$$

which can be obtained from the Fourier transform of the momentum distribution [29, 36].

In practice, we employ the 1D hard-core Bose-Hubbard model to exactly compute the one-particle Green's function $G_{ij}=\langle\hat{b}_i\hat{b}_j^\dagger\rangle$ by using the Jordan-Wigner transformation (JWT) [27, 48]

$$\hat{b}_i^\dagger=\hat{f}_i^\dagger\prod_{\beta-1}^{i-1}e^{-i\pi\hat{f}_\beta^\dagger\hat{f}_\beta},\quad \hat{b}_i=\prod_{\beta-1}^{i-1}e^{i\pi\hat{f}_\beta^\dagger\hat{f}_\beta}\hat{f}_i, \tag{S10}$$

where $f_i^\dagger$ and f_i are the creation and annihilation operators for spinless fermions. The bosonic creation $\hat{b}^\dagger$ and annihilation $\hat{b}$ operators satisfy the on-site anti-commutation rule $\{\hat{b}_i,\hat{b}_i^\dagger\}=1$, while they commute on different sites $[\hat{b}_i,\hat{b}_j^\dagger]=0$. In the end, the one-particle density matrix correspondingly writes

$$\rho_{ij}=\langle\hat{b}_i^\dagger\hat{b}_j\rangle=G_{ij}+\delta_{ij}(1-2G_{ii}). \tag{S11}$$

S3. NUMERICAL METHODS

A. Details of exact numerics

We model the experimental system as a one-dimensional tube with a fixed number of atoms, described by the periodic many-body Hamiltonian in the presence of a confining potential $\mathcal{V}_{\rm ext}$ as presented in the main text. In our experiment, the weighted averaged number of atoms per tube can be estimated by $\overline{N}=\sum_{x_i,y_i}N_{x_iy_i}^2/\sum_{x_i,y_i}N_{x_iy_i}\approx 18$, so we always choose $N=18$ unless stated otherwise. The dimensionless potential $\mathcal{V}_{\rm ext}$ takes the form

$$\mathcal{V}_{\rm ext}(\zeta)=\frac{4k_{\rm L}^2T^2}{m}\left[V_1\left(1-e^{-\frac{\zeta^2}{2k_{\rm L}^2w_1^2}}\right)+V_2\left(e^{-\frac{\zeta^2}{2k_{\rm L}^2w_2^2}}-1\right)\right], \tag{S12}$$

which is a sum of a Gaussian trap and a Gaussian anti-trap. The parameters are $V_1\approx 45.7E_{\rm r}$, $V_2\approx 9.3E_{\rm r}$, $w_1=300\,\mu$m and $w_2=135\,\mu$m.

Here we focus on the calculations in the TG limit ($\gamma\to\infty$). The Bose-Fermi mapping allows us to compute the exact many-body wave function of bosons and calculate the corresponding correlation functions in trapped systems both in equilibrium and far from equilibrium [28]. This mapping directly leads to many similar quantities between strongly interacting bosons and free fermions, for example, the kinetic energy and the entropy [29]. However, there are still several non-local observables that are strongly modified due to the symmetry of the bosonic wavefunction, e.g. the one-particle density matrix, since fermionized bosons do not obey the Pauli exclusion principle in momentum space.

In detail, the simulation involves following steps for two the limiting scenarios:

For the non-interacting limit ($\gamma=0$), the number of atoms is irrelevant and all bosons initially occupy the ground state.

(i) We discretize space to obtain the matrix form of the single-particle Hamiltonian with dimension $N_{\rm dim}\times N_{\rm dim}$, and then carry out exact diagonalization in the real-space basis to obtain the ground state $|\psi_0\rangle$ of the system.

(ii) Starting from the ground state, we evolve it by the Floquet operator using a split-step fast Fourier transform

method to alternate between the real-space basis and the momentum-space basis. This allow us to obtain the momentum distribution $n(k,\tau) = |\langle k|\psi_0(\tau)\rangle|^2$ and kinetic energy $E_z(\tau) = \langle\psi_0(\tau)|k^2|\psi_0(\tau)\rangle$.

For the TG limit ($\gamma \to \infty$), the number of atoms is fixed at $N = 18$. The N bosons are considered being fermionized, meaning that they cannot occupy the same eigenstate because of the Pauli exclusion principle.

(i) We exactly diagonalize the single-particle Hamiltonian in the real-space basis to obtain the lowest N eigenstates (i.e. $\{|\psi_i\rangle\}, i=0,1,\cdots,N-1$) of the system.

(ii) These N eigenstates are evolved separately according to the single-particle Hamiltonian, giving us N time-dependent wavefunctions $|\psi_i(\tau)\rangle$ with $i = 0,1,\cdots,N-1$. The dynamics of the kinetic energy $E_z(\tau) = \sum_i \langle\psi_i(\tau)|k^2|\psi_i(\tau)\rangle$ for the TG gas is simply the sum of the kinetic energies of these N fermions.

(iii) Since we have the N wavefunctions of the free fermions, we calculate the one-particle Green's function $G_{ij}(\tau) = \langle\Psi_B(\tau)|\hat{b}_i\hat{b}_j^\dagger|\Psi_B(\tau)\rangle$ for the bosons. Through the Jordan-Wigner transformation [27, 48], we have

$$G_{ij}(\tau) = \langle\Psi_F(\tau)| \prod_{\beta-1}^{i-1} e^{i\pi\hat{f}_\beta^\dagger\hat{f}_\beta}\hat{f}_i\hat{f}_j^\dagger \prod_{\mu-1}^{j-1} e^{-i\pi\hat{f}_\mu^\dagger\hat{f}_\mu}\,|\Psi_F(\tau)\rangle\,, \tag{S13}$$

where $|\Psi_F(\tau)\rangle = \prod_i^N \sum_\sigma^{N_{\rm dim}} \psi_{i\sigma}(\tau)\hat{f}_\sigma^\dagger|0\rangle$ is the fermionic many-body wavefunction and $\psi_{i\sigma}(\tau)$ corresponds to the σ-th element of the wavefunction $\psi_i(\tau)$ [27]. Furthermore, we obtain the one-particle density matrix $\rho_{ij} = \langle\hat{b}_i^\dagger\hat{b}_j\rangle = G_{ij} + \delta_{ij}(1-2G_{ii})$ and the other related observables such as the density (diagonal part), the momentum distributions (Fourier transform) and the von-Neumann entropy $S_{\rm vN} = -{\rm Tr}\rho\log\rho$. The correlation function $G^{(1)}$ is then determined by the Fourier transform of the momentum distributions.

We typically use a basis size of $N_{\rm dim} = 10000$ and a longitudinal length $L_z = 300\,\mu$m. As the lattice is at very low fillings ($N/N_{\rm dim} \to 0$), the system is effectively in the continuum [28].

B. Quantum Monte Carlo simulation

We use the quantum Monte Carlo (QMC) method to simulate the equilibrium state of the 1D bosons, for computing its density profile and interaction strength $\gamma \sim g/n_{\rm 1D}$. The method is path integral Monte Carlo [50] with worm-algorithm implementations [51, 52], similar to the implementation in Refs. [35, 36]. Here, we simulate the equilibrium state of one weighted average tube in the presence of the continuous flat-bottom potential within the grand-canonical ensemble. We firstly estimate the temperature of the system in equilibrium based on the thermometer proposed in [36], according to the data of the correlation function $G^{(1)}$. Then, with the estimated temperature, we compute the density profile directly from the configuration averaging in the real space. The results are shown in Fig. 1(b).

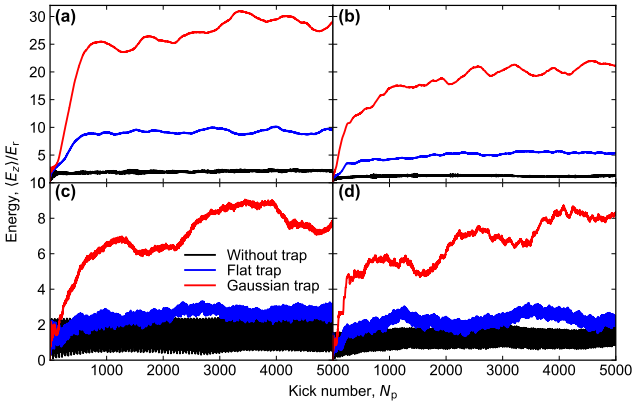

Figure S4. Evolution of the calculated kinetic energy per particle with $K = 3.3$ for $\gamma \to \infty$ (a) and $\gamma = 0$ (c) for various trapping conditions as indicated. (b) and (d) are the same as (a) and (c) but with $K = 4.4$.

C. Calculation of Jensen-Shannon divergence

The Jensen-Shannon divergence J is commonly used to determine the similarity of two probability distribution [37]. In the main text, we use this statistical tool to quantify to what extend the momentum distribution evolves. For two probability distributions $P(k)$ and $Q(k)$ it is given by

$$J = \frac{1}{2}\sum_k \left[P(k)\log_2\frac{2P(k)}{P(k)+Q(k)} + Q(k)\log_2\frac{2Q(k)}{P(k)+Q(k)}\right]. \tag{S14}$$

The value of J is between 0 (P and Q have full overlap) and 1 (P and Q have no overlap).

S4. ADDITONAL NUMERICAL RESULTS

A. Localization for various trapping conditions

Figure S4 illustrates the evolution of the kinetic energy for two kick strengths and for three different trapping conditions, namely no trap, a flat-bottom trap as it is used throughout the manuscript, and a Gaussian trap with a harmonic trapping frequency of 14.7 Hz as it is generated by the finite transversal extent of the lattice beams. Remarkably, the kinetic energy exhibits saturation at a later time for both $\gamma \to \infty$ and $\gamma = 0$ under all trapping conditions, indicating the MBDL and DL phase, respectively. Note that the localized energy and

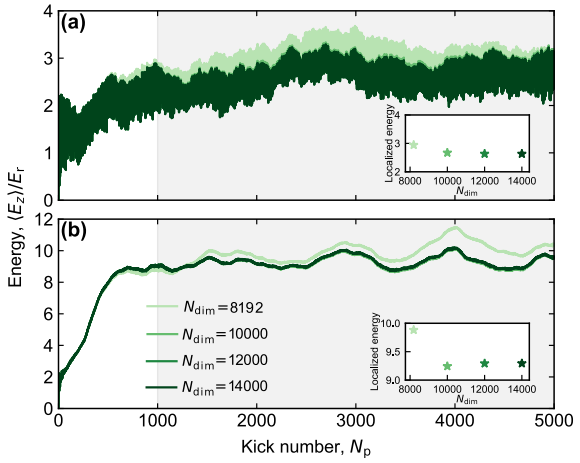

Figure S5. Evolution of the calculated kinetic energy per particle with $K=3.3$ for $\gamma=0$ (a) and $\gamma\to\infty$ (b) for different sizes of the basis set ranging from 2^{13} to 14000. Insets in (a) and (b): localized energy averaged from the grey region in (a) and (b) as a function of the basis size $N_{\rm dim}$.

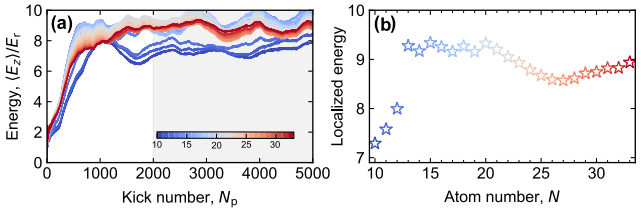

Figure S6. (a) Calculated kinetic energy per particle evolution for $K=3.3$ and $\gamma\to\infty$ for different atom numbers in a range from 10 to 33. (b) Localized energy averaged from the grey region in (a) as a function of atom number N.

onset time increase as the trap potential becomes steeper. Moreover, we find that the localized energy varies for different kick strengths, consistent with the experimental measurements shown in Fig. 3 in the main text. For all cases, when compared to the Gaussian trap, the flat-bottom trap leads to an earlier onset time of the localization and clearly decreases the localized energy. It thus helps us to observe the MBDL phase without notable heating and atom losses.

B. Convergence of the energy with basis size

To confirm the accuracy of our numerical results, we try four different basis sizes to calculate the evolution of the kinetic energy for $\gamma=0$ and $\gamma\to\infty$, as shown in Fig. S5. The energy evolution is consistent with increasing basis size after $N_{\rm dim}=10000$. The localized energy is thus constant at a basis size beyond $N_{\rm dim}=10000$, see inset in Fig. S5. Therefore, we choose $N_{\rm dim}=10000$ for all numerical simulations.

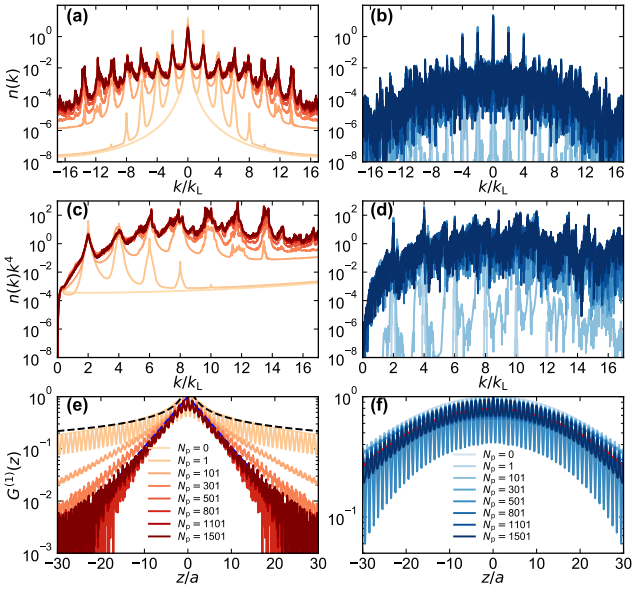

Figure S7. Calculated distributions $n(k)$ and $n(k)k^4$ and the correlation function $G^{(1)}$ for $K=3.3$ and for $\gamma\to\infty$ (left panels) and $\gamma=0$ (right panels) for different kick numbers ranging from $N_{\rm p}=0$ to 1501 as indicated. The black and blue dashed lines in (e) are fits with algebraic decay $\propto 1/\sqrt{z}$ and exponential decay $\propto e^{-z/r_c}$, respectively. The red dashed line in (f) denotes a Lorentzian fit.

C. MBDL for different atom numbers

In our experiment, for the data presented in Fig. 3, the total number of atoms is not constant. It drops by up to 25% after one thousand kicks. In Fig. S6(a), we present the evolution of the energy per particle for $\gamma\to\infty$ for varying number of atoms N ranging from 10 to 33. Since atoms cannot occupy the same eigenstate initially, the energy overall increases with increasing atom number at first, but it starts to stabilize at N beyond 15. The energy always saturates for all atom numbers in this range. As expected, the averaged localized energy exhibits a slight growth with increasing N and is then followed by a fluctuation around $9E_{\rm r}$ (Fig. S6(b)). The increase of the localized energy with more atoms in the early stage can be attributed to the Pauli exclusion principle and the finite trap depth. These results indicate that MBDL is expected to remain robust in the thermodynamic limit $N\to\infty$.

D. Momentum and $G^{(1)}$ evolution

The calculated momentum distributions after different number of kicks for $\gamma\to\infty$ and $\gamma=0$ are shown in Fig. S7 (a) and (b). Remarkably, the profiles for both scenarios remain frozen after about 501 kicks, and the momentum distributions for $\gamma\to\infty$ are much broader

than those for $\gamma = 0$. In Figs. S7(c) and (d), we investigate the $n(k)k^4$ dynamics for both two scenarios to show Tan's contact [39, 53] from theory side. As expected, the momentum distribution of a TG gas in equilibrium exhibits a power-law decay $n(k) = \mathcal{C}k^{-4}$ with $\mathcal{C}$ the Tan's constant, reflecting the local inter-atom interactions. As the kick number increases, the plateau does not perfect due to the emergence of recoil peaks. Once MBDL has been occurred, the quantity $n(k)k^4$ fluctuates around a constant for momenta beyond $6k_{\mathrm{L}}$. We notice that this constant value is much higher than the one before kicking, which is caused by the fact that the kicks enhance the interactions between the atoms. In contrast, $n(k)k^4$ for $\gamma = 0$ oscillates at high frequency over a wide range instead of being a constant.

We finally turn to the quantum correlations of the gases in the DL and MBDL phase. As we compare the one-body correlation function for the non-interacting and strongly interacting scenarios in the main text. In the ground state, the TG gas is expected to feature algebraic correlations ($G^{(1)} \propto 1/\sqrt{z}$), reflecting the quasi-long-range order [24, 34]. Thus, we numerically calculate $G^{(1)}$ for different kick numbers ranging from the ground state to the MBDL regime. As shown in Fig. S7(e), the $G^{(1)}$ of an equilibrium TG gas is well fitted by an algebraic decay, but it gradually turns into an exponential decay ($G^{(1)} \propto e^{-z/r_c}$) after hundreds of kicks. In addition, the correlation length r_{c} is frozen after the kick number $N_{\mathrm{p}} = 501$, which is consistent with the observed onset of MBDL. In contrast, the $G^{(1)}$ for $\gamma = 0$ at different kick numbers are shown in Fig. S7(f). Once DL has occurred, $G^{(1)}$ exhibits a Lorentzian decay indicating an exponential structure in momentum space. These calculations are consistent with our experimental results presented in the main text. This again highlights the many-body effect.

Cooling bosons by dimensional reduction

Yanliang Guo,[1,*] Hepeng Yao,[2,*] Sudipta Dhar,[1] Lorenzo Pizzino,[2] Milena Horvath,[1] Thierry Giamarchi,[2] Manuele Landini,[1] and Hanns-Christoph Nägerl[1,†]

[1] *Institut für Experimentalphysik und Zentrum für Quantenphysik, Universität Innsbruck, Technikerstraße 25, Innsbruck, 6020, Austria*

[2] *DQMP, University of Geneva, 24 Quai Ernest-Ansermet, Geneva, CH-1211 , Switzerland*

Cold atomic gases provide a remarkable testbed to study the physics of interacting many-body quantum systems. They have started to play a major role as quantum simulators, given the high degree of control that is possible. A crucial element is given by the necessarily non-zero temperature. However cooling to the required ultralow temperatures or even simply measuring the temperature directly on the system can prove to be very challenging tasks. Here, we implement thermometry on strongly interacting two- and one-dimensional Bose gases with high sensitivity in the nano-Kelvin temperature range. Our method is aided by the fact that the decay of the first-order correlation function is very sensitive to the temperature when interactions are strong. We find that there may be a significant temperature variation when the three-dimensional quantum gas is cut into two-dimensional slices or into one-dimensional tubes. Strikingly, the temperature for the one-dimensional case can be much lower than the initial temperature. Our findings show that this decrease results from the interplay of dimensional reduction and strong interactions.

Cold atomic gases allow a remarkable degree of control over crucial parameters such as the interaction strength and the confining potentials, making them ideal systems for studying the properties of strongly correlated quantum matter [1] . Their dimensionality can be set freely, via, e.g., optical lattice potentials, and with this they have enabled the study of a host of properties of interacting one-dimensional (1D) and two-dimensional (2D) quantum systems. Highlights in 1D include the observation of bosonic fermionization into the Tonks-Girardeau (TG) state [2–5], the driving of quench dynamics [6–9], the investigation into localization effects driven by longitudinal lattices [10–14] and disorder [15–18], and the recent observation of spin-charge separation [19, 20]. Similarly, 2D systems based on cold atoms have allowed the study of the Berezinskii-Kosterlitz-Thouless (BKT) transition [21, 22], the investigation of topological properties [23, 24], and the probing of frustrated phases [25]. In all these works, it has been important to assure that the temperature is low enough compared to the point of quantum degeneracy as non-zero temperatures play a crucial role for the physical phenomena observed.

The presumably lowest temperatures for 2D and 1D systems have so far been achieved by slicing low-entropy 3D samples such as essentially pure atomic Bose-Einstein condensates (BEC) into layers or tubes by means of lattice potentials. While the temperatures of the 3D sources can be determined to high accuracy, with values in the low-nK range [1], estimates of the temperatures of the low-D systems have always been rather vague. In fact, it is widely believed that creating low-D gases within anisotropic potentials usually leads to heating [17, 21, 26, 27]. Attempts to obtain a temperature value from e.g. Bragg-spectroscopy data on 1D Luttinger liquids together with exact Bethe-ansatz modeling [28] were hampered by rather large systematic uncertainties. Here, we implement precise thermometry at the 1-nK level for strongly-interacting 2D and 1D Bose gases. We utilize the fact that the first-order correlation function $g^{(1)}$ sensitively depends on temperature when interactions are strong. In the experiment, it is determined from a careful measurement of the momentum distribution, and the results of ab-initio state-of-the-art quantum Monte Carlo calculations for various values of the temperature are used as a thermometer scale. We use the thermometer to determine temperatures in 1D that are significantly lower than the starting temperatures. We are able to interpret this anomalous phenomenon by invoking an entropy argument and find that our data fits well with the theoretical prediction. We attribute our findings to the interplay of tight confinement and strong interactions for bosons that are subject to fermionization.

The experiment starts with an interaction-tunable 3D Bose-Einstein condensate (BEC) of 1.5×10^5 Cs atoms [30] prepared in the lowest magnetic hyperfine state $|F, m_F\rangle = |3, 3\rangle$, held in a crossed-beam dipole trap with trap frequencies $\omega_{x,y,z} = 2\pi \times (18.6(2), 19.3(3), 26.8(3))$Hz along the three main axes x, y, and z of the setup and levitated along the vertical x-direction against gravity by a magnetic field gradient. The BEC is in the Thomas-Fermi regime with the 3D s-wave scattering length a_{3D} tuned to $a_{3D} \approx 190a_0$. One (or two) counterpropagating optical lattice beams along the z- (and y-) direction are gradually ramped up in 500 ms to a potential depth of $V_z = 30E_r$ ($V_y = 30E_r$), with $E_r = \pi^2\hbar^2/(2ma^2)$ the recoil energy, cutting the 3D system into an ensemble of 2D layers that lie in the x-y-plane (or an array of 1D tubes along the x-direction), as sketched in Fig. 1A. Here, $a = \lambda/2$ is the lattice spacing with $\lambda = 1064.5$ nm the wavelength of the lattice light. After loading the atoms into the lattice, the initial crossed-beam dipole trap is ramped

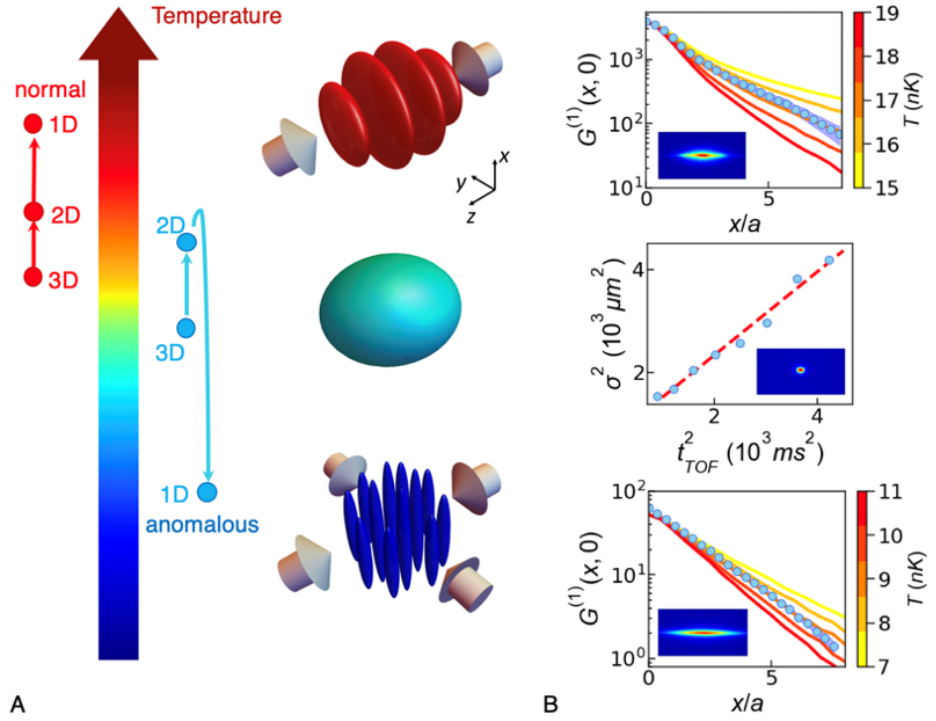

Figure 1. **Sketch of the experimental setup and typical thermometry data for the various dimensions.** (A) The initial nearly spherical 3D BEC (center) is cut either into an ensemble of 2D layers (top) or into an array of 1D tubes (bottom) via the optical force of one or two pairs of counter-propagating and interfering laser beams (arrows). The temperature scale illustrates the normal and anomalous temperature change when the dimensionality is switched for two slightly different initial conditions. (B) Example data for the temperature measurements in 2D (top), 3D (middle), and 1D (bottom). For 2D and 1D, the calculated one-body correlation function $G^{(1)}(x,0)$ is plotted as a function of distance x/a for various temperatures (solid lines, with the temperature indicated by the color coding) and compared to the measured data (blue circles). The experimental statistical error from 20 repetitions is smaller than the size of the symbols. For 2D case, the system has a weighted atom number $\overline{N}_{2D} \sim 3950$ with radial trapping frequency $\omega_x^{2D}/2\pi = 10.1$Hz. For 1D case, the system has a weighted atom number $\overline{N}_{1D} \sim 63$ with longitudinal trapping frequency $\omega_x^{1D}/2\pi = 14.3$Hz. The scattering length is set to $a_{3D} = 620a_0$ for both 2D and 1D. The QMC calculations are under the experimental conditions and its error bars are less than 1%. For the 3D case, a typical TOF dataset with the squared Gaussian waist σ^2 obtained from a bimodal fit as a function of the squared TOF duration t_{TOF} is presented. The linear fit (dashed line) directly gives the 3D temperature. The three insets are example TOF absorption images for the respective dimensionality [29].

down in 100 ms. For the layers, the trap frequencies are $\omega_{x,y,z} = 2\pi \times (10.1(2), 10.1(2), 11\text{k})$Hz, and these change to $\omega_{x,y,z} = 2\pi \times (14.3(2), 11\text{k}, 11\text{k})$Hz for the set of 1D tubes. The offset magnetic field is then ramped up adiabatically to set $a_{3D} \approx 620a_0$. This takes the 3D BEC into the strictly-2D regime with 2D interaction parameter $\gamma_{2D} = 1.5$ or into the strictly-1D regime with Lieb-Linger parameter $\gamma_{1D} = 20$ [29]. For this value, the 1D system is deep in the fermionized TG regime [3, 4].

We now detail the thermometer operation in the various dimensionalities. The method for 3D is standard and has been used widely in the past. In short, the temperature is determined from the expansion rate of the non-condensed fraction of the quantum gas in time-of-flight (TOF) after switching off all trapping fields. Crucially, the inter-particle interaction is zeroed at the start of TOF by means of a Feshbach resonance's zero crossing [30] to avoid any residual interaction effects. Bimodal fits on the density profiles for varying TOF-times give the 3D temperature [29]. Typically, 8 different TOF-times are chosen, and each time the experiment is repeated 2 times. Fig. 1B provides the results of a typical measurement, for which we find $T_{3D} = 12.5(4)$nK. In 2D and 1D, the interacting gases do not show a bimodal distribution and a Boltzmann fit cannot be done. However, the one-body correlation function $g^{(1)}(x,x',y,y') = \langle \hat{\Psi}^\dagger(x',y')\hat{\Psi}(x,y)\rangle$ shows a decay that has a strong temperature dependence. In the experiment, we determine it by a measurement of the momentum distribution $n(k)$ via the TOF technique to obtain the integrated correlation function $G^{(1)}(x,y) = \iint dx'dy' g^{(1)}(x'+x, y'+y, x', y')$ via Fourier transform. We then compare it to the results of an ab-initio quantum Monte Carlo (QMC) approach to simulate

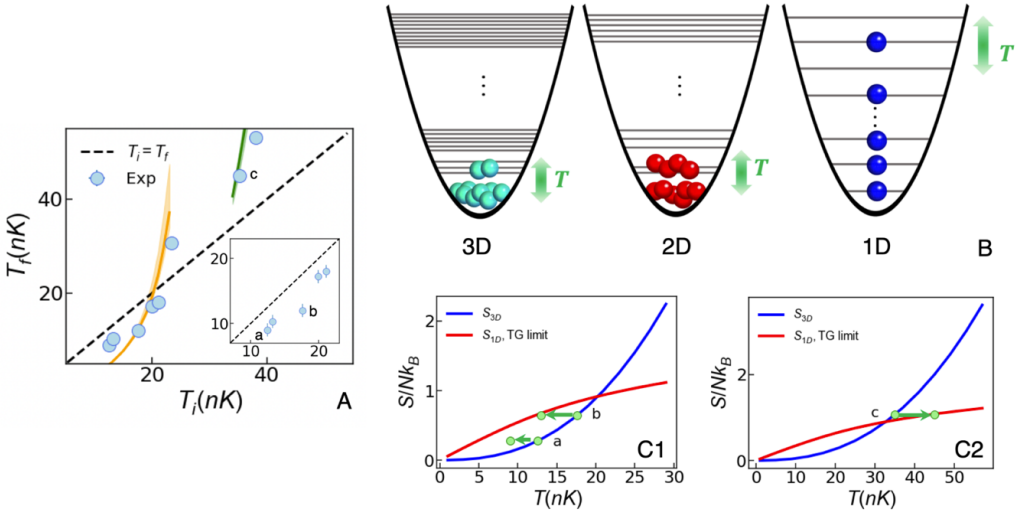

Figure 2. **Cooling vs. heating and the physical picture behind anomalous cooling.** (A) The final temperature of the 1D system T_f (blue circles) as a function of the initial temperature of the 3D system T_i. The error bars are smaller than the size of the symbols. The analytical predictions are shown as orange and green solid curves. For this data, the 1D systems are always deeply in the TG regime. The inset displays the low-temperature data for which cooling is observed. The letters a, b, and c mark data points that are referenced in C1 and C2. (B) Illustration of the configuration picture in 3D, 2D, and 1D on the basis of the quantum harmonic oscillator. The green arrows indicate the effect of the non-zero temperatures. (C1-C2) The entropy per particle $S/Nk_{\rm B}$ for the 3D trapped system (blue line) and the 1D tubes deeply in the TG regime (red line) as a function of the temperature T. The experimental parameters are $\omega_{x,y,z} = 2\pi\times(18.6, 19.3, 26.8)$Hz and $\overline{N}_{1\rm D} = 72$ for the data in C1 and $\omega_{x,y,z} = 2\pi\times(29.4, 27.1, 39.9)$Hz and $\overline{N}_{1\rm D} = 120$ for the data in C2. The green dots reflect the three cases shown in (A), among which a and b show the cooling effect, while c shows heating.

the system [31]. Its many-body Hamiltonian is given by

$$\hat{H} = \sum_j \left[-\frac{\hbar^2}{2m}\nabla_j^2 + V(\hat{\mathbf{r}}_j) \right] + \sum_{j<k} U(\hat{\mathbf{r}}_j - \hat{\mathbf{r}}_k), \qquad (1)$$

with $U(\hat{\mathbf{r}})$ the short-range repulsive two-body interaction and $V(\mathbf{r})$ the external harmonic potential. The function $G^{(1)}(x, y)$ is then computed for various temperatures using the worm algorithm. Note that simulating one weighted tube (layer) gives us the same result for $G^{(1)}(x, y)$ as taking into account the whole atom distribution in the array of tubes (layers) [29]. Fig. 1 B presents typical experimental data for $G^{(1)}(x, 0)$ in 1D and 2D and compares the data to the results of the QMC simulations for various temperatures. Clearly, the QMC data serves as a very sensitive ruler for the temperature. For 2D, we obtain $T_{2\rm D} = 17(1)$ nK, and the temperature in 1D is $T_{1\rm D} = 9(1)$ nK. Evidently, the system is hotter in 2D, and then colder in 1D. The 1D data can be cross-checked using the analytical form of the correlation function. For a trapped 1D TG gas it reads $G^{(1)}(x) \sim e^{-\eta x/a}$ with $\eta = k_{\rm B}Ta/(2\hbar^2 n_0)$ [32]. With $n_0 = 0.9/a$ and $\eta_{\rm exp} = 0.48$, we find $T_{1\rm D}^{\rm analytical} = 9.1$ nK. This agrees well with the QMC prediction.

The data above was taken for a specific set of parameters. We now perform cross-checks by varying the initial 3D temperature, the trapping frequency, and the interaction strength to elucidate the mechanism behind the anomalous cooling. For example, by changing the efficiency of the evaporative cooling process in the initial 3D dipole trap, we prepare 3D quantum-degenerate samples at various initial temperatures T_i with varying condensate fractions [29]. These samples are then transferred into 1D tubes and we measure the final temperature T_f as before. Such temperature data is shown in Fig. 2A. Clearly, anomalous cooling occurs when the initial temperatures are sufficiently low, i.e., 20 nK and below. Typcially, we see a decrease of 20% to 40% from the initial 3D temperature, with a temperature difference that is far more than 1-nK thermometer resolution. However, above $T_i \approx 20$ nK the dimensional change leads to heating.

Invoking the entropy picture sheds light onto the anomalous cooling phenomenon and demonstrates the important role played by the dimensionality of the quantum many-body system. Fig. 2B illustrates the population of the energy levels of the quantum harmonic oscillator in the different dimensionalities. When the dimension of the system is reduced from 3D, two processes happen. On one hand, the condensate nature of the initial system is undermined. In 3D, the system is a nearly pure BEC with a small non-condensed fraction at low temperatures. Most of the atoms populate the ground state. In 2D, the nature of condensate is weakened and the system exists only as a quasicondensate with a decay of the first-order correlations. This suggests an increase of the number of

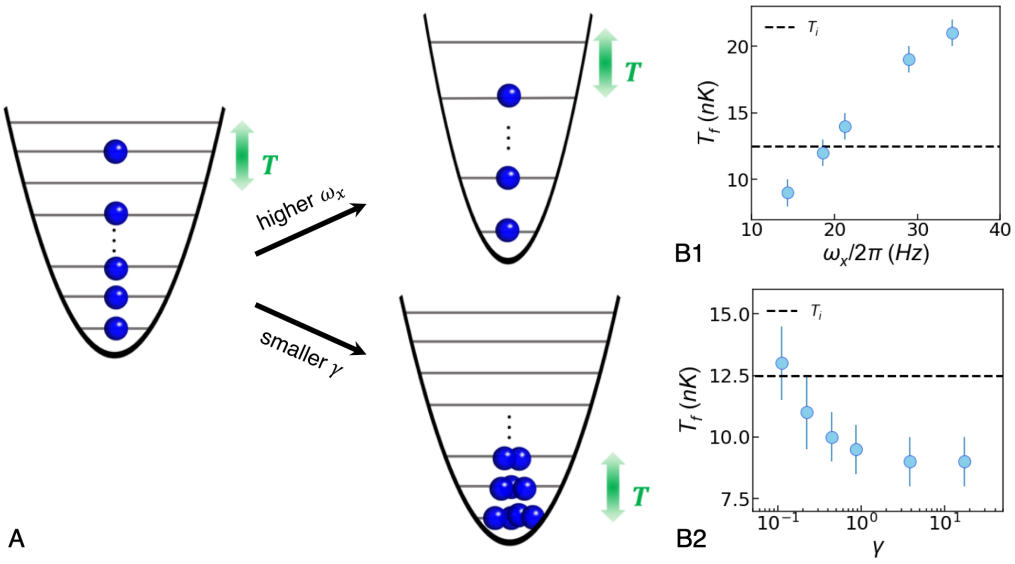

Figure 3. **Conditions for anomalous cooling.** (A) Illustration of the configuration picture for the fermionized TG gas, comparing to the one with a higher trapping frequency ω_x or a weaker interaction strength. (B1-B2) The measured 1D temperature T_f as a function of the longitudinal trapping frequency ω_x (B1) and the interaction strength γ (B2). The black dashed line indicates the initial 3D temperature T_i.

possible configurations C in energy space for a given non-zero temperature T. In the extreme case of a strongly-interacting gas in 1D, the system has fermionized. The particles are filled into the energy levels as ideal fermions and the excitations happen around the Fermi surface. On the other hand, the degeneracy of the energy levels becomes less as the dimensionality is reduced. This leads to the decrease of the number of possible configurations C. Thus, as a result of the competition of these two processes, one can reach a situation $C_{1D} > C_{3D} > C_{2D}$. For constant entropy, as a result of careful adiabatic loading the lattice, one may thus obtain $T_{1D} < T_{3D} < T_{2D}$.

This physical picture is confirmed by calculations of the entropy. For 3D trapped bosons [33], the entropy is $S_{3D} = (7A\zeta(3)/5\sqrt{2})(15a_{3D}N/\sigma)^{1/5}(T/\hbar\bar{\omega})^{5/2}$ with $A = 10.6$, $\sigma = \sqrt{\hbar/m\bar{\omega}}$ the oscillator length and $\bar{\omega} = (\omega_x\omega_y\omega_z)^{1/3}$. In the 1D case, the entropy $S_{1D} = -\partial\ \Omega_{TG}/\partial\ T$ of a TG gas can be computed from the grand potential Ω_{TG} [34], with the trap treated under the local density approximation [29]. These entropy curves are shown in Fig. 2C for our set of parameters. Below a certain temperature T_i^c, the entropy for 1D is higher than in 3D. When keeping the entropy constant, the system's temperature has to drop when the dimensionality is reduced from 3D to 1D, see e.g. a and b in Fig. 2A. Our data reflects this. Above T_i^c, a temperature increase is expected. This is also captured by our data. In Fig. 2A, we add the prediction for the temperature decrease resp. increase during dimensional reduction. Our data fits the predictions reasonably well. Only for the lowest temperatures we find a decrease that is not as pronounced as predicted, most likely due to some small non-adiabaticity during the lattice-loading process. We note that the cooling mechanism observed here is reminiscent of the adiabatic demagnetization cooling technique [35, 36]. However, in our case there is no discrete spin degree of freedom into which entropy can be pumped.

We next turn to the influence of a change of the longitudinal trapping frequency ω_x for the 1D systems. By means of the crossed-beam trap, we can tune $\omega_x/2\pi$ from 14.3(2) Hz to 34.2(3) Hz. Our data, shown in Fig. 3B1, shows that the 1D temperature then varies from 9 nK to 21 nK. This confirms our entropy and configuration picture: stiffening of the confinement reduces the number of accessible configurations, as shown schematically in Fig. 3A, and hence leads to an increase of the temperature. As is well know, adiabatic compression of a Boltzmann gas leads to heating, and decompression leads to cooling. Indeed, our data shows that also a TG gas has the same behavior. We note that the lower limit 14.3 Hz for ω_x is set by the residual transversal trapping force of the y- and z-lattice beams. Reducing this value would require some anti-trapping, which could be done by means of an additional blue-detuned laser beam, and with this even lower 1D temperatures should be possible.

We finally address the role of strong interactions. In the experiment, after preparing the 1D tubes, we ramp a_{3D} to a value between $7a_0$ and $620a_0$, varying γ between 0.1 and 20 by more than 2 orders of magnitude given our typical atom number $\bar{N}$ [29]. We find a clear temperature dependence on γ as seen in Fig. 3B2 [29]. As

γ is increased, the 1D temperature drops continuously. Above $\gamma \approx 1$ the temperature settles to a constant value. Evidently, more configurations become accessible as the system starts to fermionize, as sketched in Fig. 3A, leading to a reduction of the temperature, and beyond $\gamma_{1D} \approx 1$ the system's fermionization is complete for a system in equilibration.

In conclusion, we have realized a thermometer for strongly-interacting 1D and 2D quantum gases. We are capable of measuring temperatures for such strongly-correlated systems in the low-nK range with 1-nK precision. With this thermometer, we have found that cooling may occur as the dimensionality is reduced from 3D to 1D. Given such a thermometer, one can now optimize the formation process of the low-D quantum gases, in particular for the case of non-harmonic box-like trapping conditions [37]. For example, a detailed probing of the 2D-to-1D crossover regime is possible [38]. The principle demonstrated here could be used to generate even lower temperatures in a Carnot-cycle process. Next, a variety of phenomena in low-D becomes accessible for which the temperature plays an important role, such as Anderson localization [15], the pinning [12] and Bose glass transitions [16, 18], and out-of-equilibrium dynamics with e.g. pre-thermalization [9], dynamical fermionization [8], correlated transport [39], and the implementation of quantum-field machines [40].

The Innsbruck team acknowledges funding by a Wittgenstein prize grant under project number Z336-N36 and by the European Research Council (ERC) under project number 789017. This research was funded in part by the Austrian Science Fund (FWF) W1259-N27 and MH thanks the doctoral school ALM for hospitality. This work is also supported by the Swiss National Science Foundation under grant number 200020-188687. The numerical calculations make use of the ALPS scheduler library and statistical analysis tools [41–43].

The data that support the findings of this study are made publicly available from Zenodo by the authors at [44].

SUPPLEMENTAL MATERIAL

The atom number distribution

For the calculations of this paper, we use one single layer or one single tube with a weighted average number $\bar{N}$ given by

$$\bar{N} = \frac{\sum_i N_i^2}{\sum_i N_i} \tag{2}$$

with N_i the atom number of the i-th tube (or layer). This method uses the atom number as a weight of itself and it takes into account that the tube with more atoms will contribute more significantly to the physical properties of the systems than tubes with less atoms. Such a standard method has been used in previous works [27, 28, 45]. During the lattice-loading process almost all layers (2D) or tubes (1D) are in the Thomas-Fermi regime for weak repulsive interactions, so we can calculate the initial occupation number in each layer in 2D or each tube in 1D case through the global chemical potential and the total atom number. In the following, we check that this method is proper for the physical quantities studied here. First, we compute the correlation function $G^{(1)}(x,0)$ for the 1D systems as done for the QMC calculations shown in Fig. 1B of the main text, see Fig. 4 A. The results for one single weighted tube agree with the calculations for the full tube distribution. The difference is less than 5%, showing that the use of the weighted average atom number is good enough for estimating the temperature in low dimensions. Second, we check that also the result for the entropy using one weighted tube agrees with the calculation using the distribution of tubes. The results are shown Fig. 4 B for a TG gas under the condition $\bar{N} = 40$ and $\omega_x = 2\pi \times 14.3$ Hz. Also here we find good agreement.

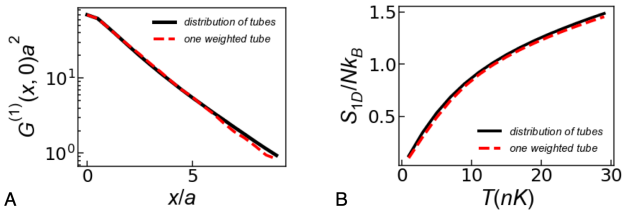

Figure 4. **Check that $\bar{N}$ is a proper input for the numerical calculations.** (A) The correlation function $G^{(1)}(x,0)$ as a function of the position x/a for the same parameters as for the 1D experimental data shown in Fig. 1B of the main text and for $T = 9$ nK. (B) The entropy per particle S/Nk_B as a function of temperature T for a TG gas with $\bar{N} = 40$ and $\omega_x = 2\pi \times 14.3$ Hz. The red dashed line indicates the calculation for the case of one weighted tube, while the black solid line assumes the distribution of tubes.

The interaction strengths in 1D and 2D are then determined by the using the weighted atom number. In 1D, the coupling constant is [1, 46]

$$g_{1D} = \frac{2\hbar^2 a_{3D}}{m l_\perp^2}\left(1 - \frac{1.036 a_{3D}}{l_\perp}\right)^{-1} \tag{3}$$

with $l_\perp = \sqrt{\hbar/m\omega_\perp}$ the characteristic transverse length, and the 1D Lieb-Liniger parameter is hence given by $\gamma_{1D} = m g_{1D}/\hbar^2 \bar{n} a$ with the density $\bar{n}$ of the weighted average tube. In 2D, the coupling constant writes [1, 47]

$$g_{2D} \simeq \frac{2\hbar^2\sqrt{2\pi}}{m l_\perp / a_{3D} + 1/\sqrt{2\pi}\ln(1/\pi q^2 l_\perp^2)} \tag{4}$$

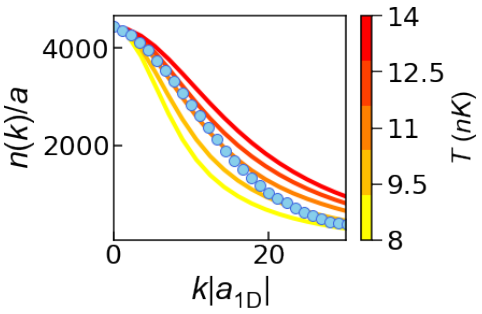

Figure 5. **Thermometer for 1D weakly-interacting systems based on the momentum distribution.** The blue balls are experimental data with weighted atom number $\overline{N}_{1D} \sim 70$, longitudinal trapping frequency $\omega_x/2\pi = 14.3$ Hz and 1D coupling constant $mg_{1D}a/\hbar^2 = 0.11$. The momentum axis is rescaled by $a_{1D}{=}{-}2\hbar^2/mg_{1D}$. The solid lines are the results of QMC simulations for the same conditions as the experiment for various values of the temperature as indicated.

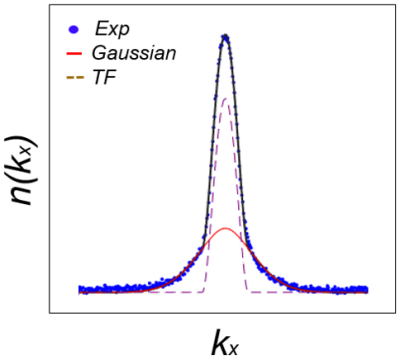

Figure 6. **Bimodal fit for the momentum distribution $n(k_x)$ in 3D.** Example of the $n(k_x)$ for the 3D gas under a 50-ms TOF in Fig. 1 (B) in the main text with a bimodal fit.

with $q = \sqrt{2m|\mu|/\hbar^2}$ the quasi-momentum, and μ the chemical potential corresponding to the weighted average layer. The 2D interaction parameter thus is $\gamma_{2D} = mg_{2D}/\hbar^2$.

Thermometer in the weakly-interacting regime

For most of the cases in the main text, we estimate the temperature of the system by using the one-body correlation function $G^{(1)}(x, 0)$. In the strongly interacting regime, this quantity follows a purely exponential decay and its decay exponent has a strong and clear dependence on temperature. However, in the weakly interacting regime, the correlation decay becomes slower and it is not a purely exponential decay, which makes the analysis more complicated. In this case, we extract the temperature of the system directly from the momentum distribution $n(k_x)$. This method has been used to estimate the temperature of 1D weakly-interacting gases in previous experimental studies [26, 48, 49]. In Fig. 5, we present one example for $\overline{N}_{1D} \sim 70$, longitudinal trapping frequency $\omega_x/2\pi = 14.3$ Hz and 1D coupling constant $mg_{1D}a/\hbar^2 = 0.11$, resulting in $\gamma \sim 0.2$. Our QMC simulations provide a thermometer scale with a temperature sensitivity of $\delta T \approx 1.5\,\mathrm{nK}$, see the colored solid curves. With the data from the range $ka_{1D} < 20$, the measurement suggests 1D temperature $T_{1D} = 11\,\mathrm{nK} \pm 1.5\,\mathrm{nK}$. Notably, such an estimate for weakly-interacting gases according to the small-k part of the momentum distribution is similar to the one mentioned in Refs. [26, 48]. Instead of using the analytical formula for the width of the distribution, our calculation directly simulates the continuous trapped system and avoids the local density approximation.We notice that the resolution of the thermometer in the regime of weak interactions is not quite as good as the resolution the regime of strong interactions. This is due to the fact that for weak interaction the system is less sensitive to the temperature due to the more pronounced quantum coherence.

The preparation of different initial 3D temperatures

In Fig. 2 A of the main text we show how the final temperature of the 1D system varies with the initial 3D temperature. In the experiment, we are able to prepare a 3D gas at different temperatures by changing the efficiency of the evaporative cooling process, i.e., varying the trap depth through altering the power of the crossed dipole beam. However, once the trap depth is modified, the 3D trapping frequency and the weighted atom number in 1D are changed consequently, resulting in different entropy for both cases in 3D and 1D, as shown in Fig 2 C. To systematically compare the measured 1D temperature to the theoretical predicted value that drawn as the orange and the green solid lines in Fig 2A , we have to keep the 3D trapping frequency constant. So after evaporative cooling, we first ramp up the power of the crossed dipole beam to a fixed value, which provides a constant 3D trapping frequency to $\omega_{3D} = 2\pi\times(18.6, 19.3, 26.8)$Hz and then load atoms into the lattice. However, such a trap depth limits the reachable highest temperature for a 3D gas. For preparing an even hotter 3D cloud, we need to increase the power of the crossed-dipole beams setting the final trapping frequency $\omega_{3D} = 2\pi \times (29.4, 27.1, 39.9)$Hz. This allows us to measure the 1D temperatures to the predicted value given by the entropy curves in Fig 2 C1 and C2.

Moreover, we argue that the process of measuring the 3D temperature is accurate. The 3D temperatures in the main text are all measured after ramping up the crossed

dipole beam for the desired ω_{3D}. In addition, the inter-particle interaction is switched off during TOF expansion. The resulting true momentum distribution $n(k_x)$ shows an obverse thermal part that can be perfectly fitted by a bimodal (Gaussian plus Thomas-Fermi), see Fig 6. It help us to extract the 3D temperature accurately as shown in Fig. 1B.

The imaging setup

Our setup consists of two lattice beams perpendicular to each other along the y and z axes. There is an angle of $\theta \sim 57°$ between the propagation axis of the imaging beam and the y-direction, see Fig. 7. However, x axis is always perpendicular to the imaging beam. We note that, to determine the temperature in any dimensions, we capture our momentum distributions $n(k_x)$ or the correlation functions $G^{(1)}(x,0)$ along the longitudinal direction x in the main text, which is not affected by this angle.

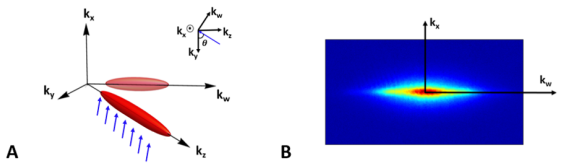

Figure 7. **A schematic of our imaging setup and an example of the image.** (A) The vectors k_y, k_z, k_w and the imaging direction (blue arrows) all lie in one plane, with k_x perpendicular to this plane, see also inset. The red 3D ellipsoid along the k_z direction indicates the atomic cloud after TOF starting from an ensemble of 2D layers for $V_y = 0E_r$. The light red 2D ellipsoid along the k_w direction is the shadow in our absorption image. (B) The projected image after TOF for the 2D case.

The entropy of the TG gas

The entropy of the TG gas in an harmonic trap can be computed based on the equations in Ref. [34]. The grand potential density Ω of a homogeneous TG system can be expressed to the lowest order as

$$\Omega(\mu,T) = -\frac{\sqrt{m}(k_B T)^{3/2}}{\hbar\sqrt{2\pi}} f_{3/2}(\mu/k_B T) \tag{5}$$

with μ the chemical potential and $f_\nu(x)$ the completed Fermi-Dirac integral at index j. Correspondingly, the entropy density s of this point can be obtained by

$$s(\mu,T) = -\left.\frac{\partial\Omega(\mu,T)}{\partial T}\right|_\mu. \tag{6}$$

Then, the presence of the harmonic trap can be taken care of by using the local density approximation (LDA) by taking the equation of state for the low temperature TG gas, namely

$$n = \sqrt{\frac{2m\mu}{\pi^2\hbar^2}}. \tag{7}$$

This means that the entropy of the trapped system can be expressed as

$$S_{\rm trap}(N,T) = \int_{-R}^{+R} dx\ s(\mu(x),T) \tag{8}$$

under the constrain of the total number of particles $\int_{-R}^{+R} dx\ n(\mu - 1/2m\omega^2x^2) = N$.

* These authors contributed equally to this work.
† christoph.naegerl@uibk.ac.at

[1] I. Bloch, J. Dalibard, and W. Zwerger, Many-body physics with ultracold gases, Rev. Mod. Phys. **80**, 885 (2008).
[2] B. Paredes, A. Widera, V. Murg, O. Mandel, S. Fölling, I. Cirac, G. V. Shlyapnikov, T. W. Hänsch, and I. Bloch, Tonks-Girardeau gas of ultracold atoms in an optical lattice., Nature (London) **429**, 277 (2004).
[3] T. Kinoshita, T. Wenger, and D. S. Weiss, Observation of a one-dimensional Tonks-Girardeau gas, Science **305**, 1125 (2004).
[4] E. Haller, M. Gustavsson, M. J. Mark, J. G. Danzl, R. Hart, G. Pupillo, and H.-C. Nägerl, Realization of an excited, strongly-correlated quantum gas phase, Science **325**, 1224 (2009).
[5] F. Meinert, M. Knap, E. Kirilov, K. Jag-Lauber, M. B. Zvonarev, E. Demler, and H.-C. Nägerl, Bloch oscillations in the absence of a lattice, Science **356**(6341), 945 (2017).
[6] S. Hofferberth, I. Lesanovsky, B. Fischer, T. Schumm, and J. Schmiedmayer, Non-equilibrium coherence dynamics in one-dimensional Bose gases, Nature **449**, 324 (2007).
[7] F. Meinert, M. J. Mark, E. Kirilov, K. Lauber, P. Weinmann, M. Gröbner, A. J. Daley, and H.-C. Nägerl, Observation of many-body dynamics in long-range tunneling after a quantum quench, Science **344**(6189), 1259 (2014).
[8] J. Wilson, N. Malvania, Y. Le, Y. Zhang, M. Rigol, and D. S. Weiss, Observation of dynamical fermionization, Science **367**(6485), 1461 (2020).
[9] Y. Le, Y. Zhang, S. Gopalakrishnan, M. Rigol, and D. S. Weiss, Observation of hydrodynamization and local prethermalization in 1d Bose gases, Nature (London) **618**, 494 (2023).
[10] T. Stöferle, H. Moritz, C. Schori, M. Köhl, and T. Esslinger, Transition from a strongly interacting 1d superfluid to a mott insulator, Physical review letters **92**(13), 130403 (2004).
[11] D. Clément, N. Fabbri, L. Fallani, C. Fort, and M. Inguscio, Exploring correlated 1D Bose gases from the

superfluid to the Mott-insulator state by inelastic light scattering, Phys. Rev. Lett. **102**, 155301 (Apr 2009).
[12] E. Haller, R. Hart, M. J. Mark, J. G. Danzl, L. Reichsöllner, M. Gustavsson, M. Dalmonte, G. Pupillo, and H.-C. Nägerl, Pinning quantum phase transition for a Luttinger liquid of strongly interacting bosons, Nature (London) **466**, 597 (2010).
[13] N. Fabbri, S. D. Huber, D. Clément, L. Fallani, C. Fort, M. Inguscio, and E. Altman, Quasiparticle dynamics in a Bose insulator probed by interband Bragg spectroscopy, Phys. Rev. Lett. **109**, 055301 (Jul 2012).
[14] G. Boéris, L. Gori, M. D. Hoogerland, A. Kumar, E. Lucioni, L. Tanzi, M. Inguscio, T. Giamarchi, C. D'Errico, G. Carleo, et al., Mott transition for strongly interacting one-dimensional bosons in a shallow periodic potential, Phys. Rev. A **93**, 011601(R) (2016).
[15] J. Billy, V. Josse, Z. Zuo, A. Bernard, B. Hambrecht, P. Lugan, D. Clément, L. Sanchez-Palencia, P. Bouyer, and A. Aspect, Direct observation of Anderson localization of matter waves in a controlled disorder, Nature (London) **453**, 891 (2008).
[16] C. D'Errico, E. Lucioni, L. Tanzi, L. Gori, G. Roux, I. P. McCulloch, T. Giamarchi, M. Inguscio, and G. Modugno, Observation of a disordered bosonic insulator from weak to strong interactions, Phys. Rev. Lett. **113**, 095301 (2014).
[17] L. Gori, T. Barthel, A. Kumar, E. Lucioni, L. Tanzi, M. Inguscio, G. Modugno, T. Giamarchi, C. D'Errico, and G. Roux, Finite-temperature effects on interacting bosonic one-dimensional systems in disordered lattices, Phys. Rev. A **93**, 033650 (2016).
[18] M. Sbroscia, K. Viebahn, E. Carter, J.-C. Yu, A. Gaunt, and U. Schneider, Observing localization in a 2D quasicrystalline optical lattice, Phys. Rev. Lett. **125**, 200604 (Nov 2020).
[19] J. Vijayan, P. Sompet, G. Salomon, J. Koepsell, S. Hirthe, A. Bohrdt, F. Grusdt, I. Bloch, and C. Gross, Time-resolved observation of spin-charge deconfinement in fermionic Hubbard chains, Science **367**(6474), 186 (2020).
[20] R. Senaratne, D. Cavazos-Cavazos, S. Wang, F. He, Y.-T. Chang, A. Kafle, H. Pu, X.-W. Guan, and R. G. Hulet, Spin-charge separation in a one-dimensional Fermi gas with tunable interactions, Science **376**(6599), 1305 (2022).
[21] Z. Hadzibabic, P. Krüger, M. Cheneau, B. Battelier, and J. Dalibard, Berezinskii-Kosterlitz-Thouless crossover in a trapped atomic gas, Nature (London) **441**(7097), 1118 (2006).
[22] L.-C. Ha, C.-L. Hung, X. Zhang, U. Eismann, S.-K. Tung, and C. Chin, Strongly interacting two-dimensional Bose gases, Phys. Rev. Lett. **110**(14), 145302 (2013).
[23] N. Goldman, J. Dalibard, A. Dauphin, F. Gerbier, M. Lewenstein, P. Zoller, and I. B. Spielman, Direct imaging of topological edge states in cold-atom systems, Proceedings of the National Academy of Sciences **110**(17), 6736 (2013).
[24] M. Tarnowski, F. N. Ünal, N. Fläschner, B. S. Rem, A. Eckardt, K. Sengstock, and C. Weitenberg, Measuring topology from dynamics by obtaining the Chern number from a linking number, Nature communications **10**(1), 1728 (2019).
[25] J. Struck, C. Ölschläger, R. Le Targat, P. Soltan-Panahi, A. Eckardt, M. Lewenstein, P. Windpassinger, and K. Sengstock, Quantum simulation of frustrated classical magnetism in triangular optical lattices, Science **333**(6045), 996 (2011).
[26] N. Fabbri, D. Clément, L. Fallani, C. Fort, and M. Inguscio, Momentum-resolved study of an array of one-dimensional strongly phase-fluctuating Bose gases, Phys. Rev. A **83**, 031604 (Mar 2011).
[27] C. Li, T. Zhou, I. Mazets, H.-P. Stimming, F. S. Møller, Z. Zhu, Y. Zhai, W. Xiong, X. Zhou, X. Chen, et al., Relaxation of bosons in one dimension and the onset of dimensional crossover, SciPost Physics **9**(4), 058 (2020).
[28] F. Meinert, M. Panfil, M. J. Mark, K. Lauber, J.-S. Caux, and H.-C. Nägerl, Probing the excitations of a Lieb-Liniger gas from weak to strong coupling, Phys. Rev. Lett. **115**, 085301 (2015).
[29] See details in supplemental material.
[30] T. Kraemer, J. Herbig, M. Mark, T. Weber, C. Chin, H.-C. Nägerl, and R. Grimm, Optimized production of a cesium Bose-Einstein condensate, Applied Physics B **79**, 1013 (2004).
[31] H. Yao, L. Pizzino, and T. Giamarchi, Strongly-interacting bosons at 2d-1d dimensional crossover, SciPost Physics **15**, 050 (2023).
[32] A. Minguzzi and P. Vignolo, Strongly interacting trapped one-dimensional quantum gases: Exact solution, AVS Quantum Science **4**(2) (2022).
[33] T.-L. Ho and Q. Zhou, Intrinsic heating and cooling in adiabatic processes for bosons in optical lattices, Phys. Rev. Lett. **99**, 120404 (Sep 2007).
[34] W. Xu and M. Rigol, Universal scaling of density and momentum distributions in Lieb-Liniger gases, Phys. Rev. A **92**, 063623 (2015).
[35] W. F. Giauque and D. P. MacDougall, Attainment of temperatures below 1° absolute by demagnetization of $gd_2(SO_4)_3{\cdot}8h_2o$, Phys. Rev. **43**, 768 (May 1933).
[36] M. Fattori, T. Koch, S. Goetz, A. Griesmaier, S. Hensler, J. Stuhler, and T. Pfau, Demagnetization cooling of a gas, Nature Physics **2**, 765 (2006).
[37] N. Navon, R. P. Smith, and Z. Hadzibabic, Quantum gases in optical boxes, Nature Physics **17**(12), 1334 (2021).
[38] Y. Guo, H. Yao, S. Ramanjanappa, S. Dhar, M. Horvath, L. Pizzino, T. Giamarchi, M. Landini, and H.-C. Nägerl, Experimental observation of the 2d-1d dimensional crossover in strongly interacting ultracold bosons, arXiv preprint arXiv:2308.00411 (2023).
[39] C. J. M. Mathy, M. B. Zvonarev, and E. Demler, Quantum flutter of supersonic particles in one-dimensional quantum liquids, Nature Physics **8**, 881 (2012).
[40] M. Gluza, J. a. Sabino, N. H. Ng, G. Vitagliano, M. Pezzutto, Y. Omar, I. Mazets, M. Huber, J. Schmiedmayer, and J. Eisert, Quantum field thermal machines, PRX Quantum **2**, 030310 (Jul 2021).
[41] M. Troyer, B. Ammon, and E. Heeb, in International Symposium on Computing in Object-Oriented Parallel Environments, Springer (1998), pp. 191–198.
[42] A. Albuquerque, F. Alet, P. Corboz, P. Dayal, A. Feiguin, S. Fuchs, L. Gamper, E. Gull, S. Guertler, A. Honecker, et al., The ALPS project release 1.3: Open-source software for strongly correlated systems, J. Magn. Magn. Mater. **310**, 1187 (2007).
[43] B. Bauer, L. D. Carr, H. Evertz, A. Feiguin, J. Freire, S. Fuchs, L. Gamper, J. Gukelberger, E. Gull,

S. Guertler, et al., The ALPS project release 2.0: Open source software for strongly correlated systems, J. Stat. Mech.: Th. Exp. **05**, P05001 (2011).

[44] Data set is available from Zenodo at doi: 10.5281/zenodo.8212006.

[45] E. Haller, M. Rabie, M. J. Mark, J. G. Danzl, R. Hart, K. Lauber, G. Pupillo, and H.-C. Nägerl, Three-body correlation functions and recombination rates for bosons in three dimensions and one dimension, Phys. Rev. Lett. **107**, 230404 (Dec 2011).

[46] M. A. Cazalilla, R. Citro, T. Giamarchi, E. Orignac, and M. Rigol, One dimensional bosons: From condensed matter systems to ultracold gases, Rev. Mod. Phys. **83**, 1405 (2011).

[47] Z. Hadzibabic and J. Dalibard, Two-dimensional Bose fluids: An atomic physics perspective, La Rivista del Nuovo Cimento **34**(6), 389 (2011).

[48] F. Gerbier, J. H. Thywissen, S. Richard, M. Hugbart, P. Bouyer, and A. Aspect, Momentum distribution and correlation function of quasicondensates in elongated traps, Phys. Rev. A **67**, 051602 (May 2003).

[49] B. Yang, Y.-Y. Chen, Y.-G. Zheng, H. Sun, H.-N. Dai, X.-W. Guan, Z.-S. Yuan, and J.-W. Pan, Quantum criticality and the tomonaga-luttinger liquid in one-dimensional bose gases, Phys. Rev. Lett. **119**, 165701 (Oct 2017).

Experimental Observation of the 2D-1D Dimensional Crossover in Strongly Interacting Ultracold Bosons

Yanliang Guo,[1,*] Hepeng Yao,[2,*] Satwik Ramanjanappa,[1] Sudipta Dhar,[1] Milena Horvath,[1] Lorenzo Pizzino,[2] Thierry Giamarchi,[2] Manuele Landini,[1] and Hanns-Christoph Nägerl[†]

[1] *Institut für Experimentalphysik und Zentrum für Quantenphysik, Universität Innsbruck, Technikerstraße 25, Innsbruck, 6020, Austria*

[2] *DQMP, University of Geneva, 24 Quai Ernest-Ansermet, Geneva, CH-1211 , Switzerland*

Dimensionality plays an essential role in determining the nature and properties of a physical system. For quantum systems the impact of interactions and fluctuations is enhanced in lower dimensions, leading to a great diversity of genuine quantum effects for reduced dimensionality. In most cases, the dimension is fixed to some integer value. Here, we experimentally probe the dimensional crossover from two to one dimension using strongly interacting ultracold bosons in variable lattice potentials and compare the data to ab-initio theory that takes into account non-homogeneous trapping and non-zero temperature. From a precise measurement of the momentum distribution we analyze the characteristic decay of the one-body correlation function in the two dimensionalities and then track how the decay is modified in the crossover. A varying two-slope structure is revealed, reflecting the fact that the particles see their dimensionality as being one or two depending on whether they are probed on short or long distances, respectively. Our observations demonstrate how quantum properties in the strongly-correlated regime evolve in the dimensional crossover as a result of the interplay between dimensionality, interactions, and temperature.

Understanding the effects of interactions in a quantum system is one of the central problems of the field of quantum many-body physics. Interactions lead to phases of matter with remarkable properties, such as superfluidity or fractional quantum Hall conductance [1, 2]. Quite crucially such effects are intimately linked to the dimensionality of the system. Lower dimensions usually reinforce the effects of interactions, as well as of quantum and thermal fluctuations, allowing for even greater deviations from the physics of non-interacting systems. Taking interacting bosons as a comparatively simple example, these go from robust three-dimensional (3D) superfluids with Bogoliubov quasi-particle excitations [3] to quasi-long-range ordering with Berezinski-Kosterlitz-Thouless (BKT) topological phase transitions in 2D [4, 5] and to Tomonaga-Luttinger liquids in 1D [6], where quasi-particles do not exist and collective fermionization occurs [7–9] for strong interactions.

In most systems, the dimensionality is fixed once for all and the various phenomena are studied independently. There is, however, a very interesting class of systems for which the effective dimensionality can be controlled via parameters such as temperature, confinement lengthscale, or observational lengthscale. Examples of systems that feature such a dimensional crossover [10] are organic conductors and superconductors [11, 12] made of weakly coupled one-dimensional chains, or high-temperature superconductors made of weakly coupled planes for fermions [13], or coupled chains and ladders for bosons [14–18]. Needless to say, in such systems one of the crucial questions is to understand how the dimensionally different phases are linked together upon a variation of temperature, tunnel coupling, or distance, and how the high-dimensional phases are influenced by the exotic low-dimensional physics coming from the high-temperature or short-distance regime. Doing so requires however an excellent degree of control and the right range of parameters such as tunnelling vs temperature, which is a strong challenge in material research for condensed-matter realizations.

In this work, guided by a recent theoretical study [19], we present the first experimental observation of the quantum correlation properties for strongly-interacting cold atomic bosons in the dimensional crossover from 2D to 1D. In recent years, cold atoms [3] have provided, due to their remarkable degree of control of the microscopic Hamiltonians, a remarkable alternative playground to address strongly-correlated quantum matter [20]. First studies have been carried out for weakly interacting gases addressing non-equilibrium dynamics [21–23], excitation spectra [24] and transverse superfluidity [25] in regimes when the dimension is not strictly integer. However, testing the quantum correlation properties predicted in Ref. [19] is not possible when interactions are weak. Our Cesium quantum gas, on the contrary, offers the possibility of strong correlations and thus to have a clear distinction between the two integer dimensionalities, which prompts us to follow the evolution during the dimensional crossover. With quantum Monte Carlo (QMC) calculations, we benchmark the experimental data at both $D = 2$ and 1. Within the dimensional crossover, we observe a two-regime structure for the first-order correlation function. We explicitly show how the system evolves from a 2D gas with BKT algebraic decay for the correlation function to a system of coupled 1D tubes with exponential decay, and how it finally becomes a system of incoherently coupled 1D tubes.

The experimental sequence starts with an interaction-

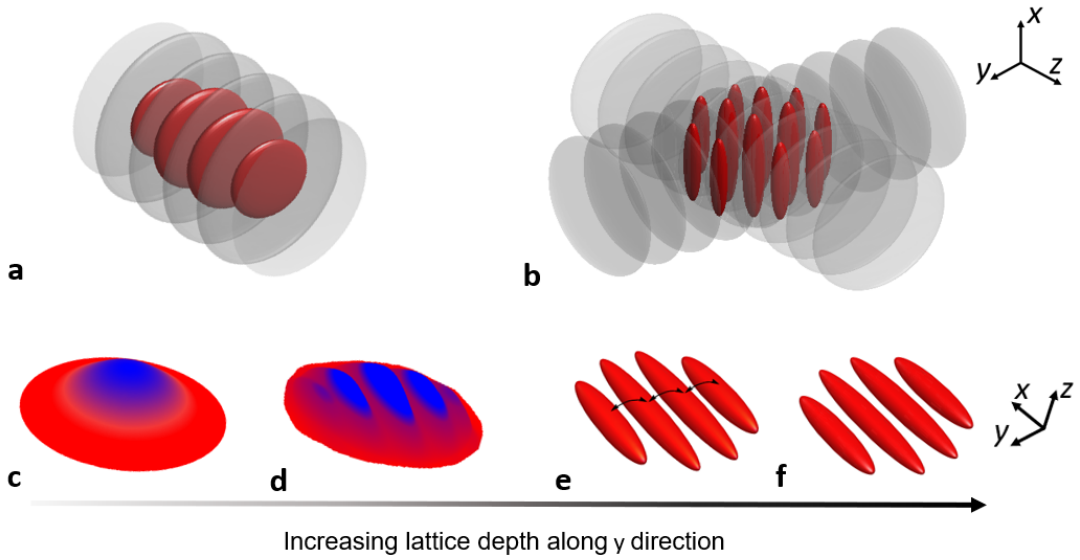

Figure 1. **Conceptual sketch of the experiment.** Starting from a 3D BEC, we generate an ensemble of low-dimensional units, namely a. 2D layers and b. 1D tubes. (c-f) Schematic plots for the evolution of one particular layer during the dimensional crossover, where the quantum gas goes from 2D (c), to modulated 2D (d), to coherently-coupled 1D (e), and then to incoherently-coupled 1D (f) by continuously increasing the lattice depth. The blue color in (c-d) indicates the high-density regime where superfluid regions appear.

tunable 3D Bose-Einstein condensate (BEC) containing typically 1.5×10^5 Cs atoms prepared in the lowest magnetic hyperfine state $|F, m_F\rangle = |3, 3\rangle$, held in a crossed-beam dipole trap and levitated against gravity by a magnetic field gradient [26]. The temperature of the 3D BEC is 10(1) nK as determined from a small non-condensed fraction in time-of-flight (TOF) measurements. With the 3D s-wave scattering length set to $a_{3D} \approx 200a_0$, the BEC is in the Thomas-Fermi regime. A 2D optical lattice with lattice beams along the y and z directions with a lattice spacing $a = \lambda/2 = 532$ nm is gradually ramped up in 500 ms to a target value, with λ the wavelength of the lattice light. The lattice depth along the z direction is always set to $V_z = 30E_r$, with $E_r = \pi^2\hbar^2/(2ma^2)$ the recoil energy, resulting in tight transversal harmonic trapping with trap frequency $\omega_z/2\pi = 11$ kHz. Along the y-direction, the lattice depth V_y is varied in the range from 0 to $30E_r$. At the two limiting values $V_y/E_r = 0$ and 30 the system forms an ensemble of 2D layers and an array of 1D tubes, respectively, see Fig. 1. With the lattice beams providing also some transversal confinement, the trapping frequency ω_x along the third direction varies from $\omega_x/2\pi = 10.1(2)$ Hz for $V_y = 0$ to $\omega_x/2\pi = 14.3(2)$ Hz for $V_y = 30E_r$.

After loading the atoms into the lattice, the offset magnetic field B is ramped adiabatically to tune a_{3D} to $620a_0$. This sets the 2D interaction parameter to $\gamma_{2D} = 1.5$ in the strictly-2D regime and the Lieb-Linger parameter to $\gamma_{1D} = 40$ in the strictly-1D regime (see Methods), putting our systems in the strongly-interacting regime in both integer dimensions [20, 27, 28]. In 1D, the interaction is strong enough that the so-called Tonks-Girardeau regime is entered, where the 1D bosons show fermionized behavior [7–9]. Given the lattice along the y direction, we are able to accurately control the dimensionality of the strongly-interacting bosonic system. By increasing V_y continuously, the system goes through the whole dimensional crossover from 2D to 1D. As V_y rises, each single layer goes through various regimes, namely: strictly 2D (S2D), modulated 2D (M2D), coupled 1D tubes (C1D) and isolated 1D tubes (I1D), as illustrated in Fig. 1 (c-f).

The main quantity we concentrate on is the one-body correlation function $g^{(1)}(x, x', y, y') = \langle\hat{\Psi}^\dagger(x', y')\hat{\Psi}(x, y)\rangle$, which allows us to extract the quantum coherence properties of the cold atomic gas. In our experiment, $g^{(1)}$ is measured via the TOF technique. After loading the lattice, we hold the gas in the trap for 50 ms. We remove all trapping potentials for 56-ms TOF with zeroed interactions [29], followed by absorption imaging. The TOF duration is long enough to satisfy the far-field approximation. Given the interaction zeroing, the measured density distribution is a faithful representation of the 2D resp. 1D momentum distribution $n(k_x, k_y)$. Fourier transform then gives the information of $g^{(1)}$. Specifically, we obtain the integrated correlation function

$$G^{(1)}(x, y) = \iint dx'dy'\langle\Psi^\dagger(x' + x, y' + y)\Psi(x', y')\rangle. \quad (1)$$

The typical decay with distance is very distinct and its analytical form in the homogeneous case for the different integer dimensionalities has been calculated. In 2D, $g^{(1)}$

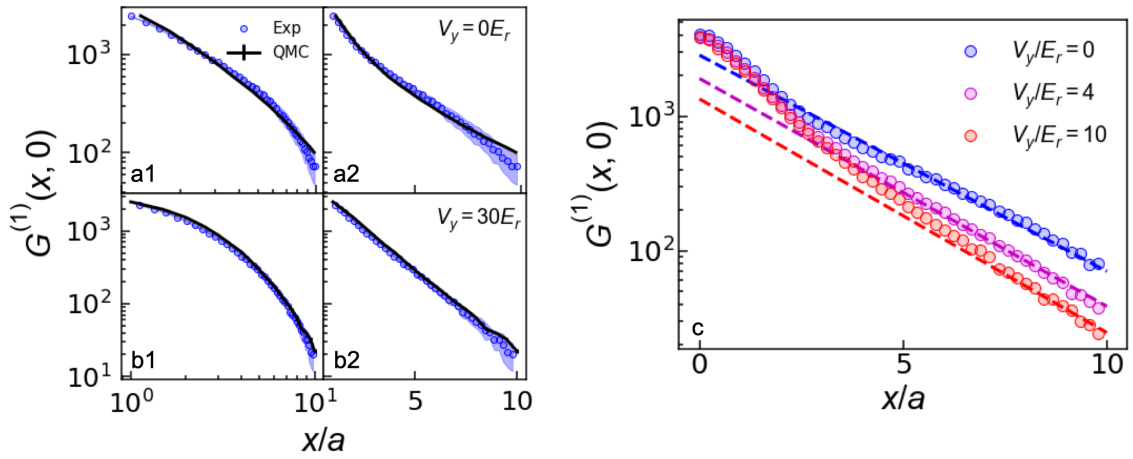

Figure 2. **Characteristic decay of the longitudinal correlation function** $G^{(1)}(x,0)$. Measured $G^{(1)}(x,0)$ in the two integer dimensions (a1-b2) and in the dimensional crossover (c) as a function of longitudinal distance x/a. In a1 and a2 (b1 and b2), the data (circles) for the 2D (1D) case with $V_y/E_r = 0$ ($V_y/E_r = 30$) is plotted on a log-log resp. semi-log scale, averaged over 30 repetitions of the experiment, and is compared to the QMC calculations (solid lines). For the data in c, the strength of the transversal lattice V_y is varied as indicated. The dashed lines are linear fits of the long-range behavior in the semi-log scale. Their slopes vary by less than 10%.

is expected to decay as

$$g^{(1)}_{2D}(\mathbf{r},0) \sim \begin{cases} |\mathbf{r}|^{-\alpha_{2D}}, & T < T_c \\ e^{-\eta_{2D}|\mathbf{r}|}, & T > T_c. \end{cases} \quad (2)$$

with 2D distance $\mathbf{r}$. Below the critical temperature T_c given by $n_s\lambda_T^2(T_c) = 4$ the decay is algebraic with a BKT-type exponent $\alpha_{2D} = 1/n_s\lambda_T^2$, where n_s is the 2D superfluid density and λ_T is the de Broglie wavelength [20, 27]. Above T_c, the decay is exponential with a thermal exponent $\eta_{2D} = \frac{\sqrt{4\pi}}{\lambda_T e^{n\lambda_T^2/2}}$ where n is the 2D density. In the strict 1D limit, $g^{(1)}$ is expected to exhibit various decay regimes at different distances

$$g^{(1)}_{1D}(x,0) \sim \begin{cases} x^{-\alpha_{1D}}, & x_0 < x < \xi(T) \\ e^{-\eta_{1D}x}, & x > \xi(T) \end{cases} \quad (3)$$

Above a short-range cutoff x_0 (which is less than the typical experimental resolution) $g^{(1)}_{1D}$ decays algebraically with a Tomonaga-Luttinger-liquid-type exponent $\alpha_{1D} = 1/2K$, where K is the Luttinger parameter. For larger distances above the thermal length $\xi(T) = 2uK/(\pi k_B T)$, it decays exponentially with exponent $\eta_{1D} = 1/\xi(T)$. Here, u is the sound velocity in the 1D gas [6, 28]. Notably, for $T > 0$, the regime of the exponential decay always exists.

Our results for $G^{(1)}(x, y = 0)$ of the trapped system in the two integer-dimension limits and in the crossover regime are displayed in Fig. 2. In 2D, the decay is algebraic for short distances and then turns over into an exponential decay. In 1D, the decay is clearly exponential. The QMC calculations recover these two regimes well. In the dimensional crossover regime, we observe a two-structure decay pattern as shown in Fig. 2 (c) and discussed in more detail below.

For the 2D case, our data suggests that the change of the decay behavior from an algebraic to an exponential happens around $r \sim 5a$. Fitting the data with $G^{(1)}(x,0) \sim x^{-\alpha}$ in the range of $r < 5a$ and $G^{(1)}(x,0) \sim e^{-\eta_{2D}x/a}$ in the range of $5a < r < 10a$ gives $\alpha = 1.1(1)$ and $\eta_{2D} = 0.36(1)$. The BKT-type algebraic decay is consistent with the existence of a superfluid core in the center of the trap (blue region in Fig. 1 (c)). At larger radii, a ring of normal fluid is formed, which contributes to the exponential decay (red region in Fig. 1 (c)).

The validity of such a simple model approach can be checked by QMC calculations. We use the continuous space path-integral MC method to simulate the system within the grand-canonical ensemble at finite temperature. In each layer, the system is modeled by the elementary many-body Hamiltonian

$$\hat{H} = \sum_j \left[-\frac{\hbar^2}{2m}\nabla_j^2 + V(\hat{\mathbf{r}}_j) \right] + \sum_{j<k} U(\hat{\mathbf{r}}_j - \hat{\mathbf{r}}_k) \quad (4)$$

with $\hat{\mathbf{r}}_j = (x_j, y_j)$ the position of the j-th particle. The term $U(\hat{\mathbf{r}})$ models the short-range repulsive two-body interaction, see Methods. The external potential reads $V(\mathbf{r}) = m\omega^2|\mathbf{r}|^2/2 + V_y \cos^2(\pi y/a)$, consisting of a 2D harmonic trap and a unidirectional lattice. The correlation function $G^{(1)}(x,y)$ is computed by the worm algorithm implementation [19, 30]. We simulate a single layer given the experimental conditions, namely with a weighted atom number $N_w = 4000$ (see Methods and Refs. [31, 32]) and for strong interactions a_{3D}=620a_0. We

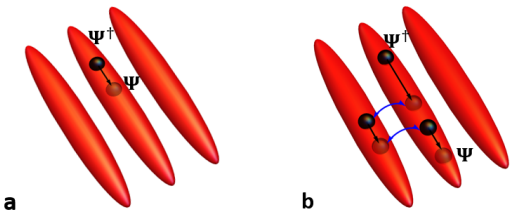

Figure 3. **Illustration of the mechanism behind the first-order correlation function and its interpretation.** (a) On short distances, the particles have less chance to tunnel into the neighboring tubes. They perceive their world as 1D. (b) For longer distances, the particles have more opportunity to tunnel between the tubes. The 2D character takes over.

find that our experimental data is well fitted by the QMC calculation when the temperature is set to T=16 nK.

In the 1D limit, the experimental data shows an exponential decay over the full range $0 < x < 10a$, see Fig. 2 b1 and b2. Given the strong interactions, the 1D system is deeply in the Tonks-Girardeau regime. In this regime, the exponential decay of the correlation function has been calculated under trapping conditions [33], giving $G^{(1)}(x) \sim e^{-\eta_{1D}x/a}$, with $\eta_{1D} = mk_BTa/2\hbar^2 n_0$ and n_0 the 1D particle density in the center of the trap. Fitting the experimental data with this formula gives $\eta_{1D} = 0.53(1)$. This is consistent with the QMC simulation with weighted atom number $N_w = 25$ and center particle density $n_0 a = 0.51$ for a temperature of T=7 nK. As a cross check, by using this temperature value and $n_0 a = 0.51$ for the central density, the analytical formula gives $\eta_{\text{estimate}} = 0.52$. This fits well with the experimental data. Note that, thanks to the strong interactions, the 1D decay constant differs greatly from the one in 2D. Note also that the temperatures in the three integer dimensions, 10(1), 16(1), and 7(1) nK, determined as discussed above, are strikingly different. This will be the subject of a forthcoming publication [34].

Our data shows that both the short-range and the long-range behavior of $G^{(1)}(x, 0)$ is subject to a significant modification as the dimensionality is switched from 2D to 1D. But how does this behavior evolve as the dimensionality is continuously changed, i.e., in the dimensional crossover regime? One naive guess could be the correlations decay faster at **all** distances as the full pattern smoothly evolves from 2D to 1D. Remarkably, we observe a different behavior, namely that the short-range behavior is governed by a stronger decay, while the long-range behavior still remains the same as in strictly-2D. This is seen in our data in Fig. 2 c as the transversal potential V_y is set to intermediate values. Although the long-range 2D decay region shrinks as the potential V_y is increased, it maintains the same decay $G^{(1)}(x, 0) \sim e^{-\eta_{2D}x}$ in 2D.

This behavior can be explained by the sketch in Fig. 3, similarly to the statement made for homogeneous systems in Ref. [19], and it is a direct visualisation of the mechanism that is behind the correlation function $g^{(1)}(x, x', y, y) = \langle \hat{\Psi}^\dagger(x', y)\hat{\Psi}(x, y)\rangle$: The probability amplitude of creating a particle at position x' and then destroying it at position x. When $|x - x'|$ is small, the particle will have less chance to tunnel into one of the neighboring tubes, and less so for higher values of the lattice depth. Thus, for short distances, the particles see themselves as living in 1D. Conversely, when $|x - x'|$ is large, the particles have more opportunity to tunnel between the tubes. In essence, they perceive their world as being 2D. As a consequence, the short-range character of the system will mimic the 1D behavior first, while the long-range behavior remains well described by the behaviour observed in 2D, as the transversal confinement is strengthened.

We now turn to the short-range behavior of $G^{(1)}(x, 0)$ in the dimensional crossover regime. To capture the transition from a 2D-power-law to a 1D-exponential decay, we use a Pearson correlation coefficient analysis by computing $P(X, Y) = \text{cov}(X, Y)/\sigma_X\sigma_Y$ for the data sets $(x, \log\ G^{(1)})$ and $(\log x, \log\ G^{(1)})$ in the range $1.7 < x/a < 4.5$. The value $P(X, Y)$ is a measure for the linearity of the dataset, and with the semi-log and log-log rescaled data it allows us to distinguish between algebraic and exponential decay. The results are shown in Fig. 4 a. The decay is closer to algebraic when $V_y < 10E_r$. Around $V_y = 10E_r$, the decay becomes an exponential. Our data can be further examined on the basis of its statistical fluctuations by computing the normalized χ^2 parameter for the algebraic and exponential fits [35], see inset of Fig. 4. We compare the data to $1 \pm 5\sigma$ (grey area), where σ is the standard deviation of χ^2 [36]. For the two limits $V_y/E_r < 7$ and $V_y/E_r > 15$, we find that the χ^2 values of the algebraic and exponential fits drop well into the grey area. This agrees with the result of the Pearson analysis.

Our data shows that the crossover from M2D to C1D happens around $10E_r$. This value sets the scale of the tight-binding regime and fits with the theoretical prediction [19, 20]. This is consistent with the behavior of χ^2 in the range $7 < V_y/E_r < 15$, where none of the two χ^2 values is close to 1 within reasonable statistical fluctuations. This can be understood in the context of our model, predicting a coexistence of the two decay behaviors. Note that the exact crossing point of the two P values may change for varying temperatures, interaction strengths and particle numbers.

We finally turn to another quantity that also sheds light onto the dimensional crossover. The transverse zero-momentum fraction $f_c^y = \sum_{k_x} n(k_x, 0)/\sum_{k_x,k_y} n(k_x, k_y)$ reflects the coherence along the transversal direction [37], see Methods. As can be seen in Fig. 4 b its value strongly drops across the M2D regime. The decay slows down in the C1D regime. Finally, in the I1D regime, it saturates and fits well with

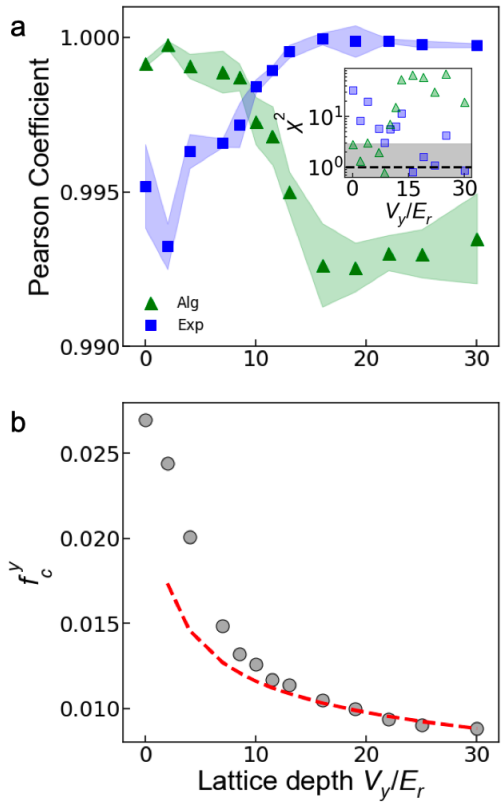

Figure 4. **Dimensional crossover analysis.** (a) Pearson correlation coefficient P as a function of the lattice depth V_y for the data in log-log (green triangles) and semi-log scale (blue squares). The shaded regions reflect the error and they are determined by shifting the window to calculate P by $\Delta x = \pm 0.25a$. The inset gives the χ^2 value for the data, with the grey region indicating the targeted area in view of statistical fluctuations. (b) Transverse zero-momentum fraction f_c^y as a function of V_y. The data (circles) is the average of 30 repetitions, and the statistical error bar is smaller than the symbol size. It is compared to the value for the ground state of quantum harmonic oscillator (red dashed line).

the prediction of the zero-momentum component for the ground state of the quantum harmonic oscillator. Such a prediction fails in the M2D regime because the system evolves into a higher dimensionality and gains more coherence. The behavior of our data is in agreement with the prediction for the homogeneous case [19].

In conclusion, we have presented an experimental characterization of the 2D-1D dimensional crossover for strongly-interacting bosons from the BKT to the Tonks-Girardeau regime. We have tracked the continuous evolution of the correlation function and the transverse zero-momentum fraction and we have shown experimentally that the short-range behavior acquires the 1D character first, while the long-range behaviour remains 2D, in agreement with the theoretical expectation. The short-range decay of $g^{(1)}$ evolves continuously from algebraic to exponential as captured by the Pearson correlation coefficient. Our experimental measurements provide the first evidence of such a two-region structure during the dimensional crossover. In principle, such behavior is also expected at the dimensional crossover between other dimensionalities (i.e., 3D-1D, 3D-2D), which could lead to further extensions of our observations. We expect that our work will trigger the study of the dimensional crossover in other types of systems, both on the bosonic and the fermionic side. Understanding such a crossover for fermionic systems will in particular be directly relevant for a host of condensed-matter realizations, such as quantum spin chains or organic and high-temperature superconductors, which exhibit the very anisotropic structure discussed in this paper, as well as very unusual properties.

The Innsbruck team acknowledges funding by a Wittgenstein prize grant under project number Z336-N36 and by the European Research Council (ERC) under project number 789017. This research was funded in part by the Austrian Science Fund (FWF) W1259-N27 and MH thanks the doctoral school ALM for hospitality. This work is also supported by the Swiss National Science Foundation under grant number 200020-188687. Numerical calculations make use of the ALPS scheduler library and statistical analysis tools [38–40].

Data access statement

The data that support the findings of this study are made publicly available from Zenodo by the authors at [41].

METHODS

Preparation of the experiment

Our experiment starts with a 3D Bose-Einstein condensate (BEC) containing typically 1.5×10^5 Cs atoms prepared in the lowest magnetic hyperfine state $|F, m_F\rangle = |3, 3\rangle$, held in a crossed-beam dipole trap with a 3D trapping frequency $\omega_{\mathrm{x,y,z}}/2\pi = (15, 8, 17)$Hz. It is levitated against gravity by means of a magnetic field gradient $\nabla B \sim 31.1$ G/cm oriented along the vertical direction, i.e., x-direction in the main text. The 3D s-wave scattering length set to $a_{\mathrm{3D}} \approx 200a_0$ where the BEC is in the Thomas-Fermi regime. The details of the trapping and cooling procedures are described in [26, 29]. To prepare an ensemble of 2D Bose gases or an array of 1D gases, we adiabatically load the BEC into an optical lattice, generated from two orthogonally and horizontally propagating retro-reflected laser beams at a wavelength $\lambda = 1064.5$ nm. After the loading procedure the lattice depth in z-direction is always set to $V_z = 30E_r$, with $E_{\mathrm{r}} = \pi^2\hbar^2/(2ma^2) = h \times 1.325$ kHz

denoting the recoil energy for Cs atoms. The lattice results in a tight transversal harmonic trapping frequency of $\omega_z/2\pi = 11\,\mathrm{kHz}$. The weak radial confinement in 2D and the longitudinal one in 1D caused by the combined lattice trapping potentials give $\omega_x^{2D}/2\pi = 10.1(2)\,\mathrm{Hz}$ and $\omega_x^{1D}/2\pi = 14.3(2)\,\mathrm{Hz}$. During the loading process almost all layers (2D) or tubes (1D) are in the Thomas-Fermi (TF) regime for weak repulsive interactions, so we can calculate the initial occupation number in each layer in 2D or each tube in 1D case through the global chemical potential and the total atom number [31, 32]. With the calculation $\bar{N} = \sum_i N_i^2/\sum_i N_i$ and N_i the atom number of the i-th tube (or layer), we obtain the weighted average number $\overline{N}_{2D} = 4000$ in 2D and $\overline{N}_{1D} = 25$ in 1D.

In the lattice, we adiabatically raise the 3D scattering length to $a_{3D} = 620a_0$ by means of a broad magnetic Feshbach resonance [29]. The ramp time (50 ms) is chosen carefully, i.e., slow enough to avoid any excitations of breathing modes in the gas. In both the 2D and 1D regimes, we calculate the coupling constants g to

$$g_{2D} \simeq \frac{2\hbar^2\sqrt{2\pi}}{ml_\perp/a_{3D} + 1/\sqrt{2\pi}\ln(1/\pi q^2 l_\perp^2)}, \quad (5)$$

$$g_{1D} = \frac{2\hbar^2 a_{3D}}{ml_\perp^2}\left(1 - \frac{1.036a_{3D}}{l_\perp}\right)^{-1} \quad (6)$$

with $l_\perp = \sqrt{\hbar/m\omega_\perp}$ the characteristic transverse length, $q = \sqrt{2m|\mu|/\hbar^2}$ the quasi-momentum, and μ the chemical potential. The interaction regime of the system can further be captured by the 2D interaction parameter $\gamma_{2D} = mg_{2D}/\hbar^2 = 1.5$ and 1D Lieb-Liniger parameter $\gamma_{1D} = mg_{1D}/\hbar^2 na = 40$. The criteria for the strongly interacting regimes in 2D and 1D are given by $\gamma_{2D} \geq 1$ and $\gamma_{1D} \gg 1$ [20, 27, 28], respectively.

Amplitude-amplitude correlation function $G^{(1)}(x,0)$

In the present work, we study the integrated correlation function of the trapped system

$$G^{(1)}(x,y) = \iint dx'dy'\langle\Psi^\dagger(x'+x,y'+y)\Psi(x',y')\rangle. \quad (7)$$

For a homogeneous system, this value can be linked with the one-body correlation function $g^{(1)}(x,y) = \langle\Psi^\dagger(x,y)\Psi(0,0)\rangle$ by $G^{(1)}(x,y) = g^{(1)}(x,y)L_xL_y$, with L_x, L_y the system sizes along the x,y-directions. Note that, due to the break of translational invariance in the trapped system, such a relation is not valid anymore and we have to focus on the quantity $G^{(1)}(x,y)$. Thanks to the correspondence of reciprocal space, it can be linked to the momentum distribution $n(k)$ by Fourier transform

$$G^{(1)}(x,y) = \sum_{k_x,k_y} n(k_x,k_y)e^{-i(k_xx+k_yy)}\Delta k_x\Delta k_y. \quad (8)$$

In the experiment, the momentum distribution $n(k_x,k_y)$ is obtained by performing a time-of-flight measurement while Δk_x and Δk_y are the resolutions in momentum space, limited by the imaging camera's pixel size. For this, applying a discrete Fourier transform on $n(k_x)\Delta k_x$ results in the integrated amplitude-amplitude correlation function $G^{(1)}(x,0)$ as plotted in Fig 2.

Resolving the image angle for the zero-momentum fraction

Our setup consists of two lattice beams perpendicular to each other along the y and z axes. There is an angle of $\theta \sim 57°$ between the propagation axis of the imaging beam and the y-direction, see Fig. 5. To determine the momentum distribution $n_y(k_y)$, we need to deconvolve the measured one $n_w(k_w)$. Specifically, the vectors k_w, k_z and k_y lie in one plane and hence k_y can be expressed in terms of k_w and k_z. The measured $n_w(k_w)$ can thus be written as a product of the momentum distributions $n_y(k_y)$ along y- and $n_z(k_z)$ along z-direction

$$n_w(k_w) = \int n_z(k_z)n_y(\frac{k_w}{\sin\theta} - \frac{k_z}{\tan\theta})dk_z, \quad (9)$$

which is a convolution of n_y and n_z. Since $V_z = 30E_r$, $n_z(k_z)$ is well approximated by the ground state of the harmonic oscillator. Thus, deconvolving and applying the inverse Fourier transform on the functions n_z and n_w gives us n_y. We then take the atom number within $\Delta k_y = 2\pi/L_y$ to calculate the zero-momentum fraction.

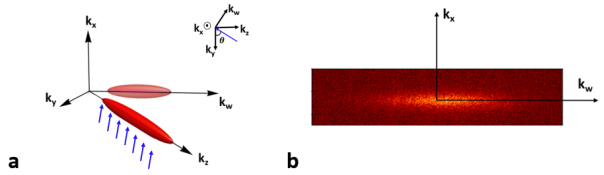

Figure 5. **A schematic of our imaging setup and an example of the image.** (a) The vectors k_y, k_z, k_w and the imaging direction (blue arrows) all lie in one plane, with k_x perpendicular to this plane, see also inset. The red 3D ellipsoid along the k_z direction indicates the atomic cloud after TOF starting from an ensemble of 2D layers for $V_y = 0E_r$. The light red 2D ellipsoid along k_w direction is the shadow in our absorption image. (b) An example of a projected image after TOF for $V_y = 0E_r$.

The quantum Monte Carlo calculation

The numerical computation of the one-body correlation function $G^{(1)}(x,y)$ is carried out by the path integral Monte Carlo method [42]. Similarly as Refs. [19, 43, 44], we simulate the system with the Hamiltonian in Eq. 4

in the main text within the grand canonical ensemble, at finite temperature T, interaction strength g_{2D} and chemical potential μ (equivalently particle number N). Notably, the two-body interaction propagator is generated by the pair-product approximation and generalized to any interaction regimes, for details see Ref. [30]. We take into account the presence of both the continuous optical lattice and the harmonic trap, with the same parameters as for the experimental setup. By properly adapting the numerical parameters, we can simulate 2D systems up to sizes of $130a$ and particle numbers 5000. Moreover, thanks to the worm algorithm implementations [45, 46], we can extended our simulations to the open wordline G sectors, where the statistics of creation and annihilation operators with open ends at (x', y') and $(x' + x, y' + y)$ are counted. This enables us to calculate the one-body correlation function defined in Eq.1 of the main text. For symmetry reasons, it is sufficient to calculate it to half of the system size. The numerical calculations make use of the ALPS scheduler library and statistical analysis tools [38–40].

* These authors contributed equally to this work.
† christoph.naegerl@uibk.ac.at

[1] D. C. Tsui, H. L. Stormer, and A. C. Gossard, Two-dimensional magnetotransport in the extreme quantum limit, Phys. Rev. Lett. **48**, 1559 (May 1982).
[2] R. B. Laughlin, Anomalous quantum Hall effect: An incompressible quantum fluid with fractionally charged excitations, Phys. Rev. Lett. **50**, 1395 (May 1983).
[3] L. Pitaevskii and S. Stringari, Bose-Einstein Condensation (Clarendon Press, Oxford, 2003).
[4] J. M. Kosterlitz and D. J. Thouless, Ordering, metastability and phase transitions in two-dimensional systems, J. Phys. C: Solid State Phys. **6**(7), 1181 (1973).
[5] Z. Hadzibabic, P. Krüger, M. Cheneau, B. Battelier, and J. Dalibard, Berezinskii–Kosterlitz–Thouless crossover in a trapped atomic gas, Nature **441**, 1118 (2006).
[6] T. Giamarchi, Quantum Physics in One Dimension, vol. 121 of International Series of Monographs on Physics (Oxford University Press, Oxford, 2004).
[7] M. Girardeau, Relationship between systems of impenetrable bosons and fermions in one dimension, Journal of Mathematical Physics **1**(6), 516 (1960).
[8] B. Paredes, A. Widera, V. Murg, O. Mandel, S. Folling, I. Cirac, GV. Shlyapnikov, TW. Hansch, and I. Bloch, Tonks-Girardeau gas of ultracold atoms in an optical lattice, Nature **429**, 277 (2004).
[9] T. Kinoshita, T. Wenger, and D. S. Weiss, Observation of a one-dimensional Tonks-Girardeau gas, Science **305**, 1125 (2004).
[10] T. Giamarchi, Quantum phase transitions in quasi-one dimensional systems (CRC Press; Taylor and Francis, Boca Raton, 2010), p. 291.
[11] A. G. Lebed, The physics of organic superconductors and conductors, vol. 110 (Springer, Heidelberg, 2008).
[12] T. Giamarchi, Theoretical framework for quasi-one dimensional systems, Chemical reviews **104**(11), 5037 (2004).
[13] J. Orenstein and A. Millis, Advances in the physics of high-temperature superconductivity, Science **288**(5465), 468 (2000).
[14] A. Ho, M. Cazalilla, and T. Giamarchi, Deconfinement in a 2D optical lattice of coupled 1D boson systems, Physical Review Letters **92**, 130405 (2004).
[15] M. Cazalilla, A. Ho, and T. Giamarchi, Interacting Bose gases in quasi-one-dimensional optical lattices, New Journal of Physics **8**(8), 158 (2006).
[16] M. Klanjšek, H. Mayaffre, C. Berthier, M. Horvatić, B. Chiari, O. Piovesana, P. Bouillot, C. Kollath, E. Orignac, R. Citro, et al., Controlling Luttinger liquid physics in spin ladders under a magnetic field, Phys. Rev. Lett. **101**, 137207 (Sep 2008).
[17] T. Hong, Y. H. Kim, C. Hotta, Y. Takano, G. Tremelling, M. M. Turnbull, C. P. Landee, H.-J. Kang, N. B. Christensen, K. Lefmann, et al., Field-induced Tomonaga-Luttinger liquid phase of a two-leg spin-1/2 ladder with strong leg interactions, Phys. Rev. Lett. **105**, 137207 (Sep 2010).
[18] G. Bollmark, N. Laflorencie, and A. Kantian, Dimensional crossover and phase transitions in coupled chains: Density matrix renormalization group results, Phys. Rev. B **102**, 195145 (Nov 2020).
[19] H. Yao, L. Pizzino, and T. Giamarchi, Strongly-interacting bosons at 2D-1D dimensional crossover, arXiv:2204.02240 (to appear in Scipost Physics) .
[20] I. Bloch, J. Dalibard, and W. Zwerger, Many-body physics with ultracold gases, Rev. Mod. Phys. **80**, 885 (2008).
[21] S. Hofferberth, I. Lesanovsky, B. Fischer, T. Schumm, and J. Schmiedmayer, Non-equilibrium coherence dynamics in one-dimensional Bose gases, Nature **449**(7160), 324 (2007).
[22] C. Li, T. Zhou, I. Mazets, H.-P. Stimming, F. S. Møller, Z. Zhu, Y. Zhai, W. Xiong, X. Zhou, X. Chen, et al., Relaxation of bosons in one dimension and the onset of dimensional crossover, SciPost Physics **9**(4), 058 (2020).
[23] F. Møller, C. Li, I. Mazets, H.-P. Stimming, T. Zhou, Z. Zhu, X. Chen, and J. Schmiedmayer, Extension of the generalized hydrodynamics to the dimensional crossover regime, Phys. Rev. Lett. **126**, 090602 (Mar 2021).
[24] T. Stöferle, H. Moritz, C. Schori, M. Köhl, and T. Esslinger, Transition from a strongly interacting 1D superfluid to a Mott insulator, Phys. Rev. Lett. **92**(13), 130403 (2004).
[25] G. Chauveau, C. Maury, F. Rabec, C. Heintze, G. Brochier, S. Nascimbene, J. Dalibard, J. Beugnon, S. M. Roccuzzo, and S. Stringari, Superfluid fraction in an interacting spatially modulated Bose-Einstein condensate, Phys. Rev. Lett. **130**, 226003 (Jun 2023).
[26] T. Kraemer, J. Herbig, M. Mark, T. Weber, C. Chin, H.-C. Nägerl, and R. Grimm, Optimized production of a cesium Bose-Einstein condensate, Applied Physics B **79**, 1013 (2004).
[27] Z. Hadzibabic and J. Dalibard, Two-dimensional Bose fluids: An atomic physics perspective, La Rivista del Nuovo Cimento **34**(6), 389 (2011).
[28] M. A. Cazalilla, R. Citro, T. Giamarchi, E. Orignac, and M. Rigol, One dimensional bosons: From condensed

matter systems to ultracold gases, Rev. Mod. Phys. **83**, 1405 (2011).

[29] V. Weber, J. Herbig, M. Mark, H.-C. Nägerl, and R. Grimm, Bose-Einstein condensation of cesium, Science **299**, 232 (2003).

[30] R. Gautier, H. Yao, and L. Sanchez-Palencia, Strongly interacting bosons in a two-dimensional quasicrystal lattice, Phys. Rev. Lett. **126**(11), 110401 (2021).

[31] E. Haller, M. Rabie, M. J. Mark, J. G. Danzl, R. Hart, K. Lauber, G. Pupillo, and H.-C. Nägerl, Three-body correlation functions and recombination rates for bosons in three dimensions and one dimension, Phys. Rev. Lett. **107**, 230404 (Dec 2011).

[32] F. Meinert, M. Panfil, M. J. Mark, K. Lauber, J.-S. Caux, and H.-C. Nägerl, Probing the excitations of a Lieb-Liniger gas from weak to strong coupling, Phys. Rev. Lett. **115**, 085301 (2015).

[33] A. Minguzzi and P. Vignolo, Strongly interacting trapped one-dimensional quantum gases: Exact solution, AVS Quantum Science **4**(2), 027102 (2022).

[34] Manuscript in preparation.

[35] P. A. Murthy, I. Boettcher, L. Bayha, M. Holzmann, D. Kedar, M. Neidig, M. G. Ries, A. N. Wenz, G. Zürn, and S. Jochim, Observation of the Berezinskii-Kosterlitz-Thouless phase transition in an ultracold Fermi gas, Phys. Rev. Lett. **115**, 010401 (Jun 2015).

[36] P. R. Bevington, D. K. Robinson, J. M. Blair, A. J. Mallinckrodt, and S. McKay, Data reduction and error analysis for the physical sciences, Computers in Physics **7**(4), 415 (1993).

[37] T. Plisson, B. Allard, M. Holzmann, G. Salomon, A. Aspect, P. Bouyer, and T. Bourdel, Coherence properties of a two-dimensional trapped Bose gas around the superfluid transition, Phys. Rev. A **84**, 061606 (Dec 2011).

[38] M. Troyer, B. Ammon, and E. Heeb, in International Symposium on Computing in Object-Oriented Parallel Environments, Springer (1998), pp. 191–198.

[39] A. Albuquerque, F. Alet, P. Corboz, P. Dayal, A. Feiguin, S. Fuchs, L. Gamper, E. Gull, S. Guertler, A. Honecker, et al., The ALPS project release 1.3: Open-source software for strongly correlated systems, J. Magn. Magn. Mater. **310**, 1187 (2007).

[40] B. Bauer, L. D. Carr, H. Evertz, A. Feiguin, J. Freire, S. Fuchs, L. Gamper, J. Gukelberger, E. Gull, S. Guertler, et al., The ALPS project release 2.0: Open source software for strongly correlated systems, J. Stat. Mech.: Th. Exp. **05**, P05001 (2011).

[41] Data set is available from Zenodo at doi:10.5281/zenodo.8167239.

[42] D. M. Ceperley, Path integrals in the theory of condensed helium, Rev. Mod. Phys. **67**, 279 (1995).

[43] H. Yao, D. Clément, A. Minguzzi, P. Vignolo, and L. Sanchez-Palencia, Tan's contact for trapped Lieb-Liniger bosons at finite temperature, Phys. Rev. Lett. **121**, 220402 (2018).

[44] H. Yao, T. Giamarchi, and L. Sanchez-Palencia, Lieb-Liniger bosons in a shallow quasiperiodic potential: Bose glass phase and fractal Mott lobes, Phys. Rev. Lett. **125**, 060401 (2020).

[45] M. Boninsegni, N. Prokof'ev, and B. Svistunov, Worm algorithm for continuous-space path integral Monte Carlo simulations, Phys. Rev. Lett. **96**, 070601 (2006).

[46] M. Boninsegni, N. V. Prokof'ev, and B. V. Svistunov, Worm algorithm and diagrammatic Monte Carlo: A new approach to continuous-space path integral Monte Carlo simulations, Phys. Rev. E **74**, 036701 (2006).

BIBLIOGRAPHY

[1] H. Hertz, "Über einen Einfluss des ultravioletten Lichtes auf die electrische Entladung", Annalen der Physik **267**, 983 (1887).

[2] J. Fraunhofer, "Bestimmung des Brechungs-und des Farbenzerstreungs-Vermögens verschiedener Glasarten, in Bezug auf die Vervollkommnung achromatischer Fernröhre", Annalen der Physik **56**, 264 (1817).

[3] G. R. Kirchhoff and R. W. Bunsen, "Chemische analyse durch Spectralbeobachtungen", (2008).

[4] M. Planck, *Über das Gesetz der Energieverteilung im Normalspektrum* (Vieweg & Teubner Verlag, Wiesbaden, 1978), pp. 178–191.

[5] A. Einstein, *Über einen die Erzeugung und Verwandlung des Lichtes betreffenden heuristischen Gesichtspunkt*, 1905.

[6] N. Bohr, "I. On the constitution of atoms and molecules", The London, Edinburgh, and Dublin Philosophical Magazine and Journal of Science **26**, 1 (1913).

[7] P. W. Anderson, "More is different: broken symmetry and the nature of the hierarchical structure of science", Science **177**, 393 (1972).

[8] S.-I. Tomonaga, "Remarks on Bloch's method of sound waves applied to many-fermion problems", Progress of Theoretical Physics **5**, 544 (1950).

[9] J. M. Luttinger, "An exactly soluble model of a many-fermion system", Journal of Mathematical Physics **4**, 1154 (1963).

[10] F. D. M. Haldane, "'Luttinger liquid theory' of one-dimensional quantum fluids. I. Properties of the Luttinger model and their extension to the general 1D interacting spinless Fermi gas", Journal of Physics C: Solid State Physics **14**, 2585 (1981).

[11] H. Bernien, S. Schwartz, A. Keesling, H. Levine, A. Omran, H. Pichler, S. Choi, A. S. Zibrov, M. Endres, M. Greiner, V. Vuletić, and M. D. Lukin, "Probing many-body dynamics on a 51-atom quantum simulator", Nature **551**, 579 (2017).

[12] I. Bloch, J. Dalibard, and W. Zwerger, "Many-body physics with ultracold gases", Rev. Mod. Phys. **80**, 885 (2008).

[13] S. Giorgini, L. P. Pitaevskii, and S. Stringari, "Theory of ultracold atomic Fermi gases", Rev. Mod. Phys. **80**, 1215 (2008).

[14] E. Haller, R. Hart, M. J. Mark, J. G. Danzl, L. Reichsöllner, M. Gustavsson, M. Dalmonte, G. Pupillo, and H.-C. Nägerl, "Pinning quantum phase transition for a Luttinger liquid of strongly interacting bosons", Nature **466**, 597 (2010).

[15] M. A. Cazalilla, R. Citro, T. Giamarchi, E. Orignac, and M. Rigol, "One dimensional bosons: from condensed matter systems to ultracold gases", Rev. Mod. Phys. **83**, 1405 (2011).

[16] T. Schweigler, V. Kasper, S. Erne, I. Mazets, B. Rauer, F. Cataldini, T. Langen, T. Gasenzer, J. Berges, and J. Schmiedmayer, "Experimental characterization of a quantum many-body system via higher-order correlations", Nature **545**, 323 (2017).

[17] E. Haller, M. Gustavsson, M. J. Mark, J. G. Danzl, R. Hart, G. Pupillo, and H.-C. Nägerl, "Realization of an excited, strongly correlated quantum gas phase", Science **325**, 1224 (2009).

[18] M. Horvath, A. Bastianello, S. Dhar, R. Koch, Y. Guo, J.-S. Caux, M. Landini, and H.-C. Nägerl, "Observing Bethe strings in an attractive Bose gas far from equilibrium", arXiv preprint arXiv:2505.10550 (2025).

[19] R. P. Feynman, "Simulating physics with computers", International journal of theoretical physics **21**, 467 (1982).

[20] I. Bloch, J. Dalibard, and S. Nascimbène, "Quantum simulations with ultracold quantum gases", Nature Physics **8**, 267 (2012).

[21] C. Gross and I. Bloch, "Quantum simulations with ultracold atoms in optical lattices", Science **357**, 995 (2017).

[22] M. H. Anderson, J. R. Ensher, M. R. Matthews, C. E. Wieman, and E. A. Cornell, "Observation of Bose-Einstein condensation in a dilute atomic vapor", Science **269**, 198 (1995).

[23] K. B. Davis, M.-O. Mewes, M. R. Andrews, N. J. van Druten, D. S. Durfee, D. M. Kurn, and W. Ketterle, "Bose-Einstein condensation in a gas of sodium atoms", Phys. Rev. Lett. **75**, 3969 (1995).

[24] C. C. Bradley, C. A. Sackett, and R. G. Hulet, "Bose-Einstein condensation of lithium: Observation of limited condensate number", Phys. Rev. Lett. **78**, 985 (1997).

[25] M. R. Andrews, C. G. Townsend, H.-J. Miesner, D. S. Durfee, D. M. Kurn, and W. Ketterle, "Observation of interference between two Bose condensates", Science **275**, 637 (1997).

[26] M. R. Matthews, B. P. Anderson, P. C. Haljan, D. S. Hall, C. E. Wieman, and E. A. Cornell, "Vortices in a Bose-Einstein condensate", Phys. Rev. Lett. **83**, 2498 (1999).

[27] K. W. Madison, F. Chevy, W. Wohlleben, and J. Dalibard, "Vortex formation in a stirred Bose-Einstein condensate", Phys. Rev. Lett. **84**, 806 (2000).

[28] S. Burger, K. Bongs, S. Dettmer, W. Ertmer, K. Sengstock, A. Sanpera, G. V. Shlyapnikov, and M. Lewenstein, "Dark solitons in Bose-Einstein condensates", Phys. Rev. Lett. **83**, 5198 (1999).

[29] J. Denschlag, J. E. Simsarian, D. L. Feder, C. W. Clark, L. A. Collins, J. Cubizolles, L. Deng, E. W. Hagley, K. Helmerson, W. P. Reinhardt, S. L. Rolston, B. I. Schneider, and W. D. Phillips, "Generating solitons by phase engineering of a Bose-Einstein condensate", Science **287**, 97 (2000).

[30] L. Khaykovich, F. Schreck, G. Ferrari, T. Bourdel, J. Cubizolles, L. D. Carr, Y. Castin, and C. Salomon, "Formation of a matter-wave bright soliton", Science **296**, 1290 (2002).

[31] M. Greiner, O. Mandel, T. Esslinger, T. W. Hänsch, and I. Bloch, "Quantum phase transition from a superfluid to a Mott insulator in a gas of ultracold atoms", Nature **415**, 39 (2002).

[32] A. Görlitz, J. M. Vogels, A. E. Leanhardt, C. Raman, T. L. Gustavson, J. R. Abo-Shaeer, A. P. Chikkatur, S. Gupta, S. Inouye, T. Rosenband, and W. Ketterle, "Realization of Bose-Einstein condensates in lower dimensions", Phys. Rev. Lett. **87**, 130402 (2001).

[33] M. Greiner, I. Bloch, O. Mandel, T. W. Hänsch, and T. Esslinger, "Exploring phase coherence in a 2D lattice of Bose-Einstein condensates", Phys. Rev. Lett. **87**, 160405 (2001).

[34] Z. Hadzibabic, P. Krüger, M. Cheneau, B. Battelier, and J. Dalibard, "Berezinskii–Kosterlitz–Thouless crossover in a trapped atomic gas", Nature **441**, 1118 (2006).

[35] J. Simon, W. S. Bakr, R. Ma, M. E. Tai, P. M. Preiss, and M. Greiner, "Quantum simulation of antiferromagnetic spin chains in an optical lattice", Nature **472**, 307 (2011).

[36] T. Kinoshita, T. Wenger, and D. S. Weiss, "Observation of a one-dimensional Tonks-Girardeau gas", Science **305**, 1125 (2004).

[37] B. Paredes, A. Widera, V. Murg, O. Mandel, S. Fölling, I. Cirac, G. V. Shlyapnikov, T. W. Hänsch, and I. Bloch, "Tonks–Girardeau gas of ultracold atoms in an optical lattice", Nature **429**, 277 (2004).

[38] A. H. van Amerongen, J. J. P. van Es, P. Wicke, K. V. Kheruntsyan, and N. J. van Druten, "Yang-Yang thermodynamics on an atom chip", Phys. Rev. Lett. **100**, 090402 (2008).

[39] A. Widera, S. Trotzky, P. Cheinet, S. Fölling, F. Gerbier, I. Bloch, V. Gritsev, M. D. Lukin, and E. Demler, "Quantum spin dynamics of mode-squeezed Luttinger liquids in two-component atomic gases", Phys. Rev. Lett. **100**, 140401 (2008).

[40] M. Gring, M. Kuhnert, T. Langen, T. Kitagawa, B. Rauer, M. Schreitl, I. Mazets, D. A. Smith, E. Demler, and J. Schmiedmayer, "Relaxation and prethermalization in an isolated quantum system", Science **337**, 1318 (2012).

[41] H. P. Büchler, G. Blatter, and W. Zwerger, "Commensurate-incommensurate transition of cold atoms in an optical lattice", Phys. Rev. Lett. **90**, 130401 (2003).

[42] T. Stöferle, H. Moritz, C. Schori, M. Köhl, and T. Esslinger, "Transition from a strongly interacting 1D superfluid to a Mott insulator", Phys. Rev. Lett. **92**, 130403 (2004).

[43] C. N. Yang, "Some exact results for the many-body problem in one dimension with repulsive delta-function interaction", Phys. Rev. Lett. **19**, 1312 (1967).

[44] M. Gaudin, "Un systeme a une dimension de fermions en interaction", Physics Letters A **24**, 55 (1967).

[45] F. Meinert, M. Knap, E. Kirilov, K. Jag-Lauber, M. B. Zvonarev, E. Demler, and H.-C. Nägerl, "Bloch oscillations in the absence of a lattice", Science **356**, 945 (2017).

[46] A. J. Daley, C. Kollath, U. Schollwöck, and G. Vidal, "Time-dependent density-matrix renormalization-group using adaptive effective Hilbert spaces", Journal of Statistical Mechanics: Theory and Experiment **2004**, P04005 (2004).

[47] U. Schollwöck, "The density-matrix renormalization group", Rev. Mod. Phys. **77**, 259 (2005).

[48] U. Schollwöck, "The density-matrix renormalization group in the age of matrix product states", Annals of Physics **326**, 96 (2011).

[49] G. Vidal, "Efficient simulation of one-dimensional quantum many-body systems", Phys. Rev. Lett. **93**, 040502 (2004).

[50] F. Verstraete, V. Murg, and J. I. Cirac, "Matrix product states, projected entangled pair states, and variational renormalization group methods for quantum spin systems", Advances in Physics **57**, 143 (2008).

[51] S. R. White and A. E. Feiguin, "Real-time evolution using the density matrix renormalization group", Phys. Rev. Lett. **93**, 076401 (2004).

[52] W. M. C. Foulkes, L. Mitas, R. J. Needs, and G. Rajagopal, "Quantum Monte Carlo simulations of solids", Rev. Mod. Phys. **73**, 33 (2001).

[53] L. Pollet, "Recent developments in quantum monte carlo simulations with applications for cold gases", Reports on Progress in Physics **75**, 094501 (2012).

[54] O. A. Castro-Alvaredo, B. Doyon, and T. Yoshimura, "Emergent hydrodynamics in integrable quantum systems out of equilibrium", Phys. Rev. X **6**, 041065 (2016).

[55] B. Bertini, M. Collura, J. De Nardis, and M. Fagotti, "Transport in out-of-equilibrium XXZ chains: exact profiles of charges and currents", Phys. Rev. Lett. **117**, 207201 (2016).

[56] L. D. Landau, "The theory of a Fermi liquid", Sov. Phys. JETP 3 **920** (1956).

[57] L. D. Landau, "On the theory of the Fermi liquid", Sov. Phys. JETP 8 **70** (1959).

[58] T. Giamarchi, *Quantum physics in one dimension*, International Series of Monographs on Physics (Clarendon Press, 2003).

[59] E. H. Lieb and W. Liniger, "Exact analysis of an interacting Bose gas. I. The general solution and the ground state", Phys. Rev. **130**, 1605 (1963).

[60] E. H. Lieb, "Exact analysis of an interacting Bose gas. II. The excitation spectrum", Phys. Rev. **130**, 1616 (1963).

[61] H. Bethe, "Zur Theorie der Metalle", Zeitschrift für Physik **71**, 205 (1931).

[62] L. Tonks, "The complete equation of state of one, two and three-dimensional gases of hard elastic spheres", Phys. Rev. **50**, 955 (1936).

[63] M. Girardeau, "Relationship between Systems of Impenetrable Bosons and Fermions in One Dimension", Journal of Mathematical Physics **1**, 516 (1960).

[64] N. J. Robinson and R. M. Konik, "Excitations in the Yang–Gaudin Bose gas", Journal of Statistical Mechanics **2017** (2017).

[65] S. Coleman, "Quantum sine-Gordon equation as the massive Thirring model", Phys. Rev. D **11**, 2088 (1975).

[66] L. D. Faddeev and V. E. Korepin, "Quantum theory of solitons", Physics Reports **42**, 1 (1978).

[67] S. Hofferberth, I. Lesanovsky, B. Fischer, T. Schumm, and J. Schmiedmayer, "Non-equilibrium coherence dynamics in one-dimensional Bose gases", Nature **449**, 324 (2007).

[68] B. Bertini, F. Heidrich-Meisner, C. Karrasch, T. Prosen, R. Steinigeweg, and M. Žnidari č, "Finite-temperature transport in one-dimensional quantum lattice models", Rev. Mod. Phys. **93**, 025003 (2021).

[69] Bose, S, "Plancks gesetz und lichtquantenhypothese", Zeitschrift für Physik **26**, 178 (1924).

[70] A. Einstein, *Quantentheorie des einatomigen idealen Gases. Zweite Abhandlung*, Albert Einstein: Akademie-Vorträge, Wiley Online Books (Dec. 2005), pp. 245–257.

[71] T. W. Hänsch and A. L. Schawlow, "Cooling of gases by laser radiation", Optics Communications **13**, 68 (1975).

[72] H. J. Metcalf and P. van der Straten, "Laser cooling and trapping of atoms", Journal of the Optical Society of America B **20**, 887 (2003).

[73] D. J. Wineland and W. M. Itano, "Laser cooling of atoms", Phys. Rev. A **20**, 1521 (1979).

[74] L. Pitaevskii and S. Stringari, *Bose-Einstein condensation and superfluidity*, Vol. 164 (Oxford University Press, 2016).

[75] C. J. Pethick and H. Smith, *Bose-Einstein condensation in dilute gases* (Cambridge university press, 2008).

[76] J. J. Sakurai and J. Napolitano, *Modern quantum mechanics* (Cambridge University Press, 2020).

[77] W. Ketterle, D. S. Durfee, and D. Stamper-Kurn, "Making, probing and understanding Bose-Einstein condensates", arXiv preprint cond-mat/9904034 (1999).

[78] S. De Groot, G. Hooyman, and C. Ten Seldam, "On the Bose-Einstein condensation", Proceedings of the Royal Society of London. Series A. Mathematical and Physical Sciences **203**, 266 (1950).

[79] V. Bagnato, D. E. Pritchard, and D. Kleppner, "Bose-Einstein condensation in an external potential", Phys. Rev. A **35**, 4354 (1987).

[80] E. P. Gross, "Structure of a quantized vortex in boson systems", Il Nuovo Cimento (1955-1965) **20**, 454 (1961).

[81] L. P. Pitaevskii, "Vortex lines in an imperfect Bose gas", Sov. Phys. JETP **13**, 451 (1961).

[82] F. Dalfovo, S. Giorgini, L. P. Pitaevskii, and S. Stringari, "Theory of Bose-Einstein condensation in trapped gases", Reviews of Modern Physics **71**, 463 (1999).

[83] W. Ketterle and N. Van Druten, in *Advances in atomic, molecular, and optical physics*, Vol. 37 (Elsevier, 1996), pp. 181–236.

[84] J. Dalibard, in *Bose-Einstein condensation in atomic gases* (IOS Press, 1999), pp. 321–349.

[85] H. Friedrich, *Scattering theory*, Vol. 872 (Springer, 2013).

[86] J. R. Taylor, *Scattering theory: the quantum theory of nonrelativistic collisions* (Courier Corporation, 2006).

[87] T. Köhler, K. Góral, and P. S. Julienne, "Production of cold molecules via magnetically tunable feshbach resonances", Rev. Mod. Phys. **78**, 1311 (2006).

[88] C. Chin, R. Grimm, P. Julienne, and E. Tiesinga, "Feshbach resonances in ultracold gases", Rev. Mod. Phys. **82**, 1225 (2010).

[89] A. S. Jensen, K. Riisager, D. V. Fedorov, and E. Garrido, "Structure and reactions of quantum halos", Rev. Mod. Phys. **76**, 215 (2004).

[90] E. A. Donley, N. R. Claussen, S. T. Thompson, and C. E. Wieman, "Atom–molecule coherence in a Bose–Einstein condensate", Nature **417**, 529 (2002).

[91] M. Mark, F. Ferlaino, S. Knoop, J. G. Danzl, T. Kraemer, C. Chin, H.-C. Nägerl, and R. Grimm, "Spectroscopy of ultracold trapped cesium Feshbach molecules", Phys. Rev. A **76**, 042514 (2007).

[92] U. Fano, "Sullo spettro di assorbimento dei gas nobili presso il limite dello spettro d'arco", Il Nuovo Cimento (1924-1942) **12**, 154 (1935).

[93] U. Fano, G. Pupillo, A. Zannoni, and C. W. Clark, "On the absorption spectrum of noble gases at the arc spectrum limit", Journal of research of the National Institute of Standards and Technology **110**, 583 (2005).

[94] U. Fano, "Effects of configuration interaction on intensities and phase shifts", Phys. Rev. **124**, 1866 (1961).

[95] H. Feshbach, "Unified theory of nuclear reactions", Annals of Physics **5**, 357 (1958).

[96] H. Feshbach, "A unified theory of nuclear reactions. II", Annals of Physics **19**, 287 (1962).

[97] S. Inouye, M. R. Andrews, J. Stenger, H.-J. Miesner, D. M. Stamper-Kurn, and W. Ketterle, "Observation of Feshbach resonances in a Bose–Einstein condensate", Nature **392**, 151 (1998).

[98] J. van de Kraats, D. J. M. Ahmed-Braun, J.-L. Li, and S. J. J. M. F. Kokkelmans, "Emergent inflation of the Efimov spectrum under three-body spin-exchange interactions", Phys. Rev. Lett. **132**, 133402 (2024).

[99] E. Braaten and H.-W. Hammer, "Universality in few-body systems with large scattering length", Physics Reports **428**, 259 (2006).

[100] E. Braaten and H.-W. Hammer, "Three-body recombination into deep bound states in a Bose gas with large scattering length", Phys. Rev. Lett. **87**, 160407 (2001).

[101] B. D. Esry, C. H. Greene, and J. P. Burke, "Recombination of three atoms in the ultracold limit", Phys. Rev. Lett. **83**, 1751 (1999).

[102] P. O. Fedichev, M. W. Reynolds, and G. V. Shlyapnikov, "Three-body recombination of ultracold atoms to a weakly bound s level", Phys. Rev. Lett. **77**, 2921 (1996).

[103] E. Nielsen and J. H. Macek, "Low-energy recombination of identical bosons by three-body collisions", Phys. Rev. Lett. **83**, 1566 (1999).

[104] T. Kraemer, M. Mark, P. Waldburger, J. G. Danzl, C. Chin, B. Engeser, A. D. Lange, K. Pilch, A. Jaakkola, H.-C. Nägerl, and R. Grimm, "Evidence for Efimov quantum states in an ultracold gas of caesium atoms", Nature **440**, 315 (2006).

[105] T. Weber, J. Herbig, M. Mark, H.-C. Nägerl, and R. Grimm, "Three-body recombination at large scattering lengths in an ultracold atomic gas", Phys. Rev. Lett. **91**, 123201 (2003).

[106] D. A. Steck, "Cesium D line data", (2003).

[107] M. Gustavsson, "A quantum gas with tunable interactions in an optical lattice", PhD thesis (2008).

[108] M. D. Frye, B. C. Yang, and J. M. Hutson, "Ultracold collisions of Cs atoms in excited Zeeman and hyperfine states", Phys. Rev. A **100**, 022702 (2019).

[109] J. Söding, D. Guéry-Odelin, P. Desbiolles, G. Ferrari, and J. Dalibard, "Giant spin relaxation of an ultracold cesium gas", Phys. Rev. Lett. **80**, 1869 (1998).

[110] D. Guéry-Odelin, J. Söding, P. Desbiolles, and J. Dalibard, "Is Bose-Einstein condensation of atomic cesium possible?", Europhysics Letters **44**, 25 (1998).

[111] A. J. Kerman, V. Vuleti ć, C. Chin, and S. Chu, "Beyond optical molasses: 3D raman sideband cooling of atomic cesium to high phase-space density", Phys. Rev. Lett. **84**, 439 (2000).

[112] D. J. Han, M. T. DePue, and D. S. Weiss, "Loading and compressing Cs atoms in a very far-off-resonant light trap", Phys. Rev. A **63**, 023405 (2001).

[113] A. Di Carli, G. Henderson, S. Flannigan, C. D. Colquhoun, M. Mitchell, G.-L. Oppo, A. J. Daley, S. Kuhr, and E. Haller, "Collisionally inhomogeneous Bose-Einstein condensates with a linear interaction gradient", Phys. Rev. Lett. **125**, 183602 (2020).

[114] T. Weber, J. Herbig, M. Mark, H.-C. Nägerl, and R. Grimm, "Bose-Einstein condensation of cesium", Science **299**, 232 (2003).

[115] M. Berninger, A. Zenesini, B. Huang, W. Harm, H.-C. Nägerl, F. Ferlaino, R. Grimm, P. S. Julienne, and J. M. Hutson, "Universality of the three-body parameter for Efimov etates in ultracold cesium", Phys. Rev. Lett. **107**, 120401 (2011).

[116] J. Herbig, T. Kraemer, M. Mark, T. Weber, C. Chin, H.-C. Nägerl, and R. Grimm, "Preparation of a pure molecular quantum gas", Science **301**, 1510 (2003).

[117] J. G. Danzl, E. Haller, M. Gustavsson, M. J. Mark, R. Hart, N. Bouloufa, O. Dulieu, H. Ritsch, and H.-C. Nägerl, "Quantum gas of deeply bound ground state molecules", Science **321**, 1062 (2008).

[118] Z. Zhang, L. Chen, K.-X. Yao, and C. Chin, "Transition from an atomic to a molecular Bose–Einstein condensate", Nature **592**, 708 (2021).

[119] S. Dhar, B. Wang, M. Horvath, A. Vashisht, Y. Zeng, M. B. Zvonarev, N. Goldman, Y. Guo, M. Landini, and H.-C. Nägerl, "Observing anyonization of bosons in a quantum gas", Nature (2025).

[120] F. Meinert, M. J. Mark, E. Kirilov, K. Lauber, P. Weinmann, M. Gröbner, A. J. Daley, and H.-C. Nägerl, "Observation of many-body dynamics in long-range tunneling after a quantum quench", Science **344**, 1259 (2014).

[121] L. W. Clark, A. Gaj, L. Feng, and C. Chin, "Collective emission of matter-wave jets from driven Bose–Einstein condensates", Nature **551**, 356 (2017).

[122] E. Haller, "A one-dimensional quantum gas with tunable interactions", PhD thesis (2010).

[123] J. M. Leinaas and J. Myrheim, "On the theory of identical particles", Il Nuovo Cimento B (1971-1996) **37**, 1 (1977).

[124] F. Wilczek, "Quantum mechanics of fractional-spin particles", Phys. Rev. Lett. **49**, 957 (1982).

[125] F. Franchini, "Notes on Bethe ansatz techniques", International School for Advanced Studies-Trieste, Lecture Notes (2011).

[126] F. D. M. Haldane, "Effective harmonic-fluid approach to low-energy properties of one-dimensional quantum fluids", Phys. Rev. Lett. **47**, 1840 (1981).

[127] T. Giamarchi, "Theoretical framework for quasi-one dimensional systems", Chemical Reviews **104**, 5037 (2004).

[128] M. A. Cazalilla, "Bosonizing one-dimensional cold atomic gases", Journal of Physics B: Atomic, Molecular and Optical Physics **37**, S1 (2004).

[129] J. Voit, "One-dimensional Fermi liquids", Reports on Progress in Physics **58**, 977 (1995).

[130] I. Bouchoule, R. Citro, T. Duty, T. Giamarchi, R. G. Hulet, M. Klanjšek, E. Orignac, and B. Weber, "Platforms for the realization and characterization of Tomonaga–Luttinger liquids", Nature Reviews Physics (2025).

[131] A. Imambekov, T. L. Schmidt, and L. I. Glazman, "One-dimensional quantum liquids: beyond the Luttinger liquid paradigm", Rev. Mod. Phys. **84**, 1253 (2012).

[132] M. Olshanii, "Atomic scattering in the presence of an external confinement and a gas of impenetrable bosons", Phys. Rev. Lett. **81**, 938 (1998).

[133] N. D. Mermin and H. Wagner, "Absence of ferromagnetism or antiferromagnetism in one- or two-dimensional isotropic Heisenberg models", Phys. Rev. Lett. **17**, 1133 (1966).

[134] D. M. Gangardt and G. V. Shlyapnikov, "Stability and phase coherence of trapped 1D Bose gases", Phys. Rev. Lett. **90**, 010401 (2003).

[135] D. Petrov, D. M. Gangardt, and G. V. Shlyapnikov, "Low-dimensional trapped gases", in Journal de physique iv (proceedings), Vol. 116 (EDP sciences, 2004), pp. 5–44.

[136] J. B. McGuire, "Study of exactly soluble one-dimensional N-body problems", Journal of Mathematical Physics **5**, 622 (1964).

[137] Z. Wang, J. Wu, W. Yang, A. K. Bera, D. Kamenskyi, A. T. M. N. Islam, S. Xu, J. M. Law, B. Lake, C. Wu, and A. Loidl, "Experimental observation of Bethe strings", Nature **554**, 219 (2018).

[138] A. Morvan et al., "Formation of robust bound states of interacting microwave photons", Nature **612**, 240 (2022).

[139] R. Koch, A. Bastianello, and J.-S. Caux, "Adiabatic formation of bound states in the one-dimensional Bose gas", Phys. Rev. B **103**, 165121 (2021).

[140] M. T. Batchelor, M. Bortz, X. W. Guan, and N. Oelkers, "Evidence for the super Tonks–Girardeau gas", Journal of Statistical Mechanics: Theory and Experiment **2005**, L10001 (2005).

[141] M. D. Girardeau and G. E. Astrakharchik, "Wave functions of the super-Tonks-Girardeau gas and the trapped one-dimensional hard-sphere Bose gas", Phys. Rev. A **81**, 061601 (2010).

[142] K.-Y. Li, Y. Zhang, K. Yang, K.-Y. Lin, S. Gopalakrishnan, M. Rigol, and B. L. Lev, "Rapidity and momentum distributions of one-dimensional dipolar quantum gases", Phys. Rev. A **107**, L061302 (2023).

[143] K. Yang, Y. Zhang, K.-Y. Li, K.-Y. Lin, S. Gopalakrishnan, M. Rigol, and B. L. Lev, "Phantom energy in the nonlinear response of a quantum many-body scar state", Science **385**, 1063 (2024).

[144] T. Kinoshita, T. Wenger, and D. S. Weiss, "A quantum Newton's cradle", Nature **440**, 900 (2006).

[145] I. Bouchoule and J. Dubail, "Generalized hydrodynamics in the one-dimensional Bose gas: theory and experiments", Journal of Statistical Mechanics: Theory and Experiment **2022**, 014003 (2022).

[146] B. Sutherland, "Exact coherent states of a one-dimensional quantum fluid in a time-dependent trapping potential", Phys. Rev. Lett. **80**, 3678 (1998).

[147] M. Rigol and A. Muramatsu, "Fermionization in an expanding 1D gas of hard-core bosons", Phys. Rev. Lett. **94**, 240403 (2005).

[148] A. S. Campbell, D. M. Gangardt, and K. V. Kheruntsyan, "Sudden expansion of a one-dimensional Bose gas from power-law traps", Phys. Rev. Lett. **114**, 125302 (2015).

[149] J. M. Wilson, N. Malvania, Y. Le, Y. Zhang, M. Rigol, and D. S. Weiss, "Observation of dynamical fermionization", Science **367**, 1461 (2020).

[150] E. H. Lieb and D. C. Mattis, *Mathematical physics in one dimension: Exactly soluble models of interacting particles* (Academic press, 2013).

[151] M. Gaudin, *The Bethe wavefunction* (Cambridge University Press, 2014).

[152] V. E. Korepin, V. E. Korepin, N. Bogoliubov, and A. Izergin, *Quantum inverse scattering method and correlation functions*, Vol. 3 (Cambridge university press, 1997).

[153] F. S. Møller, "Hydrodynamics of quasi one-dimensional Bose gases", PhD thesis (Technische Universität Wien, 2023).

[154] E. P. Wigner, "Lower limit for the energy derivative of the scattering phase shift", Phys. Rev. **98**, 145 (1955).

[155] N. Fabbri, M. Panfil, D. Clément, L. Fallani, M. Inguscio, C. Fort, and J.-S. Caux, "Dynamical structure factor of one-dimensional Bose gases: experimental signatures of beyond-Luttinger-liquid physics", Phys. Rev. A **91**, 043617 (2015).

[156] S. Stringari, *Bose-Einstein Condensation* (Clarendon Press, 2003).

[157] M. Olshanii and V. Dunjko, "Short-distance correlation properties of the Lieb-Liniger system and momentum distributions of trapped one-dimensional atomic gases", Phys. Rev. Lett. **91**, 090401 (2003).

[158] S. Tan, "Energetics of a strongly correlated Fermi gas", Annals of Physics **323**, 2952 (2008).

[159] S. Tan, "Generalized virial theorem and pressure relation for a strongly correlated Fermi gas", Annals of Physics **323**, 2987 (2008).

[160] S. Tan, "Large momentum part of a strongly correlated Fermi gas", Annals of Physics **323**, 2971 (2008).

[161] S. Tan, "Three-boson problem at low energy and implications for dilute Bose-Einstein condensates", Phys. Rev. A **78**, 013636 (2008).

[162] J. B. McGuire, "Study of exactly soluble one-dimensional N-body problems", Journal of Mathematical Physics **5**, 622 (1964).

[163] J. Mossel and J.-S. Caux, "Generalized TBA and generalized Gibbs", Journal of Physics A: Mathematical and Theoretical **45**, 255001 (2012).

[164] N. Yao, *Emergent hydrodynamics in a strongly interacting dipolar spin ensemble*, 2020.

[165] C. Zu, F. Machado, B. Ye, S. Choi, B. Kobrin, T. Mittiga, S. Hsieh, P. Bhattacharyya, M. Markham, D. Twitchen, A. Jarmola, D. Budker, C. R. Laumann, J. E. Moore, and N. Y. Yao, "Emergent hydrodynamics in a strongly interacting dipolar spin ensemble", Nature **597**, 45 (2021).

[166] B. Doyon, S. Gopalakrishnan, F. Møller, J. Schmiedmayer, and R. Vasseur, "Generalized hydrodynamics: a perspective", Phys. Rev. X **15**, 010501 (2025).

[167] J. M. Deutsch, "Eigenstate thermalization hypothesis", Reports on Progress in Physics **81**, 082001 (2018).

[168] M. Takahashi et al., *Thermodynamics of one-dimensional solvable models* (Cambridge university press Cambridge, 1999).

[169] G. Mussardo, *Statistical field theory: an introduction to exactly solved models in statistical physics* (Oxford University Press, USA, 2010).

[170] R. J. Baxter, *Exactly solved models in statistical mechanics* (Elsevier, 2016).

[171] P. Calabrese, F. H. L. Essler, and G. Mussardo, "Introduction to 'quantum integrability in out of equilibrium systems'", Journal of Statistical Mechanics: Theory and Experiment **2016**, 064001 (2016).

[172] A. Bastianello, B. Bertini, B. Doyon, and R. Vasseur, "Introduction to the special issue on emergent hydrodynamics in integrable many-body systems", Journal of Statistical Mechanics: Theory and Experiment **2022**, 014001 (2022).

[173] V. B. Bulchandani, R. Vasseur, C. Karrasch, and J. E. Moore, "Solvable hydrodynamics of quantum integrable systems", Phys. Rev. Lett. **119**, 220604 (2017).

[174] B. Doyon, "Lecture notes on generalised hydrodynamics", SciPost Phys. Lect. Notes, 18 (2020).

[175] M. Rigol, V. Dunjko, V. Yurovsky, and M. Olshanii, "Relaxation in a completely integrable many-body quantum system: an ab initio study of the dynamics of the highly excited states of 1D lattice hard-core bosons", Phys. Rev. Lett. **98**, 050405 (2007).

[176] M. Rigol, V. Dunjko, and M. Olshanii, "Thermalization and its mechanism for generic isolated quantum systems", Nature **452**, 854 (2008).

[177] J.-S. Caux and F. H. L. Essler, "Time evolution of local observables after quenching to an integrable model", Phys. Rev. Lett. **110**, 257203 (2013).

[178] F. H. Essler, "A short introduction to generalized hydrodynamics", Physica A: Statistical Mechanics and its Applications **631**, 127572 (2023).

[179] J. L. Lebowitz, J. K. Percus, and J. Sykes, "Kinetic-equation approach to time-dependent correlation functions", Phys. Rev. **188**, 487 (1969).

[180] C. Boldrighini, R. L. Dobrushin, and Y. M. Sukhov, "One-dimensional hard rod caricature of hydrodynamics", Journal of Statistical Physics **31**, 577 (1983).

[181] L. Bonnes, F. H. L. Essler, and A. M. Läuchli, ""light-cone" dynamics after quantum quenches in spin chains", Phys. Rev. Lett. **113**, 187203 (2014).

[182] B. Doyon, T. Yoshimura, and J.-S. Caux, "Soliton gases and generalized hydrodynamics", Phys. Rev. Lett. **120**, 045301 (2018).

[183] M. Schemmer, I. Bouchoule, B. Doyon, and J. Dubail, "Generalized hydrodynamics on an atom chip", Phys. Rev. Lett. **122**, 090601 (2019).

[184] N. Malvania, Y. Zhang, Y. Le, J. Dubail, M. Rigol, and D. S. Weiss, "Generalized hydrodynamics in strongly interacting 1D Bose gases", Science **373**, 1129 (2021).

[185] A. S. Alexandrov and J. T. Devreese, *Advances in polaron physics*, Vol. 159 (Springer, 2010).

[186] A. Hewson, *The Kondo problem*, Cambridge Studies in Magnetism (Cambridge University Press, Cambridge, 1993), pp. 47–70.

[187] P. W. Anderson, "Infrared catastrophe in Fermi gases with local scattering potentials", Phys. Rev. Lett. **18**, 1049 (1967).

[188] O. Gamayun, O. Lychkovskiy, and M. B. Zvonarev, "Zero temperature momentum distribution of an impurity in a polaron state of one-dimensional Fermi and Tonks-Girardeau gases", SciPost Phys. **8**, 053 (2020).

[189] C. J. M. Mathy, M. B. Zvonarev, and E. Demler, "Quantum flutter of supersonic particles in one-dimensional quantum liquids", Nature Physics **8**, 881 (2012).

[190] M. Knap, C. J. M. Mathy, M. Ganahl, M. B. Zvonarev, and E. Demler, "Quantum flutter: signatures and robustness", Phys. Rev. Lett. **112**, 015302 (2014).

[191] J. B. McGuire, "Interacting fermions in one dimension. I. repulsive potential", Journal of Mathematical Physics **6**, 432 (1965).

[192] J. B. McGuire, "Interacting fermions in one dimension. II. attractive potential", Journal of Mathematical Physics **7**, 123 (1966).

[193] M. Gaudin, "La fonction d'onde de Bethe", (1983).

[194] T. D. Lee, F. E. Low, and D. Pines, "The motion of slow electrons in a polar crystal", Phys. Rev. **90**, 297 (1953).

[195] M. B. Zvonarev, V. V. Cheianov, and T. Giamarchi, "Edge exponent in the dynamic spin structure factor of the Yang-Gaudin model", Phys. Rev. B **80**, 201102 (2009).

[196] O. Gamayun, A. G. Pronko, and M. B. Zvonarev, "Time and temperature-dependent correlation function of an impurity in one-dimensional Fermi and Tonks–Girardeau gases as a Fredholm determinant", New Journal of Physics **18**, 045005 (2016).

[197] J. N. Fuchs, D. M. Gangardt, T. Keilmann, and G. V. Shlyapnikov, "Spin waves in a one-dimensional spinor Bose gas", Phys. Rev. Lett. **95**, 150402 (2005).

[198] F. Grusdt, N. Mostaan, E. Demler, and L. A. P. Ardila, "Impurities and polarons in bosonic quantum gases: a review on recent progress", Reports on Progress in Physics **88**, 066401 (2025).

[199] O. Gamayun, O. Lychkovskiy, E. Burovski, M. Malcomson, V. V. Cheianov, and M. B. Zvonarev, "Impact of the injection protocol on an impurity's stationary state", Phys. Rev. Lett. **120**, 220605 (2018).

[200] J. Koch, K. Menon, E. Cuestas, S. Barbosa, E. Lutz, T. Fogarty, T. Busch, and A. Widera, "A quantum engine in the BEC–BCS crossover", Nature **621**, 723 (2023).

[201] H. S. Mani, N. Ramadas, and V. V. Sreedhar, "The anyonic quantum Carnot engine", Modern Physics Letters A, 2550136 (2025).

[202] M. L. Bera, A. Pérez, M. A. García-March, R. Chhajlany, T. Grass, M. Lewenstein, U. Bhattacharya, and S. Bhattacharjee, "A Hybrid Anyon-Otto thermal machine", arXiv preprint (2025).

[203] H. Li, X.-H. Yu, M. Nakagawa, and M. Ueda, "Dissipative superfluidity in a molecular Bose-Einstein condensate", arXiv preprint (2024).

[204] X.-Y. Gao and Y. Yan, "Fate of thermalization of ultracold fermions with two-body dissipation", Phys. Rev. Lett. **134**, 153402 (2025).

[205] C.-M. Halati and T. Giamarchi, "Bose-Hubbard triangular ladder in an artificial gauge field", Phys. Rev. Res. **5**, 013126 (2023).

[206] N. Baldelli, C. R. Cabrera, S. Julià-Farré, M. Aidelsburger, and L. Barbiero, "Frustrated extended Bose-Hubbard model and deconfined quantum critical points with optical lattices at the antimagic wavelength", Phys. Rev. Lett. **132**, 153401 (2024).

[207] H. J. Schulz, "Fermi liquids and non–Fermi liquids", arXiv preprint (1995).

[208] L. N. Cooper, "Bound electron pairs in a degenerate Fermi gas", Phys. Rev. **104**, 1189 (1956).

[209] J. Greensite, *An introduction to the confinement problem*, Vol. 821 (Springer, 2011).

[210] F. J. Dyson, "Divergence of perturbation theory in quantum electrodynamics", Phys. Rev. **85**, 631 (1952).

[211] J. M. Gerton, D. Strekalov, I. Prodan, and R. G. Hulet, "Direct observation of growth and collapse of a Bose–Einstein condensate with attractive interactions", Nature **408**, 692 (2000).

[212] E. A. Donley, N. R. Claussen, S. L. Cornish, J. L. Roberts, E. A. Cornell, and C. E. Wieman, "Dynamics of collapsing and exploding Bose–Einstein condensates", Nature **412**, 295 (2001).

[213] K. E. Strecker, G. B. Partridge, A. G. Truscott, and R. G. Hulet, "Formation and propagation of matter-wave soliton trains", Nature **417**, 150 (2002).

[214] P. Solano, Y. Duan, Y.-T. Chen, A. Rudelis, C. Chin, and V. Vuleti ć, "Strongly correlated quantum gas prepared by direct laser cooling", Phys. Rev. Lett. **123**, 173401 (2019).

[215] W. Kao, K.-Y. Li, K.-Y. Lin, S. Gopalakrishnan, and B. L. Lev, "Topological pumping of a 1D dipolar gas into strongly correlated prethermal states", Science **371**, 296 (2021).

[216] Y. Chen and X. Cui, "Ultrastable super Tonks-Girardeau gases under weak dipolar interactions", Phys. Rev. Lett. **131**, 203002 (2023).

[217] X.-W. Guan and P. He, "New trends in quantum integrability: recent experiments with ultracold atoms", Reports on Progress in Physics **85**, 114001 (2022).

[218] A. K. Bera, J. Wu, W. Yang, R. Bewley, M. Boehm, J. Xu, M. Bartkowiak, O. Prokhnenko, B. Klemke, A. T. M. N. Islam, J. M. Law, Z. Wang, and B. Lake, "Dispersions of many-body Bethe strings", Nature Physics **16**, 625 (2020).

[219] M. Kardar, G. Parisi, and Y.-C. Zhang, "Dynamic scaling of growing interfaces", Phys. Rev. Lett. **56**, 889 (1986).

[220] M. Ljubotina, M. Žnidarič, and T. Prosen, "Spin diffusion from an inhomogeneous quench in an integrable system", Nature Communications **8**, 16117 (2017).

[221] S. Gopalakrishnan and R. Vasseur, "Anomalous transport from hot quasiparticles in interacting spin chains", Reports on Progress in Physics **86**, 036502 (2023).

[222] E. Ilievski, J. De Nardis, S. Gopalakrishnan, R. Vasseur, and B. Ware, "Superuniversality of superdiffusion", Phys. Rev. X **11**, 031023 (2021).

[223] P. N. Jepsen, J. Amato-Grill, I. Dimitrova, W. W. Ho, E. Demler, and W. Ketterle, "Spin transport in a tunable Heisenberg model realized with ultracold atoms", Nature **588**, 403 (2020).

[224] A. Scheie, N. E. Sherman, M. Dupont, S. E. Nagler, M. B. Stone, G. E. Granroth, J. E. Moore, and D. A. Tennant, "Detection of Kardar–Parisi–Zhang hydrodynamics in a quantum Heisenberg spin-1/2 chain", Nature Physics **17**, 726 (2021).

[225] D. Wei, A. Rubio-Abadal, B. Ye, F. Machado, J. Kemp, K. Srakaew, S. Hollerith, J. Rui, S. Gopalakrishnan, N. Y. Yao, I. Bloch, and J. Zeiher, "Quantum gas microscopy of Kardar-Parisi-Zhang superdiffusion", Science **376**, 716 (2022).

[226] E. R. *et al.*, "Dynamics of magnetization at infinite temperature in a Heisenberg spin chain", Science **384**, 48 (2024).

[227] N. Beisert, C. Ahn, L. F. Alday, Z. Bajnok, J. M. Drummond, L. Freyhult, N. Gromov, R. A. Janik, V. Kazakov, T. Klose, G. P. Korchemsky, C. Kristjansen, M. Magro, T. McLoughlin, J. A. Minahan, R. I. Nepomechie, A. Rej, R. Roiban, S. Schäfer-Nameki, C. Sieg, M. Staudacher, A. Torrielli, A. A. Tseytlin, P. Vieira, D. Volin, and K. Zoubos, "Review of AdS/CFT integrability: an overview", Letters in Mathematical Physics **99**, 3 (2012).

[228] A. Bastianello, V. Alba, and J.-S. Caux, "Generalized hydrodynamics with space-time inhomogeneous interactions", Phys. Rev. Lett. **123**, 130602 (2019).

[229] B. Paredes, A. Widera, V. Murg, O. Mandel, S. Fölling, I. Cirac, G. V. Shlyapnikov, T. W. Hänsch, and I. Bloch, "Tonks-Girardeau gas of ultracold atoms in an optical lattice", Nature **429**, 277 (2004).

[230] T. Kinoshita, T. Wenger, and D. S. Weiss, "Observation of a one-dimensional Tonks-Girardeau gas", Science **305**, 1125 (2004).

[231] P. Calabrese and J.-S. Caux, "Correlation functions of the one-dimensional attractive Bose gas", Phys. Rev. Lett. **98**, 150403 (2007).

[232] L. Piroli, P. Calabrese, and F. H. L. Essler, "Multiparticle bound-state formation following a quantum quench to the one-dimensional Bose gas with attractive interactions", Phys. Rev. Lett. **116**, 070408 (2016).

[233] J. C. Zill, T. M. Wright, K. V. Kheruntsyan, T. Gasenzer, and M. J. Davis, "Quantum quench dynamics of the attractive one-dimensional Bose gas via the coordinate Bethe ansatz", SciPost Phys. **4**, 011 (2018).

[234] T. Kraemer, J. Herbig, M. Mark, T. Weber, C. Chin, H.-C. Nägerl, and R. Grimm, "Optimized production of a cesium Bose–Einstein condensate", Applied Physics B **79**, 1013 (2004).

[235] L. Dubois, G. Thémèze, F. Nogrette, J. Dubail, and I. Bouchoule, "Probing the local rapidity distribution of a one-dimensional Bose gas", Phys. Rev. Lett. **133**, 113402 (2024).

[236] See Supplementary Materials.

[237] P. Vignolo and A. Minguzzi, "Universal contact for a Tonks-Girardeau gas at finite temperature", Phys. Rev. Lett. **110**, 020403 (2013).

[238] G. Lang, P. Vignolo, and A. Minguzzi, "Tan's contact of a harmonically trapped one-dimensional Bose gas: strong-coupling expansion and conjectural approach at arbitrary interactions", The European Physical Journal Special Topics **226**, 1583 (2016).

[239] H. Yao, D. Clément, A. Minguzzi, P. Vignolo, and L. Sanchez-Palencia, "Tan's contact for trapped Lieb-Liniger bosons at finite temperature", Phys. Rev. Lett. **121**, 220402 (2018).

[240] F. Møller, C. Li, I. Mazets, H.-P. Stimming, T. Zhou, Z. Zhu, X. Chen, and J. Schmiedmayer, "Extension of the generalized hydrodynamics to the dimensional crossover regime", Phys. Rev. Lett. **126**, 090602 (2021).

[241] F. Cataldini, F. Møller, M. Tajik, J. Sabino, S.-C. Ji, I. Mazets, T. Schweigler, B. Rauer, and J. Schmiedmayer, "Emergent Pauli blocking in a weakly interacting Bose gas", Phys. Rev. X **12**, 041032 (2022).

[242] P. Schüttelkopf, M. Tajik, N. Bazhan, F. Cataldini, S.-C. Ji, J. Schmiedmayer, and F. Møller, "Characterising transport in a quantum gas by measuring Drude weights", arXiv preprint (2024).

[243] E. Braaten and H.-W. Hammer, "Efimov physics in cold atoms", Annals of Physics **322**, January Special Issue 2007, 120 (2007).

[244] V. B. Bulchandani, S. Gopalakrishnan, and E. Ilievski, "Superdiffusion in spin chains", Journal of Statistical Mechanics: Theory and Experiment **2021**, 084001 (2021).

[245] S. Birnkammer, A. Bastianello, and M. Knap, "Prethermalization in one-dimensional quantum many-body systems with confinement", Nature Communications **13**, 7663 (2022).

[246] J.-S. Caux, B. Doyon, J. Dubail, R. Konik, and T. Yoshimura, "Hydrodynamics of the interacting Bose gas in the quantum Newton cradle setup", SciPost Phys. **6**, 070 (2019).

[247] X. Cao, V. B. Bulchandani, and J. E. Moore, "Incomplete thermalization from trap-induced integrability breaking: lessons from classical hard rods", Phys. Rev. Lett. **120**, 164101 (2018).

[248] A. Bastianello, A. De Luca, B. Doyon, and J. De Nardis, "Thermalization of a trapped one-dimensional Bose gas via diffusion", Phys. Rev. Lett. **125**, 240604 (2020).

[249] J. D. Nardis, A. Krajenbrink, P. L. Doussal, and T. Thiery, "Delta-Bose gas on a half-line and the Kardar–Parisi–Zhang equation: boundary bound states and unbinding transitions", Journal of Statistical Mechanics: Theory and Experiment **2020**, 043207 (2020).

[250] Y. Guo, H. Yao, S. Ramanjanappa, S. Dhar, M. Horvath, L. Pizzino, T. Giamarchi, M. Landini, and H.-C. Nägerl, "Observation of the 2D–1D crossover in strongly interacting ultracold bosons", Nature Physics **20**, 934 (2024).

[251] Research data are freely available from Zenodo at doi.org/10.5281/zenodo.15426226.

[252] F. Meinert, M. Panfil, M. J. Mark, K. Lauber, J.-S. Caux, and H.-C. Nägerl, "Probing the excitations of a Lieb-Liniger gas from weak to strong coupling", Phys. Rev. Lett. **115**, 085301 (2015).

[253] B. Doyon and T. Yoshimura, "A note on generalized hydrodynamics: inhomogeneous fields and other concepts", SciPost Phys. **2**, 014 (2017).

[254] X. Li, M. Ke, B. Yan, and Y. Wang, "Reduction of interference fringes in absorption imaging of cold atom cloud using eigenface method", Chin. Opt. Lett. **5**, 128 (2007).

[255] M. Girardeau, "Relationship between systems of impenetrable bosons and fermions in one dimension", Journal of Mathematical Physics **1**, 516 (1960).

[256] A. Lenard, "One-dimensional impenetrable bosons in thermal equilibrium", Journal of Mathematical Physics **7**, 1268 (1966).

[257] A. Bastianello, M. Collura, and S. Sotiriadis, "Quenches from bosonic Gaussian initial states to the Tonks-Girardeau limit: stationary states and effects of a confining potential", Phys. Rev. B **95**, 174303 (2017).

[258] R. Koch, J.-S. Caux, and A. Bastianello, "Generalized hydrodynamics of the attractive non-linear Schrödinger equation", Journal of Physics A: Mathematical and Theoretical **55**, 134001 (2022).

[259] K. V. Kheruntsyan, D. M. Gangardt, P. D. Drummond, and G. V. Shlyapnikov, "Pair correlations in a finite-temperature one-dimensional Bose gas", Phys. Rev. Lett. **91**, 040403 (2003).

[260] V. I. Arnol'd, *Mathematical methods of classical mechanics*, Vol. 60 (Springer Science & Business Media, 2013).

[261] D. C. Tsui, H. L. Stormer, and A. C. Gossard, "Two-dimensional magnetotransport in the extreme quantum limit", Phys. Rev. Lett. **48**, 1559 (1982).

[262] R. B. Laughlin, "Anomalous quantum Hall effect: an incompressible quantum fluid with fractionally charged excitations", Phys. Rev. Lett. **50**, 1395 (1983).

[263] D. Arovas, J. R. Schrieffer, and F. Wilczek, "Fractional statistics and the quantum Hall effect", Phys. Rev. Lett. **53**, 722 (1984).

[264] A. Kitaev, "Fault-tolerant quantum computation by anyons", Annals of Physics **303**, 2 (2003).

[265] C. Nayak, S. H. Simon, A. Stern, M. Freedman, and S. Das Sarma, "Non-Abelian anyons and topological quantum computation", Rev. Mod. Phys. **80**, 1083 (2008).

[266] M. Ogata and H. Shiba, "Bethe-ansatz wave function, momentum distribution, and spin correlation in the one-dimensional strongly correlated Hubbard model", Phys. Rev. B **41**, 2326 (1990).

[267] J. Vijayan, P. Sompet, G. Salomon, J. Koepsell, S. Hirthe, A. Bohrdt, F. Grusdt, I. Bloch, and C. Gross, "Time-resolved observation of spin-charge deconfinement in fermionic Hubbard chains", Science **367**, 186 (2020).

[268] R. Senaratne, D. Cavazos-Cavazos, S. Wang, F. He, Y.-T. Chang, A. Kafle, H. Pu, X.-W. Guan, and R. G. Hulet, "Spin-charge separation in a one-dimensional Fermi gas with tunable interactions", Science **376**, 1305 (2022).

[269] O. I. Pâţu, V. E. Korepin, and D. V. Averin, "Correlation functions of one-dimensional Lieb-Liniger anyons", Journal of Physics A: Mathematical and Theoretical **40**, 14963 (2007).

[270] G. Tang, S. Eggert, and A. Pelster, "Ground-state properties of anyons in a one-dimensional lattice", New Journal of Physics **17**, 123016 (2015).

[271] Y. Hao, Y. Zhang, and S. Chen, "Ground-state properties of one-dimensional anyon gases", Phys. Rev. A **78**, 023631 (2008).

[272] A. del Campo, "Fermionization and bosonization of expanding one-dimensional anyonic fluids", Phys. Rev. A **78**, 045602 (2008).

[273] L. Piroli and P. Calabrese, "Exact dynamics following an interaction quench in a one-dimensional anyonic gas", Phys. Rev. A **96**, 023611 (2017).

[274] F. Liu, J. R. Garrison, D.-L. Deng, Z.-X. Gong, and A. V. Gorshkov, "Asymmetric particle transport and light-cone dynamics induced by anyonic statistics", Phys. Rev. Lett. **121**, 250404 (2018).

[275] P. Dirac, *The principles of quantum mechanics* (Clarendon Press, Oxford, 1930).

[276] F. D. M. Haldane, ""Fractional statistics" in arbitrary dimensions: a generalization of the Pauli principle", Phys. Rev. Lett. **67**, 937 (1991).

[277] M. Greiter and F. Wilczek, "Fractional statistics", Annual Review of Condensed Matter Physics **15**, 131 (2024).

[278] H. Bartolomei, M. Kumar, R. Bisognin, A. Marguerite, J.-M. Berroir, E. Bocquillon, B. Plaçais, A. Cavanna, Q. Dong, U. Gennser, Y. Jin, and G. Fève, "Fractional statistics in anyon collisions", Science **368**, 173 (2020).

[279] J. Nakamura, S. Liang, G. C. Gardner, and M. J. Manfra, "Direct observation of anyonic braiding statistics", Nature Physics **16**, 931 (2020).

[280] G. Q. AI and Collaborators, "Non-Abelian braiding of graph vertices in a superconducting processor", Nature **618**, 264 (2023).

[281] S. Xu, Z.-Z. Sun, K. Wang, H. Li, Z. Zhu, H. Dong, J. Deng, X. Zhang, J. Chen, Y. Wu, et al., "Non-Abelian braiding of Fibonacci anyons with a superconducting processor", Nature Physics **20**, 1469 (2024).

[282] M. Iqbal, N. Tantivasadakarn, R. Verresen, S. L. Campbell, J. M. Dreiling, C. Figgatt, J. P. Gaebler, J. Johansen, M. Mills, S. A. Moses, et al., "Non-Abelian topological order and anyons on a trapped-ion processor", Nature **626**, 505 (2024).

[283] M. Greiter, "Statistical phases and momentum spacings for one-dimensional anyons", Phys. Rev. B **79**, 064409 (2009).

[284] T. Keilmann, S. Lanzmich, I. McCulloch, and M. Roncaglia, "Statistically induced phase transitions and anyons in 1D optical lattices", Nature Communications **2**, 361 (2011).

[285] S. Greschner, L. Cardarelli, and L. Santos, "Probing the exchange statistics of one-dimensional anyon models", Phys. Rev. A **97**, 053605 (2018).

[286] C. Sträter, S. C. L. Srivastava, and A. Eckardt, "Floquet realization and signatures of one-dimensional anyons in an optical lattice", Phys. Rev. Lett. **117**, 205303 (2016).

[287] T. M. Wright, M. Rigol, M. J. Davis, and K. V. Kheruntsyan, "Nonequilibrium dynamics of one-dimensional hard-core anyons following a quench: complete relaxation of one-body observables", Phys. Rev. Lett. **113**, 050601 (2014).

[288] A. Kundu, "Exact solution of double δ function Bose gas through an interacting anyon gas", Phys. Rev. Lett. **83**, 1275 (1999).

[289] M. Bonkhoff, K. Jägering, S. Eggert, A. Pelster, M. Thorwart, and T. Posske, "Bosonic continuum theory of one-dimensional lattice anyons", Phys. Rev. Lett. **126**, 163201 (2021).

[290] S. Greschner and L. Santos, "Anyon Hubbard model in one-dimensional optical lattices", Phys. Rev. Lett. **115**, 053002 (2015).

[291] Y. Hao, Y. Zhang, and S. Chen, "Ground-state properties of hard-core anyons in one-dimensional optical lattices", Phys. Rev. A **79**, 043633 (2009).

[292] C. S. Chisholm, A. Frölian, E. Neri, R. Ramos, L. Tarruell, and A. Celi, "Encoding a one-dimensional topological gauge theory in a Raman-coupled Bose-Einstein condensate", Phys. Rev. Res. **4**, 043088 (2022).

[293] A. Frölian, C. S. Chisholm, E. Neri, C. R. Cabrera, R. Ramos, A. Celi, and L. Tarruell, "Realizing a 1D topological gauge theory in an optically dressed BEC", Nature **608**, 293 (2022).

[294] J. Kwan, P. Segura, Y. Li, S. Kim, A. V. Gorshkov, A. Eckardt, B. Bakkali-Hassani, and M. Greiner, "Realization of one-dimensional anyons with arbitrary statistical phase", Science **386**, 1055 (2024).

[295] O. Gamayun, E. Quinn, K. Bidzhiev, and M. B. Zvonarev, "Emergence of anyonic correlations from spin and charge dynamics in one dimension", Phys. Rev. A **109**, 012209 (2024).

[296] O. Gamayun, O. Lychkovskiy, and M. B. Zvonarev, "Zero temperature momentum distribution of an impurity in a polaron state of one-dimensional Fermi and Tonks-Girardeau gases", SciPost Phys. **8**, 053 (2020).

[297] L. Yang and H. Pu, "One-body density matrix and momentum distribution of strongly interacting one-dimensional spinor quantum gases", Phys. Rev. A **95**, 051602 (2017).

[298] J. B. McGuire, "Interacting fermions in one dimension. I. repulsive potential", Journal of Mathematical Physics **6**, 432 (1965).

[299] M. Fishman, S. R. White, and E. M. Stoudenmire, "The ITensor Software Library for Tensor Network Calculations", SciPost Phys. Codebases, 4 (2022).

[300] M. Rigol and A. Muramatsu, "Fermionization in an expanding 1D gas of hard-core bosons", Phys. Rev. Lett. **94**, 240403 (2005).

[301] A. Minguzzi and D. M. Gangardt, "Exact coherent states of a harmonically confined Tonks-Girardeau gas", Phys. Rev. Lett. **94**, 240404 (2005).

[302] S. S. Alam, T. Skaras, L. Yang, and H. Pu, "Dynamical fermionization in one-dimensional spinor quantum gases", Phys. Rev. Lett. **127**, 023002 (2021).

[303] L. Cardarelli, S. Greschner, and L. Santos, "Engineering interactions and anyon statistics by multicolor lattice-depth modulations", Phys. Rev. A **94**, 023615 (2016).

[304] M. T. Batchelor, X.-W. Guan, and N. Oelkers, "One-dimensional interacting anyon gas: low-energy properties and Haldane exclusion statistics", Phys. Rev. Lett. **96**, 210402 (2006).

[305] F. Lange, S. Ejima, and H. Fehske, "Anyonic Haldane insulator in one dimension", Phys. Rev. Lett. **118**, 120401 (2017).

[306] W. Zhang, S. Greschner, E. Fan, T. C. Scott, and Y. Zhang, "Ground-state properties of the one-dimensional unconstrained pseudo-anyon Hubbard model", Phys. Rev. A **95**, 053614 (2017).

[307] M. Bonkhoff, K. Jägering, S. Hu, A. Pelster, S. Eggert, and I. Schneider, "Anyonic phase transitions in the 1D extended Hubbard model with fractional statistics", Phys. Rev. Lett. **135**, 036601 (2025).

[308] L. L. Lau and S. Dutta, "Quantum walk of two anyons across a statistical boundary", Phys. Rev. Res. **4**, L012007 (2022).

[309] F. Grusdt, N. Y. Yao, D. Abanin, M. Fleischhauer, and E. Demler, "Interferometric measurements of many-body topological invariants using mobile impurities", Nature Comms. **7**, 11994 (2016).

[310] D. Lundholm and N. Rougerie, "Emergence of fractional statistics for tracer particles in a Laughlin liquid", Phys. Rev. Lett. **116**, 170401 (2016).

[311] T. Graß, B. Juliá-Díaz, N. Baldelli, U. Bhattacharya, and M. Lewenstein, "Fractional angular momentum and anyon statistics of impurities in Laughlin liquids", Phys. Rev. Lett. **125**, 136801 (2020).

[312] K. K. Kesharpu and E. A. Kochetov, "Spin-flip-induced superfluidity in a ring of spinful hard-core bosons", Phys. Rev. A **106**, 033323 (2022).

[313] M. D. Girardeau, "Anyon-fermion mapping and applications to ultracold gases in tight waveguides", Phys. Rev. Lett. **97**, 100402 (2006).

[314] G. Valentí-Rojas, A. J. Baker, A. Celi, and P. Öhberg, "Topological gauge fields and the composite particle duality", Phys. Rev. Res. **5**, 023128 (2023).

[315] G. Valentí-Rojas and P. Öhberg, "A lower-dimensional remnant of flux attachment", arXiv preprint arXiv 2412.03346 (2024).

[316] M. Fishman, S. R. White, and E. M. Stoudenmire, "Codebase release 0.3 for ITensor", SciPost Phys. Codebases, 4 (2022).

[317] B. Wang, A. Vashisht, Y. Guo, S. Dhar, M. Landini, H.-C. Nägerl, and N. Goldman, "Anyonization of bosons in one dimension: an effective swap model", arXiv preprint arXiv:2504.21208 (2025).

[318] S. Basak and H. Pu, "Generalized effective spin-chain formalism for strongly interacting spinor gases in optical lattices", Phys. Rev. A **108**, 063315 (2023).

[319] O. Gamayun, A. G. Pronko, and M. B. Zvonarev, "Time and temperature-dependent correlation function of an impurity in one-dimensional Fermi and Tonks–Girardeau gases as a Fredholm determinant", New Journal of Physics **18**, 045005 (2016).

[320] M. Horvath, S. Dhar, A. Das, M. D. Frye, Y. Guo, J. M. Hutson, M. Landini, and H.-C. Nägerl, "Bose-Einstein condensation of non-ground-state caesium atoms", Nature Communications **15**, 3739 (2024).

[321] L. D. Landau and E. M. Lifshitz, *Fluid mechanics: Landau and Lifshitz: course of theoretical physics*, Vol. 6 (Elsevier, 2013).

[322] P. Kapitza, "Viscosity of liquid helium below the λ-point", Nature **141**, 74 (1938).

[323] J. F. Allen and A. D. Misener, "Flow of liquid helium II", Nature **141**, 75 (1938).

[324] L. Landau, "Theory of the superfluidity of helium II", Phys. Rev. **60**, 356 (1941).

[325] R. J. Donnelly, *Quantized vortices in helium II*, Vol. 2 (Cambridge University Press, 1991).

[326] M. R. Matthews, B. P. Anderson, P. C. Haljan, D. S. Hall, C. E. Wieman, and E. A. Cornell, "Vortices in a Bose-Einstein condensate", Phys. Rev. Lett. **83**, 2498 (1999).

[327] M. W. Zwierlein, J. R. Abo-Shaeer, A. Schirotzek, C. H. Schunck, and W. Ketterle, "Vortices and superfluidity in a strongly interacting Fermi gas", Nature **435**, 1047 (2005).

[328] C. Raman, M. Köhl, R. Onofrio, D. S. Durfee, C. E. Kuklewicz, Z. Hadzibabic, and W. Ketterle, "Evidence for a critical velocity in a Bose-Einstein condensed gas", Phys. Rev. Lett. **83**, 2502 (1999).

[329] A. P. Chikkatur, A. Görlitz, D. M. Stamper-Kurn, S. Inouye, S. Gupta, and W. Ketterle, "Suppression and enhancement of impurity scattering in a Bose-Einstein condensate", Phys. Rev. Lett. **85**, 483 (2000).

[330] A. Y. Cherny, J.-S. Caux, and J. Brand, "Theory of superfluidity and drag force in the one-dimensional Bose gas", Frontiers of Physics **7**, 54 (2012).

[331] F. Grusdt, K. Seetharam, Y. Shchadilova, and E. Demler, "Strong-coupling Bose polarons out of equilibrium: dynamical renormalization-group approach", Phys. Rev. A **97**, 033612 (2018).

[332] K. Seetharam, Y. Shchadilova, F. Grusdt, M. B. Zvonarev, and E. Demler, "Dynamical quantum Cherenkov transition of fast impurities in quantum liquids", Phys. Rev. Lett. **127**, 185302 (2021).

[333] K. Seetharam, Y. Shchadilova, F. Grusdt, M. Zvonarev, and E. Demler, "Quantum Cherenkov transition of finite-momentum Bose polarons", Phys. Rev. A **110**, 063306 (2024).

[334] A. Schirotzek, C.-H. Wu, A. Sommer, and M. W. Zwierlein, "Observation of Fermi polarons in a tunable Fermi liquid of ultracold atoms", Phys. Rev. Lett. **102**, 230402 (2009).

[335] M. Koschorreck, D. Pertot, E. Vogt, B. Fröhlich, M. Feld, and M. Köhl, "Attractive and repulsive Fermi polarons in two dimensions", Nature **485**, 619 (2012).

[336] C. Kohstall, M. Zaccanti, M. Jag, A. Trenkwalder, P. Massignan, G. M. Bruun, F. Schreck, and R. Grimm, "Metastability and coherence of repulsive polarons in a strongly interacting Fermi mixture", Nature **485**, 615 (2012).

[337] M.-G. Hu, M. J. Van de Graaff, D. Kedar, J. P. Corson, E. A. Cornell, and D. S. Jin, "Bose polarons in the strongly interacting regime", Phys. Rev. Lett. **117**, 055301 (2016).

[338] N. B. Jørgensen, L. Wacker, K. T. Skalmstang, M. M. Parish, J. Levinsen, R. S. Christensen, G. M. Bruun, and J. J. Arlt, "Observation of attractive and repulsive polarons in a Bose-Einstein condensate", Phys. Rev. Lett. **117**, 055302 (2016).

[339] M. Cetina, M. Jag, R. S. Lous, I. Fritsche, J. T. M. Walraven, R. Grimm, J. Levinsen, M. M. Parish, R. Schmidt, M. Knap, and E. Demler, "Ultrafast many-body interferometry of impurities coupled to a Fermi sea", Science **354**, 96 (2016).

[340] M. G. Skou, T. G. Skov, N. B. Jørgensen, K. K. Nielsen, A. Camacho-Guardian, T. Pohl, G. M. Bruun, and J. J. Arlt, "Non-equilibrium quantum dynamics and formation of the Bose polaron", Nature Physics **17**, 731 (2021).

[341] T. Kinoshita, T. Wenger, and D. S. Weiss, "Observation of a one-dimensional Tonks-Girardeau gas", Science **305**, 1125 (2004).

[342] M. Girardeau, "Relationship between systems of impenetrable bosons and fermions in one dimension", Journal of Mathematical Physics **1**, 516 (2004).

[343] V. Dunjko, V. Lorent, and M. Olshanii, "Bosons in cigar-shaped traps: Thomas-Fermi regime, Tonks-Girardeau regime, and in between", Phys. Rev. Lett. **86**, 5413 (2001).

[344] T. Kraemer, J. Herbig, M. Mark, T. Weber, C. Chin, H.-C. Nägerl, and R. Grimm, "Optimized production of a cesium Bose–Einstein condensate", Appl. Phys. B **79**, 1013 (2004).

[345] O. Jürgensen, F. Meinert, M. J. Mark, H.-C. Nägerl, and D.-S. Lühmann, "Observation of density-induced tunneling", Phys. Rev. Lett. **113**, 193003 (2014).

[346] C.-L. Hung, X. Zhang, N. Gemelke, and C. Chin, "Observation of scale invariance and universality in two-dimensional Bose gases", Nature **470**, 236 (2011).

[347] Y. Guo, H. Yao, S. Dhar, L. Pizzino, M. Horvath, T. Giamarchi, M. Landini, and H.-C. Nägerl, "Anomalous cooling of bosons by dimensional reduction", Sci. Adv. **10**, eadk6870 (2024).

[348] D. M. Stamper-Kurn and M. Ueda, "Spinor Bose gases: symmetries, magnetism, and quantum dynamics", Rev. Mod. Phys. **85**, 1191 (2013).

[349] C. R. Cabrera, L. Tanzi, J. Sanz, B. Naylor, P. Thomas, P. Cheiney, and L. Tarruell, "Quantum liquid droplets in a mixture of Bose-Einstein condensates", Science **359**, 301 (2018).

[350] X.-Q. Wang, G.-Q. Luo, J.-Y. Liu, W. V. Liu, A. Hemmerich, and Z.-F. Xu, "Evidence for an atomic chiral superfluid with topological excitations", Nature **596**, 227 (2021).

[351] M. Berninger, A. Zenesini, B. Huang, W. Harm, H.-C. Nägerl, F. Ferlaino, R. Grimm, P. S. Julienne, and J. M. Hutson, "Feshbach resonances, weakly bound molecular states, and coupled-channel potentials for cesium at high magnetic fields", Phys. Rev. A **87**, 032517 (2013).

[352] P. J. Leo, C. J. Williams, and P. S. Julienne, "Collision properties of ultracold ^{133}Cs atoms", Phys. Rev. Lett. **85**, 2721 (2000).

[353] J. M. Hutson, "Feshbach resonances in the presence of inelastic scattering: threshold behavior and suppression of poles in scattering lengths", New J. Phys. **9**, 152 (2007).

[354] M. D. Frye and J. M. Hutson, "Characterizing Feshbach resonances in ultracold scattering calculations", Phys. Rev. A **96**, 042705 (2017).

[355] C.-L. Hung, X. Zhang, N. Gemelke, and C. Chin, "Accelerating evaporative cooling of atoms into Bose-Einstein condensation in optical traps", Phys. Rev. A **78**, 011604 (2008).

[356] J.-L. Li, T. Secker, P. M. A. Mestrom, and S. J. J. M. F. Kokkelmans, "Strong spin-exchange recombination of three weakly interacting ^{7}Li atoms", Phys. Rev. Res. **4**, 023103 (2022).

[357] J. van de Kraats, D. J. M. Ahmed-Braun, J.-L. Li, and S. J. J. M. F. Kokkelmans, "Emergent inflation of the Efimov spectrum under three-body spin-exchange interactions", Phys. Rev. Lett. **132**, 133402 (2024).

[358] R. Chapurin, X. Xie, M. J. Van de Graaff, J. S. Popowski, J. P. D'Incao, P. S. Julienne, J. Ye, and E. A. Cornell, "Precision test of the limits to universality in few-body physics", Phys. Rev. Lett. **123**, 233402 (2019).

[359] X. Xie, M. J. Van de Graaff, R. Chapurin, M. D. Frye, J. M. Hutson, J. P. D'Incao, P. S. Julienne, J. Ye, and E. A. Cornell, "Observation of Efimov universality across a nonuniversal Feshbach resonance in ^{39}K", Phys. Rev. Lett. **125**, 243401 (2020).

[360] J. Wolf, M. Deiß, A. Krükow, E. Tiemann, B. P. Ruzic, Y. Wang, J. P. D'Incao, P. S. Julienne, and J. H. Denschlag, "State-to-state chemistry for three-body recombination in an ultracold rubidium gas", Science **358**, 921 (2017).

[361] J. Wolf, M. Deiß, and J. Hecker Denschlag, "Hyperfine magnetic substate resolved state-to-state chemistry", Phys. Rev. Lett. **123**, 253401 (2019).

[362] S. Haze, J. P. D'Incao, D. Dorer, M. Deiß, E. Tiemann, P. S. Julienne, and J. H. Denschlag, "Spin-conservation propensity rule for three-body recombination of ultracold Rb atoms", Phys. Rev. Lett. **128**, 133401 (2022).

[363] E. Haller, M. Rabie, M. J. Mark, J. G. Danzl, R. Hart, K. Lauber, G. Pupillo, and H.-C. Nägerl, "Three-body correlation functions and recombination rates for bosons in three dimensions and one dimension", Phys. Rev. Lett. **107**, 230404 (2011).

[364] M. Gröbner, P. Weinmann, E. Kirilov, H.-C. Nägerl, P. S. Julienne, C. R. Le Sueur, and J. M. Hutson, "Observation of interspecies Feshbach resonances in an ultracold ^{39}K $-^{133}$Cs mixture and refinement of interaction potentials", Phys. Rev. A **95**, 022715 (2017).

[365] L. Reichsöllner, A. Schindewolf, T. Takekoshi, R. Grimm, and H.-C. Nägerl, "Quantum engineering of a low-entropy gas of heteronuclear bosonic molecules in an optical lattice", Phys. Rev. Lett. **118**, 073201 (2017).

[366] P. D. Gregory, M. D. Frye, J. A. Blackmore, E. M. Bridge, R. Sawant, J. M. Hutson, and S. L. Cornish, "Sticky collisions of ultracold RbCs molecules", Nature Comms. **10**, 3104 (2019).

[367] Research data are freely available from Zenodo at doi:`10.5281/zenodo.8403669`.

CHAPTER 7

ACKNOWLEDGEMENTS

"Better to light one candle with a friend than to curse the darkness alone."

— Celtic proverb

Science isn't just about the data and the experiments, it's about the people. And I have had the absolute privilege of encountering some pretty damn amazing people throughout my PhD.

I would like to begin by thanking my supervisor Hanns-Christoph for giving me the opportunity to work in Cs III. For trusting me and giving me the freedom to pursue my interests. Throughout this journey, there were probably two people that had the biggest positive impact on the trajectory of my PhD. Firstly, Manuele who not only brought structure to the group, but also an amazing store of technical knowledge. He was always available for discussion and questions and is amazing at troubleshooting, even from a distance. Secondly, Sudipta. I couldn't have asked for a better person to share the lab with! Not only does he have a true passion for physics that is infectious, and an unmatched intuition for every situation, be it for troubleshooting a PID or analyzing data, or understanding the dynamics of an impurity in a Tonks gas, but he is also an extremely kind person. It has been an absolute delight working with you!

I want to thank our theory collaborators. Especially, Misha for all of the long discussions and the occasional watermelons - but you do still owe Cs III a tour of Paris (!). Also thank you to Alvise for your endurance over the years! And thank you to Elisabeth and Michael for their patience and professionalism.

Thank you also to the ultracold community in Innsbruck. Over the years, there have been too kind people to mention, many of whom I have probably forgotten in this list, but who were an equal joy to be around. Thank you to: Deborah, Anamika who was there to talk when I needed it most, Rianne, Andreas, Dario, Camilo who has a fantastic sense of humor, Arpita, Charly, Krysztof who's poetry remains unrivaled, Saloni, Satwik who's swag lights up every room that he enters,

Reza, Luisa, Karthik who is just full of incredible kindness and compassion, Emilio, Xaver, and Good who always brings a bit of joy with him. Specifically also thank you to Cornee for all those amazing trips that he took me on (despite my fear of heights), and for always lead climbing and setting up a top rope for me. A very special thanks to Erich and Gregor for all those wonderful cooking and board game evenings. They are memories that I cherish.

This list would not be complete without acknowledging the wider staff in the building. So thank you to, Manuela and Verena. To Babara, who always went far beyond her job and even took us on hikes and mushroom hunts and introduced us to some curious Tyrolean traditions. A big thank you also to Heide who is a secret guardian of the department and always there for anyone who needs a caring hand. Thank you to the electronic and mechanical workshop: Wolfgang, Kilian, who helped out with countless PID issues and Armin, Christoph and Toni who's work was always perfection.

Throughout the years there were uncountable moments of kindness that probably bore no significance to that person themselves but meant the world to me. Here I would like to mention just a few. Firstly, I am grateful to Katherina for the kindness that she showed me at the beginning of my PhD, and the crash course that she gave me of the lab! To Mariusz, who visited on a sabbatical for a few months during the first years of my PhD and not only brought a wealth of knowledge about every detail of the lab with him, but an equal amount of enthusiasm and joy. Emil for looking out for me over the years and always taking a moment to chat. Tracy, my second supervisor, for the support and encouragement. And also thank you to Niels for cheering me on from a distance.

Outside of university, I would also like to mention Lukas and Bernhard. Sarah, who has always been the coolest person that I know and who is just full of so much kindness and generosity. It is something one can only aspire to! I am truly grateful to be able to call you a friend!

I also want to thank my family for their incredible love and support throughout! Especially thank you to Sebastian, who was always there during the hardest times. For the first years when I was by myself in the lab he became like an honorary member of Cs III. I am internally grateful to be able to have someone like you in life to be able to call upon for advice or just a simple chat. Thank you also to Stephanie, who was there from the the beginning. Not hesitating to help me to move even on her birthday! Thank you also to Lisi and Michi and the wonderful Rosa. Thank you to Raphael, and Lucy, for all of your advice and encouragement throughout the years. To Samuel, Isabelle, Felix and Inara for just being the greatest! Finally thank you to Erwin and Paula for all of your love and support!

Most of all thank you to my candle who lit up the darkness.